

Strategies for hydrogen evolution catalyst integration in Microbial Electrosynthesis



Sanne Mensje de Smit

Propositions

1. All electrochemical methods have potential invasive effects on microbial electrosynthesis (*This thesis*)
2. Ethylenediaminetetraacetic acid shows janus-like behaviour in microbial electrosynthesis systems (*This thesis*)
3. Scientific developments are accelerated by accurate and complete transfer of methods
4. Communication is the most crucial skill for interdisciplinary projects
5. We distance ourselves too far from meat production cycles to understand the impact of meat consumption
6. Collaborative European investments in the international railroad infrastructure are necessary to fight global warming

Propositions belonging to the thesis, entitled

“Strategies for hydrogen evolution catalyst integration in microbial electrosynthesis”

Sanne M. de Smit

Wageningen, 3 February 2023

Strategies for hydrogen evolution catalyst integration in microbial electrosynthesis

Sanne de Smit

Thesis committee

Promotors

Prof. Dr C.J.N. Buisman

Professor of Biological Recovery and Re-use Technology

Wageningen University & Research

Prof. Dr J.H. Bitter

Professor of Biobased Chemistry and Technology

Wageningen University & Research

Co-promotor

Dr. D.P.B.T.B. Strik

Associate Professor, Environmental Technology group

Wageningen University & Research

Other members

Prof. Dr. D.Z. Machado de Sousa, Wageningen University & Research

Dr. M. Kokko, Tampere University, Finland

Prof. Dr. P.E. de Jongh, Utrecht University

Dr. J. Rodrigo Quejigo, Electrochaea, Germany, München

This research was conducted under the auspices of the Graduate School for Socio-Economic and Natural Sciences of the Environment (SENSE).

Strategies for hydrogen evolution catalyst integration in microbial electrosynthesis

Sanne Mensje de Smit

Thesis

submitted in fulfilment of the requirements for the degree of doctor

at Wageningen University,

by the authority of the Rector Magnificus,

Prof. Dr. A.P.J. Mol,

in the presence of the

Thesis Committee appointed by the Academic Board

to be defended in public

on Friday 3 February 2023

at 1.30 p.m. in the Omnia Auditorium.

Sanne Mensje de Smit

Strategies for hydrogen evolution catalyst integration in microbial electrosynthesis

256 pages.

PhD thesis, Wageningen University, Wageningen, the Netherlands (2023)

With references, with summary in English and Dutch

ISBN: 978-94-6447-519-7

DOI: <https://doi.org/10.18174/582721>

Table of contents

Chapter 1: Introduction	7
Chapter 2: Cyclic Voltammetry is invasive on microbial electrosynthesis	23
Chapter 3: Trace metals from microbial growth media form <i>in situ</i> electro-catalysts	83
Chapter 4: Mixed trace metals from microbial growth medium act as hydrogen evolution catalyst during microbial electrosynthesis at high current density	121
Chapter 5: Methodology for in-situ microsensor profiling of hydrogen, pH, ORP and electric potential throughout 3D porous cathodes of (bio)electrochemical systems	153
Chapter 6: Alternating direction of catholyte forced flow through 3D-electrodes improves start-up time in microbial electrosynthesis at applied high current density	185
Chapter 7: General discussion	223
Summary	243



Chapter 1

General Introduction



1.1 CO₂ valorisation to reduce greenhouse gas emissions

With industrialization, technological developments have not only brought greater convenience, but also increased emissions of environmental pollutants, such as greenhouse gases (Figure 1.1)¹. Greenhouse gases absorb infrared (solar) energy in their molecular bonds, so increased emissions result in a global temperature rise. This temperature rise is detrimental for several species resulting in species loss and thus biodiversity decrease². On top of that, the Intergovernmental Panel on Climate Change has predicted that the Climate Change, induced by the high emissions of greenhouse gases, can result in extreme weather events, such as drought, heavy precipitation or storms³. These extreme weather events will affect agriculture and challenge the global food supply², but also affect infrastructure and buildings³. The increased amounts of greenhouse gases also affect marine life: acidification of oceans due to higher dissolved carbon dioxide (CO₂) concentrations⁴ decreases the amount of calcite (CaCO₃), which forms the building material for all shell-forming marine organisms (e.g. molluscs). Higher greenhouse gas emissions therefore endanger both terrestrial and marine life⁵.

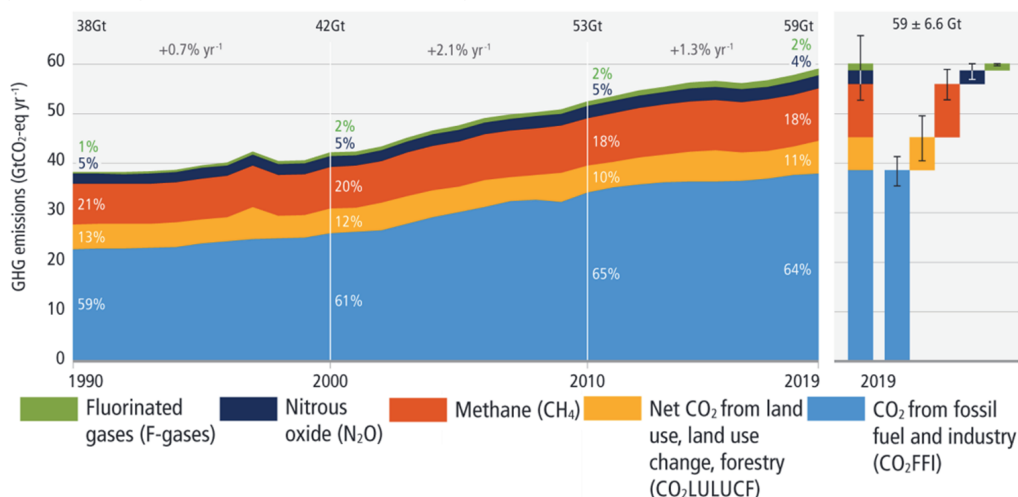


Figure 1.1. Annual greenhouse gas emissions, with CO₂ emissions divided over two categories (yellow and blue). Source: IPCC 2022 report: *Mitigation of climate change*⁶.

To prevent the abovementioned scenarios from deteriorating, greenhouse gas emissions need to be decreased. This global issue was divided into national challenges in 2015, when 195 countries signed the climate agreement in Paris on achieving net-zero greenhouse gas emissions by 2050. Achieving 0 greenhouse emissions requires mitigation measures in different sectors, e.g. agriculture, forestry, buildings, transport, energy and industry⁶. In this thesis, the focus will be on the greatest fraction of greenhouse gases: CO₂ in industrial emission streams (Figure 1.1). For certain industries, e.g. fermentation processes, CO₂ production is unavoidable⁷. To get rid of the CO₂, industries can e.g. change to renewable energy sources that don't net emit CO₂ or capture and store or utilise their CO₂ emissions. Storage of CO₂ can be performed by mineralization to carbonates, and utilisation can be performed by valorisation of CO₂ into valuable and sustainable chemicals⁸. Upgrading of industrial CO₂ by valorisation to valuable and sustainable chemicals is attractive since it contributes to reuse of waste streams and carbon storage in chemical precursors.

1.2 Electrochemical CO₂ valorisation by electrosynthesis

Due to the thermodynamic stability of CO₂ all CO₂ valorisation processes need energy like chemical energy (from co-substrates), thermal energy (heat) or sunlight (during photosynthesis). The use of sunlight is an age-old example: conversion of CO₂ to sugars with energy from sunlight during photosynthesis by plants and some microorganisms. More recently, in 1954, a similar process was discovered: conversion of CO₂ to chemicals with electrical energy during electrochemical reduction of CO₂⁹. Since then, the use of electrical energy has become more attractive in the transition of fossil to renewable energy sources. Renewable energy has become more and more abundant. In 2019, solar panels and wind turbines provided over 13 million terajoules of energy worldwide¹⁰. These sources of renewable energy do not produce electricity at a constant rate, but show variations over different periods of the day or year, dependent on the temporarily available solar or wind power¹¹. This excess intermittent energy can be used for electrochemical CO₂ reduction to lower the CO₂ oxidation state and in this way work towards net-zero emissions.

In general electrochemical CO₂ reduction can be described by two electrode reactions (Figure 1.2). At the anode, water is split into oxygen, protons and electrons. The electrons are continuously moving to the cathode as a current, where typically a catalyst facilitates the reduction of CO₂. Different products can be obtained from the CO₂ reduction reaction, depending on the potential applied to the cathode and the catalyst present at the cathode (Figure 1.2). The catalyst plays an important role, besides determining the product spectrum of the CO₂ conversion and thus the reaction selectivity, it also influences the reaction rate¹². Next to the metal-based catalysts in electrochemical CO₂ reduction (Figure 1.2)¹², microbial catalysts can be used for electrochemical CO₂ reduction (Figure 1.3). The advantage of combining electrochemical CO₂ reduction with a microbial catalyst is the possibility to form multicarbon (>C₂) compounds.

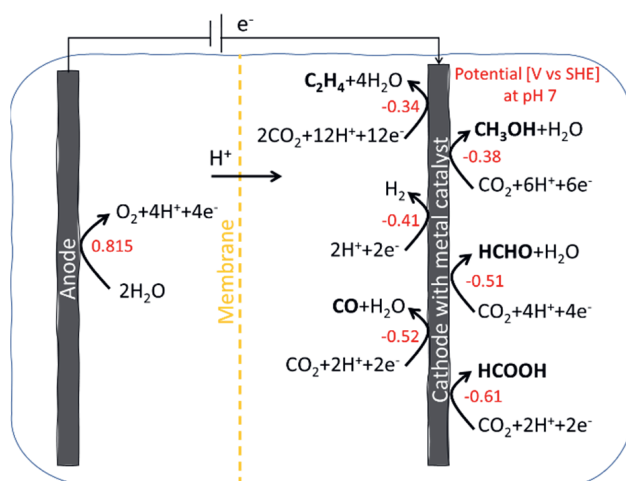


Figure 1.2. Overview of different electrochemical CO₂ reduction reactions. At the anode, electrons are generated by oxidation of water. At the cathode, electrons are used for CO₂ reduction reactions. Depending on the electrode potential (in red) and the catalyst, various products (bold) can be formed.

1.3 CO₂ valorisation by microbial electrosynthesis yields carboxylic acids

Microbial catalysts cover a different product spectrum compared to chemical catalysts¹³. Microbial electrosynthesis with CO₂ as substrate usually results in either methane (C1) or acetate (C2)¹⁴, depending on the microbial species that are enriched in the system. Methane can be used for power to gas applications, while acetate forms a precursor for the formation of platform chemicals, such as medium chain fatty acids. Within microbial electrochemistry systems, acetate can be reduced to medium chain fatty acids, such as the carboxylates *n*-butyrate (C4) and *n*-caproate (C6), within the same system^{15,16} (Figure 1.3). Both *n*-butyrate and *n*-caproate have many applications in the pharmaceutical, chemical and food and beverage industry¹⁷. The market for carboxylic acids accounted for 13.7 billion euros in 2020, with a predicted growth rate of 5.3% during the coming ten years¹⁸. *N*-caproate is a valuable compound with a market value (per ton or per electron) almost two times higher than the value of *n*-butyrate¹³.

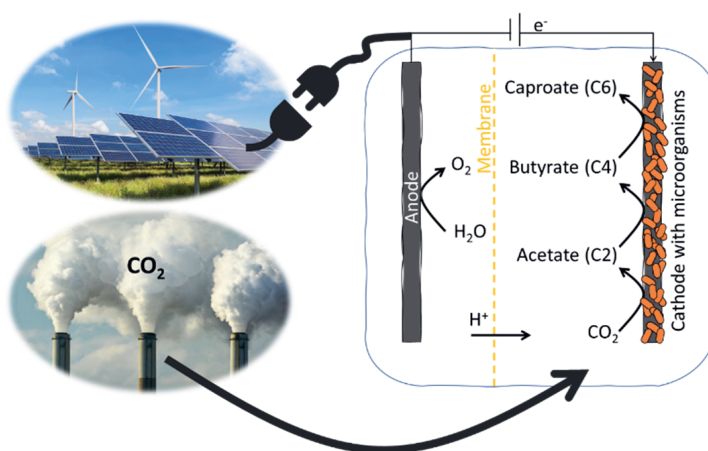


Figure 1.3. Microbial electrosynthesis of medium chain fatty acids from CO₂.

Bio-electrochemical conversion of renewable energy and CO₂ to medium chain fatty acids would offer a sustainable alternative for the current commercial production process. *N*-butyrate is currently commercially produced by the liquid-phase oxidation (with O₂) of propene-based *n*-butyric aldehyde, the latter being petroleum based¹⁹. *N*-caproate is not obtained from the petroleum industry, but mainly formed from coconut or palm kernel oil¹⁹. Microbial production of these fatty acids offers an alternative that does not depend on the petroleum industry or compete with the food industry. Further advantages of microbiological carboxylic acid production are higher selectivity, milder process conditions and possibilities to work with complex inflow streams or even waste streams^{8,19,20}. An example of this can be found in a pilot plant facility in Amsterdam, where Chaincraft is converting acidified organic waste to medium chain fatty acids²¹.

During the chain elongation process performed by Chaincraft, ethanol is supplied as microbial energy source. The ethanol needs to be transported and supplied from external sources, a process step that could be avoided when an electrode forms the microbial energy source. However, to electrify the CO₂ valorisation into fatty acids, some challenges need to be tackled.

An important challenge is a low electron availability for microorganisms in bio-electrochemical systems. During bio-electrochemical CO₂ reduction, bacteria or Archaea use electrons from the cathode as energy input. These microorganisms can grow either suspended in the electrolyte (reactor liquid) and/or in a biofilm attached to the electrode, depending on e.g., substrate availability, hydraulic retention time and their electron uptake mechanism²². Apart from electrons and CO₂, the microorganisms also need macro- and micronutrients, which are supplied via a biotic medium catholyte. The micronutrients or trace elements are used as e.g. part of (extra)polymeric structures²³ or as enzyme co-factor^{22,24-26}, but could potentially also form an electrocatalyst at the cathode.

1.4 Microbial electron uptake improvement for CO₂ valorisation

For the uptake of electrons by the microorganisms, different mechanisms have been proposed:

- Some bacteria are capable of direct electron transfer with the electrode, with membrane-bound enzymes that are reduced and oxidized to facilitate the transport of electrons over the membrane into the microbial cells²⁷
- Other microorganisms can form conductive pili, or nanowires with many aromatic structures to allow electron transfer²⁸
- Besides direct electron transfer, more common mechanisms are indirect electron transfer, where a mediator compound is reduced at the cathode and oxidized by the microorganisms and thus works like an electron shuttle between the electrode and the microbial community.

Examples of mediator compounds range from inorganic compounds, e.g. hydrogen and several metal ions to organic compounds, e.g. cytochromes and NADH^{22,29}. For most microorganisms conclusive information regarding their electron transfer mechanisms is still lacking. Some microorganisms have shown abilities to change between different electron uptake mechanisms based on reactor conditions^{30,31}. In bio-electrochemical CO₂ valorisation reactors, several studies have observed that improved hydrogen production led to higher productivity^{16,32-34}. Therefore, strategies to improve the hydrogen availability in bio-electrochemical systems will tackle the challenge of low electron availability.

The state of art, industrial scale technology for microbial CO₂ valorisation with hydrogen as energy source is electro-fermentation. In electro-fermentation processes, a dual stage approach is used where hydrogen is produced with an electrolyser and subsequently supplied to a fermentation reactor. An example of such industrial scale electro-fermentation process is power to methane. Microbial production of methane from CO₂ and electricity is at demonstration plant scale: Electrochaea is performing microbial CO₂ methanation with a patented Archaea culture that is fed with hydrogen externally produced in an electrolyser, with pressurized bioreactor plants operating with productivities up to 250 m³ methane per m³ reactor volume per day^{35,36}. This plant shows the applicability of microbial catalysts for the utilisation of CO₂ and electricity.

Bio-electrochemical reduction of CO₂ into medium chain fatty acids allows for the valorisation of waste streams (e.g. CO₂ off gas, wastewater). The conversion of CO₂ to short (C1-C5) and medium (C6-C12) chain fatty acids is proposed to be a multiple step process (Figure 1.3). For

the first step, CO₂ is converted to acetate by autotrophic microorganisms capable of acetogenesis, via the Wood-Ljungdahl pathway²⁴ (Table 1.1, reaction 2). The consecutive steps are chain elongation steps, where acetate is elongated with 2 carbon atoms at the time via e.g. the reverse β oxidation pathway³⁷, first to *n*-butyrate (Table 1.1, reaction 3) and consecutively the *n*-butyrate elongation to *n*-caproate (Table 1.1, reaction 4)³⁸.

Table 1.1. Possible reaction mechanisms for different steps of CO₂ conversion to *n*-caproate. For reactions 2-4, H₂ is presented as (example) electron donor. Two competing reactions yielding methane (CH₄) are shown in grey.

Nr	Name	Reaction mechanism
1	Hydrogen evolution reaction ³⁹	$2H^+ + 2e^- \rightarrow H_2$
2	Acetogenesis ⁴⁰	$2CO_2 + 4H_2 \rightarrow CH_3COO^- + H^+ + 2H_2O$
3	Acetate elongation to <i>n</i> -butyrate ⁴¹	$2CH_3COO^- + 2H_2 + H^+ \rightarrow CH_3(CH_2)_2COO^- + 2H_2O$
4	<i>N</i> -butyrate elongation to <i>n</i> -caproate ⁴¹	$CH_3COO^- + CH_3(CH_2)_2COO^- + 2H_2 + H^+ \rightarrow CH_3(CH_2)_4COO^- + 2H_2O$
5	Hydrogenotrophic methanogenesis ⁴²	$CO_2 + 4H_2 \rightarrow CH_4 + 2H_2O$
6	Acetoclastic methanogenesis ⁴³	$CH_3COO^- + H^+ \rightarrow CH_4 + CO_2$

Known microorganisms performing the acetate and *n*-butyrate elongation are heterotrophic microorganisms⁴⁴. Since different microorganisms perform the different steps of the CO₂ conversion to carboxylates, the combination of all three steps within one system requires the presence of different microorganism species. This combination can be made in a defined co-culture or in a mixed culture. In the latter, no sterilization measures need to be taken, which is especially attractive when working with waste stream inflows⁴⁵. The microorganisms in mixed CO₂ reduction cultures typically grow in a biofilm on the cathode⁴⁶. A challenge to realize bio-electrochemical CO₂ valorisation into volatile fatty acids is the biofilm thickness¹⁵, which can cause mass transfer limitations⁴⁷. A disadvantage from working with mixed cultures is that microorganisms performing undesired or competitive conversions can also grow in the cathode. For example, CO₂ and acetate can also be converted to methane by methanogenic Archaea⁴⁸ (Table 1.1, reaction 5-6). Methane formation is usually undesired since it has a lower value than the carboxylates⁴⁹⁻⁵². To steer product selectivity in mixed microbial cultures, selective pressure can be applied to influence biological growth rates of different species, e.g. by operating the system with inhibiting compounds, or at certain pH or temperature or by adjusting the CO₂ and H₂ levels^{49,53}.

In 2018¹⁵, the first proof of principle study was published which showed bio-electrochemical production of fatty acids up to *n*-caproate from pure CO₂ as single carbon source. In this study, production rates of 9.8 g acetate L⁻¹day⁻¹, 3.2 g *n*-butyrate L⁻¹day⁻¹ and 0.95 g *n*-caproate L⁻¹day⁻¹ were achieved. The process also showed high efficiency, 60-88% of the supplied electrons was recovered into the aforementioned products. Additionally, the microbial electrosynthesis system showed robust continuous operation over one year, which displays process stability¹⁵. After this promising study, Jourdin, et al.¹³ performed a techno-economic analysis to investigate whether a business case could be feasible for bio-electrochemical conversion of CO₂. From the techno-economic analysis, it was concluded that the state-of-the-art performance and process parameters were not yet resulting in a viable business case. However, with improvements in the

performance and configuration of the microbial electrosynthesis system for CO₂ conversion, a profitable business case could be built¹³. One way to improve the performance is enhancing the electron availability for microorganisms. Since increased hydrogen availability has led to higher productivity in earlier work, this PhD thesis aimed to enhance the electron availability for the microorganisms by developing strategies for hydrogen evolution catalysts. The strategies development included investigating the catalysing function of the trace elements normally added via the microbial medium, developing a new start-up strategy with increased electron availability and creating steering mechanisms for improved mass-transfer to the microbial community.

1.5 Strategies for hydrogen evolution catalysts use in microbial electrosynthesis

In the state of art studies of bio-electrochemical CO₂ valorisation, the start-up of *n*-butyrate and *n*-caproate production from CO₂ are slow, with concentrations up to 20 mM C (carbon) *n*-butyrate after 20 days¹⁶, while *n*-caproate was only detected after at least 100 days^{15,54}. This slow start up time for the production of multi carbon compounds leads to low process efficiency and high operating costs¹³, which is a disadvantage from a process engineering perspective. To pursue faster start-up, productivity stimulating parameters were investigated. Acetate production from CO₂ occurred already at high rates^{15,55}, but the transition from acetate to longer carboxylate production took longer due to the requirement for both certain acetate concentrations (suggested 2-4 g/L¹⁵) and high current densities ($\sim > 2$ kA/m³ cathode^{15,16}). In the study from Jourdin, et al. ¹⁵, a 3-fold increase in current density was observed at day 175 after start-up, interestingly after a system analysis with a cyclic voltammetry scan. During such a cyclic voltammetry scan, the electrode potential is increased and decreased in a cyclic manner^{56,57}. After this increase in current, *n*-butyrate production started and was followed by *n*-caproate production within 20 days. It was hypothesised that the cyclic voltammetry analysis triggered the current density increase and consequently the production of *n*-butyrate and *n*-caproate. To further elucidate the mechanisms behind the current increase, the aim of **Chapter 2** was to investigate the effects of the cyclic voltammetry scan on microbial electrosynthesis.

1.5.1 Investigating the effects of cyclic voltammetry scan in microbial electrosynthesis

In **Chapter 2**, we show that the changing potential of the cyclic voltammetry scan causes the release of metal compounds originating from trace elements and biomass structures from the cathodes into the electrolyte. Trace elements are supplied to the bio-electrochemical systems via the microbial medium as metal salts. The metal cations of these salts will be attracted by the negatively charged electrode surface and, at certain cathode potentials, be reduced and deposited in solid form at the cathode⁵⁸. When bio-electrochemical systems are operated over long time, such as the 175 days in the study of Jourdin, et al. ¹⁵, trace elements will accumulate on the cathode surface over time. During the cyclic voltammetry scan, the electrode potential is changed which caused the release of the attached trace elements from the cathode. After the cyclic voltammetry scan, the released, high amount of trace elements attached to the cathode simultaneous with the current increase, so it was hypothesised that the attachment of trace

elements to the cathode caused the current increase (Figure 1.4, chapter 2). To further investigate this, **Chapter 3** aimed to investigate the catalysing role of trace metal compounds.

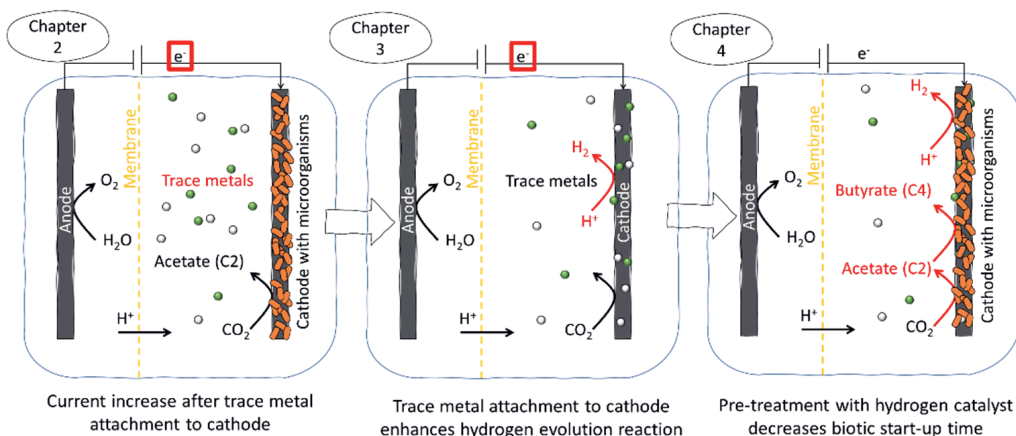


Figure 1.4. Overview of main findings (in red) in the first three research chapters (numbered 2-4) in this PhD thesis. Below each sub-image, the most important conclusions are written.

1.5.2 Catalysing role of trace metal compounds

To study the effect on the current, a concentrated trace element solution was added to an electrochemical reactor without microorganisms. It was discovered that the addition of a concentrated trace element solution results in the attachment of the trace elements on the cathode. With the attachment of these elements, a hydrogen evolution catalyst is formed on the cathode (Figure 1.4, chapter 3). With the addition of the trace metal mix, the hydrogen production was increased up to 28 times. A hydrogen evolution catalyst is a metal-based or microbial catalyst that increases the rate of hydrogen formation at the cathode and decreases the required overpotential (energy input). Since hydrogen is suggested to be an important electron donor in bio-electrochemical CO_2 valorisation, the formation of a hydrogen evolution catalyst can boost the electron bioavailability in bio-electrochemical systems. The electron bioavailability was hypothesized to be one of the limiting factors for fast start-up of multi carbon compound ($>C_4$) formation from CO_2 .

However, to form a hydrogen evolution catalyst, specific experimental conditions are required. Differences in e.g. crystallographic orientation of the metal, support material will result in different reaction rates and product spectra, so metal catalysts are often modified for performance optimisation¹². During modification, the crystal face of the catalyst is influenced by parameters such as metal concentrations during crystallization⁵⁹, addition of a different metal or a metal oxide¹², atmosphere and temperature⁶⁰. Therefore, the aim of **Chapter 4** was to investigate the feasibility of integrating a trace metal mix-based hydrogen evolution catalyst in microbial electrosynthesis systems with microbial compatible conditions.

1.5.3 Integrated trace metal mix hydrogen evolution catalyst in microbial electrosynthesis

In **Chapter 4**, a hydrogen evolution catalyst was integrated in bio-electrochemical systems for CO_2 valorisation. After start-up of the electrochemical CO_2 valorisation system, *n*-butyrate

production was observed after 20 days, with concentrations up to 100 mM C after 40 days (Figure 1.4, chapter 4). The metal compounds from the trace metal mix remained quite stable on the cathode during the biotic operation. To identify the microbial community, the active microorganisms in the acetogenesis and chain elongation conversions were studied. In our studies, the microorganisms were mainly found in biofilms attached to the cathode. Microorganisms typically form biofilms by adhering to an electrode surface and subsequently excreting so called extracellular polymeric substances to form film-like structures⁴⁶. In developed systems, biofilms can become several millimetres thick¹⁵. Especially at high thickness, diffusion is limited, and mass transfer limitations can be expected⁴⁷. Mass transfer of substrates, protons and products occurs through the biofilm via channels or diffusion^{46,61}. To monitor mass-transfer and the limitations thereof, it is of great importance to monitor not only bulk conditions and concentrations, but also local conditions and concentrations. Therefore, in **Chapter 5**, the aim was to develop a method for *in situ* measurement of local concentration gradients.

1.5.4 Developed method for *in situ* measurement of local concentration gradients

In **Chapter 5**, a method is developed to measure local concentration gradients of e.g. hydrogen, pH and oxidation reduction potential with microsensors. An adapted reactor design allows for the *in situ* monitoring of these (and other) parameters whilst maintaining the electrolyte recirculation and electron supply to the cathode (Figure 1.5, chapter 5). Especially the measurements of pH and oxidation reduction potential was not performed inside microbial electrosynthesis cathodes before, since the presence of an electric field would interfere with the microsensors. In **Chapter 5**, a method to overcome this interference is described, with protocols and video instructions for the application of the microsensors. During this study, significant gradients of hydrogen were found throughout the depth of the cathode, showing that the hydrogen was not distributed homogeneous throughout the biofilm. To facilitate better transfer of hydrogen to the biofilm, **Chapter 6** aimed to apply a new recirculation flow-through regime to facilitate better hydrogen transfer to the microorganisms during start-up at high current density.

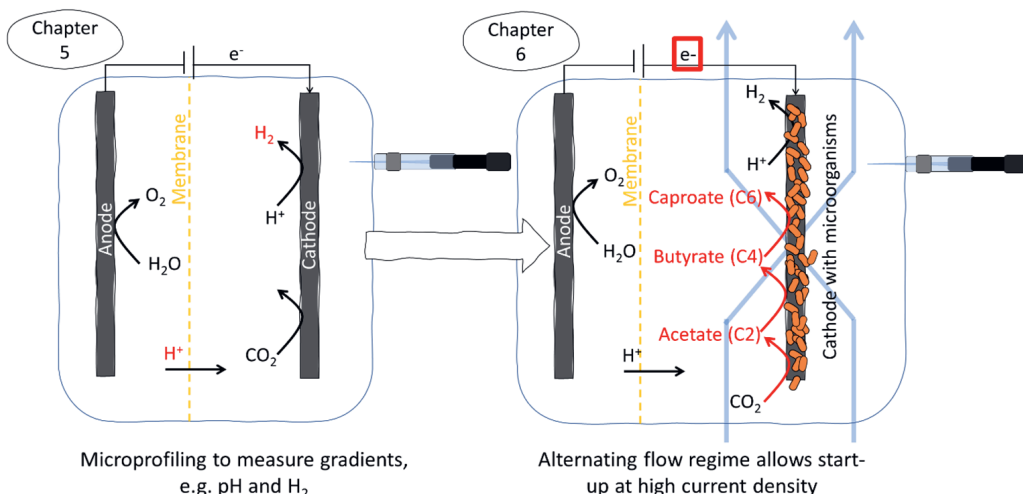


Figure 1.5. Overview of main findings (in red) in the last two research chapters (numbered 5-6) in this PhD thesis. Below each sub-image, the most important conclusions are written.

1.5.5 New recirculation flow-through regime for start-up at high current density

Different flow configuration strategies were tested in **Chapter 6**. The optimization of mass transfer has been the focus of some studies, in which three-dimensional flow-through cathodes are used to force the recirculation flow through the cathodes⁶². However, this caused issues at high current densities due to the build-up of surplus hydrogen gas between the electrode and the membrane. The build-up gas resulted in high resistances leading to high energy input to overcome the resistance. To solve the issue, an alternating flow-through strategy was tested in which the recirculation flow input of the electrochemical reactor was alternated between two locations at both sides of the cathode. This alternating flow-through regime allowed for alternating release of the gas build up and hydrogen transfer to the biofilm layers at the cathode. Bio-electrochemical CO_2 valorisation systems were successfully started at high current density with the alternating flow-through strategy (Figure 1.5, chapter 6). *N*-caproate was observed 45 days after the start-up.

1.6 Outlook and future applications

Finally, in the general discussion in **Chapter 7**, an outlook is presented for the developed process. Since the importance of hydrogen production became evident, another method to supply external electrocatalytic hydrogen is discussed, and compared to the integrated hydrogen evolution catalyst discovered in this thesis. The integration of the discovered hydrogen evolution catalyst and the alternating flow-through strategy allow for fast start-up of medium chain fatty acid production and *in situ* hydrogen production. The developed method to measure microprofiles of concentration gradients can be widely applied in mass-transfer studies. The microprofiling method can also be applied in future upscaling studies, to investigate substrate and energy availability in different system designs.

Since the discovered hydrogen evolution catalysts showed to enhance hydrogen formation under microbial compatible conditions and with relatively complex catholyte (containing buffer salts, microbial nutrients and microbial cells/cellular compounds), it is likely that the catalyst could be used in microbial electrosynthesis systems treating wastewater streams and/or gas streams with impurities. Besides the source of the substrates, also the source of the catalyst could be waste based. The hydrogen evolution catalyst was formed from a trace metal mix, so with further investigation, metal-rich waste sludges could be considered as potential source for the catalyst mix. With the work presented in this thesis, the conversion of waste streams (CO_2 , wastewater) to valuable products (volatile fatty acids up to C6) could be achieved. With upscaling, the improved method provides a sustainable alternative for the production of essential precursors for e.g. pharmaceuticals, chemicals, fuels and feed additives.

References

- 1 Allan, R. P., Hawkins, E., Bellouin, N. & Collins, B. IPCC, 2021: summary for Policymakers. (2021).
- 2 Abbass, K. *et al.* A review of the global climate change impacts, adaptation, and sustainable mitigation measures. *Environmental Science and Pollution Research*, 1-21 (2022).
- 3 IPCC. 1-3676 (Cambridge University Press. In Press Cambridge, 2022).
- 4 Cao, L. & Caldeira, K. Atmospheric CO₂ stabilization and ocean acidification. *Geophysical Research Letters* **35** (2008).
- 5 Doney, S. C., Fabry, V. J., Feely, R. A. & Kleypas, J. A. Ocean acidification: the other CO₂ problem. *Annual review of marine science* **1**, 169-192 (2009).
- 6 Shukla, P. *et al.* Climate Change 2022 Mitigation of Climate Change. (2022 Intergovernmental Panel on Climate Change, 2022).
- 7 Bains, P., Psarras, P. & Wilcox, J. CO₂ capture from the industry sector. *Progress in Energy and Combustion Science* **63**, 146-172 (2017).
- 8 Pan, S.-Y., Chiang, P.-C., Pan, W. & Kim, H. Advances in state-of-art valorization technologies for captured CO₂ toward sustainable carbon cycle. *Critical reviews in environmental science and technology* **48**, 471-534 (2018).
- 9 Teeter, T. E. & Van Rysselberghe, P. Reduction of carbon dioxide on mercury cathodes. *The Journal of Chemical Physics* **22**, 759-760 (1954).
- 10 Agency, I. E. *Total energy supply (TES) by source, World 1990-2019*, <<https://www.iea.org/data-and-statistics/data-browser?country=WORLD&fuel=Energy%20supply&indicator=TESbySource>> (2022).
- 11 Gowrisankaran, G., Reynolds, S. S. & Samano, M. Intermittency and the value of renewable energy. *Journal of Political Economy* **124**, 1187-1234 (2016).
- 12 Jones, J. P., Prakash, G. S. & Olah, G. A. Electrochemical CO₂ reduction: recent advances and current trends. *Israel Journal of Chemistry* **54**, 1451-1466 (2014).
- 13 Jourdin, L., Sousa, J., Stralen, N. v. & Strik, D. P. B. T. B. Techno-economic assessment of microbial electrosynthesis from CO₂ and/or organics: An interdisciplinary roadmap towards future research and application. *Applied Energy* **279**, doi:10.1016/j.apenergy.2020.115775 (2020).
- 14 Marshall, C. W., Ross, D. E., Fichot, E. B., Norman, R. S. & May, H. D. Electrosynthesis of commodity chemicals by an autotrophic microbial community. *Appl. Environ. Microbiol.* **78**, 8412-8420 (2012).
- 15 Jourdin, L., Raes, S. M. T., Buisman, C. J. N. & Strik, D. P. B. T. B. Critical Biofilm Growth throughout Unmodified Carbon Felts Allows Continuous Bio-electrochemical Chain Elongation from CO₂ up to Caproate at High Current Density. *Frontiers in Energy Research* **6**, doi:10.3389/fenrg.2018.00007 (2018).
- 16 Ganigué, R., Puig, S., Batlle-Vilanova, P., Balaguer, M. D. & Colprim, J. Microbial electrosynthesis of butyrate from carbon dioxide. *Chemical Communications* **51**, 3235-3238 (2015).
- 17 Szilagyi, M. Aliphatic carboxylic acids: Saturated. *Patty's Toxicology*, 471-532 (2001).
- 18 Market Research Future. *Global Carboxylic Acid Market Research Report*. <<https://www.marketresearchfuture.com/reports/carboxylic-acid-market-8238>> (2021).
- 19 Kubitschke, J., Lange, H. & Strutz, H. in *Ullmann's Encyclopedia of Industrial Chemistry* 1-18 (2014).
- 20 Jiang, L. *et al.* Butyric acid: Applications and recent advances in its bioproduction. *Biotechnology Advances* **36**, 2101-2117 (2018).
- 21 Hazards, E. P. o. B. *et al.* Evaluation of the application for a new alternative processing method for animal by-products of Category 3 material (ChainCraft BV). *EFSA Journal* **16**, e05281 (2018).
- 22 Kracke, F., Vassilev, I. & Krömer, J. O. Microbial electron transport and energy conservation—the foundation for optimizing bio-electrochemical systems. *Frontiers in microbiology* **6**, 575 (2015).

- 23 Wingender, J., Neu, T. R. & Flemming, H.-C. in *Microbial extracellular polymeric substances* 1-19 (Springer, 1999).
- 24 Ragsdale, S. W. & Pierce, E. Acetogenesis and the Wood–Ljungdahl pathway of CO₂ fixation. *Biochimica et Biophysica Acta (BBA)-Proteins and Proteomics* **1784**, 1873-1898 (2008).
- 25 Irving, H. & Williams, R. Order of stability of metal complexes. *Nature* **162**, 746-747 (1948).
- 26 Waldron, K. J., Rutherford, J. C., Ford, D. & Robinson, N. J. Metalloproteins and metal sensing. *Nature* **460**, 823-830 (2009).
- 27 Seelam, J. S., Pant, D., Patil, S. A. & Kapadnis, B. P. in *Microbial factories* 155-183 (Springer, 2015).
- 28 Shu, C., Xiao, K. & Sun, X. Structural basis for the high conductivity of microbial pili as potential nanowires. *Journal of Nanoscience and Nanotechnology* **20**, 64-80 (2020).
- 29 Lovley, D. R. & Nevin, K. P. Electrobiocommodities: powering microbial production of fuels and commodity chemicals from carbon dioxide with electricity. *Curr Opin Biotechnol* **24**, 385-390, doi:10.1016/j.copbio.2013.02.012 (2013).
- 30 Rotaru, A. E. *et al.* Direct interspecies electron transfer between *Geobacter metallireducens* and *Methanosarcina barkeri*. *Appl Environ Microbiol* **80**, 4599-4605, doi:10.1128/AEM.00895-14 (2014).
- 31 Walker, D. J. *et al.* Syntrophus conductive pili demonstrate that common hydrogen-donating syntrophs can have a direct electron transfer option. *The ISME journal* **14**, 837-846 (2020).
- 32 Bajracharya, S. *et al.* Carbon dioxide reduction by mixed and pure cultures in microbial electrosynthesis using an assembly of graphite felt and stainless steel as a cathode. *Bioresour Technol* **195**, 14-24, doi:10.1016/j.biortech.2015.05.081 (2015).
- 33 Blanchet, E. *et al.* Importance of the hydrogen route in up-scaling electrosynthesis for microbial CO₂ reduction. *Energy & Environmental Science* **8**, 3731-3744 (2015).
- 34 Flexer, V. & Jourdin, L. Purposely Designed Hierarchical Porous Electrodes for High Rate Microbial Electrosynthesis of Acetate from Carbon Dioxide. *Acc Chem Res* **53**, 311-321, doi:10.1021/acs.accounts.9b00523 (2020).
- 35 Angenent, L. T. *et al.* Upgrading anaerobic digestion within the energy economy—the methane platform. (2022).
- 36 Bailera, M., Lisbona, P., Romeo, L. M. & Espatolero, S. Power to Gas projects review: Lab, pilot and demo plants for storing renewable energy and CO₂. *Renewable and Sustainable Energy Reviews* **69**, 292-312 (2017).
- 37 Kallscheuer, N., Polen, T., Bott, M. & Marienhagen, J. Reversal of β -oxidative pathways for the microbial production of chemicals and polymer building blocks. *Metabolic engineering* **42**, 33-42 (2017).
- 38 Raes, S. M. T., Jourdin, L., Buisman, C. J. N. & Strik, D. P. B. T. B. Continuous Long-Term Bio-electrochemical Chain Elongation to Butyrate. *ChemElectroChem* **4**, 386-395, doi:10.1002/celc.201600587 (2017).
- 39 Lasia, A. Mechanism and kinetics of the hydrogen evolution reaction. *international journal of hydrogen energy* **44**, 19484-19518 (2019).
- 40 Jourdin, L., Lu, Y., Flexer, V., Keller, J. & Freguia, S. Biologically induced hydrogen production drives high rate/high efficiency microbial electrosynthesis of acetate from carbon dioxide. *ChemElectroChem* **3**, 581-591 (2016).
- 41 Raes, S. M., Jourdin, L., Buisman, C. J. & Strik, D. P. Bio-electrochemical Chain Elongation of Short-Chain Fatty Acids Creates Steering Opportunities for Selective Formation of n-Butyrate, n-Valerate or n-Caproate. *ChemistrySelect* **5**, 9127-9133 (2020).
- 42 Lyu, Z., Shao, N., Akinyemi, T. & Whitman, W. B. Methanogenesis. *Current Biology* **28**, R727-R732 (2018).
- 43 Mayumi, D. *et al.* Carbon dioxide concentration dictates alternative methanogenic pathways in oil reservoirs. *Nature communications* **4**, 1-6 (2013).

- 44 Batlle-Vilanova, P. *et al.* Microbial electrosynthesis of butyrate from carbon dioxide: production and extraction. *Bioelectrochemistry* **117**, 57-64 (2017).
- 45 Angenent, L. T. *et al.* Chain elongation with reactor microbiomes: open-culture biotechnology to produce biochemicals. *Environmental science & technology* **50**, 2796-2810 (2016).
- 46 Sevdá, S. *et al.* Biofilm formation and electron transfer in bio-electrochemical systems. *Environmental Technology Reviews* **7**, 220-234 (2018).
- 47 De Lichterfelde, A., Ter Heijne, A., Hamelers, H., Biesheuvel, P. & Dykstra, J. Theory of ion and electron transport coupled with biochemical conversions in an electroactive biofilm. *Phys. Rev. Appl.* **12**, 014018 (2019).
- 48 Leahy, S. C. *et al.* The genome sequence of the rumen methanogen *Methanobrevibacter ruminantium* reveals new possibilities for controlling ruminant methane emissions. *PloS one* **5**, e8926 (2010).
- 49 Molenaar, S. D. *et al.* Competition between methanogens and acetogens in biocathodes: a comparison between potentiostatic and galvanostatic control. *International journal of molecular sciences* **18**, 204 (2017).
- 50 Jourdin, L. & Burdyny, T. Microbial electrosynthesis: where do we go from here? *Trends in Biotechnol.* **39**, 359-369 (2021).
- 51 Izadi, P., Fontmorin, J.-M., Godain, A., Yu, E. H. & Head, I. M. Parameters influencing the development of highly conductive and efficient biofilm during microbial electrosynthesis: the importance of applied potential and inorganic carbon source. *npj Biofilms and Microbiomes* **6**, 1-15 (2020).
- 52 Bajracharya, S. *et al.* Long-term operation of microbial electrosynthesis cell reducing CO₂ to multi-carbon chemicals with a mixed culture avoiding methanogenesis. *Bioelectrochemistry* **113**, 26-34 (2017).
- 53 de Araújo Cavalcante, W., Leitão, R. C., Gehring, T. A., Angenent, L. T. & Santaella, S. T. Anaerobic fermentation for n-caproic acid production: A review. *Process Biochemistry* **54**, 106-119 (2017).
- 54 Vassilev, I. *et al.* Microbial electrosynthesis of isobutyric, butyric, caproic acids, and corresponding alcohols from carbon dioxide. *ACS Sustainable Chemistry & Engineering* **6**, 8485-8493 (2018).
- 55 Jourdin, L. *et al.* High Acetic Acid Production Rate Obtained by Microbial Electrosynthesis from Carbon Dioxide. *Environ Sci Technol* **49**, 13566-13574, doi:10.1021/acs.est.5b03821 (2015).
- 56 Elgrishi, N. *et al.* A Practical Beginner's Guide to Cyclic Voltammetry. *Journal of Chemical Education* **95**, 197-206 (2017).
- 57 Harnisch, F. & Freguia, S. A basic tutorial on cyclic voltammetry for the investigation of electroactive microbial biofilms. *Chemistry—An Asian Journal* **7**, 466-475 (2012).
- 58 Perez, N. *Electrochemistry and corrosion science*. 209 (Springer, 2004).
- 59 Schubert, U. S. & Hüsing, N. *Synthesis of inorganic materials*. (John Wiley & Sons, 2019).
- 60 Smovzh, D., Boyko, E. & Kostogrud, I. in *Journal of Physics: Conference Series*. 012109 (IOP Publishing).
- 61 Pereira, J. *et al.* Real-time monitoring of biofilm thickness allows for determination of acetate limitations in bio-anodes. *Bioresource Technology Reports* **18**, 101028 (2022).
- 62 Katuri, K. *et al.* Three-dimensional microchanelled electrodes in flow-through configuration for bioanode formation and current generation. *Energy & Environmental Science* **4**, 4201-4210 (2011).



Chapter 2

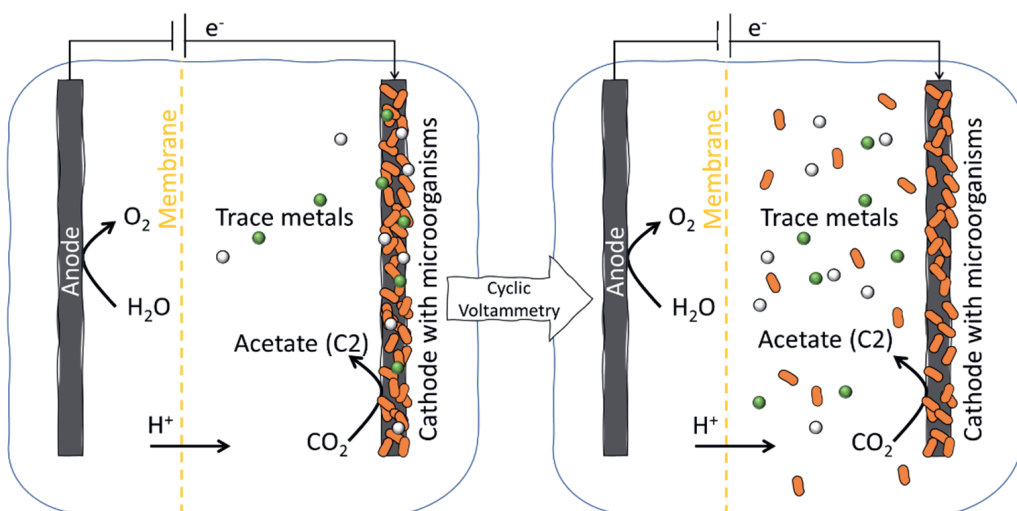
Cyclic Voltammetry is invasive on microbial electrosynthesis



Published as: de Smit, S. M., Buisman, C. J. N., Bitter, J. H. & Strik, D. P. B. T. B. Cyclic Voltammetry is invasive on microbial electrosynthesis. *ChemElectroChem* **8**, 3384-3396 (2021).

Abstract

Cyclic Voltammetry (CV) can be expected to cause changes in the biocathode composition, especially when using low scan rates. A recent finding stated that CV triggered further biocatalytic activity in Microbial Electrosynthesis Systems (MES), leading to the aim of our study: to investigate the invasiveness of CV on MES. The present study confirms that a CO_2 elongation MES biocathode composition changes during and right after the CV. Oxidation peaks differ over repeated CV-cycles while metal compounds and biomass were released in the biocatholyte. After CV, the current increased temporarily for up to 20 days and the metal compounds decreased, from the biocatholyte solution. Further, the sole short application of open cell voltage was shown to shortly increase the current. Evidently CV affects the studied biocathode which complicates the use of CV as an analysis technique in MESs. However, the positive effect CV can have on biocathode current density may provide methods to boost reactor performance and maintain productivity.



2.1 Introduction

Microbial electrosynthesis (MES) is a promising emerging technique for carbon capture and utilization. MES systems consist of an anode and a cathode, where an oxidation and a reduction reaction occur, respectively. The anode and cathode chamber are in most systems separated by a membrane and filled with electrolyte¹. The electrons resulting from the oxidation reaction are transferred to the cathode where they are used as energy source. The reduction reaction at the cathode is catalysed by microorganisms, which grow either attached to the cathode as a biofilm or suspended in the catholyte²⁻⁹.

Various MES processes were developed to reduce CO₂ to methane, alcohols and/or elongated carboxylates up to six carbon-chains^{4,10}. The technique is promising due to a broad spectrum of biochemicals as products^{5,10} and the low use of water and arable land¹¹. Additionally, the increasing number of sustainable electrical energy sources make MES a promising alternative method for chemical production. However, since the systems are so multifaceted, many parts of the processes remain black boxes. To get more insights in e.g. electron transfer mechanisms, system resistances, mass transfer or electrocatalysts, a broad spectrum of electrochemical analysis techniques can be used.

In electrochemistry, Cyclic Voltammetry (CV) is used to study mechanisms, kinetics and irreversibility of homogeneous reactions¹², electrode kinetics^{13,14}, catalyst performance¹⁵ and electrode surface composition^{16,17}. E.g. metal electrodeposition is investigated by reversibly depositing and removing the compound from the electrode during CV¹⁸⁻²¹. A system with a microbial biofilm can be considered to be more complex compared to an abiotic electrochemical system. The electrochemical reactions that are catalysed by bacteria include multiple steps and transfer processes, especially when enzymatic catalysts are involved²². Furthermore, a biofilm contains many charged compounds and a pH gradient^{23,24} which both slow down charge transfer across the biofilm. The biofilm composition and productivity change over time as the biofilm develops²⁵. The electrolyte in bio-electrochemical systems is used as microbial medium and therefore contains multiple compounds, while the electrolytes in electrochemical experiments are often less complex²². Trace metals from the biotic medium could deposit on the cathode²⁶. The insights from a CV in a biotic system also differ from those in an abiotic system, biotic CVs are mostly used to indirectly measure biocatalytic activity^{3,6-8,22,27-32}, but also kinetic analysis²², electron transfer³³ and biofilm formation³⁴ can be studied with CV.

CV in bio-electrochemical systems is mostly performed with different settings compared to abiotic systems due to the different characteristics. For example, lower scan rates (1 mV/s) are applied in bio-electrochemical CVs^{35,36}, to allow the system to recover as much as possible from the potential change and thus minimize the effect of the capacitive current²². The disadvantage of this lower scan rate is the longer duration of the CV scan, which can affect the experiment. Ruiz, et al.³⁶ reported significant changes in the culture medium induced by low scan rate CVs in bio-electrochemical systems. Additional indications for invasive effects of CV were found by Jourdin, et al.⁴. They operated a bio-electrochemical system in which CO₂ was elongated to fatty acids at current densities up to -14 kA/m³ porous cathode. In some cases, after running a CV on a biocathode experiment, the current increased abruptly with 200% compared to before the CV. It was however not clear whether the biocathode composition changed during and/or

after the CV. Jourdin, et al. ⁴ suggested that CV enhances the current only when a fully developed biofilm is present since the CVs did not affect the current earlier in the same experiment. The mentioned increase of current has applicable relevance, as higher current densities leads to a higher availability of electron donors for (microbial) cathodic reactions. Although it is clear that CV may cause irreversible changes, especially at low scan rates, the effect of CV on the biocathode composition and microbial electrosynthesis system performance has never been studied before.

Therefore, our study objective was to investigate the invasiveness of cyclic voltammetry on the biocathode of a microbial electrosynthesis system⁴. We measured the effect of CV on system performance and biocathode composition during CO₂ elongation to acetate in a system comparable to that of Jourdin, et al. ⁴. The biotic reactor was inoculated with a mixed culture of microorganisms from various chain elongation processes^{4,11,37}. The effect on system performance is shown by the current response. Between long-term operation and the CV scan, open cell voltage (OCV) was shortly applied to switch the operation mode. Since the OCV goes paired with a change in cathode potential, the effects on current of OCVs as well as some operational difficulties (pH instability, reactor leakage) were investigated. The effect of CV on current was also studied in abiotic systems. Three sets of duplicate abiotic experiments were used to study the effect of a smaller potential range and of a longer application of reducing potentials during CV. Both the biotic and abiotic systems were operated in continuous mode with a 3D carbon felt electrode as used by Jourdin, et al. ⁴. The effect of CV on the biocathode composition was measured by monitoring the (bio)catholyte metal species elements concentrations (Al, Ba, Co, Cu, Fe, Mg, Mn, Mo, Ni and Zn) and optical density (i.e. biomass concentration) during and after the CV scan.

2.2 Experimental Section

2.2.1 Reactor setup and experimental conditions

Three continuous electrochemical cells built in the same way as by Jourdin, et al. ⁴ were used for this study. One reactor was used for the biotic experiment and six reactors were used as three duplicate abiotic reactors. The cathodes were made from carbon felt. The carbon felt was prepared by leaving it overnight in 1 M HCl, subsequently overnight in 1 M NaOH and finally overnight in demi water. Three layers of carbon felt were used, the size of the cathodes was 25.9 cm³. The carbon felt layers were held together by a titanium wire (grade 2) with 0.8 mm thickness, this wire was also used as current collector. The total volumes of the catholyte and anolyte were 345-442 ml and 301-351 ml, respectively including the recirculation tubing (Figure 2.1). The liquids from the catholyte and anolyte were recirculated at 12 L/h and 10 L/h, respectively. The catholyte recirculation rate was increased from 8 to 12 L/h on day 107 for the biotic reactor.

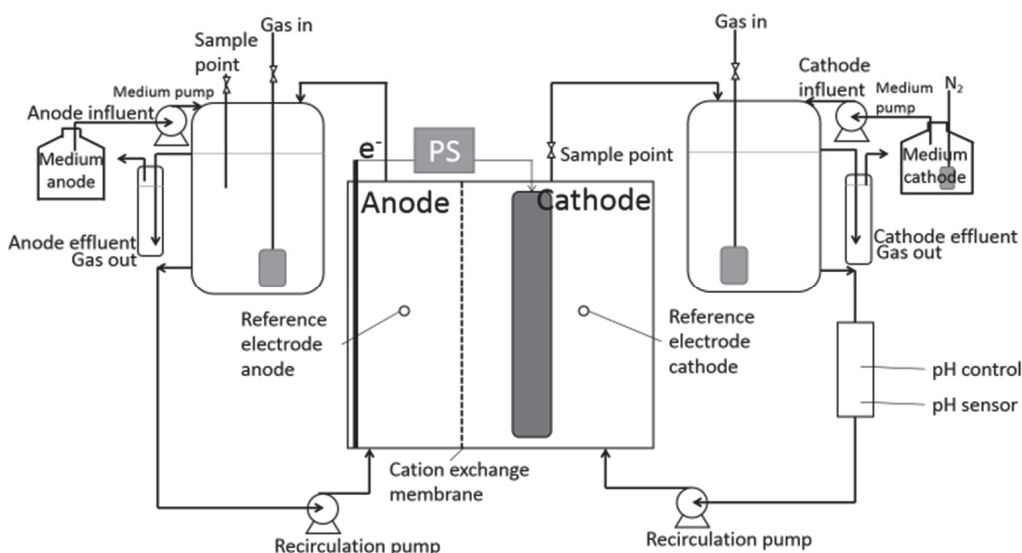


Figure 2.1. Schematic overview of the (bio)electrochemical cell setup.

The pH of the catholyte was controlled at 5.8 with addition of 1 M HCl and 1 M NaOH by a pH controller (Ontwikkelwerkplaats, Elektronica ATV, the Netherlands). The reactor potential was controlled at -0.85 vs SHE with the same potentiostat and reference electrodes (in 3 M KCl) as used by Jourdin, et al. ⁴. The current was measured every minute with the Ivium potentiostat as done by Jourdin, et al. ⁴. The reactors were situated in a cabinet in which the temperature was controlled at 30°C .

The samples were not taken with a needle but from a plastic sample port to prevent external addition of metals into the system. For the same reason, contact with metal sources was also avoided for all medium stocks and supplies. The sample port was placed directly after the cathode chamber in the recirculation to ensure the samples represented the catholyte next to the cathode.

The biotic reactor was run for 237 days and the abiotic experiments were run for 12 days (Table 2.1). The biotic reactor was inoculated with mixed culture consortiums from various chain elongation reactors on day 0, 98 and 112. The abiotic experiments were run for a shorter time to prevent microbial growth. The biotic reactor had neoprene gaskets, while the two abiotic reactors had silicone gaskets. CO_2 and N_2 were supplied via a gas sparger (spargerhead was 22 mm height and 12 mm diameter) in the catholyte recirculation bottle at 10 and 23.3 LN/d, respectively for the first phases of the biotic (58 days) experiment. During the second phase of the biotic and during the whole abiotic experiments, the catholyte gas supply was 100 LN CO_2 /d and 233.3 LN N_2 /d. The gas was led through a bottle filled with demi water to humidify the gas before flushing it into the reactor. The CO_2 formed the carbon source for chain elongation during the biotic experiments. The anolyte recirculation bottle was flushed with N_2 to flush away the formed O_2 .

Table 2.1. Overview of cyclic voltammetry, open cell voltage and pH effects performed with or occurred to the biotic reactor and the duplicate abiotic reactors.

	Biotic reactor					Abiotic reactors
Total run time	237					12
Cyclic Voltammetry	CV1	CV2	CV3	CV4	CV5	Abiotic CV
Day CV	125	133	147	174	224	8
Open Cell Voltage	OCV1	OCV2	OCV3	OCV4	OCV5	
Day OCV	42	55	75	166	217	
Duration OCV (min)	180	95	119	941	109	
pH effect	1	2	3	4		
Day pH effect	139	159	168	183		

The standard catholyte medium was equal to the medium used by Jourdin, et al. ⁴ and consisted of (added in this order) 3.17 g/L, sodium 2-bromoethanesulfonic acid, 7.5 g/L Na₂HPO₄·2H₂O, 3.0 g/L KH₂PO₄, 0.2 g/L NH₄Cl, 0.04 g/L MgCl₂·6H₂O, 0.02 g/L CaCl₂·2H₂O and 1 ml/L trace element solution. NH₄Cl was left out of the abiotic media to prevent microbial growth. The trace elements used both in this study and by Jourdin, et al. ⁴ consisted of (added in this order) 1.5 g/L FeCl₃·6H₂O, 0.15 g/L H₃BO₃, 0.03 g/L CuSO₄·5H₂O, 0.18 g/L KI, 0.12 g/L MnCl₂·4H₂O, 0.06 g/L Na₂MoO₄·2H₂O, 0.075 g/L ZnSO₄·H₂O, 0.15 g/L CoCl₂·6H₂O, 0.023 g/L NiCl₂·6H₂O and 10 g/L EDTA (C₁₀H₁₄N₂Na₂O₈·2H₂O, CAS 6381-92-6). After addition of the EDTA, 7 ml 3M NaOH was added to the trace element solution to allow dissolving of the metal salts. The pH of the medium was adjusted to 5.8 using 1 M HCl. The anolyte medium was similar to the catholyte medium, but did not contain the 2-bromoethanesulfonic acid and no trace elements. Further experiment conditions are all equal to the conditions described by Jourdin, et al. ⁴. During the continuous biotic experiment, the catholyte and anolyte medium were added with a rate of 3.6 and 3 ml/h respectively to reach a hydraulic retention time (HRT) of 4 days. The duplicate set of abiotic reactors was run continuous (HRT 4 d) with abiotic medium to simulate the biotic starting conditions.

The effect of CV on a developed biofilm was investigated by performing CV on a continuous bio-electrochemical CO₂ elongation reactor that was running for 125 days. Five CV scans with each three cycles were performed on day 125, 133, 147, 174 and 224 (Table 2.1). One cyclic voltammetry scan with three cycles was performed on all abiotic reactors at day 8. When performing the cyclic voltammetry (CV), the bio-electrochemical cell was operated at open cell voltage (OCV) 1 minute prior to the CV. OCV also occurred five times during the continuous reactor operation separate from the CVs for 180 min, 95 min, 119 min, 941 min and 109 min on days 42, 55, 75, 166 and 217, respectively (Table 2.1). As for the CV itself, the start potential was -1.06 V, the potential range was from -1.41 V to -0.21 V for the biotic reactor and abiotic reactors I and II (all vs Ag/AgCl 3 M KCl). For abiotic reactor III, IV, V and VI the potential range was -0.21 to -1.10 V to prevent voltage overload. In the CVs of reactor V and VI, the potential was held at -1.10 for 620 sec during the CV to allow a similar time under reducing conditions as for the CVs performed in abiotic reactors I and II. The scan rate and potential step were both 1 mV/s and 3 repetitive cycles were performed. Directly after the CV the continuous operation

was proceeded (at -1.06 V vs Ag/AgCl) without OCV. For biotic CV4 and CV5 and the CV's in all abiotic reactors, the catholyte was sampled during the CV scans as well. These samples were taken at the start ($t=0$ sec) and end ($t=120$ sec) and at the highest (-0.21 V vs Ag/AgCl) ($t=1550$, 3950 and 6350 sec) and lowest potential (-1.41 V vs Ag/AgCl) ($t=350$, 2750 and 5150 sec) and when the current switched from positive to negative ($t= \pm 1740$, ± 4140 and ± 6540 sec) or vice versa ($t= \pm 1060$, ± 3460 and ± 5860 sec). This last moment differed slightly for the different CV scans and the cycles within the scans.

2.2.2 Preliminary tests

Two preliminary tests were performed to further clarify the results found in this study. Firstly, different reactor parts were placed in tubes with fresh catholyte medium for five hours to measure whether these reactor parts would leach ions into the catholyte. For these leaching tests, the ion concentrations in the fresh medium were compared to those in the media with the reactor parts after five hours. The results can be found in SI Table 2.4. Secondly, a 50 ml sample with the highest optical density from biotic CV5 (day 224; $t=1550$ sec) was centrifuged to measure which metallic compounds were present in the supernatant and which in the pellet. The supernatant was measured and the pellet was measured separately after suspending in MilliQ (SI Table 2.6).

2.2.3 Analysis methods

The metal concentrations in the catholyte and anolyte were analysed with an inductively coupled plasma analyzer (ICP-OES, Varian Vista MPX). A multi-element standard solution was prepared in concentration ranges of 0-100 and 0-1000 $\mu\text{g/L}$. The measured compounds included Fe, Cu, Ni, Mn, Zn, Co and Mo for the first four CV scans of the biotic experiments. For the fifth CV in the biotic system and the CV in the abiotic systems, Ag, Al, Ba, Bi, Ca, Cd, Co, Cr, Cu, Fe, Ga, In, K, Li, Mg, Mn, Na, Ni, Pb, Sr, Zn, Mo, B, Tl, S and P were measured. The samples were acidified and pre-treated by addition of 40 μl 65% HNO_3 and 40 μl 0.1 g/L Yttrium (internal standard) to 3920 μl sample. Since a leakage occurred prior to CV5, the measurements of Fe, Co, Cu, Ni, Mn and Mo of CV5 were compared to those of CV2-4. No significant change in metal concentrations due to CV was found, so the metal measurements from CV5 are presented as well. ICP samples were also taken from the anolyte influent and effluent to verify whether metal species were exchanged with the anolyte. The OD_{600} values of the reactor liquid were measured (Hach Lange DR 3900 Spectrophotometer) before and after the CV to monitor the change in suspended compounds due to the CV. The fatty acid productivities were measured with the same gas chromatography method as described by Jourdin, et al. ⁴. The measurements of formic acid and lactic acid were performed with High Pressure Liquid Chromatography (HPLC, Ultimate 3000, Thermo Fisher Dionex). 20 μl sample was loaded on an Aminex HPX-87H, 300x7.8 mm (Bio-Rad 125-0140) column at 35°C. The flow rate was 0.5 ml/min and the mobile phase was 5 mM sulfuric acid.

In the experiments from this study acetate was found to be the only product. In the abiotic experiment no fatty acids or alcohols were formed (SI Table 2.1 and Table 2.2) and in the biotic experiment no fatty acids or alcohols were formed aside from acetate. No significant butyrate or ethanol productivity was observed during the continuous biotic CO_2 elongation experiment.

Neither formate nor lactate were produced during the biotic and abiotic CVs, and the fatty acid concentrations did not measurably change during the scans.

2.3 Results

To study the invasiveness of cyclic voltammetry (CV) on a microbial electrosynthesis system, CVs were performed at five different moments during continuous long-term (239 d) operation of a CO₂ elongation system. The biocathode was continuously elongating CO₂ to acetate from day 5 onwards at an HRT of 4 days. The biocathode potential was kept at -0.85 V vs SHE and the bioreactor pH was controlled at 5.8 ± 0.1 (SI Figure S2.1 and S2.2). Since Jourdin, et al.⁴ suggested that the CV would only have effect with a biofilm present, the CVs were not performed in the biotic reactor until a well-developed by eye visible biofilm was present. The bioreactor was operated for 125 days prior to the first CV scan for the biofilm development (SI Figure S2.2). The effects of CV are split in two categories. Firstly, the effect of CV on current and acetate productivity (reactor performance) was measured. Secondly, the effect of CV on the biocathode composition was investigated, e.g. the change of biocatholyte metal species and biomass concentration.

2.3.1 The effect of Cyclic Voltammetry on reactor performance

2.3.1.1 CV enhanced the current in a bio-electrochemical CO₂ elongation reactor

The effect of CV on system performance was measured by the change in current. The current is cathodic, so a more negative value corresponds with increased current. The current in the bio-electrochemical CO₂ elongation reactor increased after every performed CV scan. Directly after the CVs, current increases to approximately 5 times the value before the CVs were observed (Figure 2.2A and SI Figure S2.3). These initial current increases lasted short (Figure 2.2A), but hereafter the current stabilized at more negative values compared to before the CVs. The value at which the current stabilized after this initial peak showed some variation over the various biotic CV scans (Figure 2.2A, SI Figure S2.2). The longest current increases occurred after CV1 and CV4, with durations of 75 days and 20 days, respectively, before stabilizing again to the value prior to those CVs.

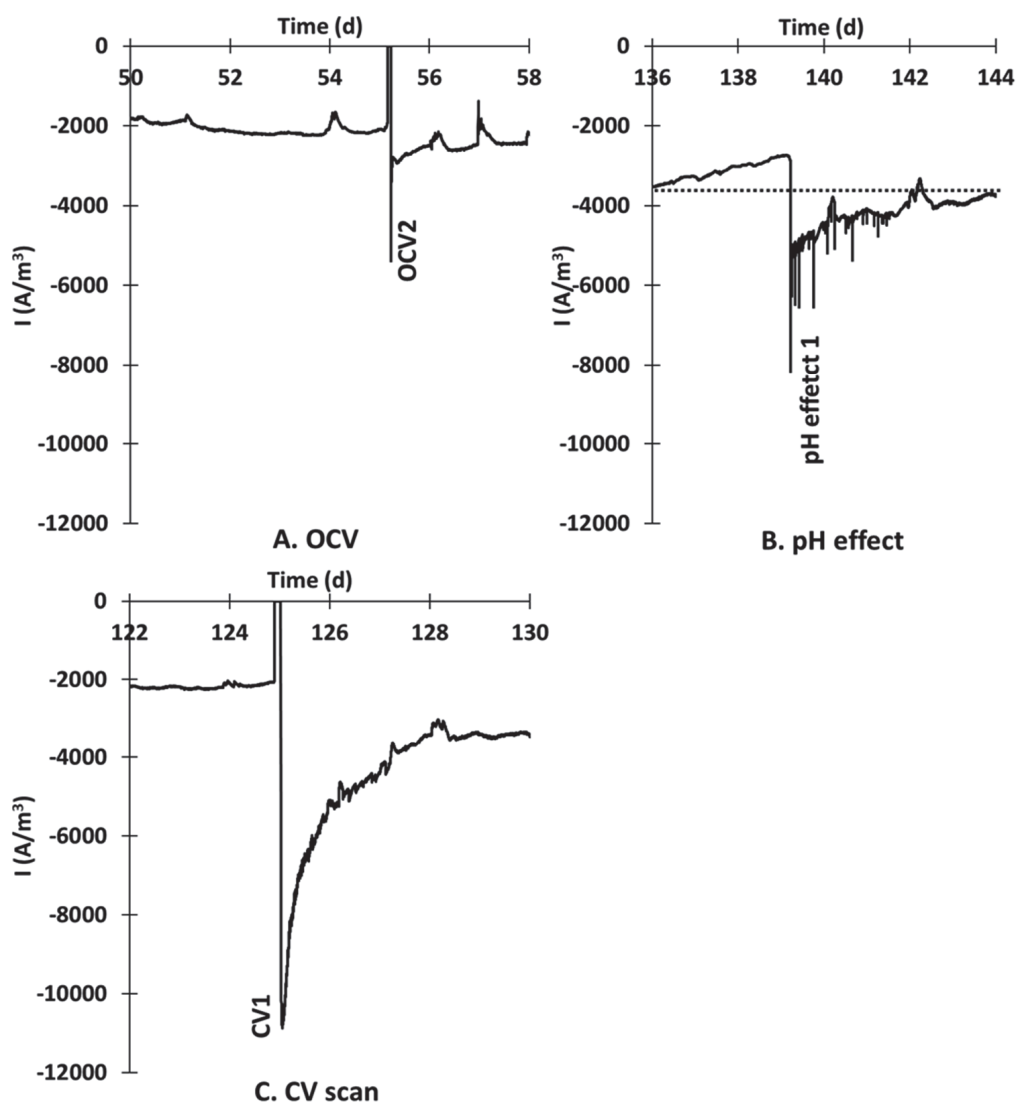


Figure 2.2. Initial and longer (3 to 5 days) term effect of cyclic voltammetry (A), open cell voltage (B) and change of pH (C) on the current in time (per m³ cathode) in a bio-electrochemical CO₂ elongation system. The dotted baseline represents the stabilized current at pH 5.8 (C). At day 136, the pH control was off so the pH increased to 6.5 until day 139, when the pH control was turned on again. The current values during the CV scan are not shown in this graph (A), they can be found in SI Figure S2.6. The full graph of current in time for this reactor is shown in SI Figure S2.2.

2.3.1.2 Current increase after biotic CV and not after abiotic CV

Three duplicates of abiotic experiments were performed to compare the effects of CV on electrochemical systems without a biofilm or suspended bacteria present. The current graphs in time during abiotic control experiments are shown in the SI Figure S2.4. The current of the abiotic reactors was higher compared to the current in the biotic reactor prior to the first biotic CV scan. After 8 days of operation, CV scans were run on these abiotic systems. One set of

abiotic CVs (reactors I and II) had the same potential range as the biotic CVs (-1.41 to -0.21 V, all vs Ag/AgCl). Since voltage overload occurred at the most negative potential values (<-1.2 V), smaller potential ranges were used for the other two sets of abiotic experiments to compare the CVs with and without voltage overload. The CVs of abiotic reactors III and IV had a potential range of -1.10 to -0.21 V. The CVs of abiotic reactors V and VI had the same potential range (-1.10 to 0.21 V) and a potential hold at 620s at potential -1.10 V to simulate the longer exposure of the cathode to negative potentials similar to the experiments with voltage overload.

In contrast with the biotic currents, the abiotic currents didn't increase but stayed unaffected by the CVs. All initial current increases (8 h after the CVs) are shown in Figure 2.3. To measure the initial current increase after the CVs, 0.34 days (8h) was depicted as the duration for the short term increase based on the shape of the current graphs. The average current values calculated over the 5 days before biotic CVs 2 to 5 are comparable (Figure 2.3), showing that the current eventually decreased after the first five days right after biotic CVs 1 to 4. In the biotic reactor, the current increased not only after CVs, but also after certain operational measures. For example, short current peaks were also observed after moments where open cell voltage (OCV) or temporary pH changes occurred. These effects are discussed in the next section.

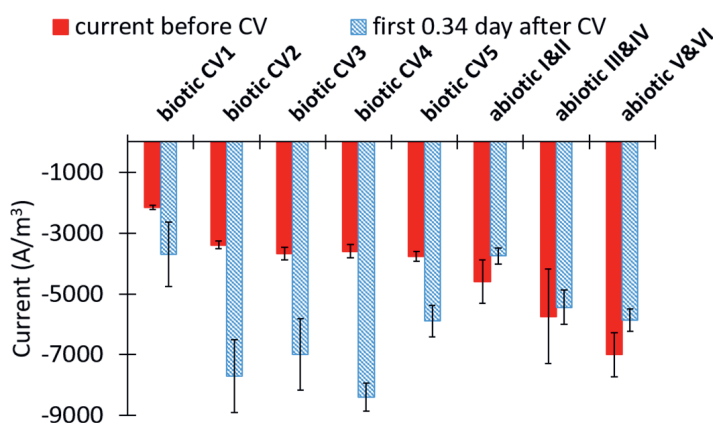


Figure 2.3. Increase in current in the first 8h after five cyclic voltammetry scans performed on a biotic (CV1 – CV5) and the three abiotic duplicates: I and II (CV from -0.21 to -1.41 V), III and IV (CV from -0.21 to -1.10 V) and V and VI (CV from -0.21 to -1.10 V with 620 sec potential hold at -1.10 V) electrochemical CO₂ elongation system. The error bars show the standard deviations between the different measurements in time (measured every minute).

2.3.1.3 OCV and HCl addition affect the current temporarily

As mentioned before, short current peaks were not only observed after biotic CV scans, but also after operational measures with OCV or short pH changes in the biotic system. Open cell voltage (OCV) is shortly applied to switch the operation mode between long-term operation and the CV scan. To study the current responses in more detail, Figure 2.2 shows the current of the biotic reactor in the days before and after OCV (B) and a pH issue (C). The current increased (to a more negative value) directly after the OCV. This initial current increase peak is smaller than the initial increase peaks after CV (Figure 2.2A). Approximately one day after the OCV, the current stabilized at a value similar to the current before the OCV, as shown in more detail in Figure 2.2B. Over the whole course of the biotic experiment, five OCVs occurred separate from

CVs, with durations ranging from 1.5 to 15 hours (see experimental section). After OCV1 to OCV4, the current increased for 19h, 43h, 5 min and 53h for OCV1-4, respectively, before decreasing to the value prior to the OCVs. The current increase after OCV5 lasted longer, as the current did not decrease to the value before OCV5 for 20 days (SI Figure S2.2).

Another operation issue that influenced the current was a change in the bioreactor pH, as shown in Figure 2.2C. The current was observed to increase when pH dropped, whereas it decreased when pH rose. For example, when the pH was not controlled and increased from 5.8 to 6.5 by day 139, the current decreased to a less negative value (Figure 2.2C). At day 139 the current increased directly after the pH controller was turned on again and HCl was added to decrease the pH to 5.8. Four days afterwards, the current stabilized at a value similar to before the pH change (Figure 2.2C). The current increases after the HCl addition had the same durations as for the OCV; the current increased the current for 44h, 10h and 1h, measured until the current was similar to the current before the pH effect (SI Figure S2.2). During the CVs, the HCl addition for the pH control did not change compared to the addition during continuous operation (SI Figure S2.1). Therefore, the effects of CV on the current can't be caused by changes in the bulk catholyte pH. Leakages of the bioreactor also affected the current. Two leakages occurred during the operation of the biotic system (indicated in SI Figure S2.2). After the first leakage (day 183) the current increased for 40 minutes, while after the second leakage (day 217) the current increased to twice its value and did not stabilize at the same value as before the leakage for the remaining 20 days of the experiment.

2.3.1.4 It could not be revealed whether acetate productivity was affected by the CV

Besides the current, the effect of the performed CVs on acetate productivity was also studied. The acetate productivity in time is shown in Figure 2.4. From day 98 to 183 the acetate productivity increased steadily and no evident direct effect of CV was revealed. To draw conclusions about the effect of CVs on the acetate productivity, steady state performances before and after a CV should be compared. With the hydraulic retention time of 4 days, a steady state period should take approximately 12 days. However, the acetate productivity was never stable for 12 days straight during the performed experiment. Therefore, the bioreactor did not perform stable enough to select steady state periods.

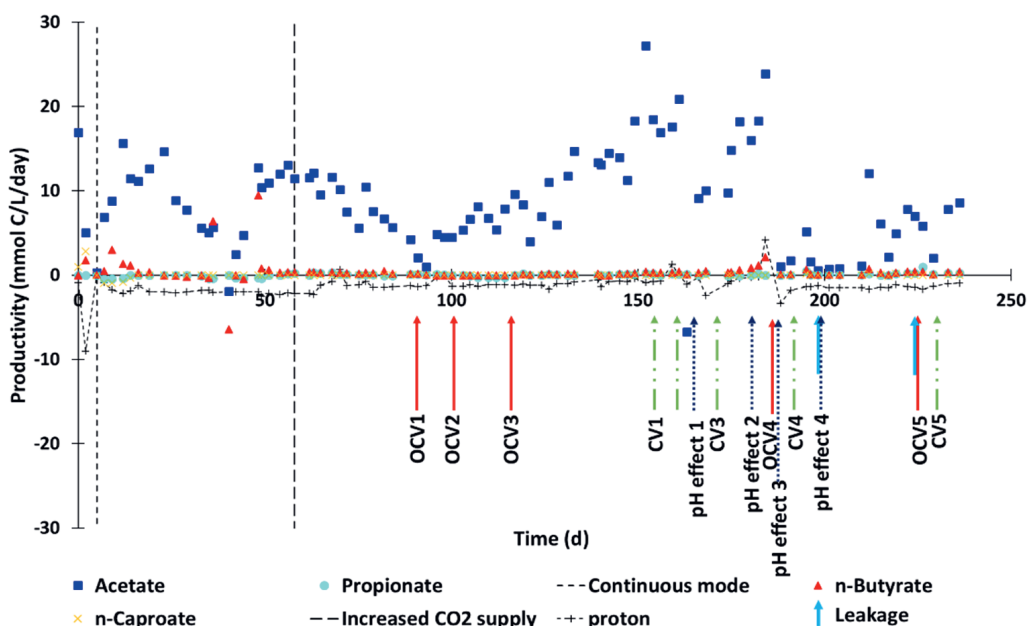


Figure 2.4. Volumetric productivity of acetate, propionate, n-butyrates and n-caproate in time in a bio-electrochemical CO_2 -fed system. The proton production is shown in $\text{mmol H}^+/\text{L}/\text{day}$. At day 5, the biotic reactor was put into continuous mode, the CO_2 supply rate was increased ten-fold at day 58. The CV scans are indicated by green long dash double dotted arrows, the open cell voltage applications are indicated by red arrows and changes in the pH that affected the current are indicated by the blue dashed arrows. The light blue arrows indicate reactor leakages.

The leakage at day 183 affected not only the current, but also the acetate productivity, as it dropped to $2.4 \pm 1.9 \text{ mmol C/L/d}$. Besides the acetate productivity, the electron recovery was also calculated and shown in the SI Figure S2.5. The electron recovery never reached high numbers (e.g. $>90\%$) so there was possibly a surplus of electron supply to the biofilm or suspended bacteria.

2.3.2 Effect of Cyclic Voltammetry on biocatholyte metal species elements and biomass concentrations

After investigation of the effect of CV on system performance, the effects of CV on the (bio)cathode composition were studied. To keep these measurements the least invasive, the biocatholyte was investigated.

2.3.2.1 Biomass and metal species increase in biocatholyte during the CV scan

During the CV scans in the biotic system, the optical density (OD_{600}) increased from 0.047 ± 0.011 to 0.142 ± 0.049 (averaged over the scans on day 147, 174 and 224). Microscopic observations supported that the amount of suspended cells was substantially higher after the first oxidation peak of the CV compared to before the CV (SI Figure S2.7). The optical density during the CV of the abiotic experiments increased only from 0.004 ± 0.000 to 0.008 ± 0.001 (SI Table S2.1 and S2.2).

In addition to biomass, the concentrations of metal atoms in the biotic catholyte before and after CV 2 to 5 were measured to investigate whether the CV caused net changes in the catholyte metal composition (Figure 2.5). Possibly the metal atoms were present in the catholyte as ions, complexes and/or as part of enzymes and microbes. The used measuring method gives the element concentrations of the metals, so the exact composition or oxidation state of the released metal species remains to be studied.

The actual catholyte concentrations (including suspended biomass) of iron, aluminium, barium, manganese and cobalt were significantly higher after the CV scan in the biotic system (Figure 2.5A). The concentration increase after the biotic CVs is highest for iron and cobalt (346 and 24 times, respectively).

In the abiotic systems; iron cobalt and molybdenum increased in the catholyte, although the concentrations of these compounds in the catholyte after the CV are lower than in the biocatholyte after the CV (Figure 2.5B). The (bio)catholyte concentrations of all the measured compounds that changed during and after the CV are shown in SI Figure S2.8, S2.9 and S2.10.

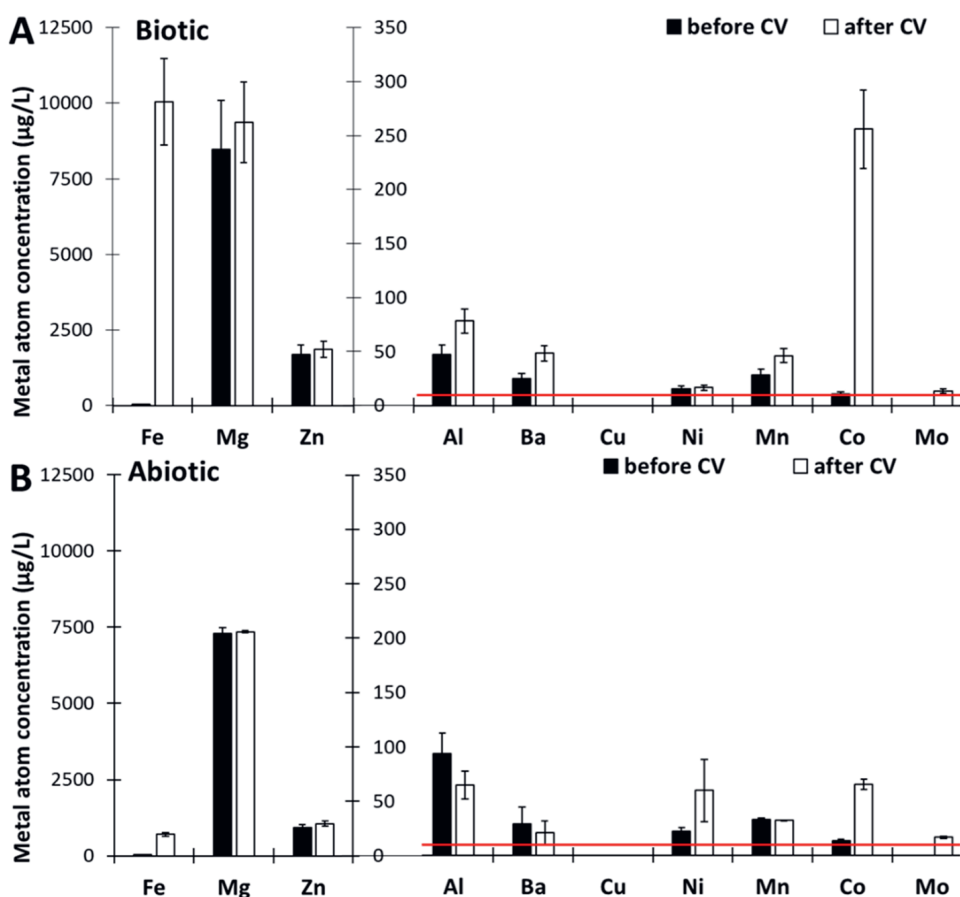


Figure 2.5. Catholyte concentrations of various metal atoms in the biotic (A) and abiotic (B) electrochemical CO₂-fed reactors before and after the CV treatments. Fe, Mn, Co and Mo were measured before and after CV2-CV5, while Mg, Al, B and Ba were only measured before and after CV5 of the biotic system. The standard deviations (error bars) of the biotic metal atom concentrations were calculated from the average relative standard deviation for Fe, Mn, Co and Ni measured before and after CV2-5 (A). The error bars for the abiotic experiments indicate the relative standard deviation between the six different reactors (B). The red line shows the detection limit of the metal atom concentrations.

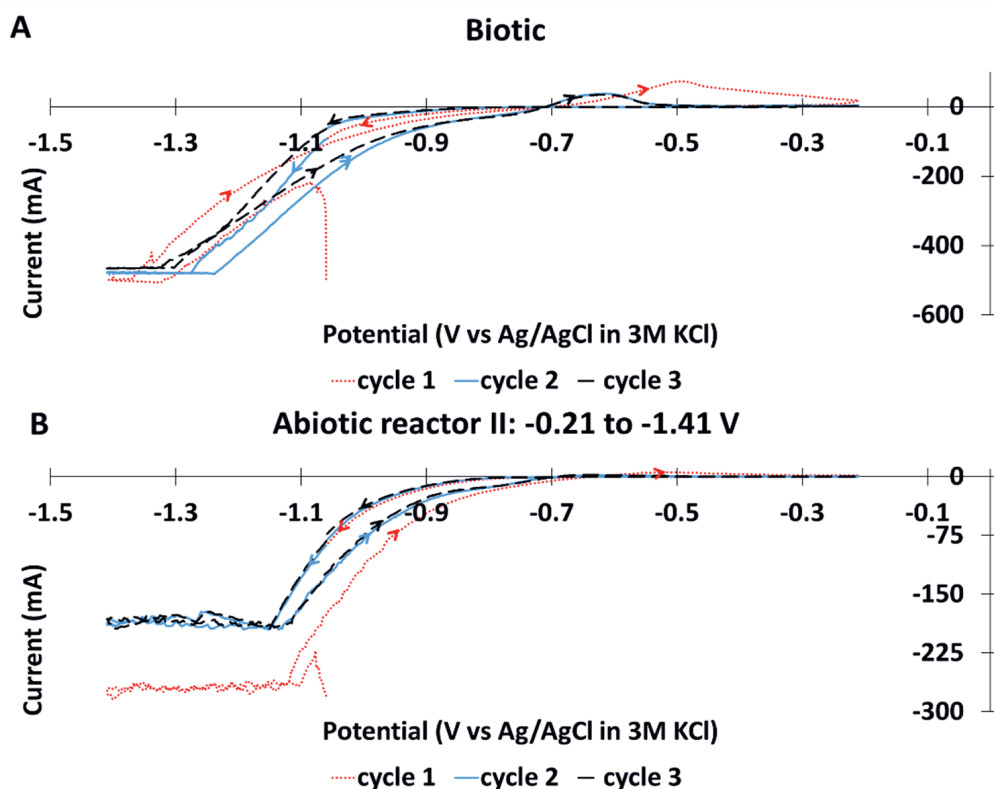
Remarkably, the zinc concentration in the biotic reactor catholyte was significantly higher compared to the medium concentrations. Compared to the microbial growth medium, the zinc concentration in the catholyte was approximately 20 times higher in the reactor catholyte after it had been added to the reactor (see SI Table S2.3). Leaching tests revealed that zinc leached from reactor parts, especially from the neoprene material used as gasket in the flat plate reactors (SI Table S2.4). The leaching already occurred before potential was applied to the system which means there is no pure electrochemical behaviour responsible for this zinc release. For the abiotic experiments, that were carried out after the biotic experiment, silicone gaskets were used to prevent zinc leaching.

Since the catholyte zinc concentrations in the biotic and abiotic experiments did not change significantly during the CVs (SI Figure S2.8, S2.9 and S2.10), the zinc leaching was considered

negligible. The release of the different metal compounds shown in Figure 2.5 led to the question whether an electrodeposition or release process could be observed from the shape of the cyclic voltammograms, which will be discussed below.

2.3.2.2 First cycle of biotic CV has a different oxidation peak as the second and third cycle

All the performed CV scans consisted of three cycles. The first cycle of the CV scan performed on the bio-electrochemical CO₂ elongation system has a different shape compared to the second and third cycle (Figure 2.6). The first cycle shows an oxidation peak at a potential around -0.5 V (vs Ag/AgCl), while the second and third cycles have oxidation peaks at a potential around -0.62 V (vs Ag/AgCl) (Figure 2.6A). The deviation of the first cycle was shown for all five CVs performed on the biotic reactor (SI Figure S2.6). The second cycle was identical to the third for all five biotic CV scans (Figure 2.6 and SI Figure S2.6).



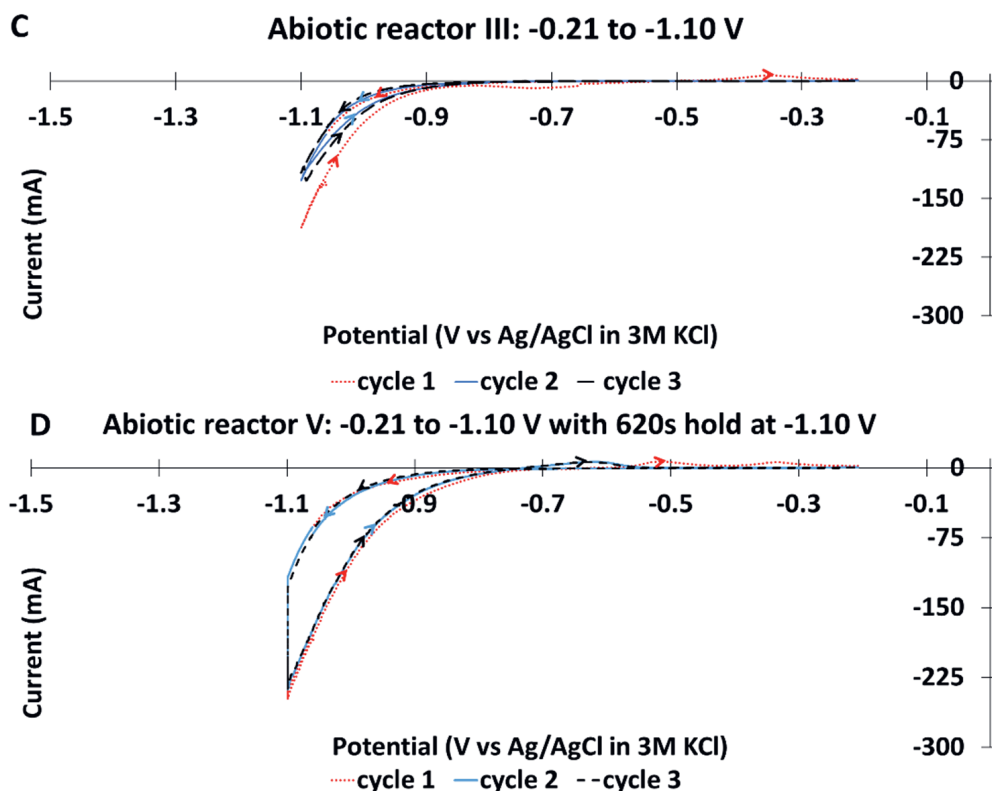


Figure 2.6. Cyclic voltammograms run with the bio-electrochemical CO₂ elongation reactor (A: day 224) and the abiotic systems (B: II) with start potential -1.06 V, the lowest potential -1.41 and the highest potential -0.21 V (all vs Ag/AgCl), the CVs contained three cycles. Potential values more negative than -1.2 V for the biotic scan (A) and more negative than -1.1 for the abiotic scan (B) could not be reached as a voltage overload occurred. Therefore, two more sets of abiotic experiments were run. The CVs of these experiments had a potential range from -0.21 to -1.10 V (C and D). For the experiments shown in Figure 2.5D, the potential was held at -1.10 V for 620 sec during each cycle. The scanning direction is indicated by arrow heads. The cyclic voltammograms for the duplicate abiotic experiments are shown in SI Figure S2.11.

For all reduction waves, potentials more negative than -1.1 V vs Ag/AgCl could not be reached (Figure 2.6A and B). The maximum voltage between anode and cathode (10 V) was not sufficient to achieve these desired cathode potentials. Two sets of duplicate abiotic CV experiments were carried out to study CVs without this voltage overload (Figure 2.6C and D). The CV of the first set was performed with a potential range of -0.21 to -1.1 V vs Ag/AgCl (Figure 2.6C and SI Figure S2.11B). During the voltage overload in Figure 2.6B, the cathode was under reducing conditions and high current in the potential range of ~1.2 to -1.41 V. To recreate this in a similar but controlled way, in the second set the potential was held at -1.1 V vs Ag/AgCl for 620 sec (Figure 2.6D and SI Figure S2.11C).

The different cycles of both the biotic and abiotic CVs have reduction peaks (potentials below -0.7 V vs Ag/AgCl) with different shapes for the different cycles. Remarkably, in all voltammograms, the forward scan (negative to positive) shows more negative current compared

to the reverse scan for the reduction peaks. This illustrates that the voltage overload didn't affect the scan cycle direction.

Since the oxidation peak of the first cycle had a different potential compared to those from the second and third cycle, the metal composition of the biocathode could also change differently in the first cycle compared to the second and third cycle. To study the metal composition, multiple catholyte samples were taken in time during the CV.

2.3.2.3 Increase of biomass and metal species in catholyte mainly occurred simultaneous with first oxidation peak

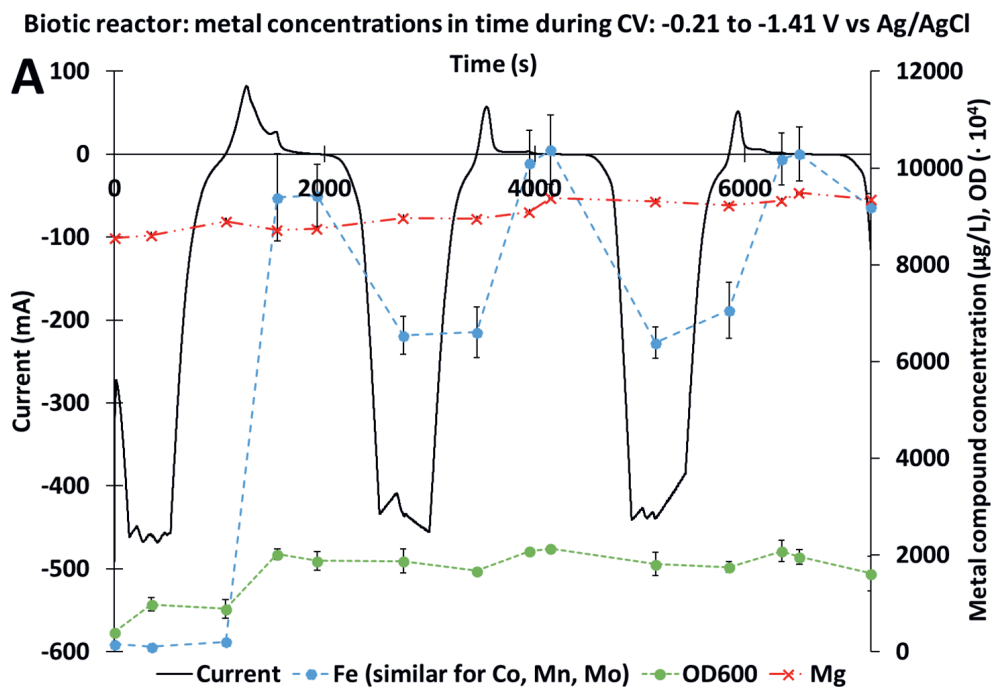
Biocatholyte samples were taken at different moments during the CVs to elucidate when the increase in biomass and metal species occurred. The major increase of iron, cobalt, manganese and molybdenum in the biocatholyte occurred simultaneous with the oxidation peak of the first cycle of the CV scan for both the biotic CVs (after 1550 min) (Figure 2.7A and SI Figure S2.8). The biocatholyte concentrations of these metal atoms decreased simultaneous with the subsequent reductive current in the reverse scan (positive to negative, from time 2000-2750 s) and increased simultaneous with the oxidation peaks. Still, the increase was less compared to the first oxidation peak (Figure 2.7A).

Aluminium, barium and magnesium show different trends. The biocatholyte concentrations of aluminium and barium increased when the CV was at low potentials and the magnesium catholyte concentration increased gradually during the complete biotic CV scans (SI Figure S2.8A and C). The biocatholyte OD₆₀₀ in the biotic system also increased simultaneous with the first oxidation peak of the CV and much less with the potential values of the reduction peak (Figure 2.7A). One test was performed to gain preliminary insights on which form (precipitated and/or more dissolved) of the metal species that increased in the catholyte, and whether the metal species could be attached to the bacteria. For this test, the centrifuged biomass/solids pellet was separated from the supernatant and separately analysed. The sample used for this experiment was taken 1550 s into the CV, so after the biggest increase of both biomass and metal compounds in the biocatholyte, performed at day 224. Only measurable amounts of iron, zinc, sulphur and phosphorous were found in the pellet. The concentrations of cobalt, iron, magnesium and zinc were lower in the supernatant sample compared to the non-centrifuged original sample (SI Table S2.5).

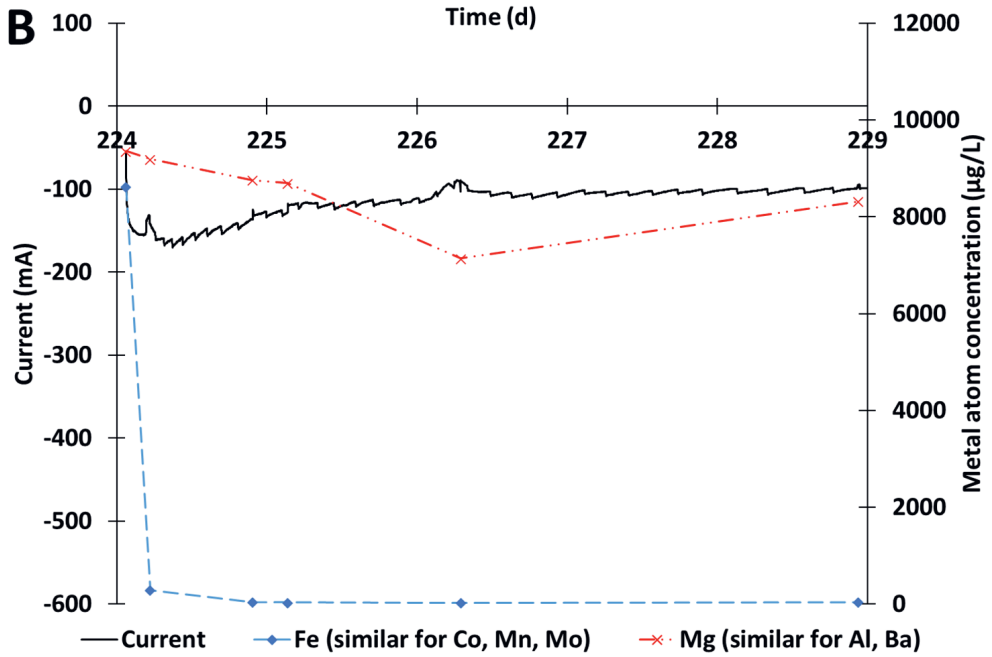
The abiotic systems showed similar trends compared to the biotic systems. The iron, cobalt, molybdenum and nickel catholyte concentrations increased also mainly simultaneous with the oxidation peak of the first CV cycle (after 1550 min) (Figure 2.7C, E and G). The concentrations of aluminium, barium and magnesium did not change significantly during the abiotic CVs, in contrast to the biotic CVs (SI Figure S2.9A and C, S2.10A, C, E and G). Remarkably, the current kept increasing although the potential was kept constant in the abiotic experiments with a potential hold at -1.10 vs Ag/AgCl for 620 sec (Figure 2.7G time 2400-3000 and 4800-5400).

After the CV scan on the biotic cell, the biocatholyte concentrations of most released metal species (iron, cobalt, manganese, molybdenum) decreased during the initial current increase, with the trend similar to the iron shown in Figure 2.7B (SI Figure S2.8B and D). Aluminium and barium take longer to reach the concentrations similar to before the CV in the biotic experiment,

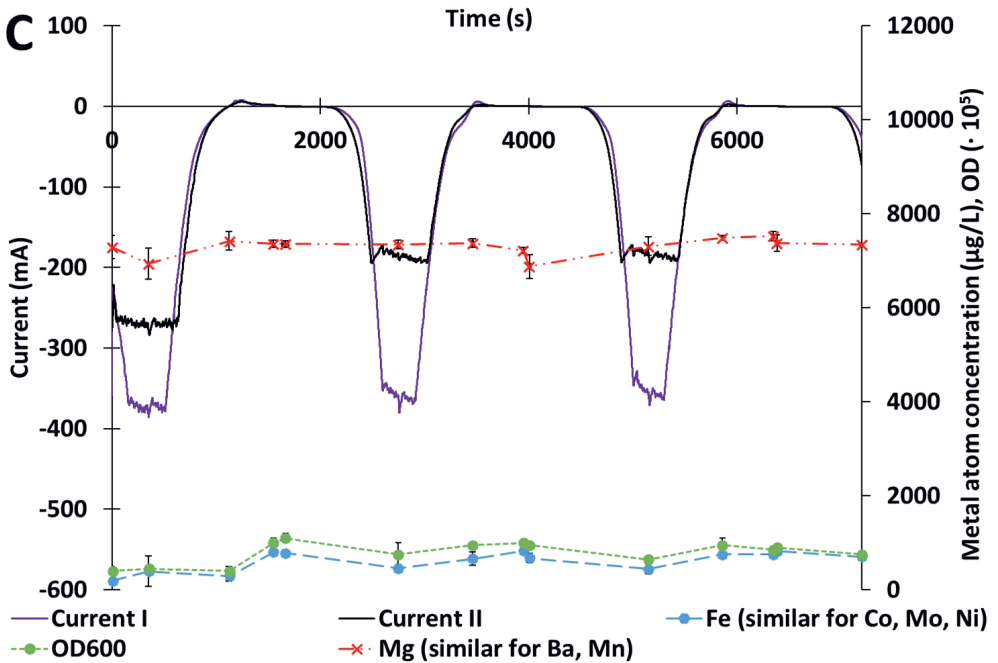
while they remain unchanged during the abiotic experiments. Their trends were similar to the magnesium shown in Figure 2.7B (SI Figure S2.8B and D). All metal atoms that significantly increased in the catholyte during the CVs of the abiotic experiments (iron, cobalt, molybdenum and nickel), decreased rapidly simultaneous with the initial current peak after the CVs as well (Figure 2.7D, F and H and SI Figure S2.9B and D and S2.10 B, D, F and H).

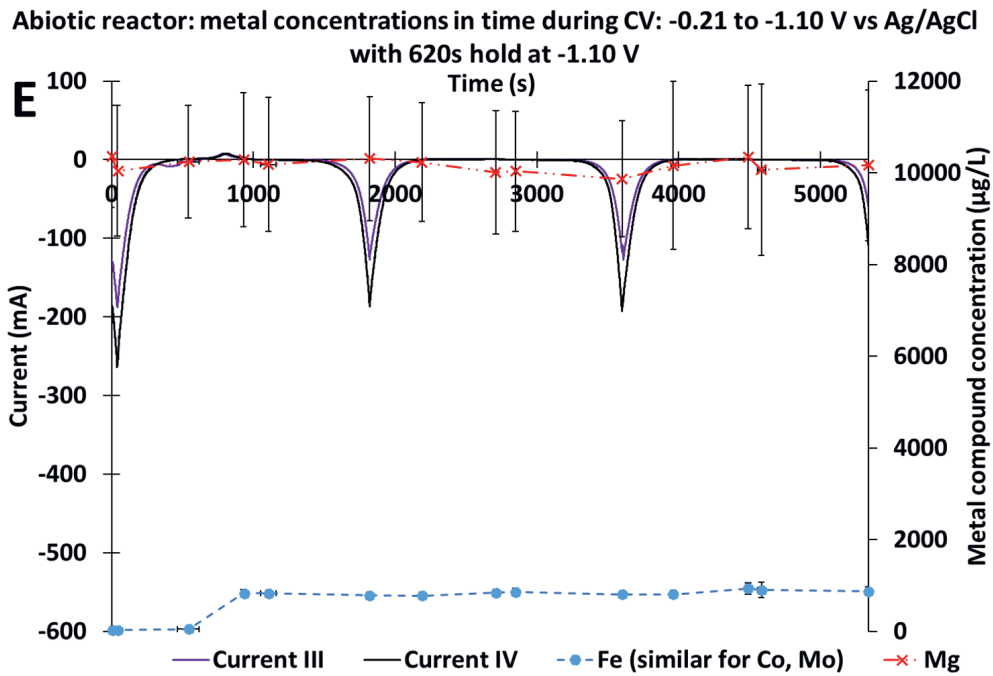
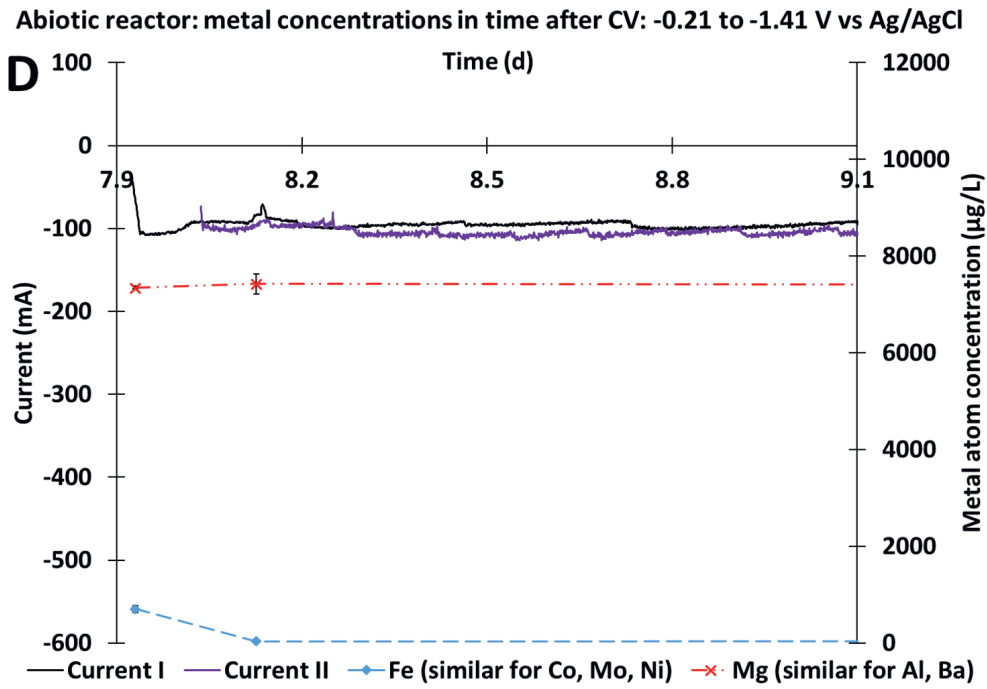


Biotic reactor: metal concentrations in time after CV: -0.21 to -1.41 V vs Ag/AgCl

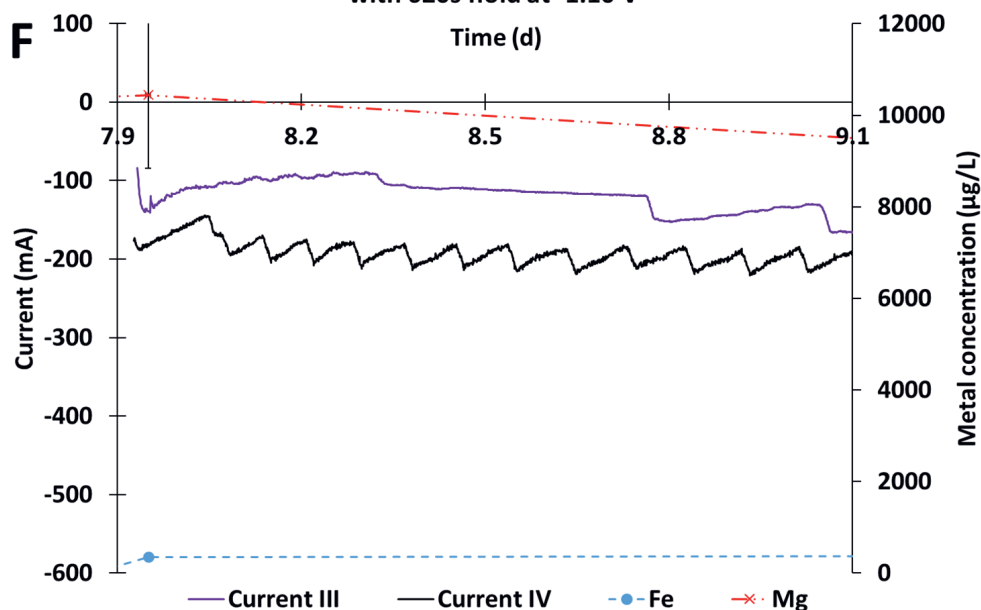


Abiotic reactor: metal concentrations in time during CV: -0.21 to -1.41 V vs Ag/AgCl

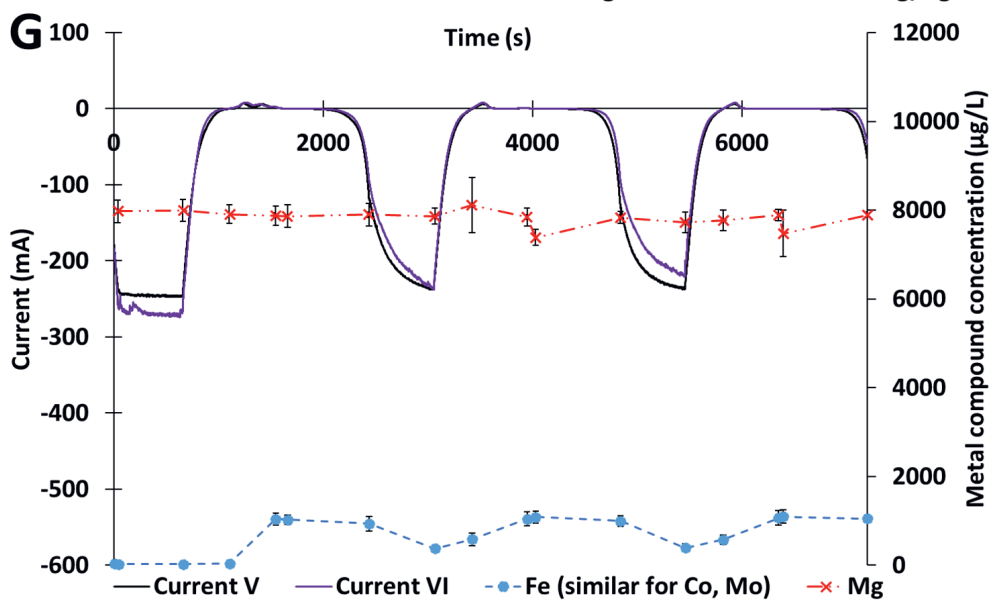




Abiotic reactor: metal concentrations in time after CV: -0.21 to -1.10 V vs Ag/AgCl with 620s hold at -1.10 V



Abiotic reactor: metal concentrations in time during CV: -0.21 to -1.10 V vs Ag/AgCl



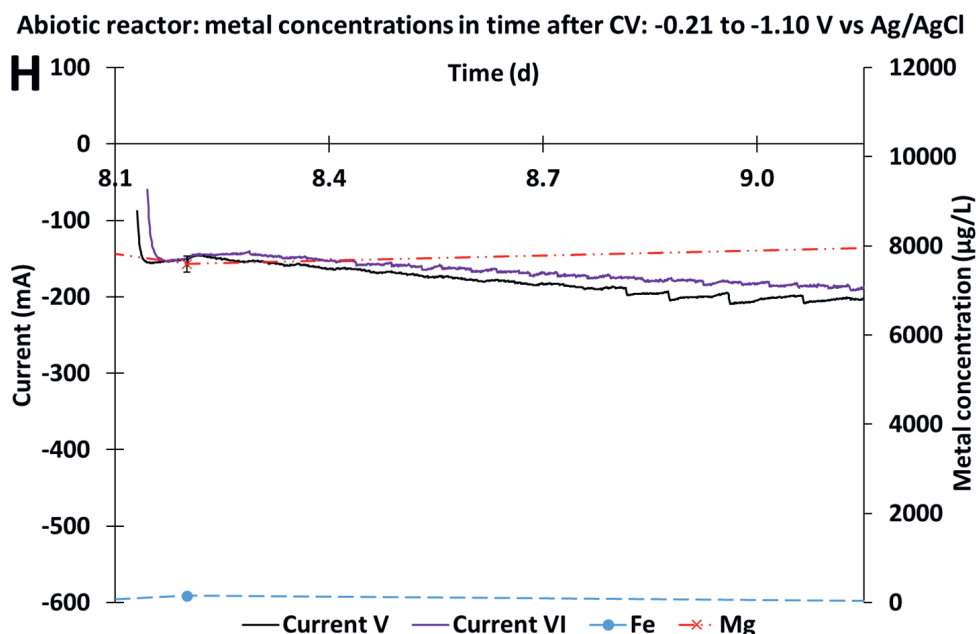


Figure 2.7. Change in concentrations of metals and the optical density (OD_{600}) of the catholyte in time with the change in current during the 3 cyclic voltammetry (CV) scan performed on day 174 (CV4) and day 224 (CV5) with the bio-electrochemical CO_2 elongation system (A) and during the CV scan performed with the three abiotic duplicates: I and II (CV from -0.21 to -1.41 V; C), III and IV (CV from -0.21 to -1.10 V; E) and V and VI (CV from -0.21 to -1.10 V with 620 sec potential hold at -1.10 V; G). The change in current and the catholyte iron and magnesium concentrations in time after the CV scan performed on day 224 (CV5) with the bio-electrochemical CO_2 elongation reactor (B) and after the CV performed with abiotic reactors are shown as well: I and II (D), III and IV (F) and V and VI (H). The vertical error bars indicate the minimum and maximum values found during the CV scans on the different days (A) and the difference between the duplicate experiments (C - H), the horizontal error bars indicate the different sampling moments during the different CV scans (A, C, E and G). The arrows indicate the axes used for the different graphs. The potential was controlled on -0.85 vs SHE after the CVs (B, D, F and H).

2.4 Discussion

2.4.1 CV is invasive on microbial electrosynthesis

Since the first cycle of the biotic CVs is different from the second and third (Figure 2.6), one can already state that the first cycle is changing the CV response of the biocathode and as such is invasive on the electrochemical CV response. The change of biotic CV scan profile after the first cycle indicates that an oxidation reaction occurs during the first cycle, which then does not occur during the second and third cycle. Three additional findings showing the invasiveness of the CVs are the changed metal compound concentrations in the biocatholyte after the CVs (Figure 2.5), the increased optical density (Figure 2.7A) and the increased current directly after the CVs (Figure 2.2A). The invasiveness is shown to be reproducible as well, as the biotic CV graphs and corresponding metal species behaviours were similar for the five different CVs.

2.4.2 Increase of metal compounds in biocatholyte can be related to metal oxidation

The metal compounds mainly increased simultaneous with the oxidation peak of the first cycle (Figure 2.7A), so the changed metal concentrations in the biocatholyte after the CV scan seems related to the different oxidation peak in the first CV cycle. As will be discussed in more detail, the metal atom measurements can represent various forms of metal containing compounds. These compounds originate from the microbial medium or from grown, metal-containing micro-organisms. Measurements in the anolyte showed no detectable metals (data not shown). Thus, the increase of the metal compounds in the catholyte was likely due to their release from the biocathode, as that was the most evident source of released metal atoms and biomass. The initial concentrations of metals present in the catholyte were lower compared to the medium concentrations, indicating accumulation of metals on the biocathode during operation prior to the CV scan.

Although only the element concentrations were measured in this study, we wanted to theoretically predict the speciation of different trace metals during the change of potential. To this end, Pourbaix diagrams were calculated from the catholyte medium concentrations, they are shown in SI Figure S2.12. The potential and pH area covered by the CV is indicated by red arrows in these diagrams. The potential range of the CV theoretically allows reduction and oxidation of most trace metals in the used medium; cobalt, copper, iron, molybdenum, nickel and zinc are predicted to change oxidation state from a suspended to a solid form within the potential range of the CVs (SI Table S2.6 and Figure S2.12). The behaviour of manganese, copper, and nickel cannot be explained based on purely their Pourbaix diagram. Manganese is released while the oxidation state theoretically does not change (SI Figure S2.12-M and S12-N) and copper and nickel are not released while their oxidation states changes from solid to suspended during oxidation according to the Pourbaix diagrams (SI Figure S2.12-G, S2.12-H, S2.12-Q and S2.12-R).

Assuming that the metal compound oxidation state change into a solid form corresponds to depositing, the Pourbaix diagrams support that the release and depositing of metals is an electrochemical process^{18,38,39}. For example, metal species could be reduced to their solid form and thereby electro-deposited at the cathode during the reduction of the CV and oxidized to their suspended form and electro-released from the cathode during the oxidation of the CV (Figure 2.8A). The oxidation reaction likely caused their release from the cathode during CV for cobalt iron and molybdenum which predominantly increased in the biocatholyte simultaneous with the first oxidation peak. During the reductive part of the reverse scan (positive to negative), part of the metals are re-electrodeposited, as the catholyte concentrations decreased again (Figure 2.7). The reductive part of the reverse scan has lower current compared to the reductive part of the forward scan, which is unusual¹². To test whether these directions were caused by the voltage overload, the current behaviour was compared to the abiotic scans without voltage overload. The current behaviour of the abiotic CVs with the voltage overload is similar to the CVs with the “potential hold”. Therefore, the voltage overload was not the reason for the scan directions during the reduction peak. The higher current in the forward scan could be explained by electrodepositing during the reverse scan³⁸⁻⁴¹, hereby forming a catalyst. Many of the microbial trace metals could be part of a hydrogen evolution catalyst (Mn, Ni, Co, Cu, Fe, Mo)⁴².

This catalyst can decrease the overpotential of e.g. hydrogen evolution, thus causing the increased current in the reductive part of the forward scan.

The catholyte metal concentrations at the end of the CV are still higher than before the CV, indicating different chemical conditions before and after the CV. An explanation for the different metal conditions after the CV could be kinetic hindrance of metal deposition and nucleation. In the abiotic scans that had a “potential hold” at -1.10 V, the current eventually reached values similar to the first reduction peak (Figure 2.7C), while this was not the case in the scans without this hold (Figure 2.7A). The current increase during the moments where the potential was held constant at -1.10 V vs Ag/AgCl indicates that equilibrium was not yet reached. Apart from the current, the metal catholyte concentrations of iron and molybdenum also change during the “potential hold”. This could indicate capacitive current or depositing of metal species on the cathode. After the CV scans, the applied reducing potential (-1.06 vs Ag/AgCl) allowed enough time for the remaining dissolved metal species to redeposit on the cathode or re-enter the electrical double layer, while a part of the released metal species is washed out due to the continuous operation. Iron, cobalt, manganese and molybdenum decreased rapidly from the biocatholyte after the CVs, suggesting that these compounds were electro-deposited at the cathode under the reductive conditions.

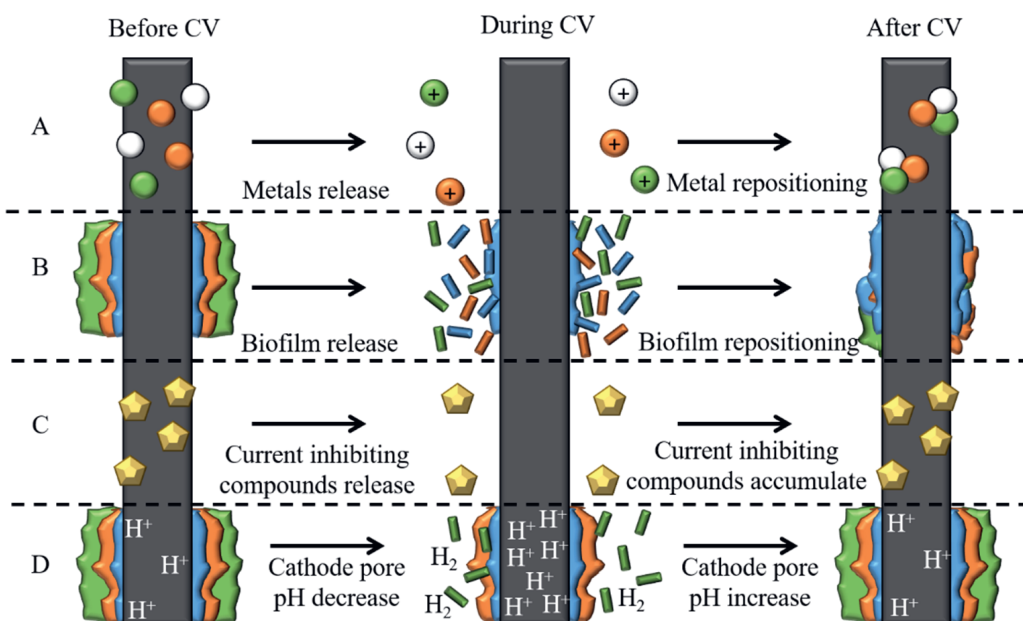


Figure 2.8. Schematic representation of possible processes that are induced by Cyclic Voltammetry in a bioelectrochemical system. CV induces release of metals (A), biofilm (B) and/or current inhibiting compounds (C) that deposited on the cathode over time. A fourth hypothesis is a Cv-induced pH decrease inside the cathode (D). After CV, the released compounds are deposited back on the cathode. The metals (A) and biomass (B) is redeposited in a different configuration.

Investigating the involved deposition mechanisms can help understand the current behaviour after the CV. Remarkably, the current was high at the moments where the metals were released from the biocathode. The supporting information contains an extensive hypothetical framework further linking the metal behaviour and the current response. by explaining 4 hypotheses: I) cofactor replacement, II) metal rearrangement, III) biomass thickness decrease and IV) release of dead bacteria (Figure S2.13). Possible ways for more in-depth research of the metal behaviour include performing the CV with various scanning rates and a study of the cathode surface.

2.4.3 Metal release possibly due to attachment to biomass

The increase of optical density and most presumably biomass after the biotic CVs raised the question whether the released metals were attached to or part of the biomass that was released from the cathode. Metals are continuously supplied via the microbial growth medium. The metals can be used as cofactor for chain elongation enzymes^{43,44} or electron transport mediators. Furthermore, it is known that metal species can attach to bacteria by the chelating properties of the bacterial membranes or by nanoparticle formation^{45,46}. It should be noted that the biomass was not fully destructed before performing ICP. This could be done by digestion of the samples, but was not performed to prevent dilution of the samples. Thus, the metals attached to the not fully degraded biomass might not have been detected in this study and the actual concentrations of metal compounds in the measured samples might be higher than shown in this study. The measurement of the separated pellet and supernatant indicates that metals were not solely present in the supernatant but also attached to precipitants and/or part of the biomass. Therefore, (parts of the) iron and zinc could have been incorporated in parts of the biofilm that was released during the CV. The reason why the biomass was released will be discussed in the next section.

2.4.4 Biomass release probably due to oxidative current

Remarkably, the major biomass release did not occur when visible bubbles are formed at the cathode during hydrogen evolution (potentials more negative than -0.56 V vs Ag/AgCl, calculated as described by Sleutels⁴⁷ for our conditions), but simultaneous with the oxidation peak of the CV scans. A possible explanation for this phenomena is the change of surface charge. When bacteria form a biofilm on a charged surface, it is likely that the biofilm components, e.g. extracellular polymeric substances (EPS), metal (ions), proteins in the bacterial cell walls, are adapted to the surface charge⁴⁸. This surface charge depends on the cathodic current, when the current is negative, the surface will be negatively charged but when the current reaches positive values, the surface will be positively charged. This change of charge could disturb the electrostatic interactions between the cathode and the biofilm and consequently detach and release biomass (Figure 2.8B). The effect of the biomass release on the system performance should be investigated in a separate study where the biofilm thickness is reduced (e.g. mechanically) with alternative methods.

2.4.5 Current after CV's initially increasing and on longer term decreasing

The current increase after the biotic CVs can be split into different phases. During the first 8 hours after the CV an initial current increase is observed and after that, the current slowly decreases back to the value similar to before the CV scan. The initial peak (peak surface equals

± 3320 Coulomb) is bigger than the amount of current that would be needed to reduce the released metals (± 56 Coulomb), presumably hydrogen formation took place during the initial current increase. As mentioned before, the effect of this additional energy availability on the biofilm performance could not be depicted from this study, since the acetate productivity was only monitored three times per week and no clear steady states on acetate productivity were gained.

The second phase, the slow decrease of the current starting 8 hours after the CVs, showed different patterns for the five different biotic CV scans. This erratic behaviour can have multiple reasons. Firstly, the biofilm develops over time, hereby the biofilm composition can change, and thereby affect the electron transfer in the biofilm. Secondly, operation difficulties could possibly have had additional effects on the current, since the duration of the current increase after the CV in our study also differed from the study of Jourdin, et al. ⁴, while the setup was the same. For example, the reactor leakage in the current study that occurred nine days after CV4 could have affected the current apart from CV4 itself, resulting in the longer duration of the increased current. Due to the non systematical timing between the different CVs a relation between the current response of the CV and the development of the biofilm over time could not be determined. Especially the first CV caused a long current increase (75 d), but the metal species concentrations were not measured after CV1, so no insights could be obtained on the metal behaviour.

2.4.6 OCV and temporary pH change affect the current as well

Apart from CV, the current was also affected by OCV and temporary pH changes. The current initially increased when OCV occurred (Figure 2.2). Therefore, studying the metal concentrations in the catholyte before and after OCV would be interesting to test the invasiveness of OCV.

During the effects of temporary pH changes, the current increased always when the pH decreased. A lower pH makes more H_3O^+ ions available for the reduction to hydrogen⁴⁹, a small change in pH can cause a big change in hydrogen productivity⁴². Another plausible reason for the effect of the pH change on the current could be that the electrostatic interactions of polymers in the EPS change⁵⁰ in such a way that the electron transport through the biofilm is potentially enhanced at lower pH. The observed pH effects support a fourth hypothesis, that the local pH on the cathode decreased as a result of the changes in the cathode composition (metals and biomass) (Figure 2.8D). The lower pH causes a current peak that lasts until the cathode composition and thus local pH is fully restored to the value prior to the CV. Local pH measurements in the cathode during and after CV could further elucidate this hypothesis.

2.4.7 No current increase after abiotic CV possibly due to shorter operation or absence of biofilm

The long term (>1 day) invasiveness of the CVs in a biotic system was not found for the abiotic systems, although cobalt, iron, molybdenum and nickel were also net released into the catholyte after the abiotic CVs (Figure 2.5). A main difference between the abiotic and the biotic experiments was the cathode composition. The biotic system was running for 125 days prior to the first CV scan, while the abiotic CVs were performed after 8 days to prevent microbial growth

in the reactors. During the 125 days in the biotic reactor, a by eye visible biofilm was formed and more metals were net supplied to the system via the continuously added medium. The continuous supply could have caused more electrodeposition of metal compounds on the cathode. The release of accumulated metals on the cathode could be more or different, inducing current enhancing mechanisms. Another electrochemical process that could have caused the current increase after the CVs is the release of current inhibiting compounds from the cathode. For example, calcium phosphate⁵¹ and calcium carbonate⁵² have shown to form current inhibiting precipitates in biocathodes, and could have slowly accumulated on the biocathode due to long-term operation (Figure 2.8C). The slow decrease of the current starting 8 hours after the CVs could then be caused by slow precipitation of current inhibiting compounds.

In the study by Jourdin, et al. ⁴, the current stayed high for the 160 days after the current increase directly after the CV scan. The current study shows a more short term current increase in the biotic reactor (Figure 2.3). This difference in CV effect is remarkable, since the conditions in both biotic CO₂ reduction experiments were similar. The results from our study suggest that, although the CV scan has invasive effects, the long-term increase in current and productivity observed by Jourdin are not (completely) caused by the CV scan. This difference could also be caused by the thicker biofilm in the study from Jourdin, during which also butyrate and caproate were produced, indicating that the biofilm could have been more developed. Elucidating the mechanisms behind the current increase after the biotic CV can provide tools for improving the system performance of bio-electrochemical systems. Thus, further research on the involved mechanism(s) causing the observed CV effects can reveal how CV could be used as biocathode booster or way to provide maintenance and remove pollutants from the electrode.

2.5 Conclusions

Cyclic voltammetry (CV) is invasive on the investigated microbial electrosynthesis system. CV affects both the reactor performance as well as the biocathode composition. The effect on reactor performance was shown as a current increase after the CV lasting up to 20 days. The effect on the biocathode composition is shown by the change in oxidation peak and release of metals and microbial biomass into the biocatholyte. Various underlying mechanisms may play a role on how CV caused invasiveness. The invasiveness is less shown for the abiotic system, since the abiotic control experiments showed no current increase after the CVs and little metal release. The difference with the biotic experiment could be due to the shorter operation time of the abiotic experiments and/or to the absence of a developed biofilm. Evidently, CV is not solely an analysis technique. Further elucidation of the described CV effects may be useful for maintenance or boost biocathode performance.

References

- 1 Rabaey, K. & Rozendal, R. A. Microbial electrosynthesis—revisiting the electrical route for microbial production. *Nat. Rev. Microbiol.* **8**, 706-716 (2010).
- 2 Ragab, A. a., Katuri, K. P., Ali, M. & Saikaly, P. E. Evidence of spatial homogeneity in an electromethanogenic cathodic microbial community. *Frontiers in microbiology* **10** (2019).
- 3 Aryal, N., Halder, A., Tremblay, P.-L., Chi, Q. & Zhang, T. Enhanced microbial electrosynthesis with three-dimensional graphene functionalized cathodes fabricated via solvothermal synthesis. *Electrochim. Acta* **217**, 117-122 (2016).
- 4 Jourdin, L., Raes, S. M. T., Buisman, C. J. N. & Strik, D. P. B. T. B. Critical Biofilm Growth throughout Unmodified Carbon Felts Allows Continuous Bio-electrochemical Chain Elongation from CO₂ up to Caproate at High Current Density. *Frontiers in Energy Research* **6**, doi:10.3389/fenrg.2018.00007 (2018).
- 5 Vassilev, I. *et al.* Microbial electrosynthesis of isobutyric, butyric, caproic acids, and corresponding alcohols from carbon dioxide. *ACS Sustainable Chem. Eng.* **6**, 8485-8493 (2018).
- 6 Zaybak, Z., Logan, B. E. & Pisciotta, J. M. Electrotrophic activity and electrosynthetic acetate production by *Desulfobacterium autotrophicum* HRM2. *Bioelectrochemistry* **123**, 150-155 (2018).
- 7 Marshall, C. W., Ross, D. E., Fichot, E. B., Norman, R. S. & May, H. D. Electrosynthesis of commodity chemicals by an autotrophic microbial community. *Appl. Environ. Microbiol.* **78**, 8412-8420 (2012).
- 8 May, H. D., Evans, P. J. & LaBelle, E. V. The bioelectrosynthesis of acetate. *Curr. Opin. Biotechnol.* **42**, 225-233 (2016).
- 9 Flexer, V. & Jourdin, L. Purposely Designed Hierarchical Porous Electrodes for High Rate Microbial Electrosynthesis of Acetate from Carbon Dioxide. *Acc. Chem. Res.* **53**, 311-321, doi:10.1021/acs.accounts.9b00523 (2020).
- 10 Arends, J. B. A., Patil, S. A., Roume, H. & Rabaey, K. Continuous long-term electricity-driven bioproduction of carboxylates and isopropanol from CO₂ with a mixed microbial community. *J. CO₂ Util.* **20**, 141-149, doi:10.1016/j.jcou.2017.04.014 (2017).
- 11 Raes, S. M. T., Jourdin, L., Buisman, C. J. N. & Strik, D. P. B. T. B. Continuous Long-Term Bio-electrochemical Chain Elongation to Butyrate. *ChemElectroChem* **4**, 386-395, doi:10.1002/celc.201600587 (2017).
- 12 Elgrishi, N. *et al.* A Practical Beginner's Guide to Cyclic Voltammetry. *J. Chem. Educ.* **95**, 197-206 (2017).
- 13 Nicholson, R. S. Theory and application of cyclic voltammetry for measurement of electrode reaction kinetics. *Anal. Chem.* **37**, 1351-1355 (1965).
- 14 Yokoyama, K. & Kayanuma, Y. Cyclic voltammetric simulation for electrochemically mediated enzyme reaction and determination of enzyme kinetic constants. *Anal. Chem.* **70**, 3368-3376 (1998).
- 15 Rountree, E. S., McCarthy, B. D., Eisenhart, T. T. & Dempsey, J. L. Evaluation of homogeneous electrocatalysts by cyclic voltammetry. *ACS Publications* **53**, 9983-10002 (2014).
- 16 Rand, D. & Woods, R. Determination of the surface composition of smooth noble metal alloys by cyclic voltammetry. *J. Electroanal. Chem.* **36**, 57-69 (1972).
- 17 Pozio, A. d., De Francesco, M., Cemmi, A., Cardellini, F. & Giorgi, L. Comparison of high surface Pt/C catalysts by cyclic voltammetry. *J. Power Sources* **105**, 13-19 (2002).
- 18 Grujicic, D. & Pesic, B. Electrodeposition of copper: the nucleation mechanisms. *Electrochim. Acta* **47**, 2901-2912 (2002).
- 19 Rodrigues, S., Shukla, A. & Munichandraiah, N. A cyclic voltammetric study of the kinetics and mechanism of electrodeposition of manganese dioxide. *J. Appl. Electrochem.* **28**, 1235-1241 (1998).
- 20 Lai, Y. *et al.* Cyclic voltammetry study of electrodeposition of Cu (In, Ga) Se₂ thin films. *Electrochim. Acta* **54**, 3004-3010 (2009).
- 21 Lee, J. Y. & Tan, T. C. Cyclic voltammetry of electrodeposition of metal on electrosynthesized polypyrrole film. *J. Electrochem. Soc.* **137**, 1402-1408 (1990).
- 22 Harnisch, F. & Freguia, S. A basic tutorial on cyclic voltammetry for the investigation of electroactive microbial biofilms. *Chemistry—An Asian Journal* **7**, 466-475 (2012).
- 23 Torres, C. I., Kato Marcus, A. & Rittmann, B. E. Proton transport inside the biofilm limits electrical current generation by anode-respiring bacteria. *Biotechnol. Bioeng.* **100**, 872-881, doi:10.1002/bit.21821 (2008).

- 24 De Lichtervelde, A., Ter Heijne, A., Hamelers, H., Biesheuvel, P. & Dykstra, J. Theory of ion and electron transport coupled with biochemical conversions in an electroactive biofilm. *Phys. Rev. Appl.* **12**, 014018 (2019).
- 25 Mao, Z. *et al.* Effect of start-up process using different electrochemical methods on the performance of CO₂-reducing methanogenic biocathodes. *Int. J. Hydrogen Energy* (2020).
- 26 Pozo, G. *et al.* Cathodic biofilm activates electrode surface and achieves efficient autotrophic sulfate reduction. *Electrochim. Acta* **213**, 66-74, doi:10.1016/j.electacta.2016.07.100 (2016).
- 27 Rabaey, K., Boon, N., Siciliano, S. D., Verhaege, M. & Verstraete, W. Biofuel cells select for microbial consortia that self-mediate electron transfer. *Appl. Environ. Microbiol.* **70**, 5373-5382 (2004).
- 28 Park, H. S. *et al.* A novel electrochemically active and Fe (III)-reducing bacterium phylogenetically related to *Clostridium butyricum* isolated from a microbial fuel cell. *Anaerobe* **7**, 297-306 (2001).
- 29 Kim, H. J. *et al.* A mediator-less microbial fuel cell using a metal reducing bacterium, *Shewanella putrefaciens*. *Enzyme Microb. Technol.* **30**, 145-152 (2002).
- 30 Marsili, E., Sun, J. & Bond, D. R. Voltammetry and growth physiology of *Geobacter sulfurreducens* biofilms as a function of growth stage and imposed electrode potential. *Electroanalysis: An International Journal Devoted to Fundamental and Practical Aspects of Electroanalysis* **22**, 865-874 (2010).
- 31 Strycharz-Glaven, S. M. *et al.* Electrochemical investigation of a microbial solar cell reveals a nonphotosynthetic biocathode catalyst. *Appl. Environ. Microbiol.* **79**, 3933-3942 (2013).
- 32 Millo, D. Spectroelectrochemical analyses of electroactive microbial biofilms. *Biochem. Soc. Trans.* **40**, 1284-1290 (2012).
- 33 Fricke, K., Harnisch, F. & Schröder, U. On the use of cyclic voltammetry for the study of anodic electron transfer in microbial fuel cells. *Energy Environ. Sci.* **1**, 144-147 (2008).
- 34 Kang, J., Kim, T., Tak, Y., Lee, J.-H. & Yoon, J. J. Ind. Eng. Chem. *Journal of Industrial and Engineering Chemistry* **18**, 800-807 (2012).
- 35 Marsili, E., Rollefson, J. B., Baron, D. B., Hozalski, R. M. & Bond, D. R. Microbial biofilm voltammetry: direct electrochemical characterization of catalytic electrode-attached biofilms. *Appl. Environ. Microbiol.* **74**, 7329-7337 (2008).
- 36 Ruiz, Y. *et al.* Repeatability of low scan rate cyclic voltammetry in bio-electrochemical systems and effects on their performance. *J. Chem. Technol. Biotechnol.* **95**, 1533-1541 (2020).
- 37 de Leeuw, K., Buisman, C. J. & Strik, D. P. Branched Medium Chain Fatty Acids: iso-caproate formation from iso-butyrate broadens the product spectrum for microbial chain elongation. *Environ. Sci. Technol.* (2019).
- 38 Grujicic, D. & Pesic, B. Electrochemical and AFM study of cobalt nucleation mechanisms on glassy carbon from ammonium sulfate solutions. *Electrochim. Acta* **49**, 4719-4732 (2004).
- 39 Hawthorne, K. L., Petek, T. J., Miller, M. A., Wainright, J. S. & Savinell, R. F. An investigation into factors affecting the iron plating reaction for an all-iron flow battery. *J. Electrochem. Soc.* **162**, A108 (2014).
- 40 Huizar, L. M., Rios-Reyes, C. & Rivera, M. Electrodeposition of cobalt nanoclusters from ammoniacal chloride solutions onto Hg-polymer electrodes. A kinetic and morphological study. *J. Chil. Chem. Soc.* **62**, 3621-3626 (2017).
- 41 Mishra, K., Singh, P. & Muir, D. Nucleation during electrocrystallization of cobalt on glassy carbon (GC). *J. Appl. Electrochem.* **32**, 1391-1396 (2002).
- 42 Zhou, Z. *et al.* Electrocatalytic hydrogen evolution under neutral pH conditions: current understandings, recent advances, and future prospects. *Energy Environ. Sci.* **13**, 3185-3206, doi:10.1039/d0ee01856b (2020).
- 43 Choi, O. & Sang, B.-I. Extracellular electron transfer from cathode to microbes: application for biofuel production. *Biotechnol. Biofuels* **9**, 11 (2016).
- 44 Ragsdale, S. W. & Pierce, E. Acetogenesis and the Wood-Ljungdahl pathway of CO₂ fixation. *Biochim. Biophys. Acta, Proteins Proteomics* **1784**, 1873-1898 (2008).
- 45 Pang, L., Close, M., Noonan, M. J., Flintoft, M. & Van den Brink, P. A laboratory study of bacteria-facilitated cadmium transport in alluvial gravel aquifer media. *J. Environ. Qual.* **34**, 237-247 (2005).
- 46 Bansal, V., Bharde, A., Ramanathan, R. & Bhargava, S. K. Inorganic materials using 'unusual' microorganisms. *Adv. Colloid Interface Sci.* **179-182**, 150-168, doi:10.1016/j.cis.2012.06.013 (2012).
- 47 Sleutels, T. H. *Microbial electrolysis kinetics and cell design.* (2010).

- 48 Palmer, J., Flint, S. & Brooks, J. Bacterial cell attachment, the beginning of a biofilm. *J. Ind. Microbiol. Biotechnol.* **34**, 577-588 (2007).
- 49 Barber, J. & Conway, B. Structural specificity of the kinetics of the hydrogen evolution reaction on the low-index surfaces of Pt single-crystal electrodes in 0.5 M dm⁻³ NaOH. *J. Electroanal. Chem.* **461**, 80-89 (1999).
- 50 Dai, S., Ravi, P. & Tam, K. C. pH-Responsive polymers: synthesis, properties and applications. *Soft Matter* **4**, doi:10.1039/b714741d (2008).
- 51 Jeremiasse, A. W., Hamelers, H. V. & Buisman, C. J. Microbial electrolysis cell with a microbial biocathode. *Bioelectrochemistry* **78**, 39-43 (2010).
- 52 Santini, M., Marzorati, S., Fest-Santini, S., Trasatti, S. & Cristiani, P. Carbonate scale deactivating the biocathode in a microbial fuel cell. *J. Power Sources* **356**, 400-407 (2017).
- 53 Hanselmann, K. Microbial energetics applied to waste repositories. *Experientia* **47**, 645-687 (1991).
- 54 Gamsjäger, H., Bugajski, J. & Preis, W. *Chemical thermodynamics of nickel*. (Elsevier Amsterdam, 2005).
- 55 HSC Database, *Chemistry Software*, South Nutfield.
- 56 UCDSB. Inorganic Compounds: Physical and Thermochemical Data. <http://www2.ucdsb.on.ca/tiss/stretton/database/inorganic_thermo.htm>
- 57 Rago, L., Guerrero, J., Baeza, J. A. & Guisasola, A. 2-Bromoethanesulfonate degradation in bio-electrochemical systems. *Bioelectrochemistry* **105**, 44-49 (2015).
- 58 Ragsdale, S. W. & Pierce, E. Acetogenesis and the Wood-Ljungdahl pathway of CO₂ fixation. *Biochimica et Biophysica Acta (BBA)-Proteins and Proteomics* **1784**, 1873-1898 (2008).
- 59 Kracke, F., Vassilev, I. & Krömer, J. O. Microbial electron transport and energy conservation—the foundation for optimizing bio-electrochemical systems. *Frontiers in microbiology* **6**, 575 (2015).
- 60 Irving, H. & Williams, R. Order of stability of metal complexes. *Nature* **162**, 746-747 (1948).
- 61 Waldron, K. J., Rutherford, J. C., Ford, D. & Robinson, N. J. Metalloproteins and metal sensing. *Nature* **460**, 823-830 (2009).
- 62 Dudev, T. & Lim, C. Competition among metal ions for protein binding sites: determinants of metal ion selectivity in proteins. *Chemical reviews* **114**, 538-556 (2014).
- 63 Foster, A. W., Osman, D. & Robinson, N. J. Metal preferences and metallation. *Journal of biological chemistry* **289**, 28095-28103 (2014).
- 64 Tottey, S. *et al.* Protein-folding location can regulate manganese-binding versus copper-or zinc-binding. *Nature* **455**, 1138-1142 (2008).
- 65 Xiao, Y. *et al.* Extracellular polymeric substances are transient media for microbial extracellular electron transfer. *Science advances* **3**, e1700623 (2017).
- 66 Hawthorne, K. L., Petek, T. J., Miller, M. A., Wainright, J. S. & Savinell, R. F. An investigation into factors affecting the iron plating reaction for an all-iron flow battery. *Journal of the Electrochemical Society* **162**, A108 (2014).
- 67 Bai, A. & Hu, C.-C. Iron-cobalt and iron-cobalt-nickel nanowires deposited by means of cyclic voltammetry and pulse-reverse electroplating. *Electrochemistry Communications* **5**, 78-82 (2003).
- 68 Yu, P. *et al.* Potential-controllable green synthesis and deposition of metal nanoparticles with electrochemical method. *Journal of Materials Chemistry* **20**, 5820-5822 (2010).
- 69 Barsan, M. M. & Brett, C. M. Recent advances in layer-by-layer strategies for biosensors incorporating metal nanoparticles. *TrAC Trends in Analytical Chemistry* **79**, 286-296 (2016).
- 70 Bansal, V., Bharde, A., Ramanathan, R. & Bhargava, S. K. Inorganic materials using 'unusual' microorganisms. *Advances in colloid and interface science* **179-182**, 150-168, doi:10.1016/j.cis.2012.06.013 (2012).
- 71 Hezard, T. *et al.* Gold nanoparticles electrodeposited on glassy carbon using cyclic voltammetry: Application to Hg (II) trace analysis. *Journal of Electroanalytical Chemistry* **664**, 46-52 (2012).
- 72 Wang, W., Zhang, B. & He, Z. Bio-electrochemical deposition of palladium nanoparticles as catalysts by *Shewanella oneidensis* MR-1 towards enhanced hydrogen production in microbial electrolysis cells. *Electrochimica Acta* (2019).
- 73 Yang, Y. *et al.* Non-precious alloy encapsulated in nitrogen-doped graphene layers derived from MOFs as an active and durable hydrogen evolution reaction catalyst. *Energy & Environmental Science* **8**, 3563-3571 (2015).
- 74 Jaramillo, T. F. *et al.* Identification of active edge sites for electrochemical H₂ evolution from MoS₂ nanocatalysts. *science* **317**, 100-102 (2007).

- 75 Aslan, E., Akin, I. & Patir, I. H. Highly active cobalt sulfide/carbon nanotube catalyst for hydrogen evolution at soft interfaces. *Chemistry–A European Journal* **22**, 5342-5349 (2016).
- 76 Miles, M. H. Evaluation of electrocatalysts for water electrolysis in alkaline solutions. *Journal of Electroanalytical Chemistry and Interfacial Electrochemistry* **60**, 89-96 (1975).
- 77 Eftekhari, A. Electrocatalysts for hydrogen evolution reaction. *International Journal of Hydrogen Energy* **42**, 11053-11077 (2017).
- 78 Sun, D. *et al.* The effect of biofilm thickness on electrochemical activity of *Geobacter sulfurreducens*. *international journal of hydrogen energy* **41**, 16523-16528 (2016).
- 79 Flemming, H.-C. & Wingender, J. The biofilm matrix. *Nature reviews microbiology* **8**, 623 (2010).
- 80 Choi, O. & Sang, B.-I. Extracellular electron transfer from cathode to microbes: application for biofuel production. *Biotechnology for biofuels* **9**, 11 (2016).
- 81 Downard, A. J. Electrochemically assisted covalent modification of carbon electrodes. *Electroanalysis: An International Journal Devoted to Fundamental and Practical Aspects of Electroanalysis* **12**, 1085-1096 (2000).
- 82 Pozo, G. *et al.* Cathodic biofilm activates electrode surface and achieves efficient autotrophic sulfate reduction. *Electrochimica Acta* **213**, 66-74, doi:10.1016/j.electacta.2016.07.100 (2016).
- 83 Pinyou, P., Blay, V., Muresan, L. M. & Noguer, T. Enzyme-modified electrodes for biosensors and biofuel cells. *Materials Horizons* (2019).
- 84 Pasula, R. R. & Lim, S. Engineering nanoparticle synthesis using microbial factories. *Engineering Biology* **1**, 12-17 (2017).

Supporting information

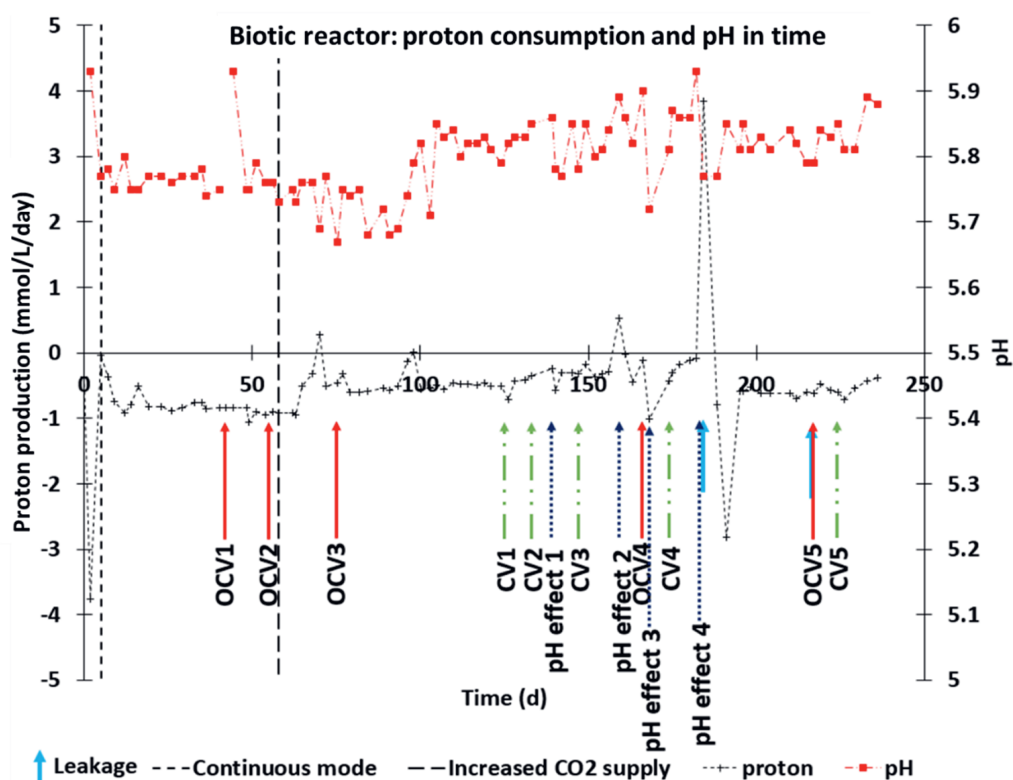


Figure S2.1. Proton production and reactor pH in time in the bio-electrochemical CO₂ elongation system. The CV scans (day 125, 133, 147, 174 and 224) are indicated by green long dash double dotted arrows, the open cell voltage applications are indicated by red arrows (day 42, 55, 75, 166 ; day 217 was OCV with repair of leak, indicated by the black arrow). Changes in the pH that affected the current are indicated by the blue dashed arrows. The pH control in the biotic reactor was not working on day 139 and 168, on day 159 the gas supply was shortly turned off and at day 183 a liquid leak occurred at the cathode compartment. The proton production was calculated by the change in weight of the bottles of 1 M HCl and NaOH that were used for controlling the reactor pH.

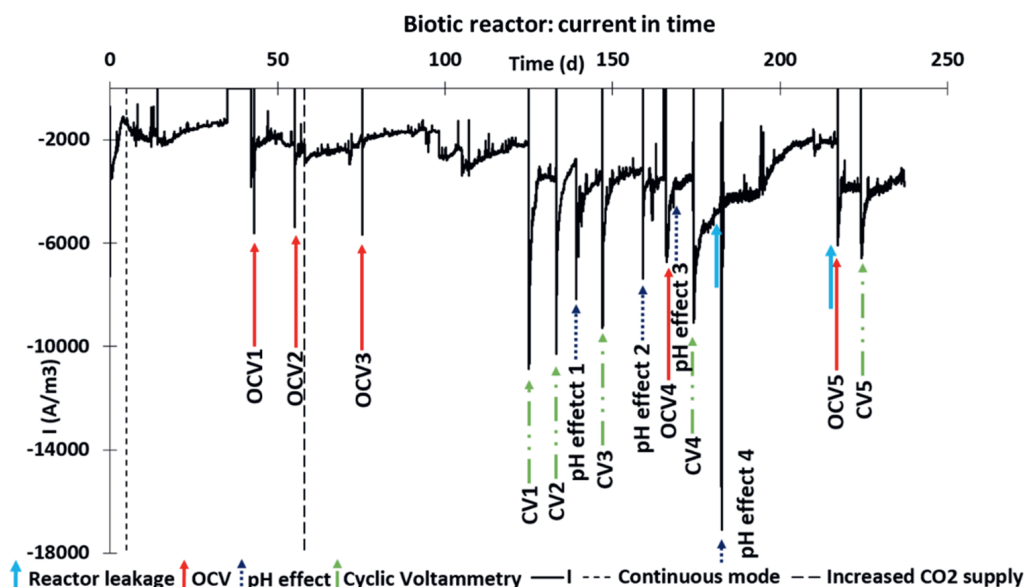


Figure S2.2. Current in time (Ampere per m^3 biocathode), at a potential of -0.85 vs SHE in a biotic electrochemical CO_2 -fed system. Carbon felt was used as cathode material. At day 5, the biotic reactor was put into continuous mode, the CO_2 supply rate was increased ten-fold at day 58. A power failure on day 42 caused a data loss from day 35-42. The CV scans (day 125, 133, 147, 174 and 224) are indicated by green long dash double dotted arrows, the open cell voltage applications are indicated by red arrows (day 42, 55, 75, 166 ; day 217 was OCV with repair of leak, indicated by the black arrow). Changes in the pH that affected the current are indicated by the blue dashed arrows. The pH control in the biotic reactor was not working on day 139 and 168, on day 159 the gas supply was shortly turned off and at day 183 a liquid leak occurred at the cathode compartment.

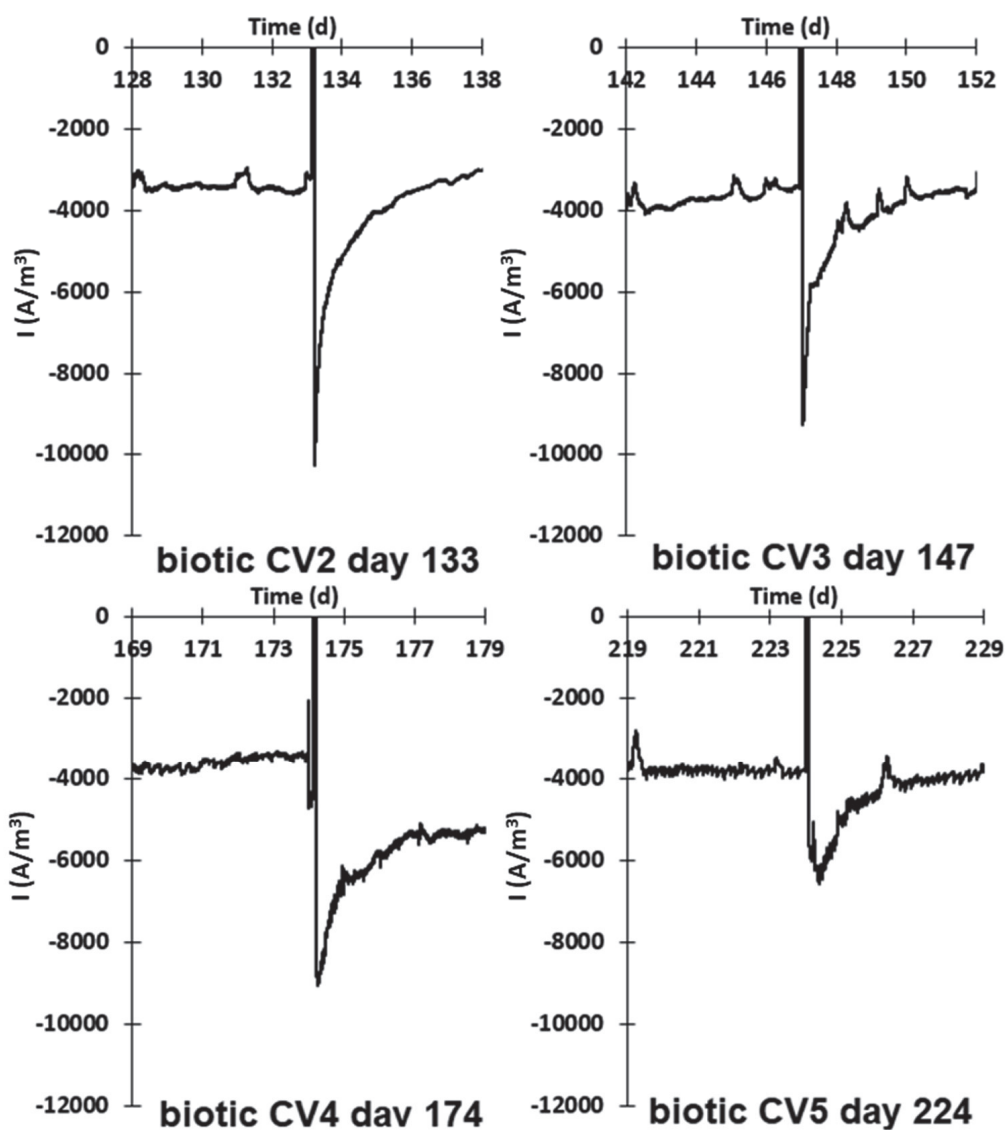


Figure S2.3. Cathodic current in time before and after the cyclic voltammograms (CV) performed with the biotic CO₂-fed elongation reactor. The current during the CVs can be found in Figure S2.6.

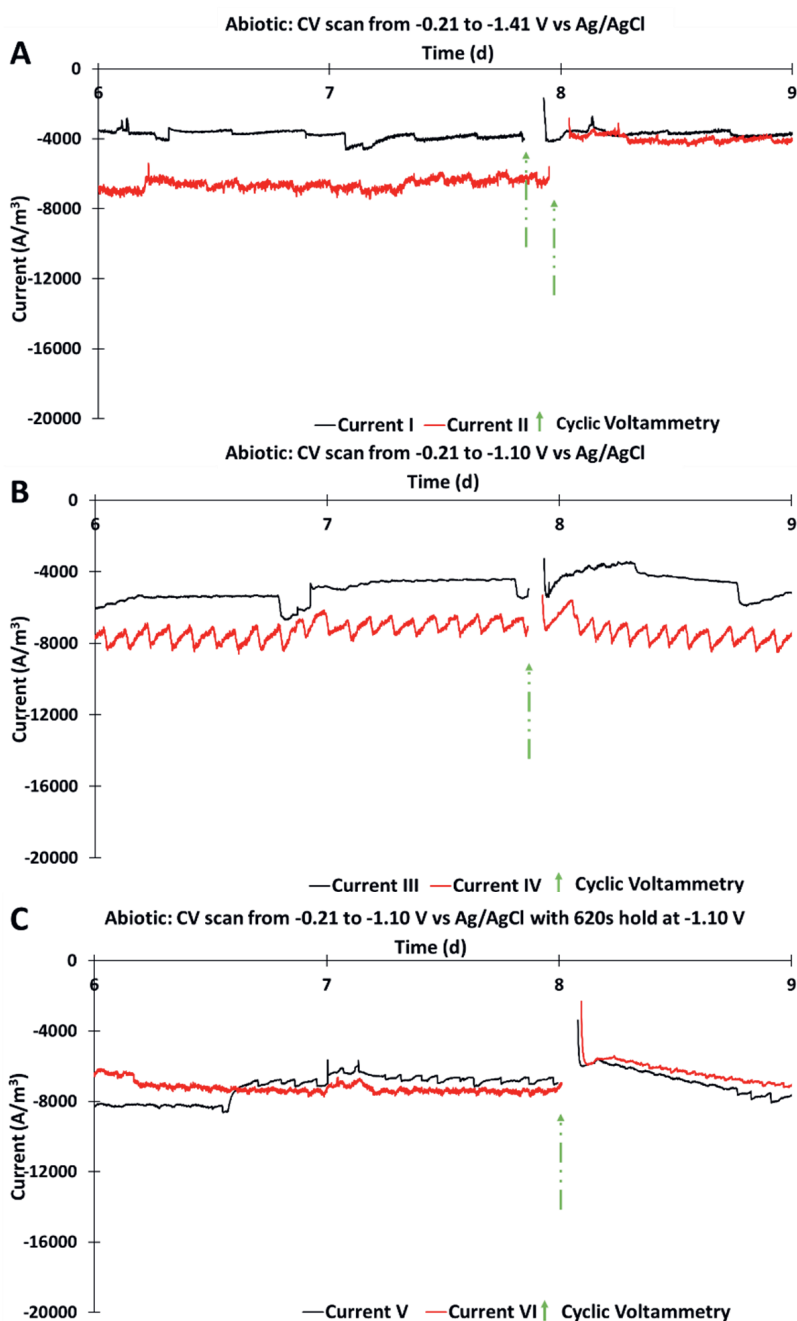


Figure S2.4. Current in time (per m³ cathode), at a potential of -0.85 vs SHE in duplicate abiotic electrochemical CO₂-fed systems. These reactors were run continuously with an ammonium-free medium. The abiotic experiments were performed in a relatively short time to prevent microbial growth in the abiotic system due to non-sterile lab conditions, which was observed to occur during long term 'abiotic' operation by Raes, et al. 11. The CV scan was performed on day 8, indicated by the green long dash double dotted arrows. Three different CV potential ranges were used; for the abiotic experiments A, B and C, the potential ranges were respectively -0.21 to -1.41 V, -0.21 to -1.10 V and -0.21 to -1.10 V with 620 sec hold at -1.10 V (all vs Ag/AgCl).

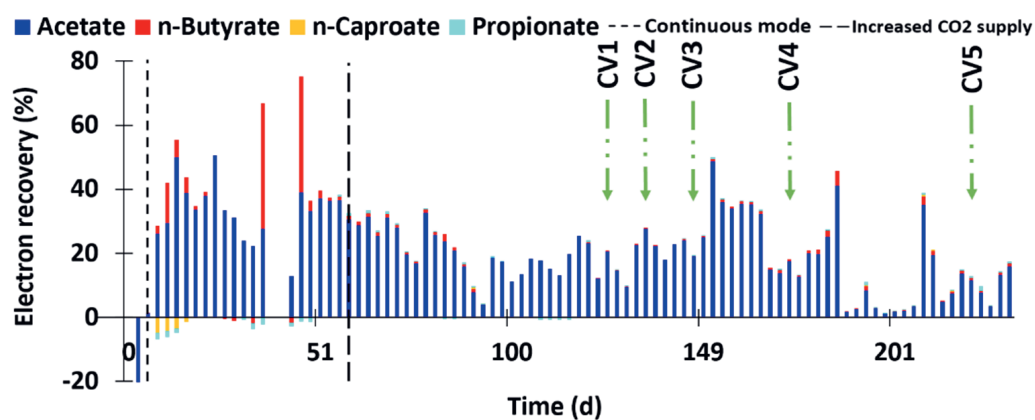
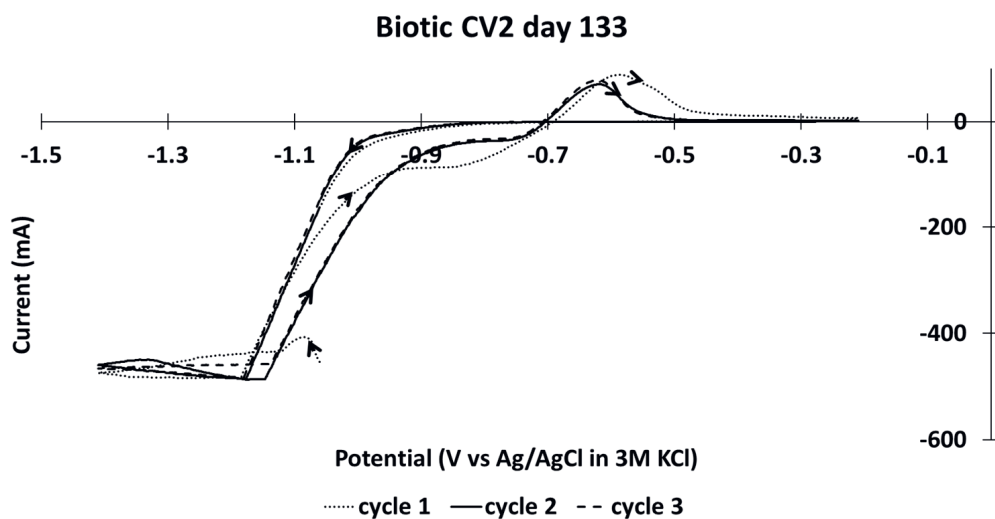
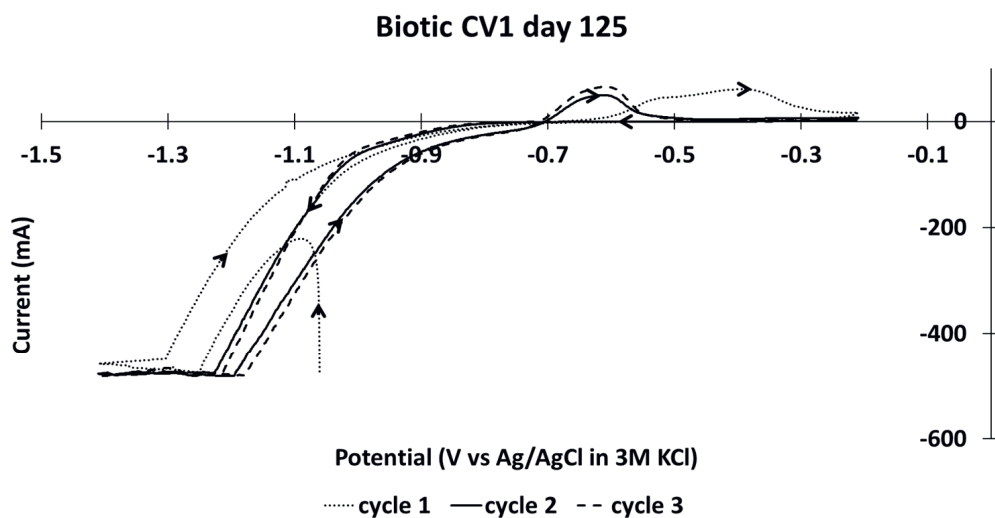


Figure S2.5. Electron recovery in acetate, n-butyrate, propionate and n-caproate in the continuous bio-electrochemical CO₂ elongation reactor. At day 5, the biotic reactor was put into continuous mode, the CO₂ supply rate was increased ten-fold at day 58. The CV scans are indicated by green long dash double dotted arrows.



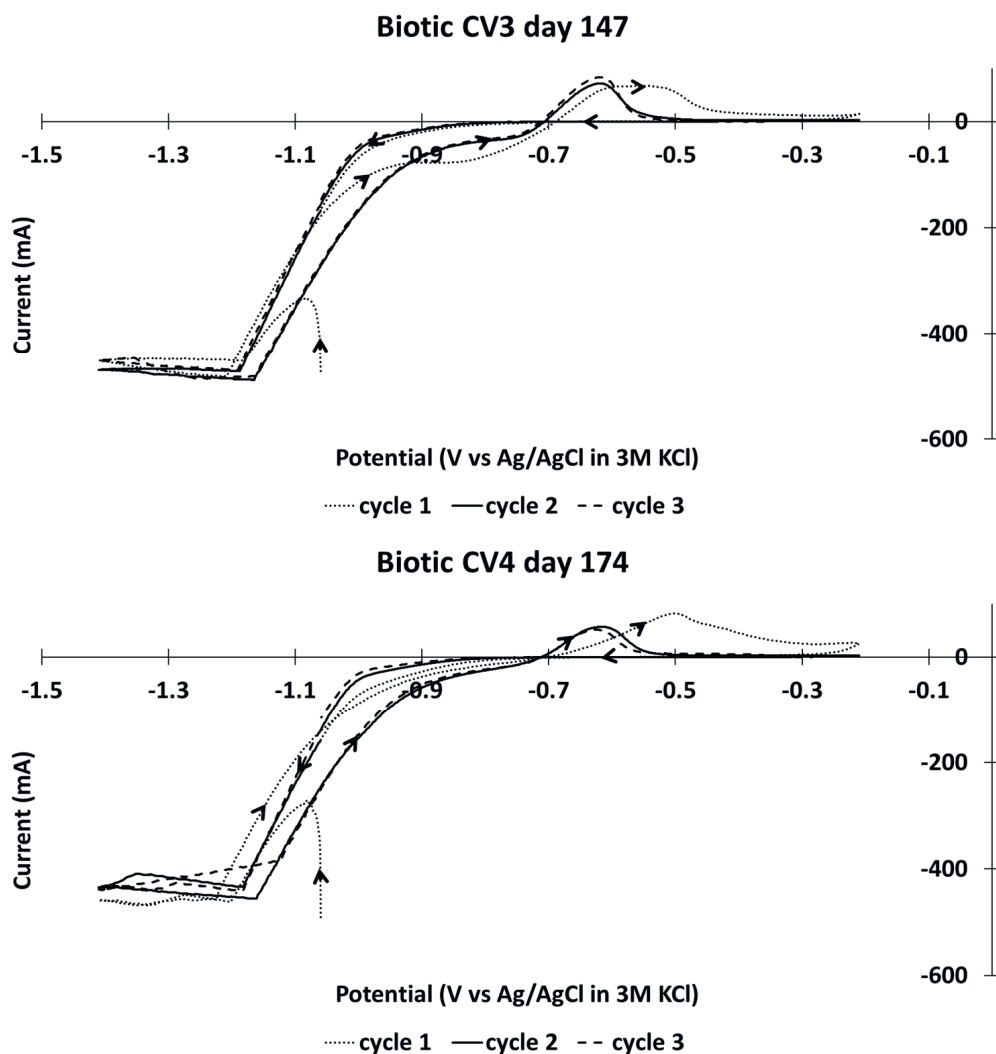


Figure S 2.6. Cyclic voltammograms run with the bio-electrochemical CO₂ elongation reactor (day 125, 133, 147 and 174). Each scan was run at 1 mV/s and consisted of three cycles. A voltage overload occurred at potential values around -1.2 V to -1.41 V vs Ag/AgCl, so more negative potentials were not reached. The arrows show the direction of the scans.

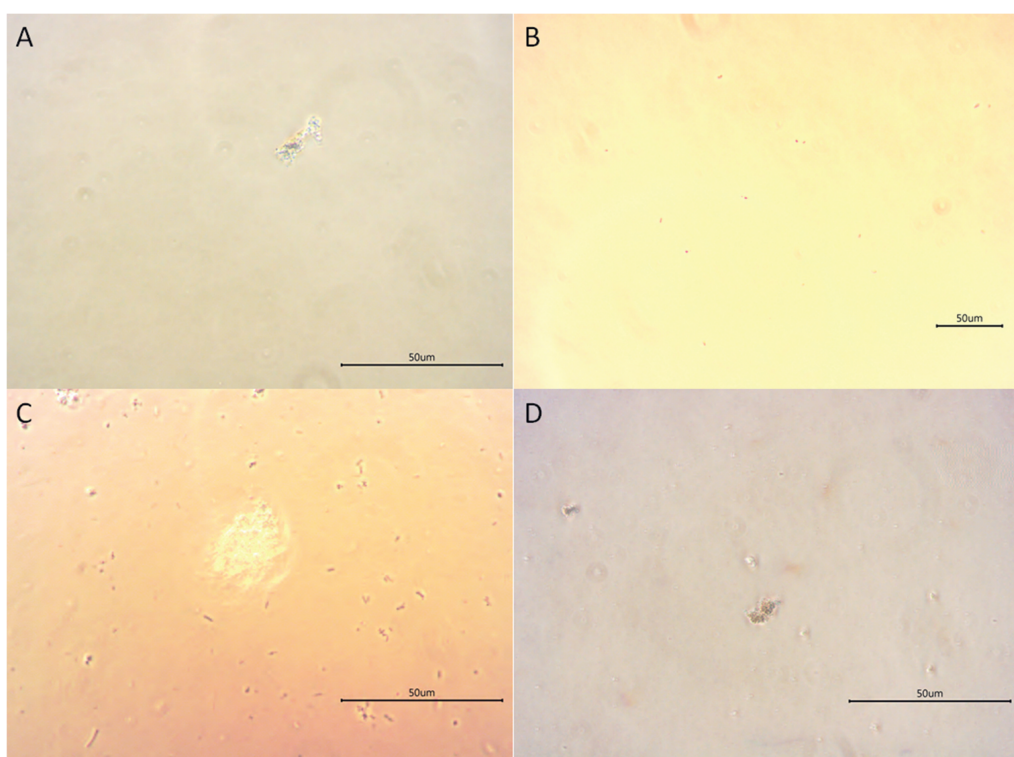
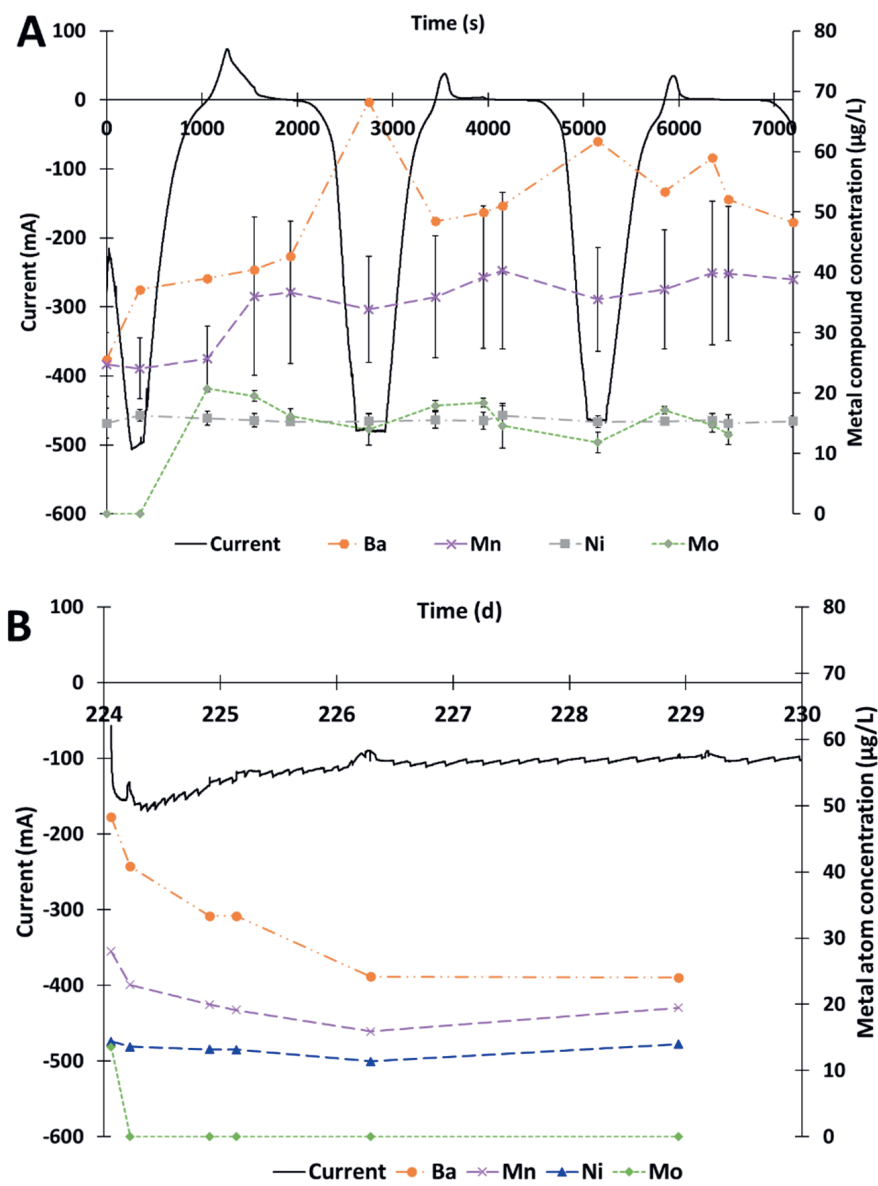


Figure S2.7. Microscopic images of catholyte from the bio-electrochemical CO_2 elongation reactor before (A) the CV run at day 224, from the abiotic reactor at day 10 (B) and simultaneous with the oxidation peak of the first CV cycle (-0.21 V vs Ag/AgCl 3 M KCl) (C and D).



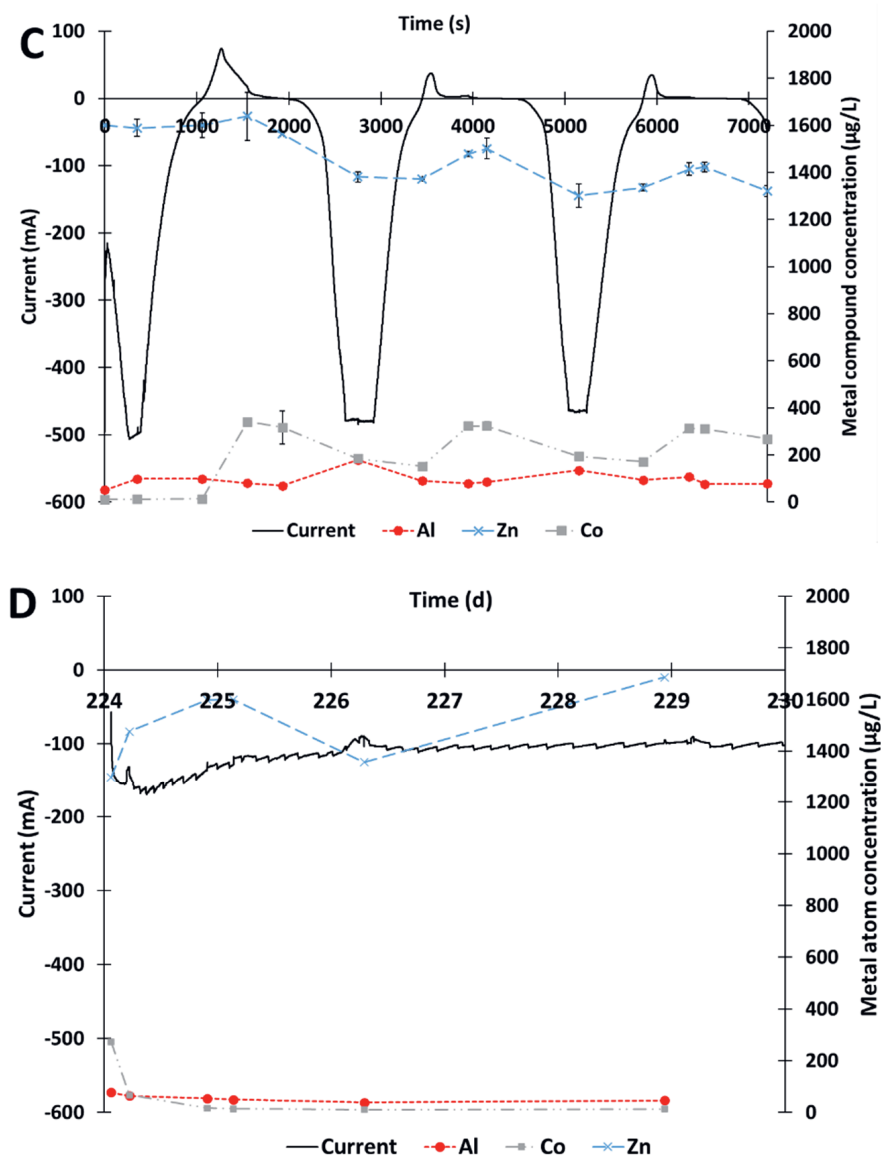
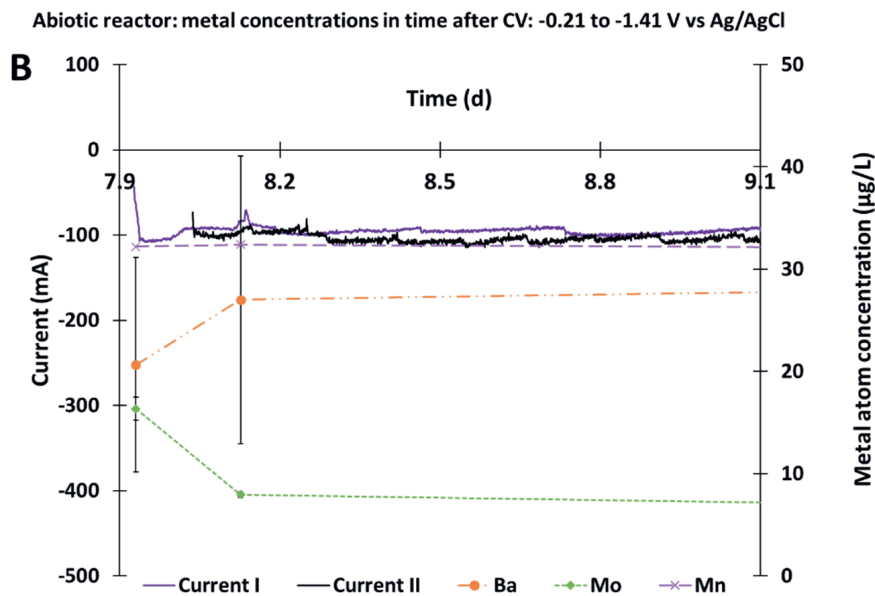
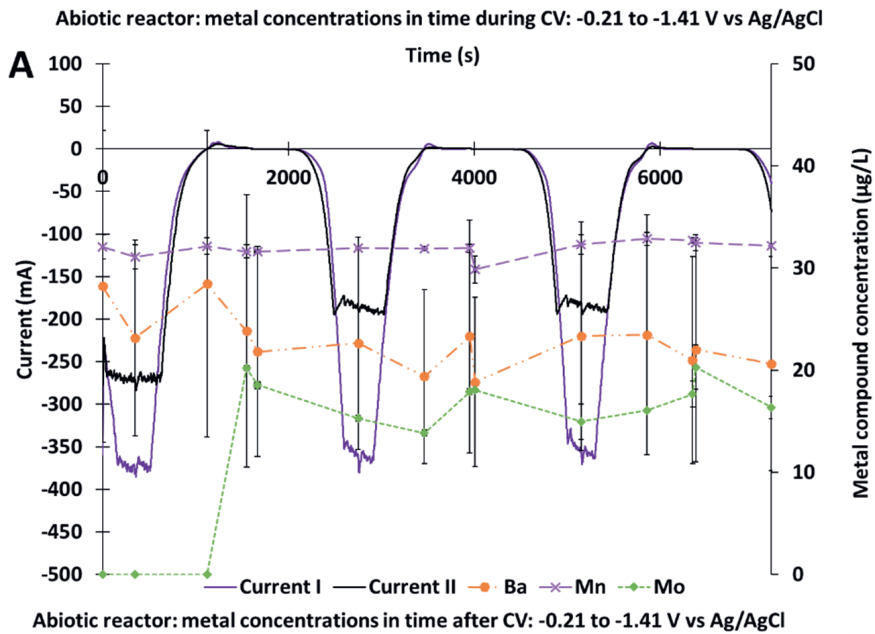


Figure S2.8. Change in concentrations of barium, manganese, molybdenum and nickel (A) and of aluminium, cobalt and zinc (C) in the catholyte in time with the change in current during the 3 cyclic voltammetry scan performed with the biotic electrochemical CO₂ elongation system (A and C). The change in current and the catholyte concentrations of barium, manganese and molybdenum (B) and of aluminium, zinc and cobalt (D) in time after the cyclic voltammetry scan on day 224 are shown as well. The error bars indicate the difference between the CV scans performed on day 174 and day 224. The potential was controlled on -0.85 vs SHE after the CVs (B and D).



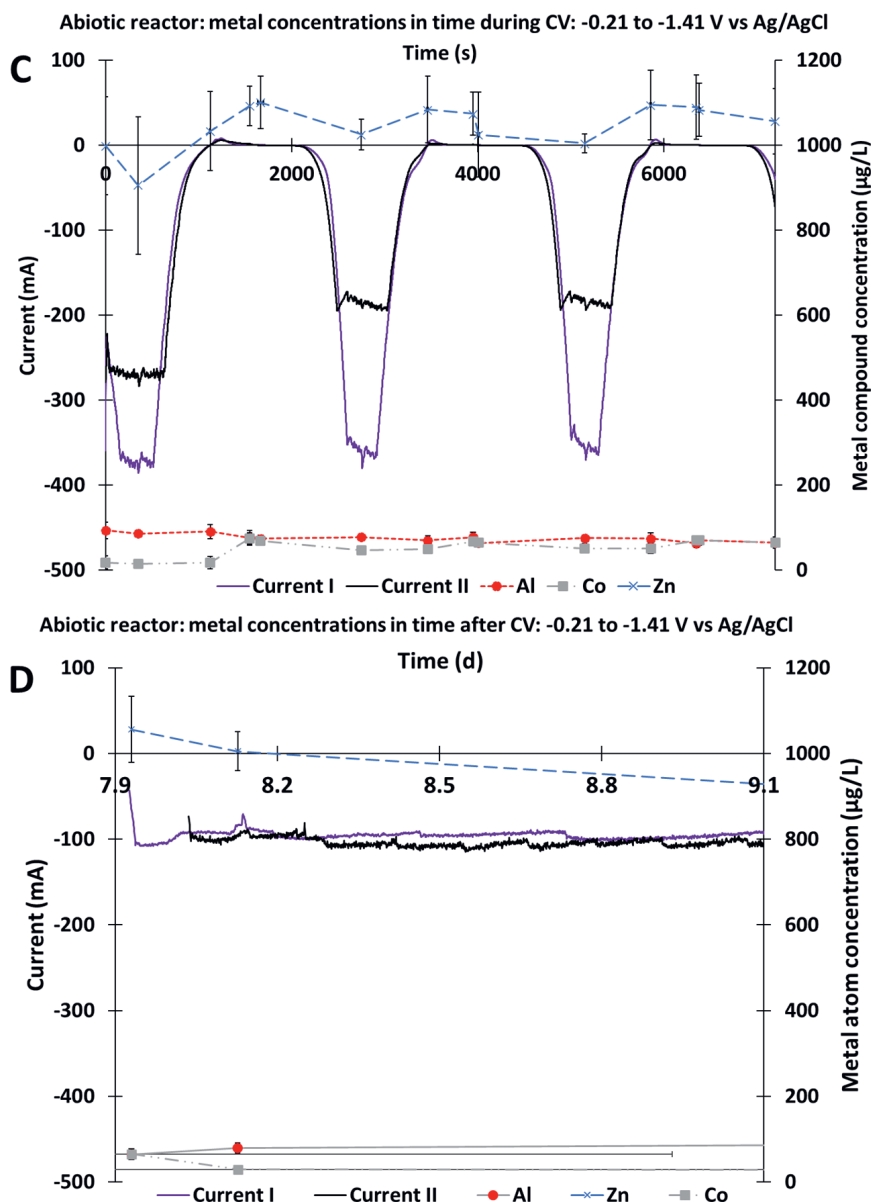
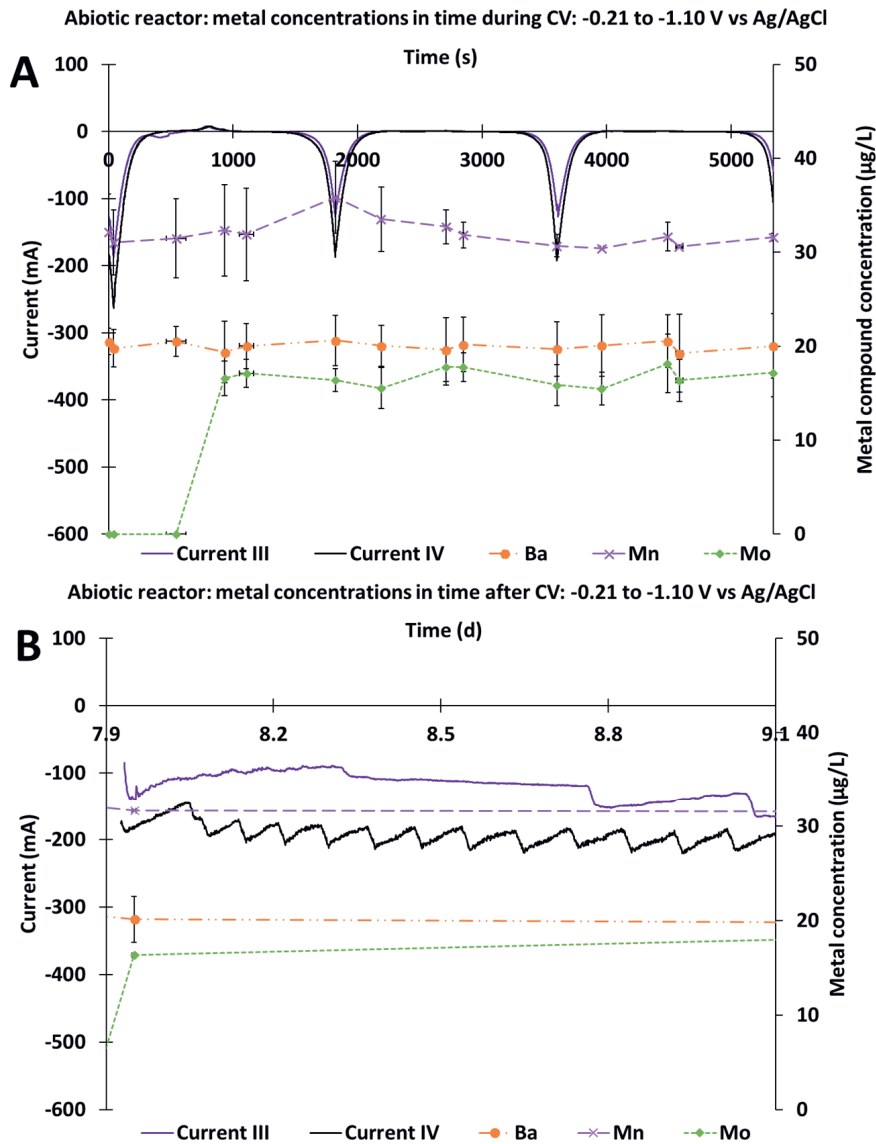
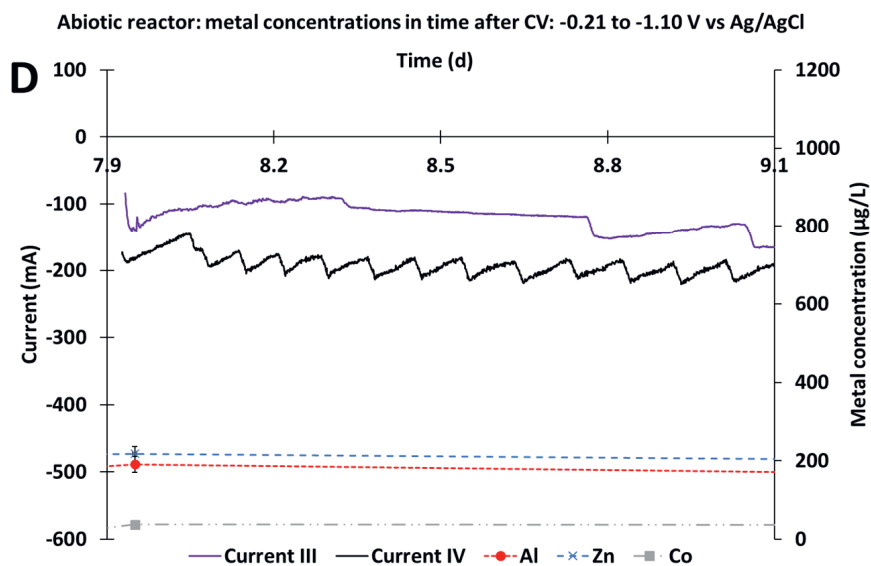
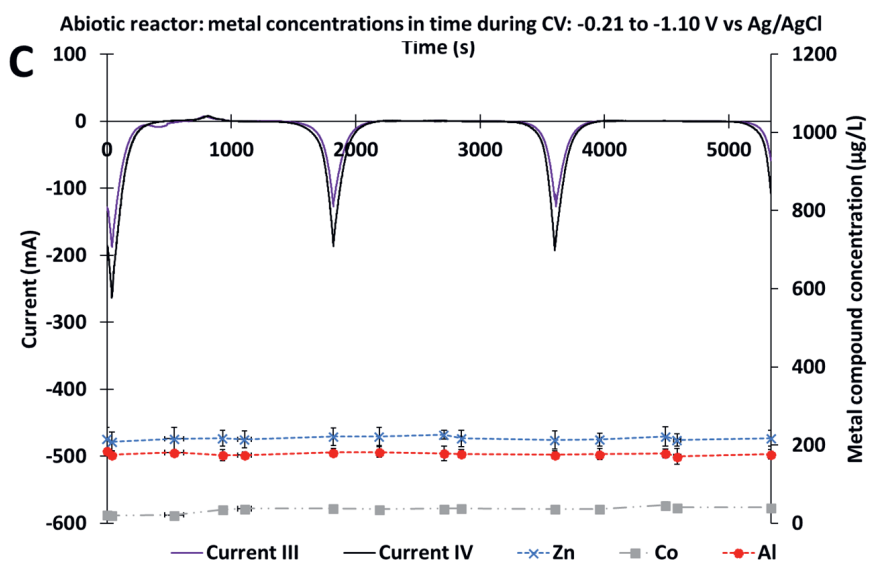
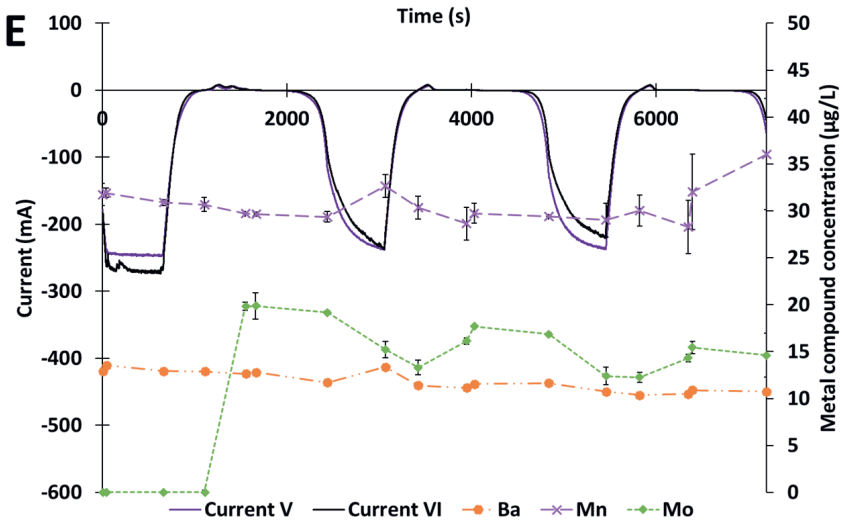


Figure S2.9. Change in concentrations of barium, manganese and molybdenum (A) and of aluminium, cobalt and zinc (C) in the catholyte in time with the change in current during the 3 cyclic voltammetry scan performed with abiotic electrochemical CO₂ elongation systems I and II (A and C). The change in current and the catholyte concentrations of barium, manganese and molybdenum (B) and of aluminium, zinc and cobalt (D) in time after the cyclic voltammetry scan are shown as well. The error bars indicate the difference between the duplicate experiments. The potential was controlled on -0.85 vs SHE after the CVs (B and D).

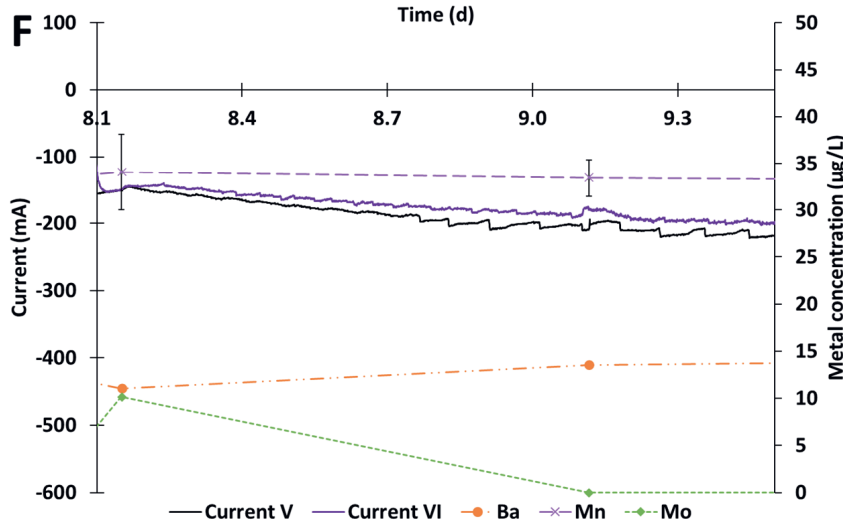




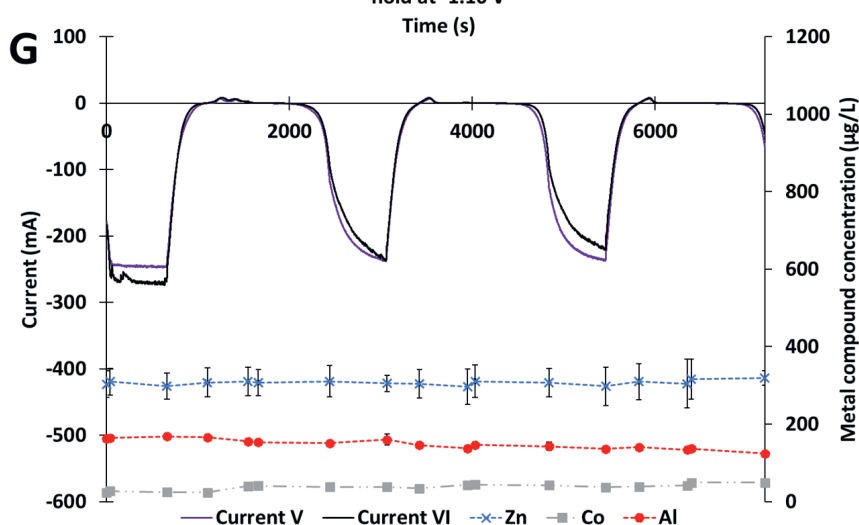
Abiotic reactor: metal concentrations in time during CV: -0.21 to -1.10 V vs Ag/AgCl with 620s hold at -1.10 V



Abiotic reactor: metal concentrations in time after CV: -0.21 to -1.10 V vs Ag/AgCl with 620s hold at -1.10 V



Abiotic reactor: metal concentrations in time during CV: -0.21 to -1.10 V vs Ag/AgCl with 620s hold at -1.10 V



Abiotic reactor: metal concentrations in time after CV: -0.21 to -1.10 V vs Ag/AgCl with 620s hold at -1.10 V

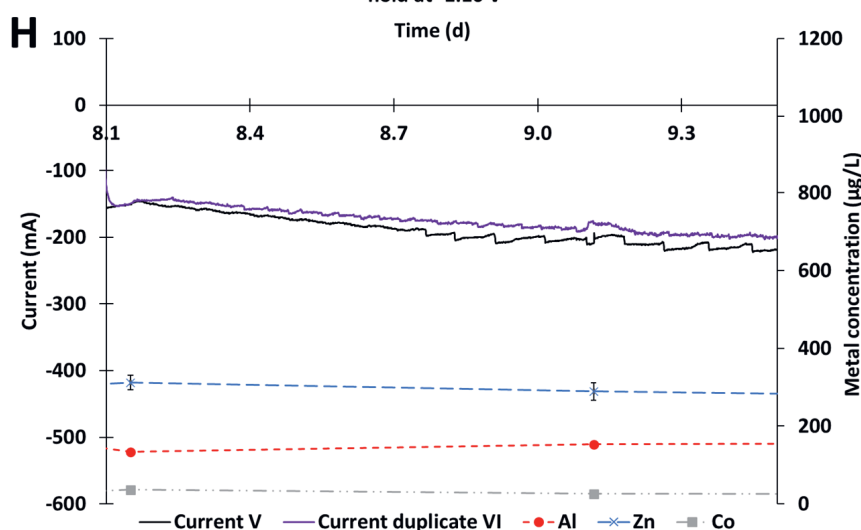


Figure S2.10. Change in catholyte metal concentrations in time with the change in current during the 3 cyclic voltammetry (CV) scan performed with the two abiotic duplicates: III and IV (CV from -0.21 to -1.10 V; A & C) and V and VI (CV from -0.21 to -1.10 V with 620 sec potential hold at -1.10 V; E & G). The change in current and the catholyte iron and magnesium concentrations in time after the CV scan performed with abiotic reactors are shown as well: III and IV (B & D) and V and VI (F and H). The vertical error bars indicate the difference between the duplicate experiments, the horizontal error bars indicate the different sampling moments during the different CV scans. The arrows indicate the axes used for the different graphs. The potential was controlled on -0.85 vs SHE after the CVs (B, D, F and H).

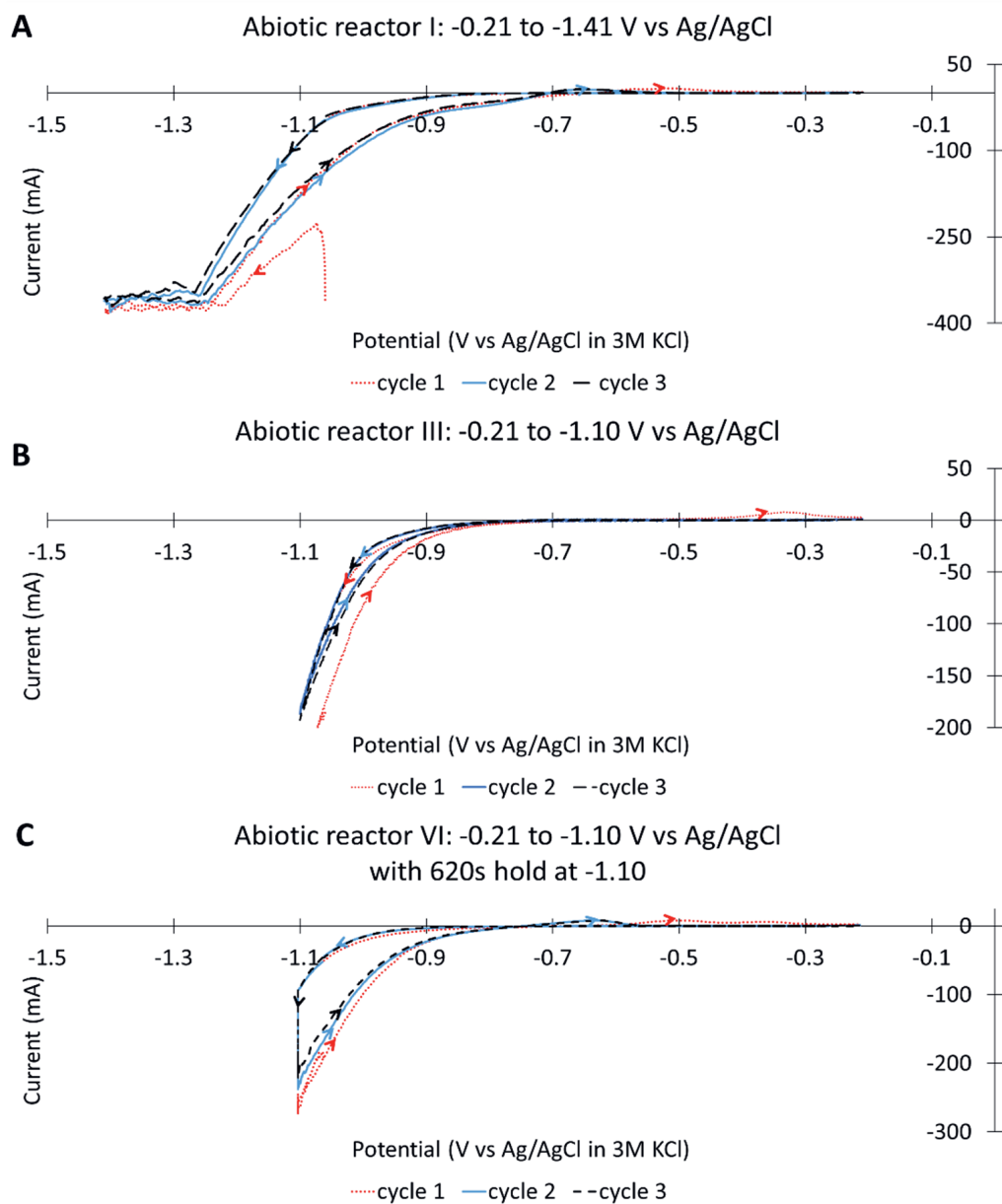


Figure S2.11. Cyclic voltammograms run with the abiotic electrochemical CO₂ elongation reactor I (A), IV (B) and VI (C). Each scan was run at 1 mV/s and consisted of three cycles. The different CV scans had potential ranges of -0.21 to -1.41 V (A), from -0.21 to -1.10 V (B) and from -0.21 to -1.10 V with 620 sec potential hold at -1.10 V (C) (all reported against Ag/AgCl). A voltage overload occurred at potential values more negative than -1.2 V vs Ag/AgCl (A), so more negative potentials were not reached. The arrows indicate the direction of the scan.

Table S2.1. Concentrations of measured alcohols, fatty acids and optical density in time for the first of the duplicate abiotic experiments. No alcohols were detected.

Day	Concentration (mM)												OD ₆₀₀
	Acetate	Propionate	iso-butyrate	n-butyrate	iso-valerate	n-valerate	iso-caproate	n-caproate	n-heptate	n-caprylate	iso-heptate		
0.0	<0.85	0	0	0	0	0	0	0	<0.15	0	0		0.005
0.7	<0.85	0	0	0	0	0	0	0	0	0	0		
3.9	<0.85	0	0	0	0	0	0	0	0	0	0		0.015
5.9	<0.85	0	0	0	0	0	0	0	0	0	0		0.008
8.0	<0.85	0	0	0	0	0	0	0	0	0	0		0.006
10.7	<0.85	<0.68	0	0	0	0	0	0	0	0	0		0.005
12.9	<0.85	<0.68	0	0	0	0	0	0	0	0	0		0.004
14.9	<0.85	<0.68	0	0	0	0	0	0	0	0	0		0.007

Table S2.2. Concentrations of measured alcohols, fatty acids and optical density in time for the second of the duplicate abiotic experiments. No alcohols were detected.

Day	Concentration (mM)												OD ₆₀₀
	Acetate	Propionate	iso-butyrate	n-butyrate	iso-valerate	n-valerate	iso-caproate	n-caproate	n-heptate	n-caprylate	iso-heptate		
0.0	<0.85	<0.68	0	0	0	0	0	0	0	0	0		0.007
0.7	<0.85	<0.68	0	0	0	0	0	0	0	0	0		
3.9	<0.85	<0.68	0	0	0	0	0	0	0	0	0		0.006
5.9	<0.85	<0.68	0	0	0	0	0	0	0	0	0		0.005
8.0	<0.85	<0.68	0	0	0	0	0	0	0	0	0		0.005
10.7	<0.85	<0.68	0	0	0	0	0	0	0	0	0		0.003
12.9	<0.85	<0.68	0	0	0	0	0	0	0	0	0		0.004
14.9	<0.85	<0.68	0	<0.46	<0.30	<0.30	<0.17	<0.17	<0.15	0	0		0.001

Table S2.3. Element concentrations in the abiotic and biotic catholyte media and in the reactor before potential was applied to the abiotic reactors. Also the reactor catholyte concentrations of cobalt, copper, iron, manganese, nickel, zinc and molybdenum in the biotic reactor on day 125 prior to the first CV scan are shown. The grey marked cell contains values that were above the range of the used calibration lines. Ag, Bi, Cd, Ga, Li, Pb and Sr were not measured above the detection limit of 10 µg/L.

Sample	Al	Ba	Ca	Co	Cr	Cu	Fe	Mg	Mn	Ni	Zn	Mo
Abiotic II catholyte medium	<10	<10	4556	33	61	11	271	4115	30	16	31	23
Abiotic II reactor catholyte before potential	64	<10	5079	35	75	18	339	4474	35	23	652	29
Abiotic I catholyte medium	<10	<10	5142	36	68	11	294	4530	34	18	34	25
Abiotic I reactor catholyte before potential	35	15	5269	36	70	16	322	4595	36	25	455	26
Biotic catholyte medium				41		16	403		43	18	101	28
Biotic reactor catholyte on day 125 before CV scan				11		<10	32		45	19	2516	<10

Table S2.4. Element concentrations in the biotic catholyte medium and of the catholyte medium after being brought in contact with various reactor parts for five hours. The grey marked cells contain values that were above the range of the used calibration lines. Ag, Bi, Cd, Li and Sr were not measured above the detection limit of 10 µg/L.

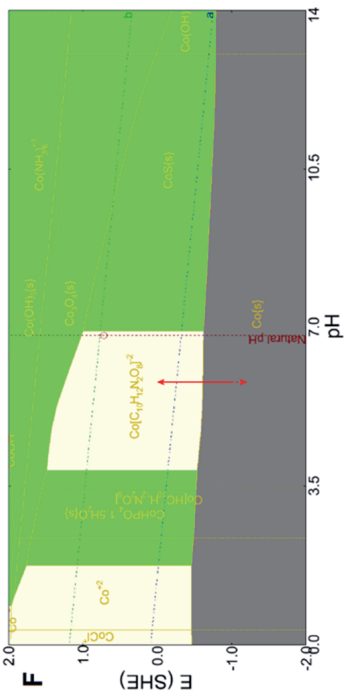
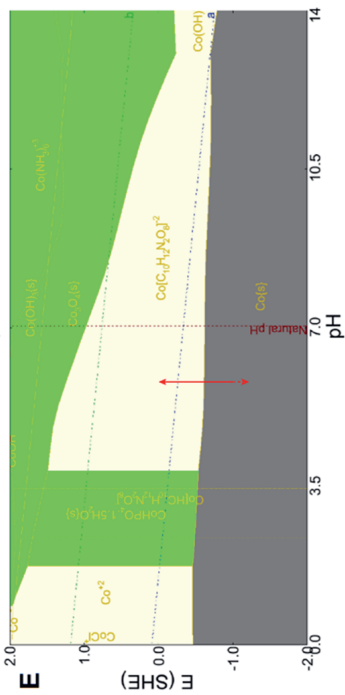
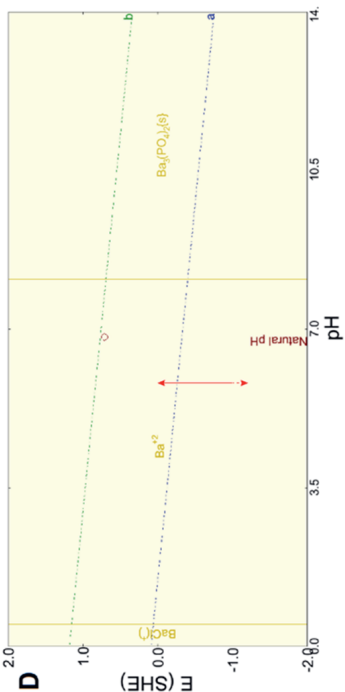
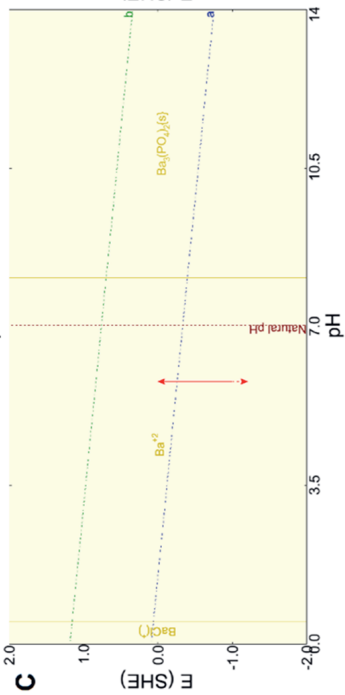
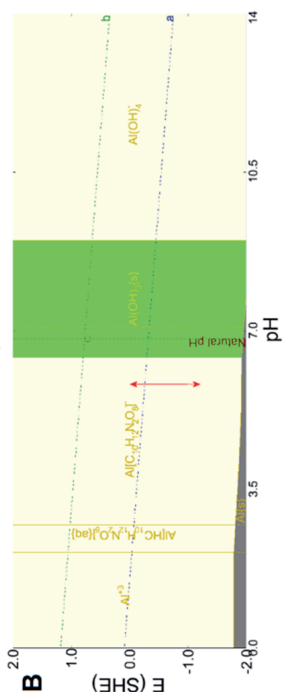
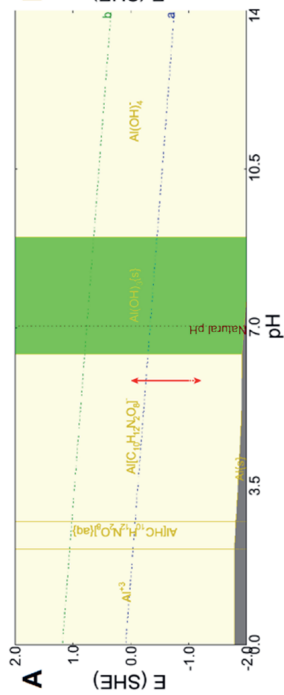
Sample	Al	Ba	Ca	Co	Cr	Cu	Fe	Ga	Mg	Mn	Ni	Pb	Zn	Mo
Catholyte medium	<10	<10	<1000	28	73	10	252	<10	4687	28	<10	<10	<100	19
Catholyte medium with glue	<10	<10	<1000	30	76	10	261	<10	4875	29	<10	<10	<100	21
Catholyte medium with sparger	13	<10	<1000	30	75	21	280	<10	4850	30	19	<10	<100	20
Catholyte medium with glass ref el capillary	<10	<10	<1000	30	74	11	256	<10	4773	29	<10	27	<100	20
Titanium wire in 1 M HCl	42	21	<1000	<10	<10	18	75	12	<1000	<10	<10	<10	227	<10
Catholyte medium with norprene tubing	<10	<10	<1000	30	73	15	270	<10	4757	29	14	<10	312	20
Catholyte medium with cation exchange membrane	45	<10	<1000	42	108	26	413	<10	1109	43	25	<10	143	30
Catholyte medium with Teflon tube	<10	<10	<1000	30	75	11	262	<10	4810	29	11	<10	<100	20
Catholyte medium with neoprene gasket material	65	<10	<1000	32	76	21	269	<10	5066	41	33	<10	2168	20
Catholyte medium with anode electrode	32	<10	<1000	29	72	26	274	<10	4702	31	20	<10	<100	20
Catholyte medium with silicone gaskets	11	<10	5838	38	68	25	325	<10	4945	36	18	<10	82	26

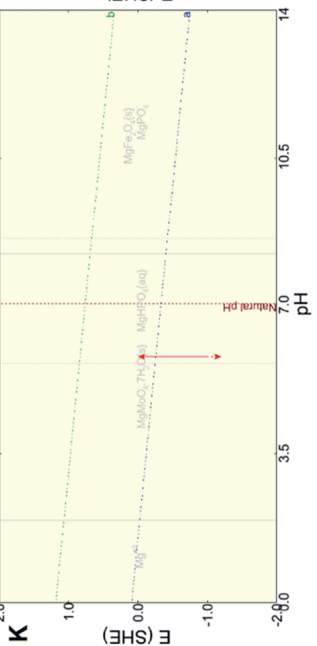
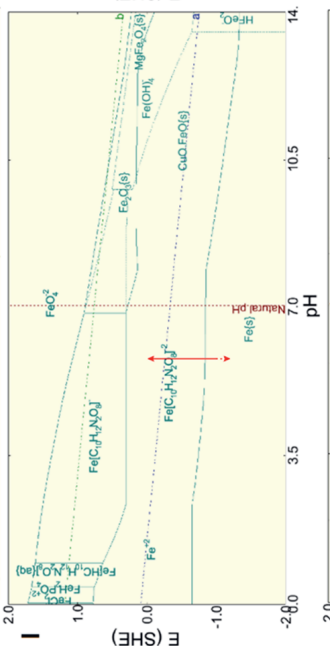
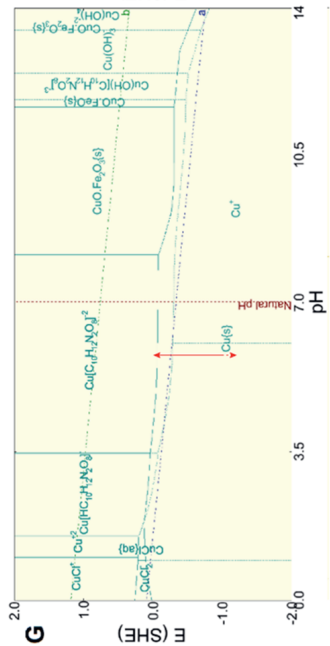
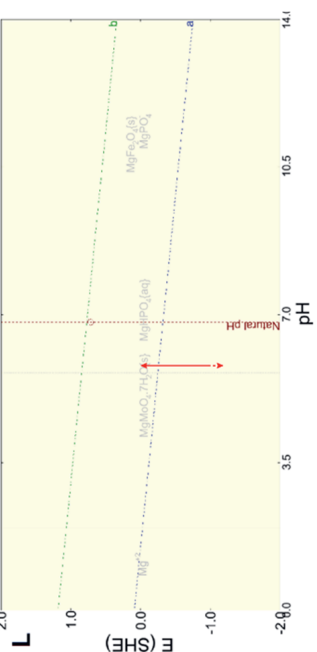
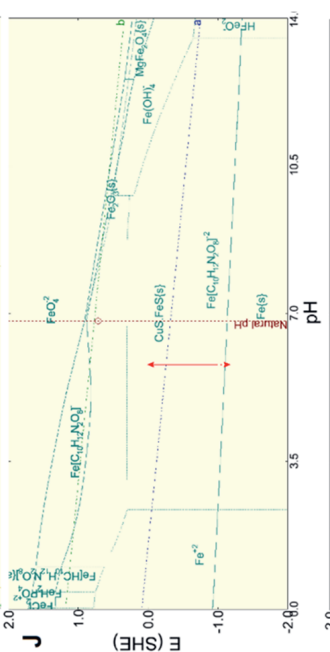
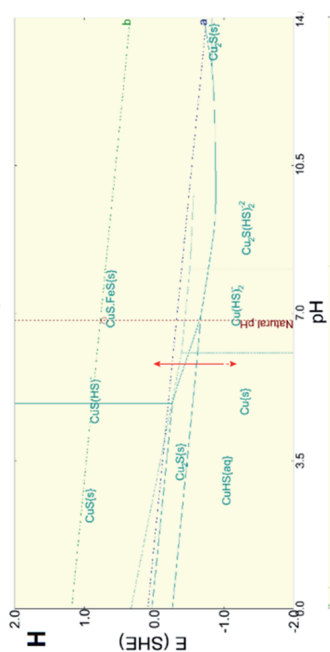
Table S2.5. Element concentrations in the non-centrifuged catholyte, and in the supernatant and pellet from the centrifuged sample taken after the first oxidation step of the Cyclic Voltammetry scan performed with the biotic CO₂ elongation system on day 224. An undefined amount of pellet was dissolved in milliQ water for an indicative measurement of the metal compound distribution between the biomass and the catholyte. The grey marked cells contain values that were above the range of the used calibration lines. Ag, Bi, Cd, Ga, Li, Pb and Sr were not detected above the detection limit of 10 µg/L.

Sample	Concentration (µg/L)												
	Al	Ba	Ca	Co	Cr	Cu	Fe	Mg	Mn	Ni	Zn	Mo	S
Non-centrifuged sample	81	40	8360	272	60	<10	7586	8717	23	14	1633	20	50830
Supernatant	<1 0	<10	<1000	239	60	<10	694	7641	18	14	928	18	319343
Pellet	20	13	<1000	<1 0	<1 0	<10	2449	<1000	<1 0	<10	183	<10	204
													197883
													161211
													<1000

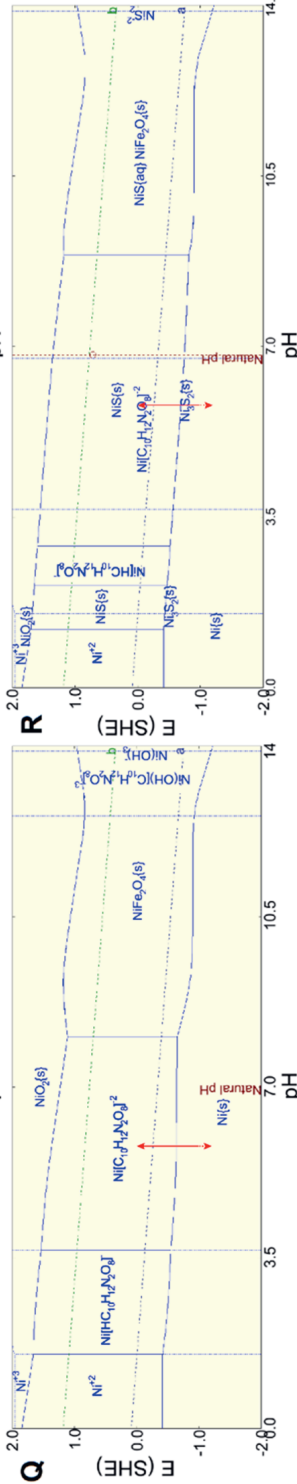
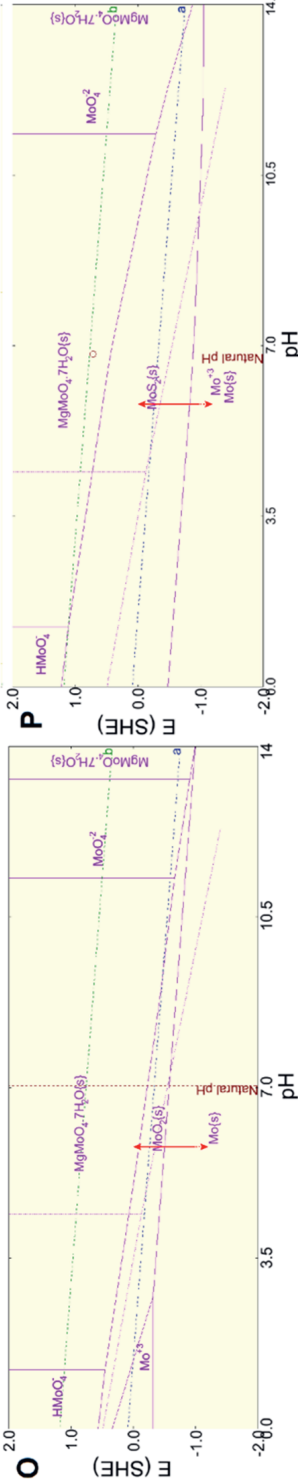
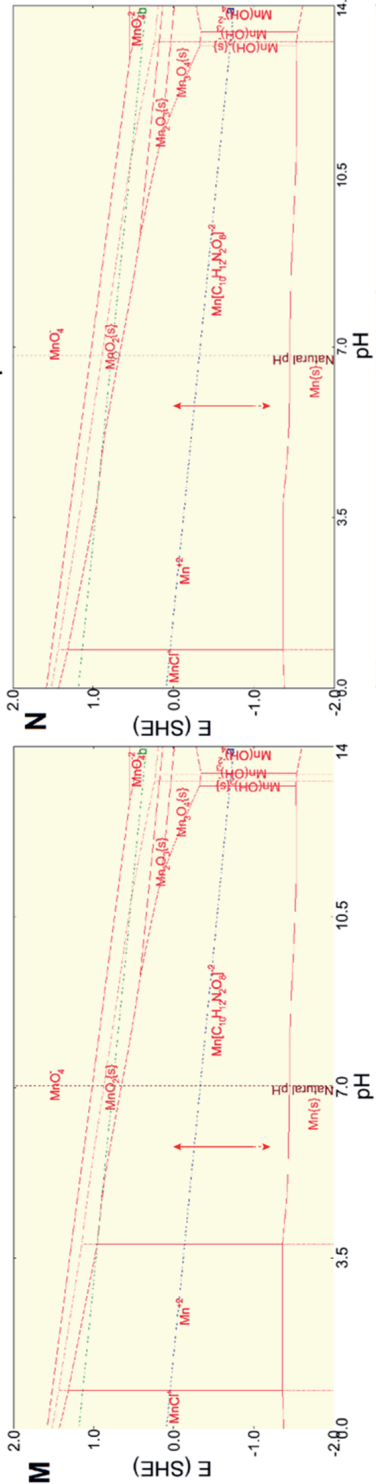
Table S2.6. Theoretical potential for the reduction of metals to their solid form at 303 K, pH 5.8 and all concentrations equal to 1 mM. All potentials were calculated as described by Sleutels⁴⁷ are reported against 3 M KCl/Ag/AgCl.

Reduction reaction	E ⁰ (V)	E (V)
$Fe^{2+} + 2e^- \rightarrow Fe(s)$	-0.619	-0.709 ⁵³
$Cu^{2+} + 2e^- \rightarrow Cu(s)$	0.127	0.037 ⁵⁴
$Mn^{2+} + 2e^- \rightarrow Mn(s)$	-1.392	-1.482 ⁵³
$Co^{2+} + 2e^- \rightarrow Co(s)$	-0.498	-0.589 ⁵⁵
$Ni^{2+} + 2e^- \rightarrow Ni(s)$	-0.446	-0.536 ⁵⁶
$Zn^{2+} + 2e^- \rightarrow Zn(s)$	-0.972	-1.062 ⁵⁶
$Al^{3+} + 3e^- \rightarrow Al(s)$	-1.886	-1.946 ⁵³
$Ba^{2+} + 2e^- \rightarrow Ba(s)$	-3.116	-3.206 ⁵⁶

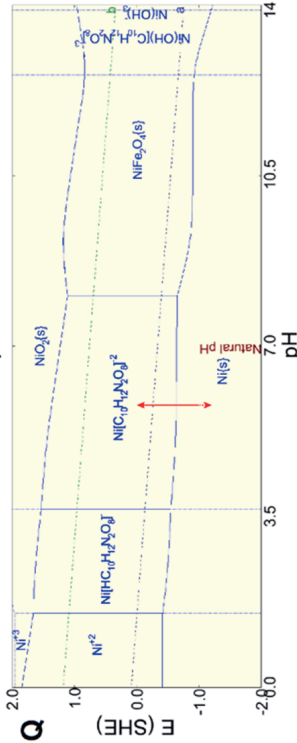
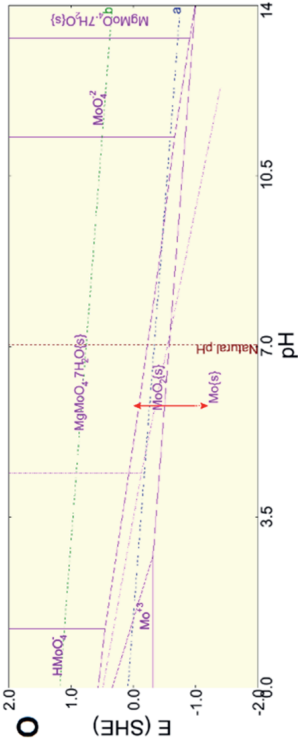
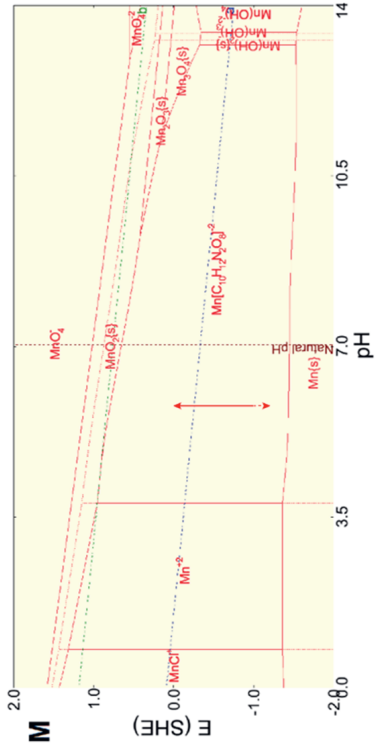




With 2-BES products



Without 2-BES



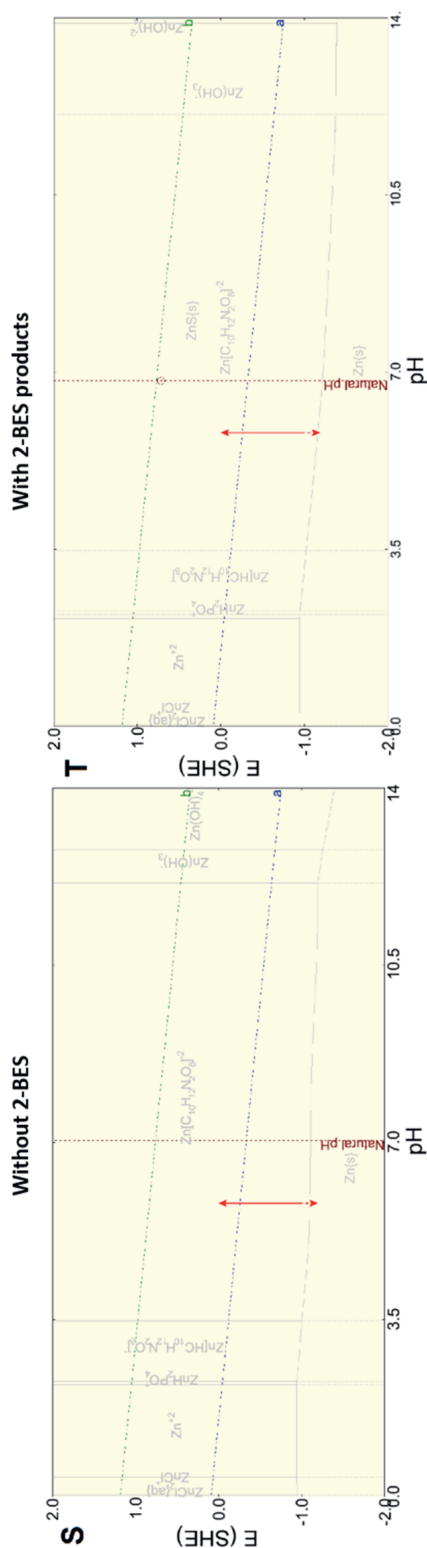


Figure S2.12. Pourbaix diagrams of aluminium (A and B), barium (C and D), cobalt (E and F), copper (G and H), iron (I and J), magnesium (K and L), manganese (M and N), molybdenum (O and P), nickel (Q and R) and zinc (S and T) with the biotic medium without sodium 2-bromoethanesulfonate (A, C, E, G, I, K, M, O, Q and S). The pourbaix diagrams were also obtained for the medium with 15 mM H_2S , NaBr and ethane, which are supposed degradation products of sodium 2-bromoethanesulfonate⁵⁷ (B, D, F, H, J, L, N, P, R and T). The dashed lines indicated by “a” and “b” respectively represent the electrochemical potentials for oxygen (a) and hydrogen (b) evolution in the presented pH range. The red arrow indicates the area that is reached during the cyclic voltammogram (CV) (0 to -1.2 vs SHE at pH 5.8). Since potentials lower than -0.99 vs SHE could not be reached during the CV due to voltage overload, the area between -0.99 and -1.2 vs SHE is dashed. The diagrams were obtained with OLI Studio 9.6.

Further hypotheses on metal induced current enhancing effects observed after the CVs

Besides the possible current enhancing mechanisms explained in the discussion section of the article, four more possible current enhancing effects have been found in literature study. These effects are summarized in Figure S2.12 and will be explained in the following section. The first current enhancing process is the replacement of metal cofactors in the enzymes present in the bacteria or in the extracellular enzymes that act as mediator in electron transfer between the cathode and the bacteria (Figure S2.12: A). Many enzymes in intracellular catabolic pathways contain metallic co-factors, for example zinc and cobalt in methyltransferase or iron sulphide in acetyl-CoA synthase⁵⁸. Furthermore, some enzymes that are used for electron transfer also contain metal co-factors, such as iron in ferredoxin, rubredoxin and cytochrome c and iron sulphide in ubiquinone⁵⁹. Exchange of metal co-factors in enzymes or other metalloproteins can change the protein stability⁶⁰. For example, metals with similar properties, such as zinc and magnesium⁶¹ or iron and manganese^{61,62} can replace each other in metalloproteins, thereby influencing the functionality of those proteins⁶³. The affinity of a protein for a certain metal co-factor can among other factors depend on the concentration of that metal⁶⁴. Therefore, when the catholyte metal concentrations increased in the biotic reactor after the CV scan, metal co-factor replacement could have occurred in the metalloproteins present on the biocathode or in the catholyte or in the extracellular polymeric substances (EPS). The latter can have conductive properties and thus aid the electron transfer⁶⁵. The different metal availability could have changed the functionality of those proteins, for example increasing the conductivity of the EPS or the electron transfer by the mediating enzymes. The increased electron transfer corresponds with a higher cathodic current, as observed after the CV treatment. In the weeks after the CVs, the metal compounds availability changed back to the value before the CVs due to reduction onto the cathode and the continuous supply of trace elements via the influent. This would then cause the metalloprotein functionality to go back to their status prior to the CVs, decreasing the electron uptake from the cathode.

A second possible process affecting the current for longer term is a reorganisation of metal species on the cathode (Figure S2.12: B). Depositing of metals could occur firstly during the long term operation at a reductive potential or secondly during the reductive waves of the CV when the metals reduced to a solid form. The combinations and configurations in which the metal species are deposited/nucleated could differ between continuous reactor operation and the reductive waves from the CV due to the difference in potential, current or catholyte composition at those moments⁶⁶. Also different concentrations of H^+ could have created pH gradients influencing the oxidation state of the deposited metals. E.g. metal alloys⁶⁷⁻⁶⁹ or metal nanoparticles⁷⁰⁻⁷² could be formed during or directly after the CV scan that were not formed during the long term continuous operation. The released iron, molybdenum and cobalt could have been redeposited as catalytic metal compounds. For example Fe-Co alloys⁷³, MoS_2 ⁷⁴ and CoS ⁷⁵ are known electrocatalysts for HER and the latter two have oxidation states within the potential range indicated by the red arrows in their Pourbaix diagrams. A more alkaline local pH could induce the shift of these transition metals towards their sulphide form, as shown in Figure S2.11-F and S2.11-P. Metal alloys could have a better performance as electrocatalyst for the hydrogen evolution reaction (HER) compared to the pure metals (for non-noble metals)⁷⁶.

In a beneficial case, the mismatch in atoms allows for both good adsorption of the H atom and good release of the H₂ molecule after the H₂ formation due to charge difference⁷⁷. To verify whether these compounds were indeed formed in such a way that enhanced HER, further analysis of the cathode surface and the structure of the hypothesized catalysts is necessary, as this can influence the catalyst performance and stability⁷⁷. An indication for the change of the metal configuration on the biocathode is supported by the formation of the oxidation peak at a more negative potential for the second and third cycle of the CV scan (Figure S2.6). This indicates that a different oxidation reaction occurs in the second and third cycle of the CV as opposed to the first cycle. The formation of a less stable electrocatalyst would explain the decreasing current (Figure 2.8), as the catalyst would perform less and less in the time after the formation. The subsequent CV would then again induce the formation of a catalyst which would again loose destabilize and loose activity in the time after the CV.

The third CV-induced process that could have influenced the current is the release of biomass that was observed during the CVs (Figure S2.12: C). This release together with biomass washout could have caused a decrease of the biofilm thickness. The biofilm thickness influences the mass transfer and electrochemical performance of the bacteria⁷⁸. Thus, a lower biofilm thickness could improve the mass transfer from the catholyte, creating more substrate availability for the bacteria closer to the cathode surface, enhancing their conversions and thus energy demand. When part of the released biomass reattached to the cathode in the days after the CV, the reattached bacteria could have made better connections to the cathode which would result in increased bioavailability of substrates from the bulk electrolyte⁷⁹, or improved electron transfer mechanisms^{59,80} resulting in a higher current.

The fourth hypothetical explanation for the increased current is release of (parts of) dead bacteria (Figure S2.12: D). Dead cells or cell parts that were trapped in the biofilm matrix could be released with the biomass release observed as OD₆₀₀ increase during the oxidative part of the CV scan. These dead cell parts could include e.g. proteinaceous materials, catalytic metal nanoparticles or electron transfer enzymes. A change in the cathode potential can create bonds⁸¹ between a cathode and other cathodes. Therefore, the change in potential during the CV could create stronger bonds between the released dead cell particles and the cathode. Several studies have shown that parts of dead cells can have catalytic activity i.e. in hydrogen formation⁸²⁻⁸⁴. Thus, depositing of the released dead cell parts at the biocathode during or after the CV could have enhanced the current with expected higher formation of hydrogen.

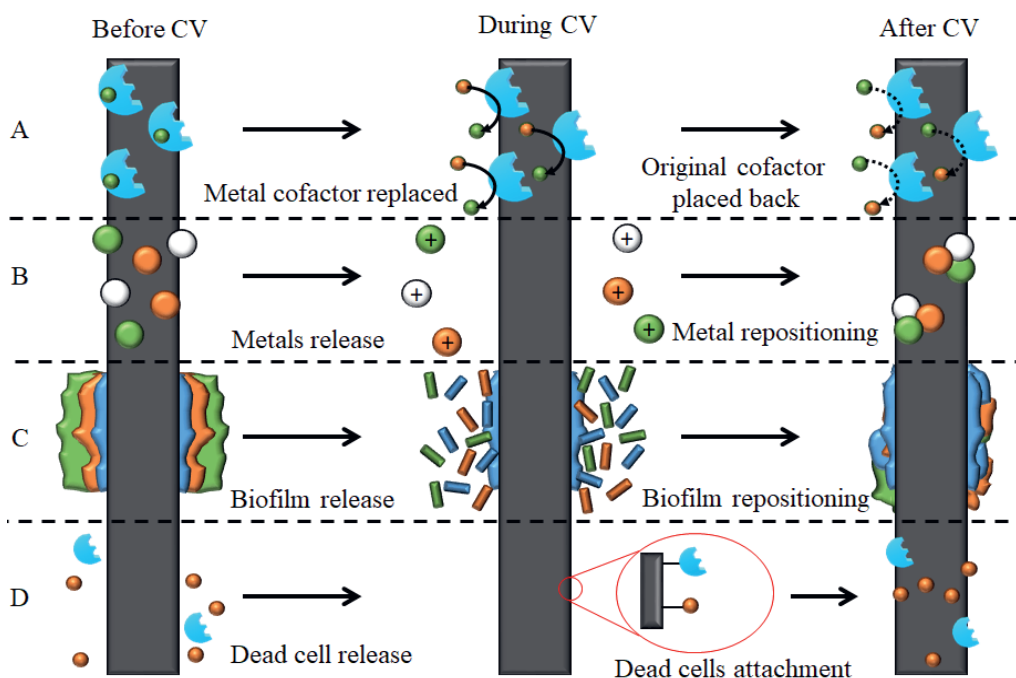


Figure S2.13. Hypothetical effects of cyclic voltammetry on microbial electrosynthesis systems. The different presented mechanisms are hypothesised based on the findings from this study and literature research.



Chapter 3

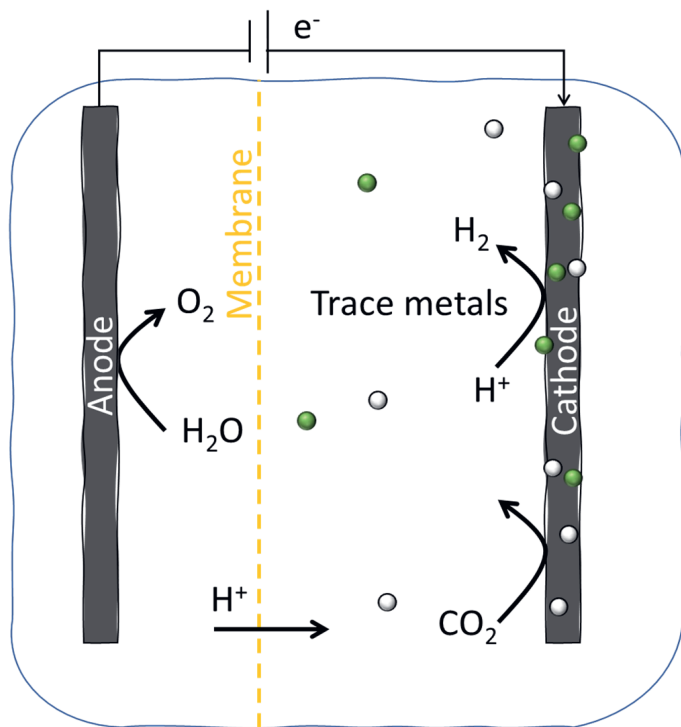
Trace metals from microbial growth media form *in situ* electro-catalysts



Submitted as: de Smit, S. M., van Mameren, T. D., Xie, Y., Strik, D. P. T. B. & Bitter, J. H. Trace metals from microbial growth media form *in situ* electro-catalysts

Abstract

Hydrogen is not only an energy carrier, a reactant in formation of chemicals, but also an important electron donor for many microbial conversions. To improve hydrogen availability in microbial processes, *in situ* hydrogen production improves system performance and feasibility. Here, we demonstrate the use of trace metal compounds from microbial medium as hydrogen evolution reaction (HER) electro-catalyst under microbial compatible conditions. Concentrated mixtures (10 vol%) of the metal compounds present in the microbial medium (trace metal mix medium; containing Co, Cu, Fe, Mn, Mo, Ni and Zn salts and ethylenediaminetetraacetic acid (EDTA)) were added to electrochemical reactors (controlled at -1.06 V vs Ag/AgCl and flushed with CO₂/N₂). After addition of the concentrated trace metal mix, the cathodic current increased up to 15 times with high electron recovery into hydrogen (70-100%). The formed HER catalyst performance was also measured in microbial growth medium (with ammonium and 0.1 vol% trace metal mix), showing similar performance rates compared to the concentrated trace metal mix medium. Further identification of the active compounds within the mix emphasized the role of Cu and Mo, a mix with Cu and Mo showed the same catalyst performance as the trace metal mix with all previously mentioned compounds. Moreover, the performance of the trace metal mix without EDTA showed the highest increased current (7 times higher up to -240 A/m²) and decreased hydrogen overpotential (55 mV at -10 A/m²). Integration of the discovered HER catalyst in biological systems will allow *in situ* hydrogen production in bio-electrochemical and fermentation systems.



3.1 Introduction

Hydrogen molecules are commonly used energy carriers and electron donors within many biological systems. Microorganisms can oxidize hydrogen to retrieve electrons as input for reduction reactions yielding e.g. alcohols, single cell proteins, volatile fatty acids or methane¹⁻⁵. In industrial microbial CO₂ methanation plants, hydrogen is often produced in an electrolyser and supplied in gaseous form in fermentation reactors⁶, but hydrogen can also be produced *in situ* during electrosynthesis⁷⁻⁹. Integration of electrochemical hydrogen production and biological conversion processes within one system (bio-electrochemistry) makes the produced hydrogen readily available for the microbial catalysts at mesophilic temperature without the need for additional process steps or reactor units. Furthermore, enhanced *in situ* hydrogen production even stimulates microbial productivity in bio-electrochemical CO₂ valorisation systems⁸.

The hydrogen evolution reaction (HER) is well known in electro catalysis. The reaction produces hydrogen in an electrochemical system where H₂ evolved at a cathode operating at potentials below -0.62 V (vs Ag/AgCl, pH 7). The difference between the theoretical required potential and the actual minimum operation potential at which hydrogen is formed, the overpotential, determines the energy input. HER overpotential depends on the local pH and the affinity of hydrogen for the electrode surface. The hydrogen atom affinity to react can be enhanced by the integration of a catalyst on the electrode surface, hereby lowering the required overpotential^{10,11}. Most HER catalysts are heterogeneous catalysts consisting of single or mixed metal (nano)particles on a support (e.g. the electrode surface)¹¹. Often the catalyst, especially in commercial electrolyzers, is based on noble metals such as Pt. However non-noble metal based catalyst are also active for HER.^{12,13} This opens the possibility to use the metal compounds present in microbial media to enhance hydrogen formation.

The electrocatalytic role of microbial growth media trace metal compounds in bio-electrochemical systems is still not confirmed and commonly overlooked. Microorganisms use a microbial growth medium to sustain their growth. Typical examples of such trace metal growth medium contain Fe, Ni, Co, Cu, Mo and Zn^{14,15}. These trace metal compounds are often continuously added via the medium as metal salts. The negative charge on the cathode might attract the metal ions present in the microbial medium resulting in metal deposition on the cathode. When the potential is low enough the deposited metal ions can even reduce to metal particles thus forming a potential HER catalyst¹⁶. Over time, the amount of metal compounds on the electrode surface could accumulate to such concentrations that correspond with a intentionally placed electrocatalyst. Although no proof of this principle is given yet, several studies have suggested that presence of trace metal compounds on the cathode affected the cathodic current. Recently, de Smit, et al.¹⁷ showed increased current simultaneous with trace metal deposition at reducing potentials. It was suggested that the metal trace metal compounds had HER catalysing properties. This relation has also been described by Pozo, et al.¹⁸, who suggested improved hydrogen production of a used biocathode (with removed bacteria) was caused by deposits of proteinaceous particles and metal compounds.

Understanding the catalytic role of trace metal compounds in the HER opens possibilities for tailoring of the metal compound dosing to stimulate the formation of a HER catalyst under

microbial compatible conditions and allow for combination of the HER catalyst with microbial electrosynthesis. In microbial electrosynthesis, microbial compatible conditions typically are near-neutral pH ranges (5-7) and mesophilic temperatures (15-30 °C)^{19,20}. Different studies showed the feasibility of CoP^{21,22}, MoS₂, NiMo²², Ni-P²³, Ni-AC²⁴ and Mo₂C²⁵ as integrated metal-based HER catalysts in bio-electrochemical systems. The trace metal mix (TMM) used by Pozo, et al.¹⁸ and de Smit, et al.¹⁷ contained Co, Cu, Fe, Mn, Mo, Ni, Zn salts^{17,18}. All of the non-noble, metallic compounds could theoretically act as HER catalyst under pH neutral conditions in some form^{26,27}, but it is yet unknown which of the elements acted as catalyst under the reactor conditions (slightly acidic, mesophilic) and working potential (-1.06 V vs Ag/AgCl).

Apart from the metal compounds, a chelating agent ethylenediaminetetraacetic acid (EDTA) is present in the microbial trace metal mix^{17,18}. EDTA chelates with metal ions, which stabilizes their ionic state. It is added to the trace metal mix to prevent formation of metal precipitates which are less bioavailable for uptake by the microorganisms²⁸. Besides increasing bioavailability, EDTA is also used in studies of HER catalyst formation. The EDTA-metal ion complex prevents deposition of metal ions right after their addition, which allows for reaction selectivity of the metal ions with added substrates instead of the support. This principle is used for formation of various HER catalysts²⁹⁻³¹. Additionally, EDTA is known for the “Rowland effect”, removing oxides from catalyst surfaces which benefits hydrogen formation by enhancing the contact between reactant and catalyst³²⁻³⁴. These characteristics raise questions about the influence of EDTA on the formation of a HER catalyst from the microbial trace metal mix.

In this study, we studied the feasibility of HER catalyst formation from trace metal mixes with and without EDTA at microbial compatible operating conditions. The contribution of the different trace metal mix elements (Co, Cu, Fe, Mn, Mo, Ni, Zn, EDTA) to the formation of the HER catalyst is shown in several sub-mix experiments. The metal mixes were added to a system with metal-free medium and reducing potentials (-1.06 V vs Ag/AgCl) and operated with slightly acidophilic, mesophilic conditions. After this addition, increasing current and hydrogen production rates were measured as HER catalyst activity indicators. We report competitive HER catalysts when compared to the reported high-performing electrolyzers in microbial electrochemical systems. Given the mild formation conditions, the catalysts show promise for implementation in bio-electrochemical and biological fermentation reactors for *in situ* production of bioavailable hydrogen.

3.2 Materials and Methods

3.2.1 Reactor design and setup

Abiotic electrochemical reactors were built from 14 mm thick Plexiglas flow-through plates (Figure 3.1). Silicon gaskets (0.5 mm thick) were used to secure the reactor parts and prevent leakage. The cathode was constructed of one layer (3 mm) graphite felt (Rayon Graphite Felt, CTG Carbon GmbH, Germany). The graphite felt non-microporous surface area was low (< 1 m²/g), as determined by N₂ physisorption. The cathode current collector consisted of a titanium wire (0.8 mm thickness, grade 2). During the initial experiments (SI Figure S3.2-3.3), significant standard deviations (up to 50%) were observed between the triplicate experiments. To create more consistency in the cathode configuration, the titanium wire was only pierced through the graphite felt at two places, at 6 mm from the edge of both sides for the short experiments (< 4

days) (Figure 3.1B). Spacers were used at both sides of the graphite felt to keep the cathode straight in the chamber (Figure 3.1A). The cathode with spacers were secured by pressing them between two Plexiglas flow through plates in a silicone gasket with a 12.5 x 3 cm hole (3 mm thick). Also the reactor volume of different set-ups was equalized. With the improvements, more consistent results were obtained and it was shown that Reactor 3 (SI Figure S3.2-3.3) showed representative results, so the results of Reactor 3 are shown as “Test reactor” in Figure 3.2 and 3.3.

The cathode and anode compartment were separated by a cation exchange membrane (Fumasep FKS, Fumatech BWT GmbH, Germany, 21.3 cm² projected surface area). For the anode, a Ti/Pt-Ir MMO plate was used (thickness 1 mm, Magneto Special Anodes BV, Netherlands). The catholyte recirculation flow entered the cathode chamber at the left bottom and exited at the top through two exit points: one at the right to ensure the catholyte to flow through the carbon felt cathode and one bypass at the left to allow excess hydrogen gas escape (Figure 3.1A). From the total catholyte recirculation flow (17 L/h), 46–88% passed through the bypass (measured in a separated test with a measuring cylinder). The anolyte was recirculated at 10 L/h.

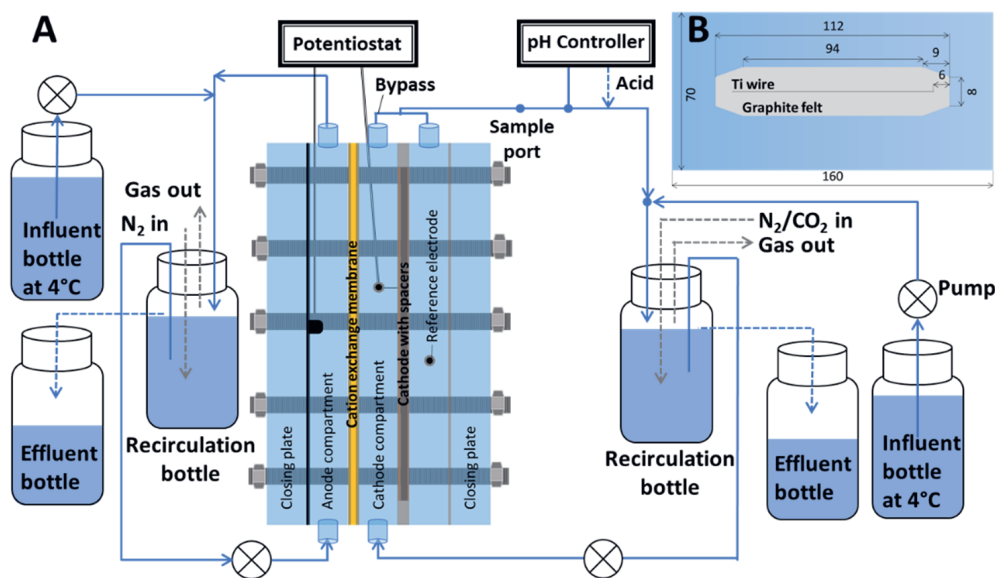


Figure 3.1. A: Reactor setup configuration with recirculation pathways, sample port location and pH control. B: Measurements of plexiglass flow-through plates used for the build-up of the reactor.

3.2.2 Reactor control

Gas was applied in the recirculation bottles of both the anolyte and catholyte recirculation. The anolyte recirculation bottle was flushed with 60 LN/d N₂ and the catholyte recirculation bottle was flushed with 100 LN/d CO₂ and 233.3 LN/d N₂. The incoming gas stream for the catholyte was humidified before entering the catholyte recirculation bottle. All reactors were operated inside a temperature controlled (30°C) and light-shielded cabinet. The catholyte pH was measured (QMP108X, Q-is, Oosterhout, the Netherlands) and controlled (Ontwikkelwerkplaats,

Elektronica ATV, the Netherlands) at 5.8 in the recirculation by the addition of 1 M HCl. The cathode was controlled at -1.06 V vs the Ag/AgCl reference electrode (QM710X, Q-is, Oosterhout, the Netherlands) by the n-stat IVIUM potentiostat (IVIUM, the Netherlands). The reference electrode was connected to the cathode chamber via a tube with 3 M KCl leading to a capillary, filled with gelified 3M KCl (BioAnalytic GmbH, Germany), which was inserted in the chamber through the Plexiglas flow-through plate (Figure 3.1A) and made water-tight with o-rings. The catholyte part was always operated in batch mode, while the anolyte part of the reactors was always operating continuously with a hydraulic retention time of 4 days.

3.2.3 Reactor pre-treatment

For the catalyst formation and performance experiments with different media, three phases were used. The first phase was a “blank medium phase”, followed by a “concentrated all metals medium phase” and a “biotic medium phase”. The medium compositions are shown in Table 3.1. To prepare the blank and biotic medium, the phosphate salts were added to demi water and a concentrated stock solution with (ammonium,) magnesium and calcium salts was added. For the anolyte, the pH was measured and the volume was adjusted to the end volume. For the catholyte, trace metal mix was pipetted in the solution (biotic medium) and the pH was adjusted from ~7.0 to 5.8 with 1 M HCl. Subsequently, the volume was adjusted by adding demi water to reach the end concentrations (Table 3.1). The concentrated trace metal mix was prepared outside the reactor, but the transition from the blank medium to concentrated all metals medium (day 7) was made by adding 10 vol% concentrated all metals mix (Table 3.2: “All metals”) with a syringe into the reactor sample port (Figure 3.1A). The transition from the high trace metal medium to biotic medium (day 17) was performed by adding three times the volume of anaerobic catholyte/anolyte to the reactor at 10 ml/min via the influent port, resulting in a washout of the high trace metal compound catholyte/anolyte. The biotic medium contained ammonium, which was left out of the blank and concentrated all metals medium to prevent microbial growth. 2-bromoethanesulfanoate was never added to any medium.

3.2.4 Tests with sub-mixes of the trace metal mix

After the experiments of the catalyst formation and stability in different media, different trace metal mixes were tested on their performance as hydrogen evolution reaction catalyst (Table 3.2). The trace metal mixes were prepared by adding the metal salts to demi water in the same order as shown in Table 3.2. After adding all the metal salts, the pH was adjusted from ~7.1 to 6.4 with 1M NaOH. The “All metals no EDTA” mix was a suspension (SI Figure S3.1), so to diminish differences in the triplicate experiment, this mix was continuously stirred whilst aspirating the 10 vol% of catholyte to add it to the reactor. The sub-mix tests were performed in shorter timeframe than the different media tests (<4 d). The sub-mix experiments started with blank medium and after 1 day, one of the metal mixes was added to the reactor with a syringe to end with 10 vol% of metal mix in the catholyte. After addition of the concentrated metal mixes, the reactors were left to stabilize for 48 hours prior to the final analyses described in the next section.

Table 3.1. Composition of “blank”, “concentrated metal mix” and “biotic” medium. The trace metal mix composition is described in table 3.2.

Compound	Unit	Blank medium	Concentrated all metals medium	Biotic medium
Catholyte				
Na ₂ HPO ₄ ·2H ₂ O	g/L	7.5	7.5	7.5
KH ₂ PO ₄	g/L	3.0	3.0	3.0
NH ₄ Cl	g/L	-	-	0.2
MgCl ₂ ·6H ₂ O	g/L	0.04	0.04	0.04
CaCl ₂ ·2H ₂ O	g/L	0.02	0.02	0.02
Trace metal mix	mL/L	-	100	1
pH		5.8	5.8	5.8
Anolyte				
Na ₂ HPO ₄ ·2H ₂ O	g/L	7.5	7.5	7.5
KH ₂ PO ₄	g/L	3.0	3.0	3.0
(NH ₄) ₂ CO ₃	g/L	-	-	0.18
MgSO ₄ ·7H ₂ O	g/L	0.05	0.05	0.05
Ca(OH) ₂	g/L	0.01	0.01	0.01
pH		~7.1	~7.1	~7.1

Table 3.2. Composition of trace metal mix during short (<4 d) hydrogen evolution reaction catalyst performance experiments. The compositions are the concentrated solutions that were diluted by addition to the catholyte (end concentration after addition was 10 vol% of trace metal mix in catholyte).

Trace metal mix	Unit	All metals	All metals no EDTA	Blank	Cu+ Mo	Cu+Mo no EDTA	Cu+Mo+ Co+Fe	Ni+Mn +Zn
FeCl ₃ ·6H ₂ O	g/L	1.5	1.5	-	-	-	1.5	-
H ₃ BO ₃	g/L	0.15	0.15	0.15	0.15	0.15	0.15	0.15
CuSO ₄ ·5H ₂ O	g/L	0.03	0.03	-	0.03	0.03	0.03	-
KI	g/L	0.18	0.18	0.18	0.18	0.18	0.18	0.18
MnCl ₂ ·4H ₂ O	g/L	0.12	0.12	-	-	-	-	0.12
Na ₂ MoO ₄ ·2H ₂ O	g/L	0.06	0.06	-	0.06	0.06	0.06	-
ZnSO ₄ ·H ₂ O	g/L	0.12	0.12	-	-	-	-	0.12
CoCl ₂ ·6H ₂ O	g/L	0.15	0.15	-	-	-	0.15	-
NiCl ₂ ·6H ₂ O	g/L	0.023	0.023	-	-	-	-	-
EDTA (C ₁₀ H ₁₄ N ₂ Na ₂ O ₈ ·2H ₂ O, CAS 6381-92-6)	g/L	10	-	10	10	-	10	10
pH (adjusted with NaOH)		6.4	6.4	6.4	6.4	6.4	6.4	6.4

3.2.5 Analysis methods

At the end of the sub-mix test concentrated metal mix phase, Tafel plot analyses were performed to measure the catalyst performance. First a current sweep from -0.5 mA to -50 mA with a rate of 0.05 mA/s (± 1 mV/s) was performed to determine the cathodic (negative) current starting potential. Subsequently, three potential sweeps from -0.80 to -1.30 V (all reported vs Ag/AgCl) were performed at 1 mV/s to determine the local Tafel slope between -1.05 and -1.07 V. Potential holds at -1.06 V of 1800 sec were added between the different steps to allow stabilization of the system.

The hydrogen production rate was measured in the “off gas” stream from the catholyte recirculation with gas chromatography analysis (detection of oxygen, carbon dioxide, methane, nitrogen and hydrogen, Shimadzu GC-2010, Japan). The hydrogen gas was measured as fraction of the gas outflow and the production was calculated based on the assumption that N₂ was inert and equal to the inflow of 233.3 LN/d (see SI section “calculation electron recovery”).

The metal concentrations in the catholyte were measured using Inductively Coupled Plasma Optical Emission spectroscopy (ICP-OES, Perkin Elmer AVIO 500), as described by de Smit, et al.¹⁷. Some adaptations were made to the method to optimize the detection of low concentrations in samples with high salinity. A multiline calibration was done with 10-100, 100-1000 and 1000-20000 $\mu\text{g/L}$ in 1% HNO₃, with 5 standards per calibration line. The autosampler was rinsed with 1% HNO₃ and after each catholyte sample, a blank sample (1% HNO₃ with 1 mg/L Yttrium) was run. The Yttrium internal standard was not used for S. Pieces of graphite felt (1x1x0.3 cm) were destructed to analyse the metal elements on the cathode. Per reactor, three pieces of graphite felt were destructed. For destruction, 4 mL 65% HNO₃, 1 mL 70% HClO₄ and 1 mL 30% H₂O₂ were added to dried graphite samples. The acid destruction was performed in a microwave (max 1000 W): ramp to 120 °C during 4 min, ramp to 150 °C during 4 min, ramp to 220 °C during 3 min, remain at 220 °C for 20 min, cool down for at least 30 min. After cooling down, the destructed samples were diluted in 50 mL end volume milliQ water and filtered over 0.2 μm filters to remove any bigger graphite parts. To measure deposits on the titanium wire, the titanium wires were incubated in 7.5 mL 37% HCl and 2.5 mL 65% HNO₃ (i.e. 10 mL aqua regia) overnight to bring the deposits into acid solution. The acid was diluted 10 times prior to measuring with ICP. The calibration line for both the destructed samples and the titanium wire deposit samples was made in a 10% aqua regia matrix without internal standard.

For theoretical prediction of the metal phases, Modelling was performed with OLI Studio 9.6 (OLI Systems, Inc.).

3.3 Results and Discussion

3.3.1 Microbial trace metal mix in bacteria growth medium enhances H₂ formation

To investigate the catalysing effect of the trace metal mix from biotic medium, the increase in current and hydrogen production were measured after the addition of a high concentration of trace metal mix. A 100 times higher concentration than regularly present in a microbial medium was added, to simulate the amount that would be normally added over time in ~100 days with 0.1 vol% trace metal mix. The experiment consisted of three subsequent phases (see next

paragraph), to measure the HER catalyst activity with different catholyte compositions, with the reactors in chronoamperometric operation at -1.06 V (vs Ag/AgCl) and with addition of 100 LN/d CO₂ as carbon source for microbial growth and conversion.

During the first phase, no metal mix was present in the reactor to show the HER catalyst activity without added metal compounds. In this “blank medium phase”, the reactor was operated in batch mode with the macronutrients of microbial medium: phosphate buffer and Ca and Mg salts for 7 days. In the second phase, the effect of adding the concentrated trace metal mix was studied. This “concentrated all metals medium phase” was initiated by addition of 10 vol% of the *all metals* mix (with EDTA, see Materials and Method) and operating the reactor in batch mode for 10 days (day 7-17). In the third phase, the HER catalyst activity was tested under microbial compatible conditions. This “biotic medium phase” was initiated by flushing the reactor electrolytes with three times their volume of biotic anolyte and catholyte on day 17. The biotic medium contained ammonium chloride and 0.1 vol% trace metal mix, next to the previously mentioned macro nutrients (Table 3.1, Materials and Method). The “biotic medium phase” lasted for 1 day (day 17-18). To enable distinction between effects of the trace metal mix and the catalytic effects of microbial growth, no microorganisms were inoculated in the reactors throughout this and the following experiments.

The resulting current densities (Figure 3.2A) and hydrogen production rates (Figure 3.2B) were measured based on the (negative) cathode current and hydrogen fraction in the off gas. Figure 3.2A shows the current as function of time for 3 different experiments. The reactor with pre-treated cathode (Test reactor) was compared to a duplicate set of control reactors (Control 1 and 2), to which the concentrated trace metal mix was not added, so these duplicate reactors only had a blank medium phase and a biotic medium phase. Right after the addition of the concentrated *all metals* mix, the resulting current increased up to a 10-fold more negative value (grey line, day 7, Figure 3.2A) compared to the initial blank medium phase (day 0-7). The current density first showed a sharp increase (day 7), followed by a stable current (higher than before the addition of the trace metals).

The third phase, with biotic medium, shows the current under microbial compatible conditions (day 17-18, Figure 3.2A). The catholyte was replaced with biotic medium on day 17 to ensure the metal component concentrations in the catholyte were potentially not too high for microorganisms. To distinguish between the effect of replacing the medium and the effect of the pre-treatment with trace metal mix addition, the “blank medium” electrolytes in the control reactors were also replaced by biotic electrolytes. In the reactor with pre-treated cathode (Test reactor), the biotic medium replacement caused an initial increasing peak in the cathodic current, after which the current remained higher than the current during the concentrated trace metal mix medium phase (Figure 3.2A). During the full 24 hours with biotic medium, the current of the reactors with added concentrated trace metal mixes was 20 times higher than the duplicate control reactors without the metal phase (Figure 3.2A, red lines), even though all reactors had the same biotic medium as catholyte.

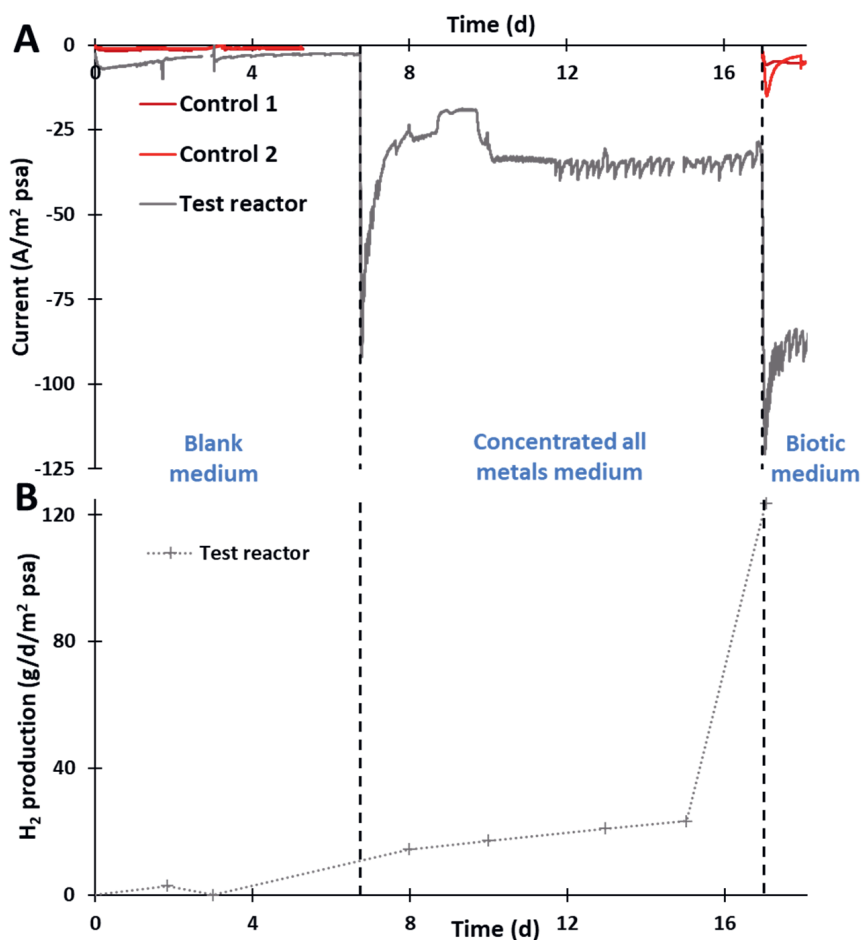


Figure 3.2. Current density (A) and hydrogen production (B) in control reactors (blank 1-2) and a test reactor over time with different media, continuously at potential -1.06 V vs Ag/AgCl. At day 7, concentrated trace metal mix was added to the test reactor and at day 17, three volumes of biotic catholyte and anolyte were added to the reactors. For the control reactors, the metal phase (day 7-17) was skipped. At day 3 and day 15, datapoints in the current density graph are missing in the test reactor due to electrochemical impedance spectroscopy measurements.

The current production was related to hydrogen production by measuring hydrogen in the gas phase and setting up an electron balance (SI section calculation electron recovery). Up to 70-100% of electron recovery went to hydrogen (SI Figure S3.4), showing that hydrogen was evidently the predominant product. The hydrogen production rate for the test reactor is shown in Figure 3.2B. The hydrogen production has the same pattern over time as the current, with increased values during the “biotic medium phase” (Figure 3.2B). It can be concluded that the hydrogen evolution reaction (HER) was catalysed by the trace metal mix. The high hydrogen production with biotic medium supports that the higher current observed during the biotic phase was not simply a consequence of higher ionic conductivity during the trace metal mix phase, but more likely a consequence of the formation of a HER catalyst. This was supported by conductivity measurements, the catholyte conductivity only changed from 24.1 to 24.6 mS/cm

with the change from the concentrated metal mix phase to the biotic medium phase. The hydrogen production increase right after the replacement of biotic medium (day 17, Figure 3.2B), is possibly related to more HER catalyst formation which took place due to the addition of the “extra” trace metal compounds from the fresh biotic medium.

3.3.2 Cu and Mo form key elements in formation HER catalyst

All metal elements present in the trace metal mix from microbial medium have shown activity as HER catalyst in some form at neutral pH in previous catalyst synthesis studies²⁶. However, during these catalyst synthesis studies, specific conditions (temperature, pressure, gas compositions) were used to steer the formation of certain compounds or crystalline structures³⁵. With the operating conditions used in this study, it is unlikely that all added compounds could function as HER catalyst. Selection of the active compounds can lead to simplification of the trace metal mix and thereby to cost reduction of the HER catalyst preparation mix. To link the hydrogen production to the activity of certain metal compounds from the trace metal mix under the conditions applied in this study, the concentrations of Co, Cu, Fe, Mn, Mo, Ni and Zn were measured in the catholyte over time with ICP after the addition of the trace metal mix to the reactor. Al was also measured since this is present as impurity in the Ti wire and can leach out¹⁷.

The behaviour of catholyte concentrations over time of different metal compounds could be divided in three groups. Figure 3.3 shows the concentrations of Fe, Zn and Cu as representatives for those three groups. The concentrations of the compounds at the moment of the trace metal mix addition (day 7) are based on the theoretical amount of elements added (10 vol% trace metal mix). First, the concentrations of Cu and Mo atoms were under the detection limit soon after their addition to the reactor (red line Figure 3.3). Second, the concentrations of Fe, Co, Mn and Ni decreased initially with approximately 60-80% of their initial concentrations (from 31 to 18-25 mg/L for Fe, blue line Figure 3.3), after which they remained constant over the rest of the concentrated trace metal mix phase. Third, the concentrations of Al and Zn increased slightly (30% increase) after the trace metal mix addition to the reactor (day 7, green line Figure 3.3).

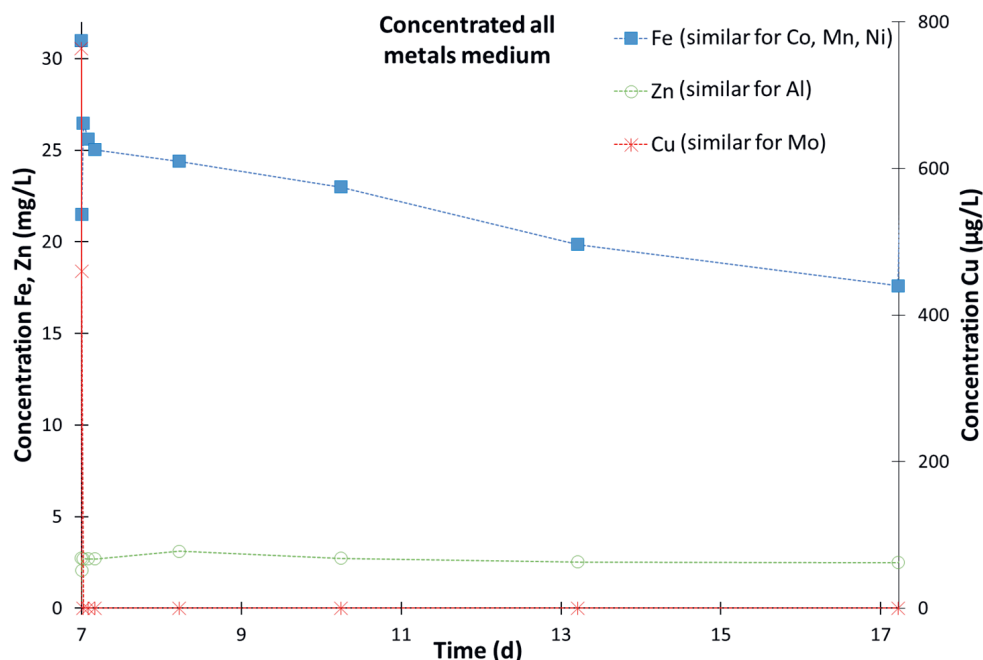


Figure 3.3. Concentrations of Fe, Zn and Cu over time in the catholyte of the Test reactor in the 10 days after addition of 10 vol% trace metal mix. The other added trace metal compounds were also measured and showed similar behaviour over time as the three elements shown here (SI Figure S3.6: R3).

The increase of Al and Zn has been observed previously as result of leaching from reactor parts¹⁷. The reactor was operated in batch mode, so the decrease in Fe, Co, Mn and Ni indicates deposition of these cations on the graphite felt cathode and/or other parts of the set-up (including transport to the anode). To verify to which parts the metal compounds deposited, ICP measurements of destructed cathode pieces were performed. The results confirmed that all added metal compounds were found on the cathode, as well as Al, K, Na, P and S (SI Figure S3.5). Since Al and Zn were both found on the cathode as well as in the catholyte, both deposition on the cathode and leaching from reactor parts phenomena are plausible to these two cations.

Both the current increase and Cu and Mo deposition on the cathode (decrease of Cu and Mo concentration in the catholyte) occurred very rapidly after the addition of the trace metal mix to the reactor (day 7, Figure 3.2 and 3.3). The combination of these two results suggests that Cu and Mo play an important role within the formation of the hydrogen evolution catalyst. The concentrations of Co, Fe, Mn and Ni also decreased in the catholyte during the initial current increase (Figure 3.3), yet the further decrease of these element concentrations over time does not correlate with the stability of the current and hydrogen production during the trace metal mix medium phase (Figure 3.2). These initial results imply that the role of Co, Fe, Mn and Ni is less important compared to Cu and Mo. Due to the occurrence of both deposition on the cathode and leaching, the role of Zn and Al in the formation of the HER catalyst remains unclear.

3.3.3 Sub-mix experiments emphasize importance of Cu and Mo and the effect of EDTA in HER catalyst formation

The initial hypotheses based on the metal behaviour over time were used for further experiments to distinguish the catalytic influence of the different elements. A series of experiments was performed with sub-mixes of the concentrated *all metals* mix. The previously used complete mix (*all metals*) was compared to a *blank* mix (with only EDTA, KI and H_3BO_3) to confirm that the metal elements from the trace metal mix are responsible for the observed HER catalysis. Furthermore, some mixes with only some of the trace metal compounds were tested (additional to the compounds present in the *blank* mix): *Ni+Mn+Zn*, *Cu+Mo* and *Cu+Mo+Fe+Co*. The sub-mixes were injected in reactors with macro nutrients controlled at -1.06 V vs Ag/AgCl , similar to the “blank medium phase” from Figure 3.2. After the addition of the sub-mixes, a stabilization time of 24 h was applied prior to further analysis. After this time, the cathode current was measured over 24 hours (24–48 h after sub-mix addition), and Tafel slope analyses were performed after 48 hours to characterize the HER catalyst(s) performance. To identify possible (by-)products, total organic carbon was measured in the recirculation catholyte, next to hydrogen measurements in the off gas. The results showed high electron recovery into hydrogen ($>83\%$, SI Figure S3.7), confirming that hydrogen was again the predominant product. To compare the different sub-mix performances, the average/stabilized cathodic currents (average over 24 hours, between 24 and 48h after metal addition) were plotted against the overpotential of the hydrogen evolution reaction at -10 A/m^2 psa (projected surface area), measured during the Tafel slope (Figure 3.4, SI Figure S3.8).

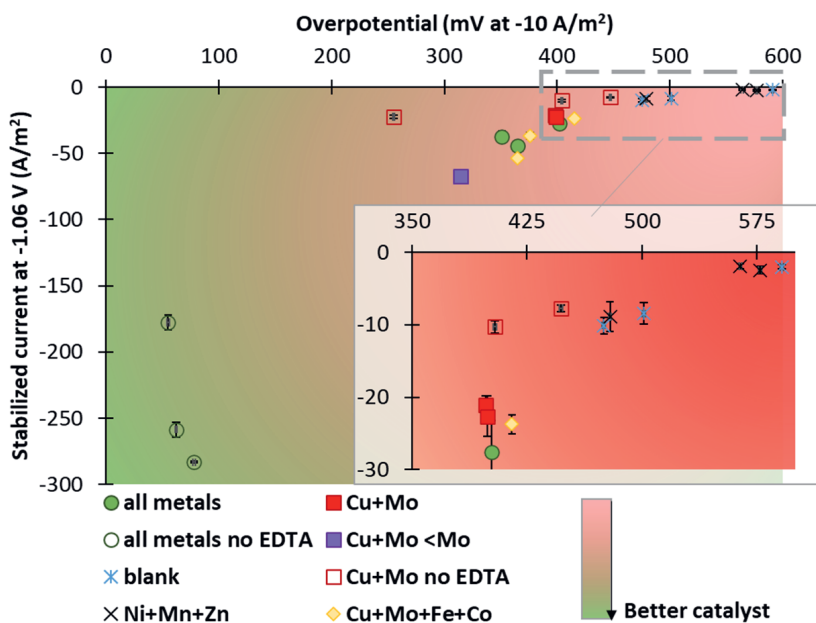


Figure 3.4. Average stabilized current measured between 24h and 48h (with potential -1.06 V vs Ag/AgCl) after sub-mix addition plotted against the HER overpotential at -10 A/m^2 for triplicate experiments with different sub-mixes. The error bars represent the deviation of the current during the 24 hours. In the $\text{Cu+Mo} < \text{Mo}$ experiment, a lower metal loading of Mo was measured on the cathode with ICP after destruction (SI Figure S3.9).

The performance with the *all metals* mix can be clearly distinguished from the performance with the *blank* mix (Figure 3.4). This difference clearly supports that the observed HER catalysing effects are caused by the addition of the trace metal compounds in the mix. (i.e. the hydrogen evolution catalyst is not evidently formed by the macro-nutrients, EDTA, KI and H_3BO_3). The *Ni+Mn+Zn* mix had no significant lower overpotential or higher stabilized current than the *blank* experiment (Figure 3.4). This indicates a minimal contribution of Mn, Ni and Zn to the formation of a hydrogen evolution catalyst.

On the contrary, the *Cu+Mo* mix showed an overpotential and stabilized current within the same range of the *all metals* mix. This results, together with the simultaneous Cu and Mo deposition and current increase (Figure 3.2A, 3.3), make it highly plausible that the addition of Cu and/or Mo to the reactor is crucial for the formation of the HER catalyst. One experiment of the triplicate with *Cu+Mo* had a significant higher stabilized current and lower overpotential (indicated with purple marker, Figure 3.4). The analysis of the metal loading on the cathode showed that this experiment had 4 times less Mo on the cathode (SI Figure S3.9). This result shows that the ratio of Mo/Cu is an important factor in the creation of a hydrogen evolution catalyst, and indicates that a lower Mo/Cu ratio is beneficial to hydrogen evolution catalysis as shown before³⁶.

The addition of Fe and Co salts to the *Cu+Mo* mixture did not significantly improve nor decrease the performance (Figure 3.4, *Cu+Mo+Fe+Co*). Although this finding suggests a limited influence of Co and Fe on the Cu and/or Mo based catalyst formation, further experiments are recommended to further elucidate whether a “Fe+Co” mix would indeed perform within the range of the *blank* mix and not show additional HER catalytic activity.

Based on previous studies showing catalysing effects of EDTA²⁹⁻³⁴, the effect of leaving out EDTA was investigated. Two experiments were performed with mixes without EDTA, *all metals no EDTA* and *Cu + Mo no EDTA* (with KI and H_3BO_3). Surprisingly, leaving out EDTA from the mix of all trace metals resulted in a much better performance. The *all metals no EDTA* mix showed a higher stabilized current (up to -280 A/m^2) compared to the *all metals* mix with EDTA ($\sim 550\%$ of *all metals* mix), and also a low overpotential (55 mV at -10 A/m^2) (Figure 3.4). This result makes the *all metals no EDTA* the best performing metal mix tested in this study.

The *Cu+Mo no EDTA* mix had an overpotential and stabilized current within the same range as the *all metals* mix and the *Cu+Mo* mix with EDTA (Figure 3.4). This means that the omission of EDTA did not improve the performance of the combination *Cu+Mo*, like the omission of EDTA did for the *all metals* mix. In fact, *Cu+Mo no EDTA* showed a slightly lower stabilized current (Figure 3.4) when compared to *Cu+Mo* with EDTA. These results suggest that Cu and Mo deposition mechanisms are unaffected by the presence or absence of EDTA.

3.3.4 EDTA decreases metal deposition on cathode and titanium wire

Since the *all metal* mix showed such significant differences in performance with and without EDTA, it is hypothesized that EDTA influences the deposition of metal compounds and thus the formation of a HER catalyst. To study this, the metal behaviour of two experiment sets with EDTA (*all metals* and *Cu+Mo*) were compared to the corresponding sub-mixes without EDTA. The catholyte concentrations of all added metal elements and some macro nutrients (calcium,

magnesium and sulphur) (Figure 3.5) were measured with ICP, at the end of the trace metal mix medium phase. Figure 3.5 shows that the catholyte metal concentrations at the end of the metal phases are significantly higher in the experiment with EDTA when compared to the experiment without EDTA. Several metal compounds, such as Co, Fe, Mn, Ni and Zn were present with higher concentrations in the catholyte when EDTA was part of the trace metal mix (*all metals EDTA*). EDTA is a chelating agent^{37,38}, so the binding of elements from the trace metal mix with EDTA likely caused their higher catholyte concentrations. Yet, not all the elements showed increased concentrations with EDTA present. For example, Cu was measured under the detection limit independent on the EDTA presence, and thus its deposition on the cathode seems unaffected by EDTA.

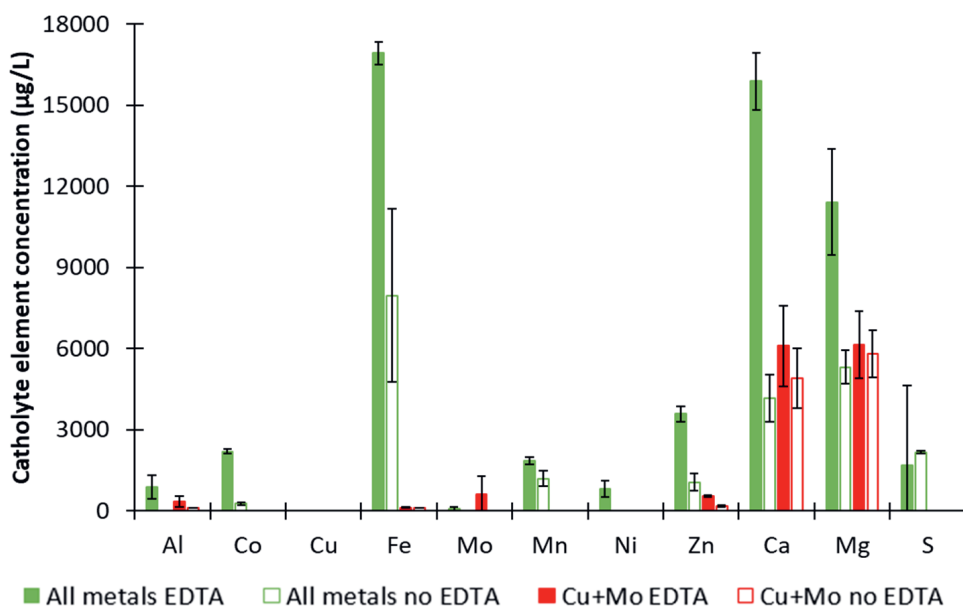


Figure 3.5. Element concentrations of compounds in the catholyte measured with ICP at the end of the concentrated trace metal mix medium phase of experiments with (EDTA) and without EDTA (no EDTA). The data is shown for the trace metal mix with all compounds (*all metals*) and only Cu and Mo (*Cu+Mo*). For the *all metals EDTA* experiment, samples were taken 10 days after trace metal mix addition (day 17, Figure 3.3) and for the other experiments, samples were taken 48 h after the trace metal mix addition.

Besides the deposition of metal compounds on the graphite felt cathode, metal deposition on the titanium wire used as current collector was also observed and measured (SI Figure S3.10). The metal element composition was determined by ICP measurements of leached elements from the titanium wire incubated in strong acid (SI Figure S3.11). Deposition of the elements Co, Fe, Mg, Mn, Mo, P and Zn on the titanium wire was measured for the *all metals no EDTA* mix. For the *all metals no EDTA* mix, the deposited metal compounds on the titanium wire could have contributed to the improved HER catalysis activity (Figure 3.4). In contrary to the *all metals no EDTA* experiment, the *all metals* experiment with EDTA showed only Al and Fe on the titanium wire (SI Figure S3.11). It should be noted that Fe is part of the alloy used for the grade 2 titanium wire used in this study, and Al leaching from the wire is observed when in an acidic

solution¹⁷. Therefore, no additional elements seem to have deposited on the titanium wire during the *all metals* experiment with EDTA. The chelating properties probably prevent deposition of metal compounds on the titanium wire. Remarkably, Cu and Mo were not detected on the titanium wire (SI Figure S3.11), while the elements were measured on the graphite cathodes (SI Figure S3.5 and S3.9), again supporting the hypothesis that Cu and Mo deposition is unaffected by the presence of EDTA.

3.3.5 Phase of Fe, Mo, Ni and Zn affected by EDTA omission

The higher hydrogen productivity in HER catalyst experiments where EDTA is left out of the *all metals* mix, is in contrast with the aforementioned beneficial use of EDTA for formation of HER catalysts²⁹⁻³¹. Therefore, the chelating properties of EDTA do not seem advantageous for HER catalyst formation with the conditions used in this study. Since the omission of EDTA from the *all metals* mix showed such improved HER catalyst activity and many metal compounds showed difference in deposition behaviour with and without EDTA, it was hypothesized that in this study, certain metal compounds have a different phase without EDTA and that this different speciation has (better) HER catalysis capacities. To investigate the effect of EDTA on the phase of the different metal compounds from the sub-mixes and Al, Pourbaix diagrams were made in OLI Studio 9.6 with the concentrated trace metal mix medium composition as added to the reactors (SI Figure S3.12-S3.14). The diagrams showed possible phases of the trace metal compounds right after their addition to the catholyte (Table 3.3). This theoretical analysis showed that both Cu and Mo were always in solid phase (Cu(s) and Mo(s), respectively), regardless of the EDTA presence (Table 3.3). Both Cu(s) and Mo(s) have shown hydrogen evolution capabilities at (near) neutral pH values in earlier studies³⁹⁻⁴².

Table 3.3. Possible phases of trace metal compounds at catholyte concentrations right after addition of trace metal mix at pH 5.8 and cathode potential of -1.06 V vs Ag/AgCl (-0.85 V vs SHE). Results were obtained by making Pourbaix diagrams with OLI Studio (SI Figure S3.12-S3.14). The compounds in bold are solid compounds present without EDTA that are not present with EDTA.

Element	Speciation with EDTA (Cu+Mo)	Speciation without EDTA (Cu+Mo no EDTA)	Speciation with EDTA (<i>all metals</i>)	Speciation without EDTA (<i>all metals no EDTA</i>)
Al	-	-	Al[C ₁₀ H ₁₂ N ₂ O ₆] ⁻ (aq)	AlPO ₄ (s)
Co	-	-	Co(s)	Co(s)
Cu	Cu(s)	Cu(s)	Cu(s)	Cu(s)
Fe	-	-	Fe(s)/Fe[C ₁₀ H ₁₂ N ₂ O ₆] ⁻² (aq)	Fe(s)/CuO.FeO(s)
Mn	-	-	Mn[C ₁₀ H ₁₂ N ₂ O ₆] ⁻² (aq)	Mn ₃ (PO ₄) ₂ (s)
Mo	Mo(s)	Mo(s)	Mo(s)	Mo(s)
Ni	-	-	Ni(s)/Ni[C ₁₀ H ₁₂ N ₂ O ₆] ⁻² (aq)	Ni(s)/Ni ₂ O ₄ (s)
Zn	-	-	Zn(s)/ Zn[C ₁₀ H ₁₂ N ₂ O ₆] ⁻² (aq)	Zn(s)/ZnHPO ₄ (aq)/ Zn ₃ (PO ₄) ₂ 2H ₂ O(s)

Because HER occurs at the electrode surface⁴³, it is commonly assumed that only attached compounds play a role as hydrogen evolution catalyst. Therefore, the solid phase compounds are expected to play a major role in the formation of a HER catalyst. Four elements were identified to be theoretically present in a solid state without EDTA (*all metals no EDTA*, Table 3.3), while the same elements were in a dissolved form with EDTA (*all metals*, Table 3.3). Of these elements, Fe has a higher stability in complex with EDTA (25.10) compared to other elements in the medium (14.04-19.50)⁴⁴, indicating that Fe speciation might be most affected by the presence or absence of EDTA. Hypothetically, the increased hydrogen production and decreased overpotential in the *all metals no EDTA* experiment is a result of the formation of the four solid elements: CuO·FeO(s), Mn₃(PO₄)₂, Ni₂O₄ and Zn₃(PO₄)₂·2H₂O. Similar to these compounds, CuO⁴⁵, FeO⁴⁶ and nickel oxides⁴⁷ have shown catalytic hydrogen formation in previous studies, albeit with different experimental conditions compared to this study. Although the theoretical predictions from the Pourbaix diagrams are insightful, the characterization of the hydrogen evolution catalysts formed with the different mixes from this study demands further practical analysis, such as in situ X-ray adsorption spectroscopy^{48,49}.

3.3.6 Outlook for optimization and application

The use of trace metal mix within bacteria growth media shows great potential for a pre-treatment for bio-electrochemical system start-up with high current densities and HER rates. To place this study in perspective, the performance of the catalysts *all metals* and *all metals no EDTA* were compared to other studies of integrated metal-based HER catalysts and microbial compatible conditions (Table 3.4). The performance of the reactors with cathodes pre-treated with the *all metals no EDTA* mix shows the highest current densities reported on 3D cathodes (-80 kA/m³ or -240 A/m² psa, Table 3.4). The only better performing HER catalyst in microbial compatible conditions was constructed from Co-P alloys on a 2D stainless steel mesh (current -350 A/m², overpotential 400 mV)²¹ (Table 3.4).

Table 3.4. Literature comparison of current production in CO₂-reducing biocathodes, measured at -1.06 V vs Ag/AgCl (-0.85 V vs SHE) during linear sweep voltammetry or chronoamperometric operation, with and without integrated hydrogen evolution catalysts.

Study	Current density (A/m ² psa)	Catalyst	Support	Products of coupled biological CO ₂ reduction
Liu, et al. ²¹	-350 [‡] -0.81 V*	Co-P alloys	Stainless steel mesh	PHB, alcohols (C3-C5)
This study (all metals no EDTA)	-240 (-80 kA/m ³)	All metals - EDTA on 3D graphite felt No catalyst, long-term operation (>175 d)	3D graphite felt	n.a.
Jourdin, et al. ⁵⁰	-175 (-14 kA/m ³)		3D graphite felt	Volatile fatty acids (C2,C4,C6)
Tian, et al. ²⁵	-140 (-28 kA/m ³)	Mo ₂ C	3D carbon felt	Acetate
This study (all metals)	-36 (-12 kA/m ³)	All metals + EDTA on 3D graphite felt	3D graphite felt	n.a.
Wang, et al. ²³	-32 [‡] (-6.4 kA/m ³) [‡] -1.05 V*	Ni-P	3D carbon felt	Ethanol, volatile fatty acids (C2,C4)
Kracke, et al. ²²	-7.5 to -22.5 [‡] -1.21 V*	CoP, MoS ₂ and NiMo	Si wafer	Methane, acetate
Chatzipanagiotou, et al. ²⁴	-7.4 (-2.5 kA/m ³)	Ni-doped	Activated Carbon granules	Acetate, formate

[‡]Measured during linear sweep voltammetry at -1.06 V vs Ag/AgCl
*Working potential used in study, here reported vs Ag/AgCl

It is interesting to study whether the enhanced hydrogen formation observed in this study also occurs in long-term operating biocathodes, since normally trace metal mix is added over time during chronoamperometric operation. The cathode current densities from this study were also comparable to long-term (>175 days) operating biocathodes (Table 3.4). Based on the results from this study, it is hypothesized that trace metal compound deposition in biotic operating systems causes HER catalyst formation. The formation of a HER catalyst from trace metal compound deposition could also explain why rapid deposition of elevated trace metal compounds on the cathode after cyclic voltammetry (CV) or open cell voltage (OCV) was observed with current increases in long-term operating microbial electrosynthesis systems^{17,50}. Rapid deposition of high amounts of released trace metal compounds, such as those measured after (O)CV cycles, can boost the formation of a HER catalyst, as also observed after the trace metal mix addition in this study.

Besides the high current density and hydrogen production, catalyst stability is also an important parameter for the evaluation of HER catalysts. In this study, the reactors were only operated for 24 hours with biotic medium, which is not representative for long-term operation, but it can give some preliminary insights on the effect of macronutrient deposition on the catalyst. The formed

HER catalyst(s) showed no deactivation under microbial compatible conditions over 24h. Since the formation of the HER catalysts occurred in “complex” microbial medium with multiple compounds and showed high stability during the 10 days of the concentrated trace metal mix medium phase, it is suggested that deactivation by leaching or poisoning by buffer salt components is minor⁵¹. Additionally, because the influence of other medium compounds was small, the trace metal mix could be obtained from a metal-rich waste stream. Since microbial trace metal compounds were used, microbial sludge streams, such as waste water treatment sludge might be suitable sources for metal extraction^{52,53}.

This finding opens possibilities for integration of electrolyzers and electro-fermentation. The integration of the trace metal mix catalysts may significantly reduce start-up time due to the high current densities obtained at the start of the biotic phase. This way, the *in-situ* produced hydrogen is directly bioavailable at the electrode surface where the active biofilm is located⁸. Optimisation studies can improve the catalyst even further, e.g. by varying the current collector, metal concentrations and reactor set-up. Besides, since the electrocatalyst was formed under operating conditions, possibilities for regeneration of the catalyst by applying a change in potential can be investigated¹⁷. An additional important next step is to investigate the feasibility of microbial growth and productivity in systems with the metal-based catalyst presented here. An important note is that the observed rapid deposition of e.g. Cu and Mo on the graphite felt cathode (Figure 3.3) could cause the depletion of trace metal compounds in the catholyte and/or cause biological activity relocation to the cathode. Integration of the discovered electrolyser in biological systems is an important step towards the integration of hydrogen evolution catalysts in bio-electrochemical and fermentation processes.

3.4 Conclusions

This study showed that trace metal compounds present in microbial growth media are key to form hydrogen evolution reaction catalyst(s) under microbial compatible conditions. Likely do several metal compounds play a role as part of the formed electro-catalyst(s). The trace metal mix with all metal compounds (Co, Cu, Fe, Mn, Mo, Ni and Zn with EDTA) showed similar hydrogen formation overpotential and stabilised current as the mix with only Cu, Mo and EDTA, strongly suggesting an important contribution of Cu and/or Mo to the formation of the hydrogen evolution reaction catalyst. The presence of EDTA decreased the deposition of metal compounds on the cathode, resulting in higher measured elements concentration in the catholyte. Leaving out EDTA from the all metals mix significantly increased the stabilized current and decreased the hydrogen formation overpotential, making that mix the best out of the tested metal mixes included in this study. Finally, the results from this study provide a starting platform for the microbial-friendly integration of electrolyzers and biological conversion systems without the need for a Pt-based electrocatalyst.

References

- 1 Zhang, F. *et al.* Fatty acids production from hydrogen and carbon dioxide by mixed culture in the membrane biofilm reactor. *Water Res* **47**, 6122-6129, doi:10.1016/j.watres.2013.07.033 (2013).
- 2 Martinez, J. B. G. *et al.* Potential of microbial protein from hydrogen for preventing mass starvation in catastrophic scenarios. *Sustainable production and consumption* **25**, 234-247 (2021).
- 3 Steinbusch, K. J., Hamelers, H. V. & Buisman, C. J. Alcohol production through volatile fatty acids reduction with hydrogen as electron donor by mixed cultures. *Water Res* **42**, 4059-4066, doi:10.1016/j.watres.2008.05.032 (2008).
- 4 Zhang, W. *et al.* Free acetic acid as the key factor for the inhibition of hydrogenotrophic methanogenesis in mesophilic mixed culture fermentation. *Bioresource technology* **264**, 17-23 (2018).
- 5 Yun, Y.-M., Shin, H.-S. & Kim, D.-H. Feasibility study of SCFAs production from microalgae during hydrogen fermentation. *International Journal of Hydrogen Energy* **41**, 4439-4445, doi:10.1016/j.ijhydene.2015.10.135 (2016).
- 6 Dowe, N. & Harrison, K. BETO 2021 Peer Review-Biomethanation to Upgrade Biogas to Pipeline Grade Methane WBS 5.1. 3.102. (National Renewable Energy Lab.(NREL), Golden, CO (United States), 2021).
- 7 Bajracharya, S. *et al.* Carbon dioxide reduction by mixed and pure cultures in microbial electrosynthesis using an assembly of graphite felt and stainless steel as a cathode. *Bioresour Technol* **195**, 14-24, doi:10.1016/j.biortech.2015.05.081 (2015).
- 8 Blanchet, E. *et al.* Importance of the hydrogen route in up-scaling electrosynthesis for microbial CO₂ reduction. *Energy & Environmental Science* **8**, 3731-3744 (2015).
- 9 Li, X., Angelidaki, I. & Zhang, Y. Salinity-gradient energy driven microbial electrosynthesis of value-added chemicals from CO₂ reduction. *Water research* **142**, 396-404 (2018).
- 10 McCrum, I. T. & Koper, M. The role of adsorbed hydroxide in hydrogen evolution reaction kinetics on modified platinum. *Nature Energy* **5**, 891-899 (2020).
- 11 Eftekhari, A. Electrocatalysts for hydrogen evolution reaction. *International Journal of Hydrogen Energy* **42**, 11053-11077 (2017).
- 12 Yu, L. *et al.* Non-noble metal-nitride based electrocatalysts for high-performance alkaline seawater electrolysis. *Nature communications* **10**, 1-10 (2019).
- 13 CHANG, J.-F. *et al.* Recent progress of non-noble metal catalysts in water electrolysis for hydrogen production. *Acta Physico-Chimica Sinica* **32**, 1556-1592 (2016).
- 14 Jarrell, K. F. & Kalmokoff, M. L. Nutritional requirements of the methanogenic archaeobacteria. *Canadian Journal of Microbiology* **34**, 557-576 (1988).
- 15 Ortnier, M., Rachbauer, L., Somitsch, W. & Fuchs, W. Can bioavailability of trace nutrients be measured in anaerobic digestion? *Applied Energy* **126**, 190-198 (2014).
- 16 Perez, N. *Electrochemistry and corrosion science*. 209 (Springer, 2004).
- 17 de Smit, S. M., Buisman, C. J., Bitter, J. H. & Strik, D. P. Cyclic Voltammetry is invasive on microbial electrosynthesis. *ChemElectroChem* **8**, 3384-3396 (2021).
- 18 Pozo, G. *et al.* Cathodic biofilm activates electrode surface and achieves efficient autotrophic sulfate reduction. *Electrochimica Acta* **213**, 66-74, doi:10.1016/j.electacta.2016.07.100 (2016).
- 19 Bian, B., Bajracharya, S., Xu, J., Pant, D. & Saikaly, P. E. Microbial electrosynthesis from CO₂: Challenges, opportunities and perspectives in the context of circular bioeconomy. *Bioresource technology* **302**, 122863 (2020).
- 20 Yang, H.-Y. *et al.* Mixed-culture biocathodes for acetate production from CO₂ reduction in the microbial electrosynthesis: Impact of temperature. *Science of The Total Environment* **790**, 148128 (2021).
- 21 Liu, C., Colón, B. C., Ziesack, M., Silver, P. A. & Nocera, D. G. Water splitting–biosynthetic system with CO₂ reduction efficiencies exceeding photosynthesis. *Science* **352**, 1210-1213 (2016).
- 22 Kracke, F. *et al.* Robust and biocompatible catalysts for efficient hydrogen-driven microbial electrosynthesis. *Commun. Chem.* **2**, 45 (2019).
- 23 Wang, G., Huang, Q., Song, T.-s. & Xie, J. Enhancing microbial electrosynthesis of acetate and butyrate from CO₂ reduction involving engineered clostridium ljungdahlii with a nickel-phosphide-modified electrode. *Energy & Fuels* **34**, 8666-8675 (2020).
- 24 Chatzipanagiotou, K.-R., Jourdin, L., Bitter, J. H. & Strik, D. P. Concentration-dependent effects of nickel doping on activated carbon biocathodes. *Catalysis Science & Technology* **12**, 2500-2518 (2022).

- 25 Tian, S. *et al.* Mo 2 C-induced hydrogen production enhances microbial electrosynthesis of acetate from CO 2 reduction. *Biotechnology for biofuels* **12**, 1-12 (2019).
- 26 Zhou, Z. *et al.* Electrocatalytic hydrogen evolution under neutral pH conditions: current understandings, recent advances, and future prospects. *Energy & Environmental Science* **13**, 3185-3206, doi:10.1039/d0ee01856b (2020).
- 27 Wu, H., Feng, C., Zhang, L., Zhang, J. & Wilkinson, D. P. Non-noble metal electrocatalysts for the hydrogen evolution reaction in water electrolysis. *Electrochemical Energy Reviews* **4**, 473-507 (2021).
- 28 Vintiloiu, A. *et al.* Effect of ethylenediaminetetraacetic acid (EDTA) on the bioavailability of trace elements during anaerobic digestion. *Chemical engineering journal* **223**, 436-441 (2013).
- 29 Dong, L., Wang, P. & Yu, H. EDTA-assisted synthesis of amorphous BiSx nanodots for improving photocatalytic hydrogen-evolution rate of TiO2. *Journal of Alloys and Compounds* **887**, 161425 (2021).
- 30 Deng, Y. *et al.* EDTA-assisted hydrothermal synthesis of flower-like CoSe2 nanorods as an efficient electrocatalyst for the hydrogen evolution reaction. *Journal of Energy Chemistry* **28**, 95-100 (2019).
- 31 Yu, X., Yang, J., Ren, X. & Sui, Z. Influences of pH and EDTA Additive on the Structure of Ni Films Electrodeposited by Using Bubble Templates as Electrocatalysts for Hydrogen Evolution Reaction. *Membranes* **11**, 165 (2021).
- 32 Jaksic, M., Brun, J. & Johansen, B. The Rowland or EDTA effect on electrochemical behavior of transition metals and in electrocatalysis for the hydrogen evolution reaction. The Rowland effect on some non-noble non-valve transition metals. *Russian journal of electrochemistry* **31** (1995).
- 33 Tunold, R., Brun, J. & Johansen, B. Effect of ethylenediaminetetraacetic acid (Rowlands effect) on electrochemical behavior of transition metals and electrocatalysis of hydrogen evolution reaction: Rowlands effect on noble metals. *Russian journal of electrochemistry* **31** (1995).
- 34 Stankovic, S., Grgur, B., Krstajic, N. & Vojnovic, M. The kinetics of the hydrogen evolution reaction on zinc in EDTA solutions in the pH 3–10 range. *Journal of Electroanalytical Chemistry* **549**, 37-47 (2003).
- 35 Schubert, U. S. & Hüsing, N. *Synthesis of inorganic materials*. (John Wiley & Sons, 2019).
- 36 Gotou, M. *et al.* Codeposition of copper and molybdenum by electroplating. *ECS Electrochemistry Letters* **3**, D19 (2014).
- 37 Harris, D. C. *Quantitative chemical analysis*. (Macmillan, 2010).
- 38 Pecso, R. L. & Sawyer, D. T. Molybdenum (V) and Molybdenum (VI) Complexes with Ethylenediaminetetraacetic Acid1. *Journal of the American Chemical Society* **78**, 5496-5500 (1956).
- 39 Zhao, J. *et al.* Achieving high electrocatalytic efficiency on copper: a low-cost alternative to platinum for hydrogen generation in water. *ACS Catalysis* **5**, 4115-4120 (2015).
- 40 Hui, L. *et al.* Loading copper atoms on graphdiyne for highly efficient hydrogen production. *ChemPhysChem* **21**, 2145-2149 (2020).
- 41 Jia, J. *et al.* Regulated synthesis of Mo sheets and their derivative MoX sheets (X: P, S, or C) as efficient electrocatalysts for hydrogen evolution reactions. *ACS Applied Materials & Interfaces* **9**, 8041-8046 (2017).
- 42 Du, J., Wang, J., Ji, L., Xu, X. & Chen, Z. A highly active and robust copper-based electrocatalyst toward hydrogen evolution reaction with low overpotential in neutral solution. *ACS applied materials & interfaces* **8**, 30205-30211 (2016).
- 43 Nørskov, J. K. *et al.* Trends in the exchange current for hydrogen evolution. *Journal of The Electrochemical Society* **152**, J23 (2005).
- 44 Dojindo. *Metal Chelates*, <https://www.dojindo.eu.com/images/Product%20Photo/Chelate_Table_of_Stability_Constants.pdf>
- 45 Bandara, J., Udawatta, C. & Rajapakse, C. Highly stable CuO incorporated TiO 2 catalyst for photocatalytic hydrogen production from H2O. *Photochemical & Photobiological Sciences* **4**, 857-861 (2005).
- 46 Sharma, A. *et al.* Advanced surface of fibrous activated carbon immobilized with FeO/TiO2 for photocatalytic evolution of hydrogen under visible light. *Chemical Engineering & Technology* **43**, 752-761 (2020).
- 47 Gong, M. *et al.* Nanoscale nickel oxide/nickel heterostructures for active hydrogen evolution electrocatalysis. *Nature communications* **5**, 1-6 (2014).
- 48 Tian, C. & Lin, F. Synchrotron X-ray Spectroscopy and Imaging for Metal Oxide Intercalation Cathode Chemistry. *Transition Metal Oxides for Electrochemical Energy Storage*, 343-373 (2022).

- 49 Seitz, L. C., Hersbach, T. J., Nordlund, D. & Jaramillo, T. F. Enhancement effect of noble metals on manganese oxide for the oxygen evolution reaction. *The Journal of Physical Chemistry Letters* **6**, 4178-4183 (2015).
- 50 Jourdin, L., Raes, S. M. T., Buisman, C. J. N. & Strik, D. P. B. T. B. Critical Biofilm Growth throughout Unmodified Carbon Felts Allows Continuous Bio-electrochemical Chain Elongation from CO₂ up to Caproate at High Current Density. *Frontiers in Energy Research* **6**, doi:10.3389/fenrg.2018.00007 (2018).
- 51 Lange, J. P. Renewable feedstocks: the problem of catalyst deactivation and its mitigation. *Angewandte Chemie International Edition* **54**, 13186-13197 (2015).
- 52 Babel, S. & del Mundo Dacera, D. Heavy metal removal from contaminated sludge for land application: a review. *Waste management* **26**, 988-1004 (2006).
- 53 Gheju, M., Pode, R. & Manea, F. Comparative heavy metal chemical extraction from anaerobically digested biosolids. *Hydrometallurgy* **108**, 115-121 (2011).

Supporting information

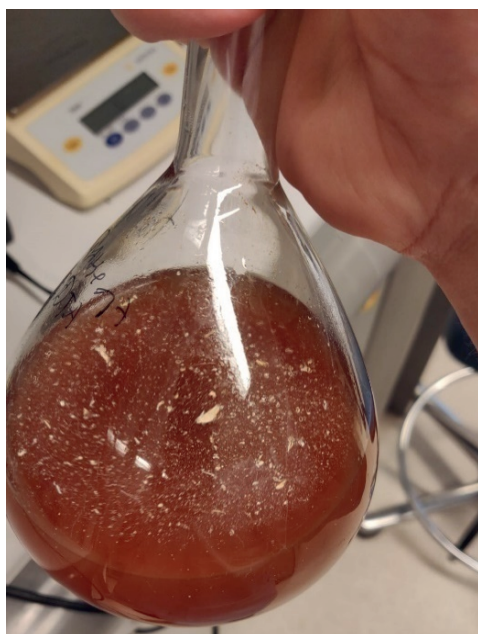


Figure S3.1. Suspension in all metals no EDTA concentrated mix (Table 3.2).

Calculation electron recovery

$$\text{Inflow } H_2 \left[\frac{LN}{h} \right] = \frac{\text{fraction } H_2 \text{ offgas } [\%] * 233.3 \frac{LN H_2}{h}}{\text{fraction } N_2 \text{ offgas } [\%]}$$

$$\text{Inflow } H_2 \left[\frac{mmol H_2}{h} \right] = \text{inflow } H_2 \left[\frac{LN H_2}{h} \right] * \frac{101325 Pa}{8.3144621 \frac{J}{K * mol} * \text{Temperature } [K]}$$

$$\text{Electron Recovery } [\%] = \frac{\text{inflow } H_2 \left[\frac{mmol H_2}{h} \right] * 2 \frac{mmol e^-}{mmol H_2} * 96485 \frac{mC}{mmol e^-}}{\text{Total cathode current } \left[\frac{mC}{h} \right]}$$

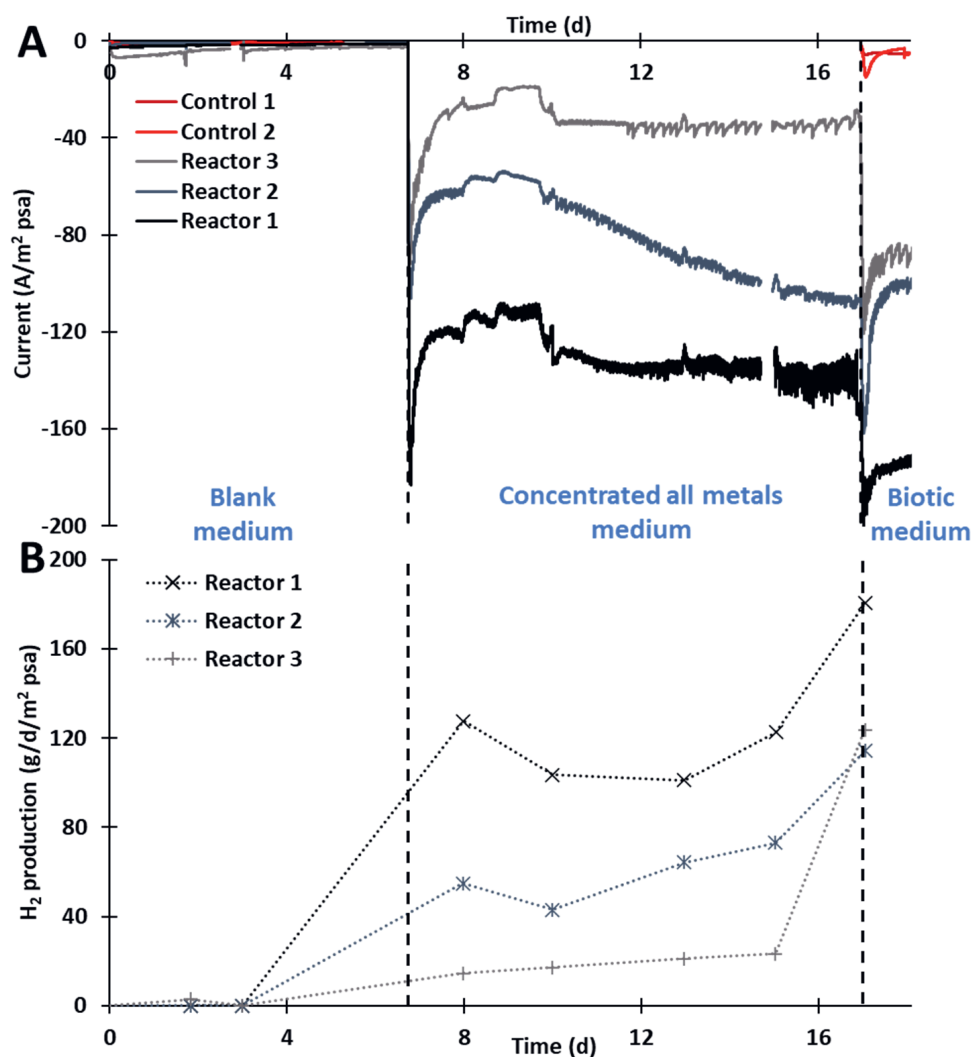


Figure S3.2. Current density (A) and hydrogen production (B) in control reactors (blank 1-2) and triplicate test reactors (reactor 1-3) over time with different media, continuously at potential -1.06 V vs Ag/AgCl. At day 7, concentrated trace metal mix was added to the test reactors and at day 17, three volumes of biotic catholyte and anolyte were added to the reactors. For the control reactors, the metal phase (day 7-17) was skipped. The test reactor shown in Figure 3.2 corresponds with Reactor 3 in this figure.

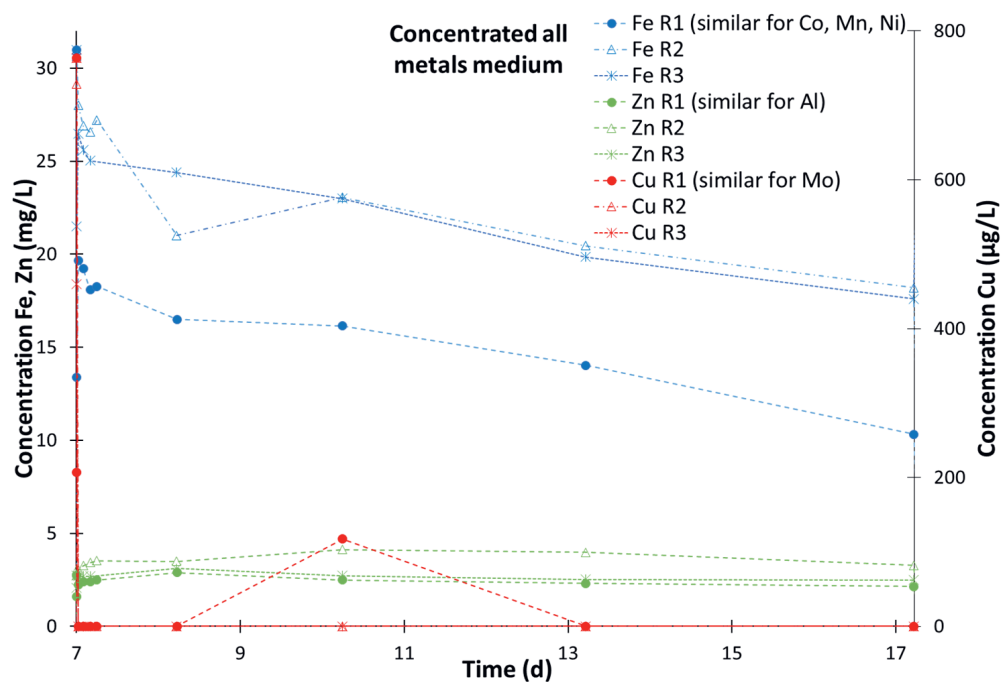


Figure S3.3. Catholyte concentrations of added trace compounds and Al over time in a triplicate reactor experiment (R1-R3). Concentrated trace metal mix medium was added at day 7. The element concentration behaviour was grouped based on the concentration behaviour over time for better readability of the graph. The additional element concentration profiles can be found in SI Figure S3.6. The test reactor shown in Figure 3.2 corresponds with R3 in this figure.

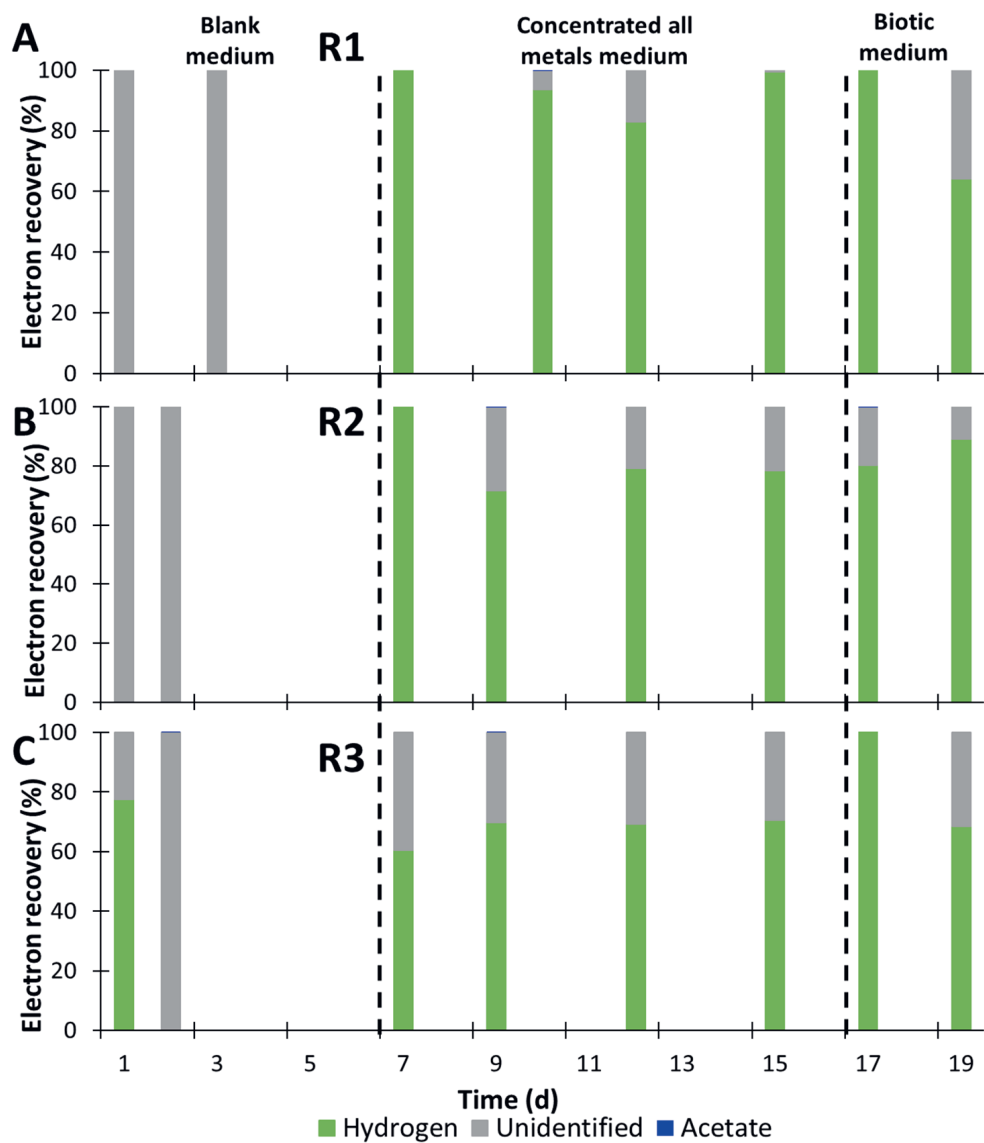
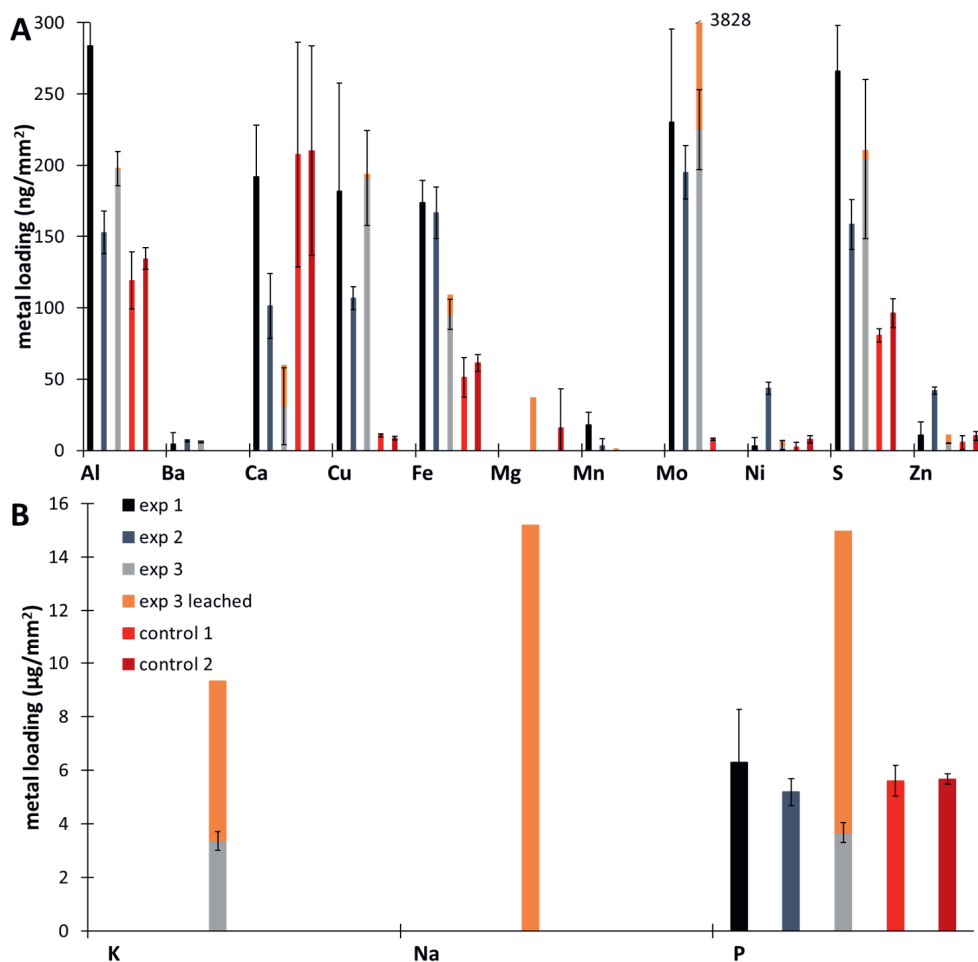


Figure S3.4. Electron recovery measured with blank medium, concentrated all metals medium and biotic medium of triplicate abiotic reactors controlled at -1.06 V vs Ag/AgCl and fed with CO_2 .



3

Figure S3.5. Metal element concentrations per mm² cathode projected surface area found on the cathodes of three reactors treated with three different media (7d blank medium, 10d concentrated all metals medium, 1d biotic medium) similar to Figure 3.2 (exp 1-exp 3) and two control reactors (7d blank medium, 1d biotic medium). The element concentrations were measured after a microwave destruction of the cathode. It was suspected that leaching occurred during the cathode sampling, therefore in experiment 3, also the released metal compounds during cathode sampling were measured (shown in orange). The error bars show the standard deviation between three measured cathode pieces from each experiment.

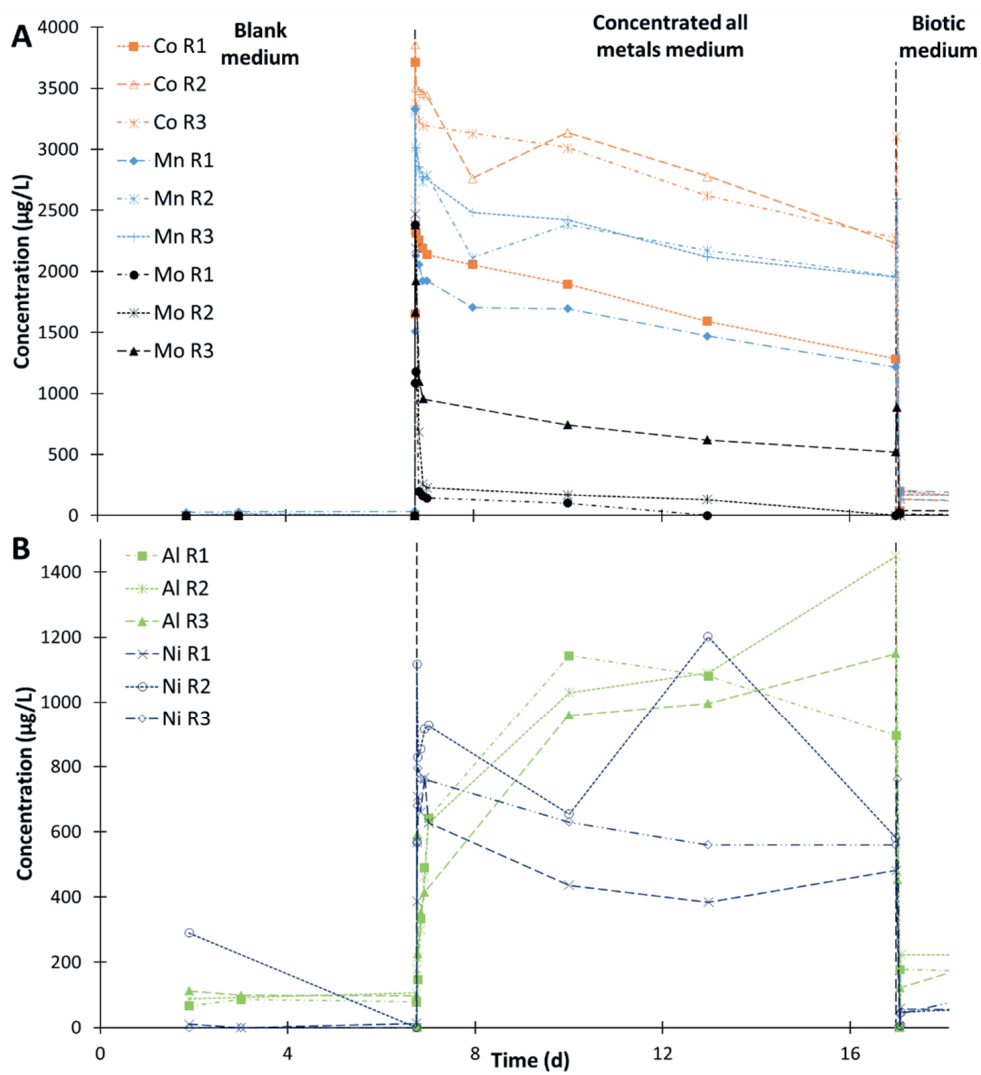


Figure S3.6. Catholyte concentrations of added trace metal compounds and Al over time in a triplicate reactor experiment (R1-R3). Concentrated trace metal compounds were added at day 7 and at day 17, the reactor was flushed with three times the volume of biotic catholyte and anolyte. The concentrations of Fe, Cu and Zn are shown in Figure 3.3.

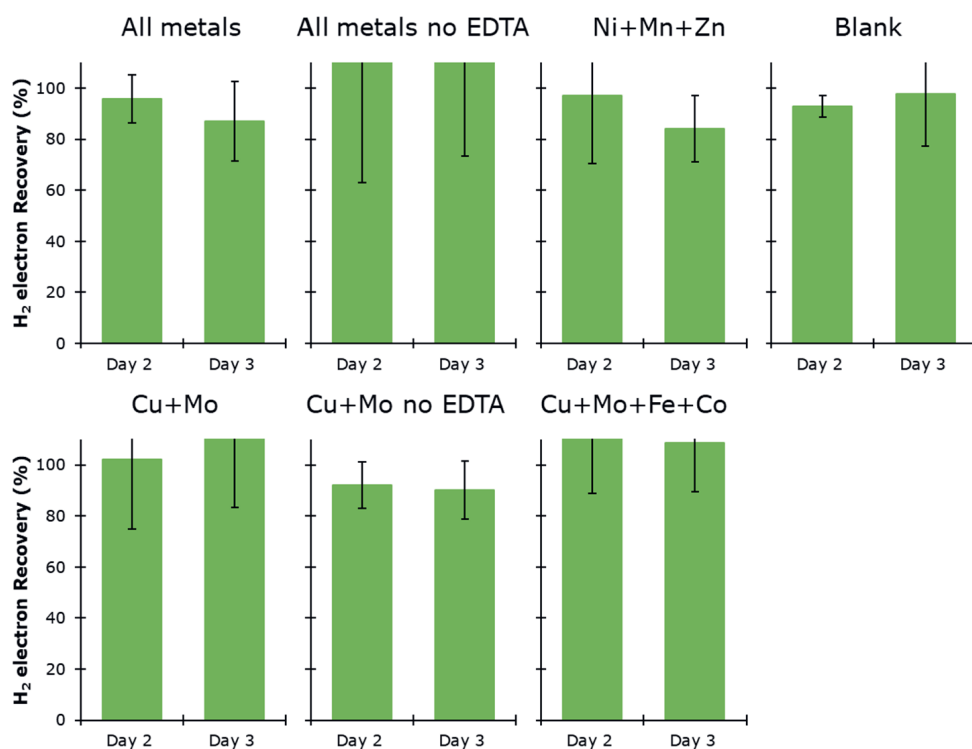


Figure S3.7. Electron recovery into hydrogen measured with concentrated sub-mixes of the metal mix medium at two days during the stabilization of the reactors after addition of the trace metal mix. The error bars show the standard deviation between the triplicate experiments.

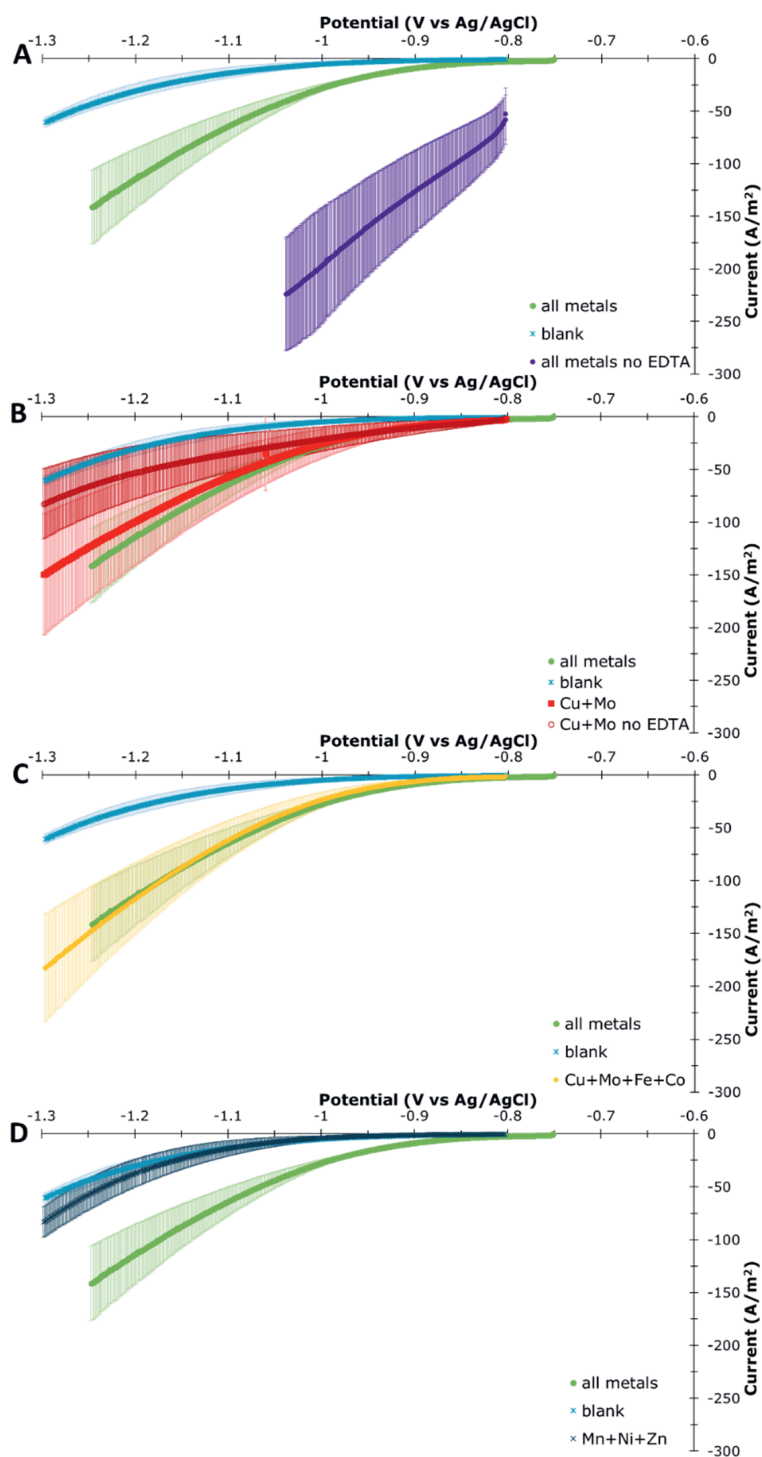


Figure S3.8. Linear sweep voltammetry plots performed after 48 hours stabilization with different metal mixes. The error bars represent the standard deviation between triplicate reactors.

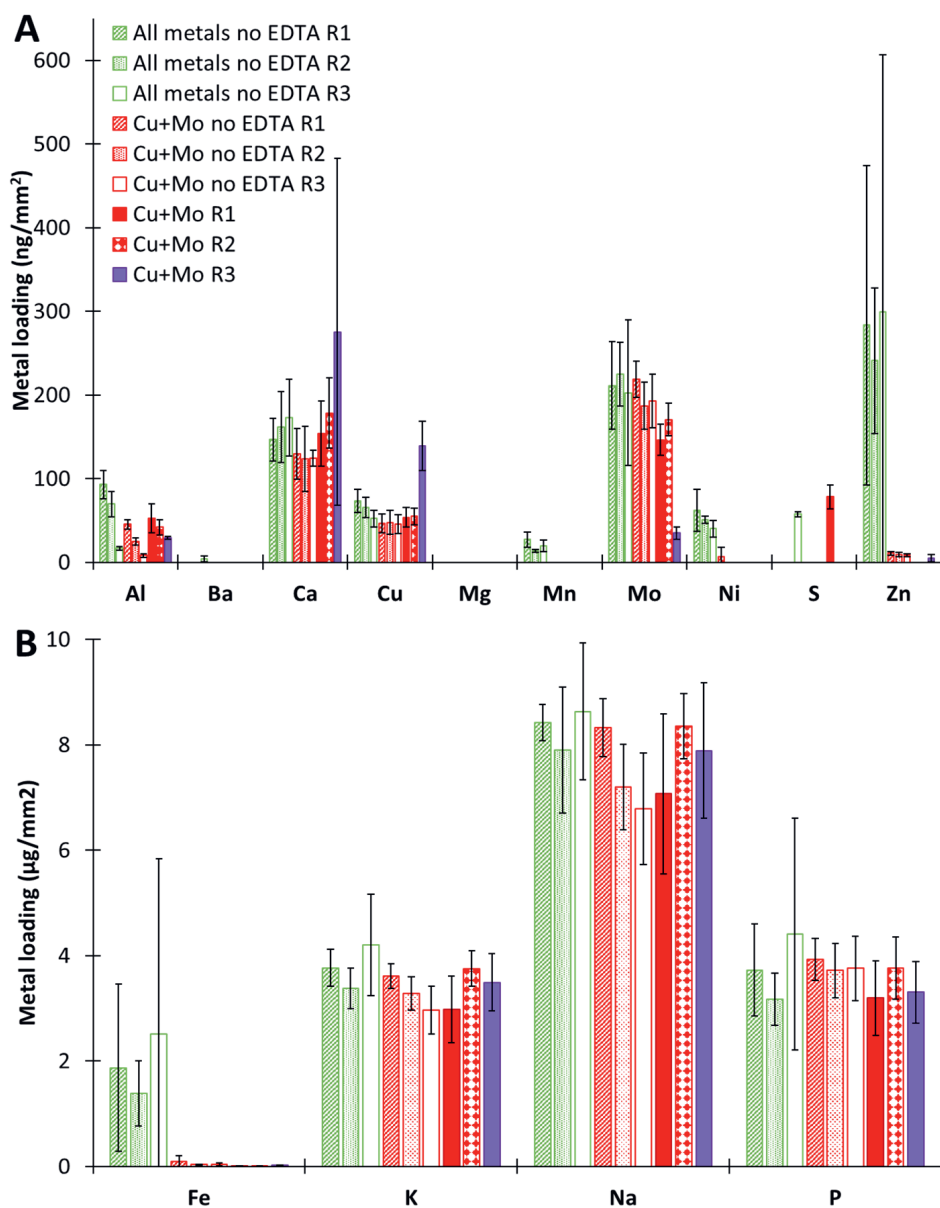


Figure S3.9. Metal element concentrations per mm^2 cathode projected surface area found on the cathodes of three reactors treated with three different sub-mixes of the trace metal mix (all metals no EDTA, Cu+Mo no EDTA, Cu+Mo). The element concentrations were measured after a microwave destruction of the cathode. The error bars show the standard deviation between three measured cathode pieces from each experiment.

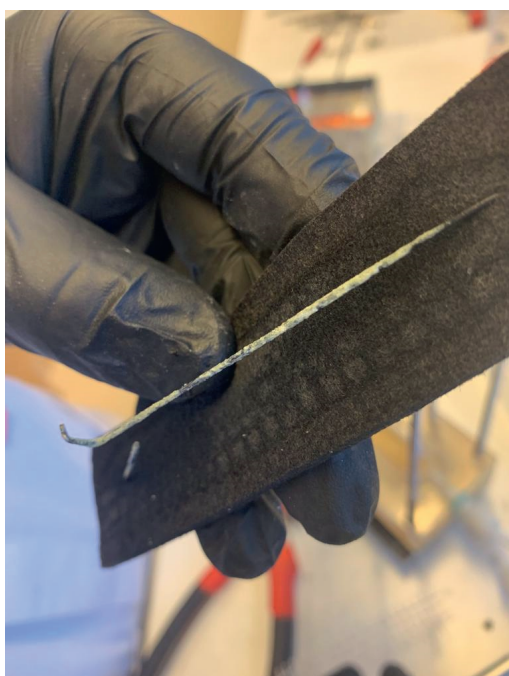


Figure S3.10. Deposits on titanium wire after experiments with the all metals no EDTA mix.

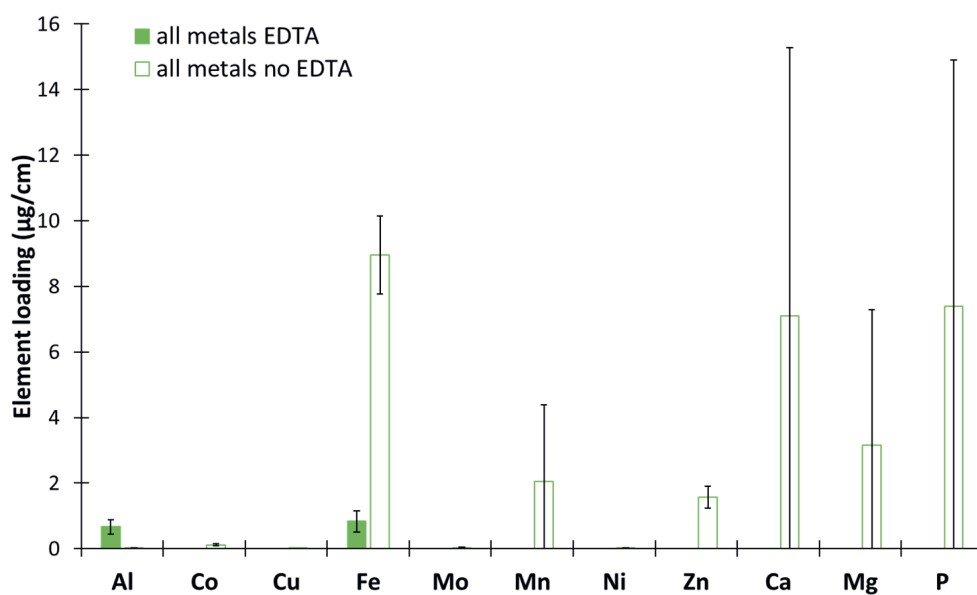
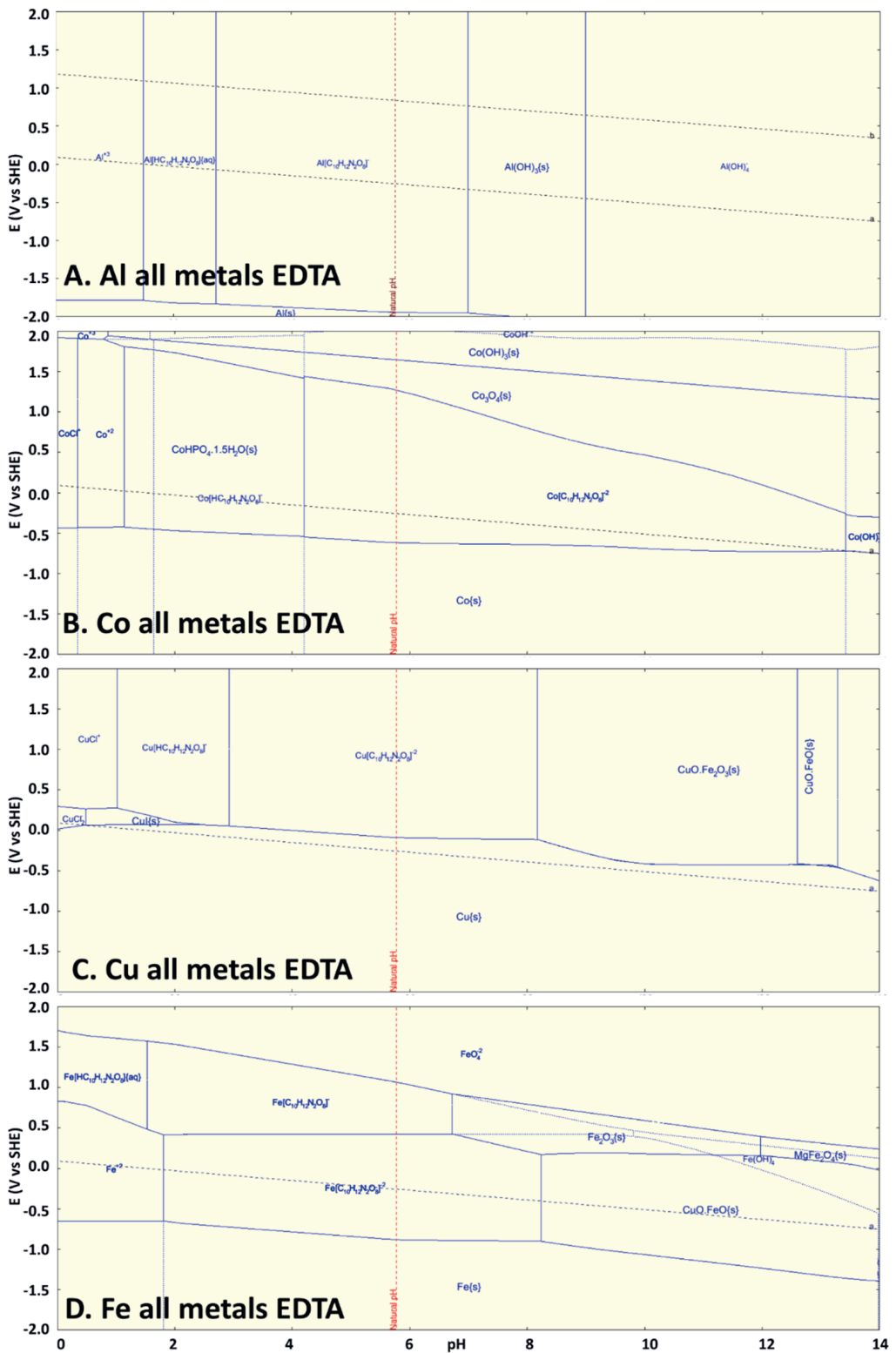


Figure S3.11. Element loading measured on titanium wire after experiments with addition of the all metals and all metals no EDTA mix. Note that the loading is calculated over the projected surface area of the titanium wire (10 cm), since deposition was only found on the side facing the membrane. The error bars represent the standard deviation between triplicate experiments.



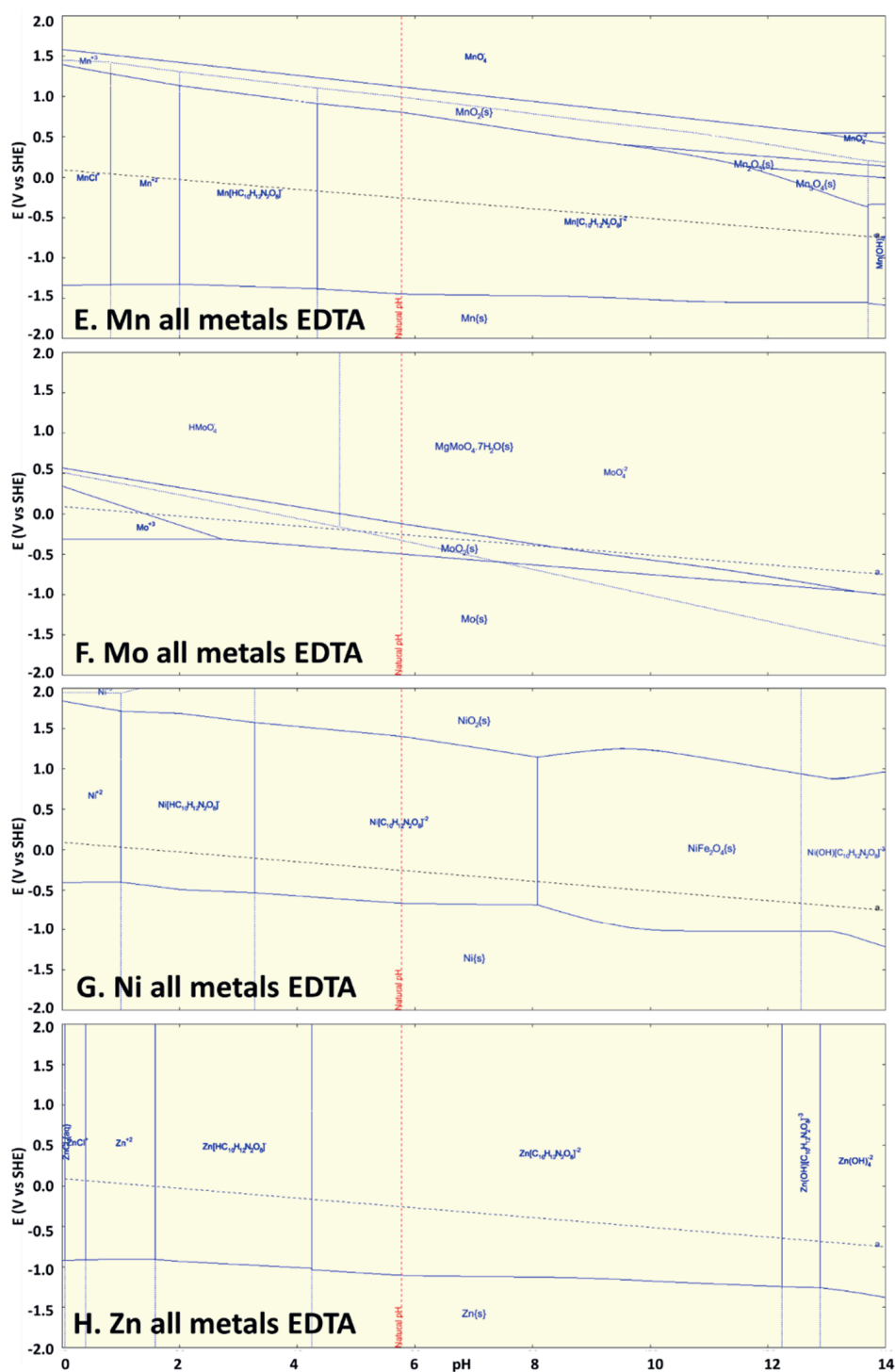
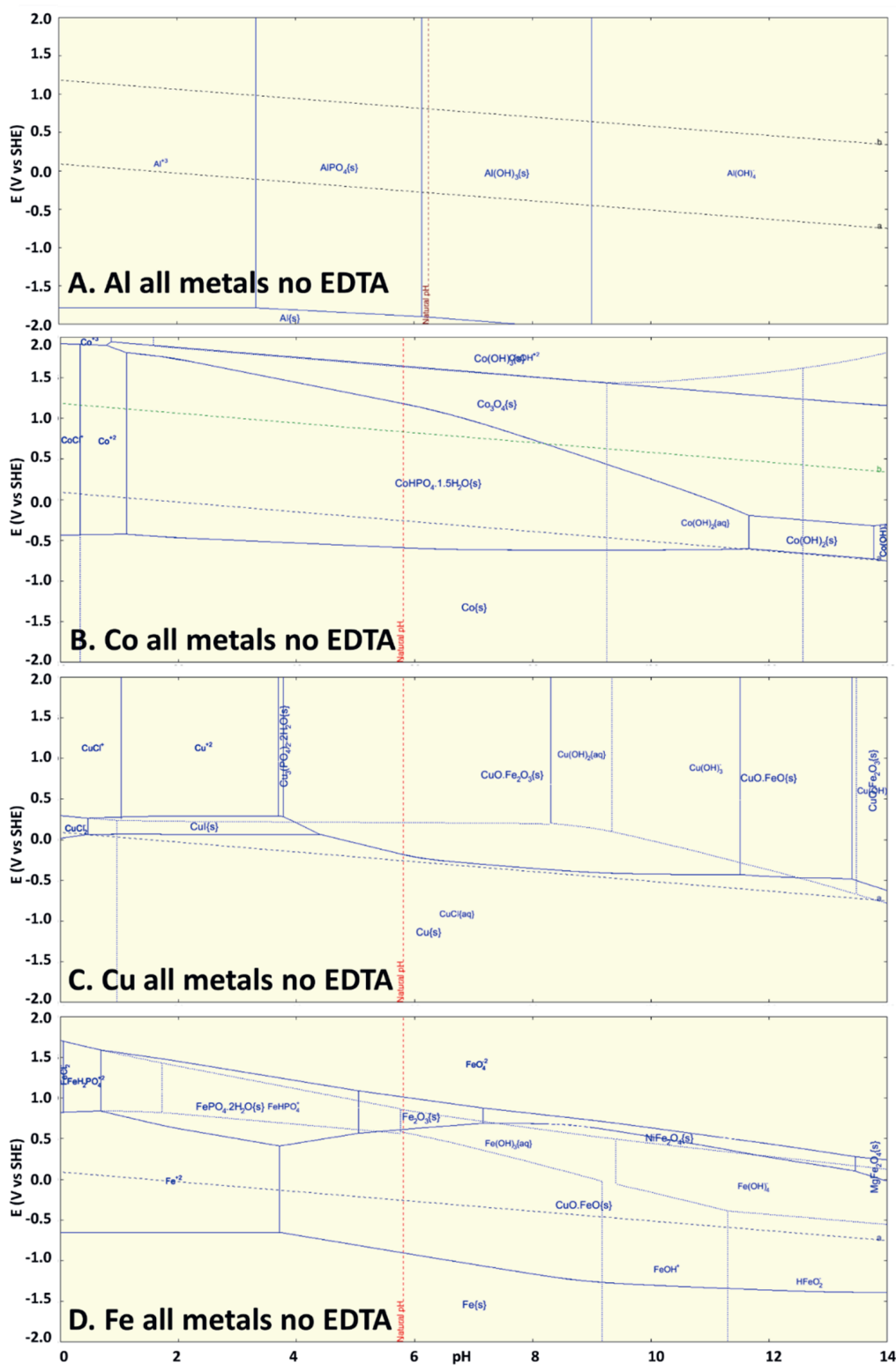
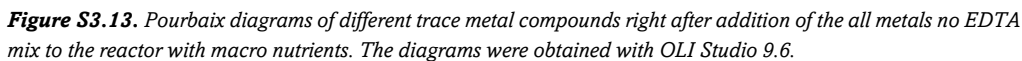


Figure S3.12. Pourbaix diagrams of different trace metal compounds right after addition of the all metals EDTA mix to the reactor with macro nutrients. The diagrams were obtained with OLI Studio 9.6.





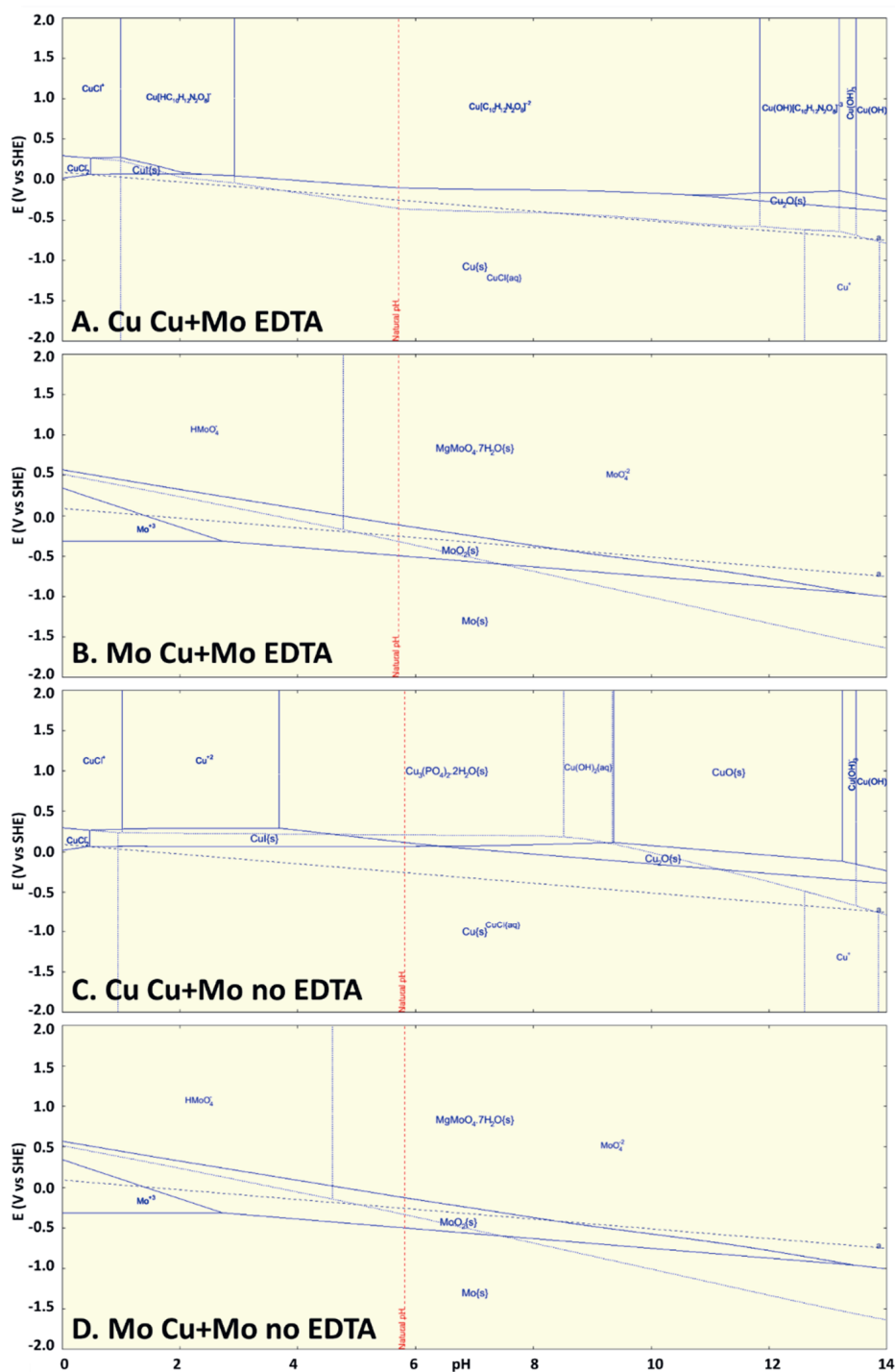
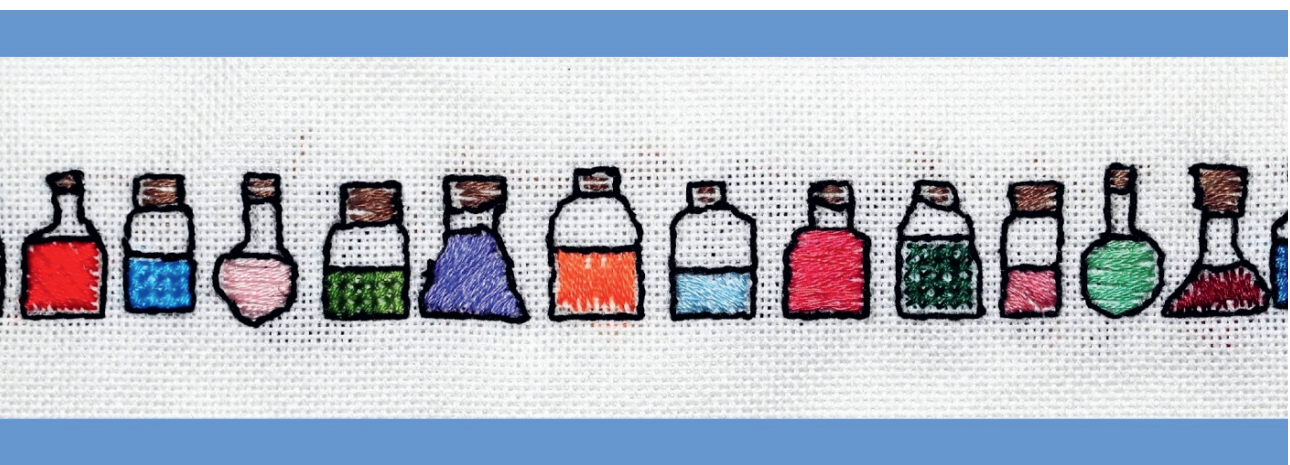


Figure S3.14. Pourbaix diagrams of Cu (A and C) and Mo (B and D) right after addition of the Cu+Mo (A and B) and Cu+Mo no EDTA (C and D) mix to the reactor with macro nutrients. The diagrams were obtained with OLI Studio 9.6.



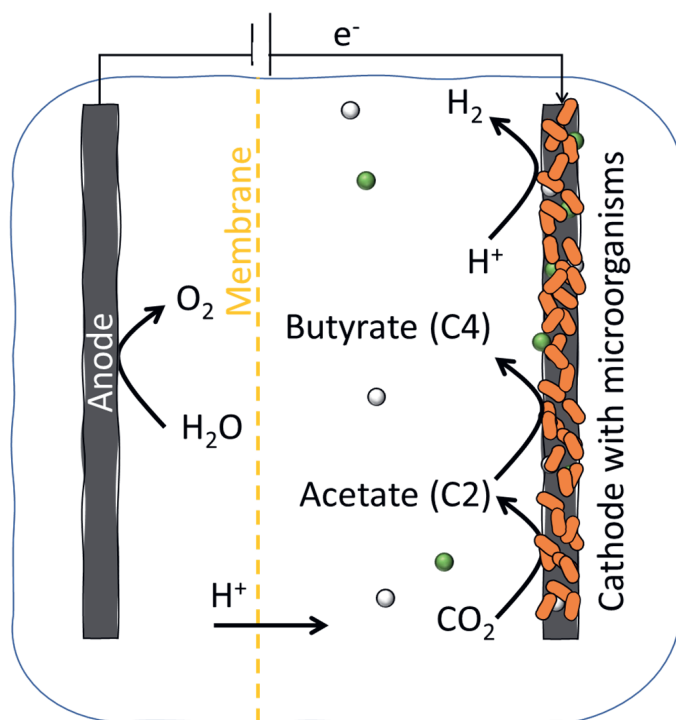
Chapter 4

Mixed trace metals from microbial growth medium act as hydrogen evolution catalyst during microbial electrosynthesis at high current density



Abstract

CO₂ reducing microbial electrosynthesis systems combine electrochemical and microbial catalysis to convert CO₂ into green chemicals, e.g., short and medium chain fatty acids. To improve process performance, a metal-based catalyst can be integrated to enhance the formation of electron carriers and thus enhance the energy supply for the biofilm. Here we show the feasibility of a hydrogen evolution reaction (HER) catalyst from microbial trace metals present in a bio-electrochemical CO₂ reduction system. HER catalysts were formed from concentrated trace metal mixes with (TMM+) and without (TMM-) chelating agent ethylenediaminetetraacetic acid (EDTA), added to electrochemical systems with graphite felt cathodes controlled at -1.06 V vs Ag/AgCl. The HER catalysts showed high current densities compared to a non-pre-treated system: -20 kA/m³ (TMM+) and -90 kA/m³ (TMM-), the latter being the highest reported current densities in microbial electrosynthesis with 3D cathodes. The integration of the HER catalyst allowed for immediate start-up of microbial activity measured as acetate formation. Also, *n*-butyrate formation showed fast start-up with observed production after twenty days. Hydrogen was always produced in excess, with higher production rates for the TMM- HER catalyst experiments, although hydrogen productivity decreased over the 36 to 50 days, possibly due to leaching of metal compounds from the cathode. Based on microbial analysis, a two-step microbial community bioprocess is suggested: acetogenesis (CO₂ to acetate) by a BRH-c20a strain and chain elongation (C2 to C4) by *Clostridium sensu stricto* 12 (related) species. The proof of principle displayed in this study shows that combination of a chemical HER catalyst with biocatalysts is feasible for CO₂ valorisation to C4 compounds under mild, microbial compatible process conditions.



4.1 Introduction

Electrochemical CO₂ reduction provides an opportunity to combine valorisation of CO₂ with storage of excess renewable energy¹. During electrochemical CO₂ reduction, C1-C2 compounds are the easiest to form from CO₂. To increase the length of the produced carbon chains and thereby the product value, the addition of a biocatalyst is promising². During this bio-electrochemistry process, the mixed microbial community catalyses CO₂ reduction in an electrosynthesis cell leading to the formation of green chemical products like ethanol³ methane⁴ ethylene⁵) and medium chain fatty acids (acetate, butyrate, caproate)⁶⁻⁹. Medium chain fatty acids (MCFAs) have many applications, ranging from antimicrobials to precursor for bioplastics or biofuels¹⁰.

These conversions are anaerobic process driven by electroactive bacteria, which grow in suspension and/or form a biofilm on the cathode. Electrons are (directly or via a carrier such as H₂) generated at the anode and charged by an external energy source.¹¹ These bio-electrochemical CO₂ reductions can be performed with non-aseptic microbial cultures which is promising for the treatment of different kind of CO₂-rich waste streams¹². MCFA production with open cultures of microbial consortia is possible via chain elongation, where during anaerobic fermentation the short-chain carboxylates can be elongated via different pathways¹³. A first step of the chain elongation process is the formation of acetate from two molecules of CO₂ during homoacetogenesis¹⁴. For bio-electrochemical acetogenesis, hydrogen was shown to be an intermediate in the electron transport between the cathode and the bacteria¹¹. Previous studies showed that bio-electrochemical CO₂ elongation was stimulated by improved hydrogen supply¹⁵. Therefore, it is hypothesized that stimulating hydrogen production from the start of the bio-electrochemical chain elongation process would benefit the production of medium chain fatty acids.

Hydrogen formation at the electrode surface (hydrogen evolution reaction) can be stimulated by the incorporation of a catalyst. To combine a hydrogen evolution reaction (HER) catalyst with a microbial catalyst in the same system, it is essential that the HER catalyst functions under conditions suitable for microbial electrosynthesis, e.g., near neutral pH and in mild temperature ranges^{16,17}. Several studies have reported HER catalysts which catalyse hydrogen formation under microbial compatible conditions. These studies used for example Co, Mo or Ni-based catalysts that required specific methods to integrate them on the cathode¹⁸⁻²². Recently, de Smit et al. (Chapter 3) showed the highest reported hydrogen production rates (up to 11 kg H₂ d⁻¹ m⁻³ cathode) with a HER catalyst generated from feeding a trace metal mix solution and EDTA (TMM+) in an abiotic system with microbial compatible conditions (bulk pH 5.8, 30°C). In that work, the generation of such catalyst was possible thanks to a pre-treatment by the addition of a 100x concentrated trace metal solution into the salt electrolyte (phosphate buffer, Mg and Ca salts) in the cathode compartment of the reactor (Chapter 3).

The main components of the trace metal solution were Co, Cu, Fe, Mn, Mo, Ni and Zn, kept into solution with ethylenediaminetetraacetic acid (EDTA). Under reducing potential (-1.06 V vs Ag/AgCl) conditions, the trace metals deposited on the porous graphite felt cathode at the start of the experiment. After this pre-treatment, the current density increased to -12 kA/m³ with around 70-100% electron recovery to hydrogen (Chapter 3). The performance was even higher

(up to 72 kg H₂ d⁻¹ m⁻³ cathode) when chelating agent EDTA was left out of the trace metal mix solution (TMM-), which led to faster and more complete deposition of the metals on the cathode (Chapter 3). Co, Cu, Fe, Mo, Ni and Zn were detected on the cathode after the experiment with loadings of respectively 275, 64, 1920, 213, 51 and 275 ng/mm² projected surface area (psa) on 3 mm thick graphite felt (Chapter 3). In additional tests, the role of the different trace metals within the mix was investigated. Cu and Mo were identified to contribute most to the HER catalyst activity of the TMM+, while Fe, Mn, Ni and Zn were suggested to have important contribution to the HER activity of the TMM- catalyst (Chapter 3).

Although it was shown that a productive HER catalyst can be formed from the trace metal solution as discussed above, it is still unknown whether microbial electrosynthesis is compatible with an integrated catalyst. Because high concentrations of trace metals were added to the electrochemical reactors, the conditions can be toxic for microorganisms and inhibit their growth²³. Regarding toxicity, not only the influence of the metal elements, but also the effect of EDTA should be considered, because EDTA can lower metal toxicity²⁴. Another factor to consider for the combination of a HER catalyst and microbial activity is that hydrogen bubble formation can cause sheer stress at the cathode surface and thus inhibit biofilm formation¹⁵. Besides the effects of the HER catalyst on the biofilm, the biofilm can also affect the HER catalyst performance. For example, the growth of microorganisms can cause uptake of the deposited trace metals from the cathode²⁵⁻²⁹, which reduces the amount of available HER catalyst.

The aim of this study was to evaluate the feasibility of combining a trace metal mix HER catalyst with microbial electrosynthesis. The HER catalyst was deposited on the cathode using the trace metal mix with (TMM+) and without (TMM-) EDTA. The system was evaluated for bio-electrochemical CO₂ elongation systems. To this purpose, mixed microbial cultures were added to bio-electrochemical systems after pre-treatment with the trace metal mix. First, the formed catalyst was evaluated based on productivity and stability. Second, the activity and composition of the microbial community was investigated. This study presents a successful first integration of an *in situ* HER catalyst generated from trace metals solution and a CO₂-utilizing microbial community in the same bio-electrochemical chain elongation system.

4.2 Materials and method

4.2.1 Reactor setup & operation

Two sets of duplicate reactors were used for this study. The reactor setup was assembled as described by de Smit et al. (Chapter 3) (Figure 4.1) and placed in a temperature controlled (30 °C) and light-shielded cabinet. The reactors consisted of a Ti/Pt-Ir MMO anode (thickness 1 mm, Magneto Special Anodes BV, Netherlands) and one layer (3 mm) graphite felt cathode (Rayon Graphite Felt, CTG Carbon GmbH, Germany), secured with spacers in the Plexiglas flow-through plates. The graphite felt was non-microporous with a surface area < 1 m²/g, as determined by N₂ physisorption. The cathode current collector consisted of a titanium wire (0.8 mm, grade 2). The cathode potential was controlled at -1.06 V vs an Ag/AgCl reference electrode (3 M KCl, QM710X, Q-is, the Netherlands) over the whole course of the experiment by a n-stat potentiostat (IVIUM, the Netherlands). The anode and cathode compartment were separated by a cation exchange membrane (Fumasep FKS, Fumatech BWT GmbH, Germany, 21.3 cm² projected surface area). The total recirculation volumes of the anolyte and catholyte

were respectively 339-365 and 391-408 mL. Both anolyte and catholyte were continuously recirculated at respectively 10 and 17 L/h. CO₂ was added in gaseous form in a 30:70 CO₂:N₂ mix, with 100 LN/d CO₂, which was sparged (spargerhead 22 mm height, 12 mm diameter) into the catholyte recirculation bottle (Figure 4.1). The CO₂:N₂ gas mix was flushed through a demi water bottle prior to entering the reactors to ensure the gas stream was humidified. The anolyte recirculation bottle was continuously sparged with 60 LN/d N₂ to remove excess O₂ (60 L/d). Previous studies showed hydrogen gas build-up between the cathode and the membrane, so a bypass was installed to release gas (Figure 4.1B). Flow measurements revealed that 46-88% of the total catholyte recirculation flow passed through the bypass. In the catholyte recirculation loop, a pH controller (Ontwikkelwerkplaats, Elektronica ATV, the Netherlands) with measuring probe (QMP108X, Q-is, the Netherlands) was installed to maintain the pH of the recirculated catholyte at 5.8.

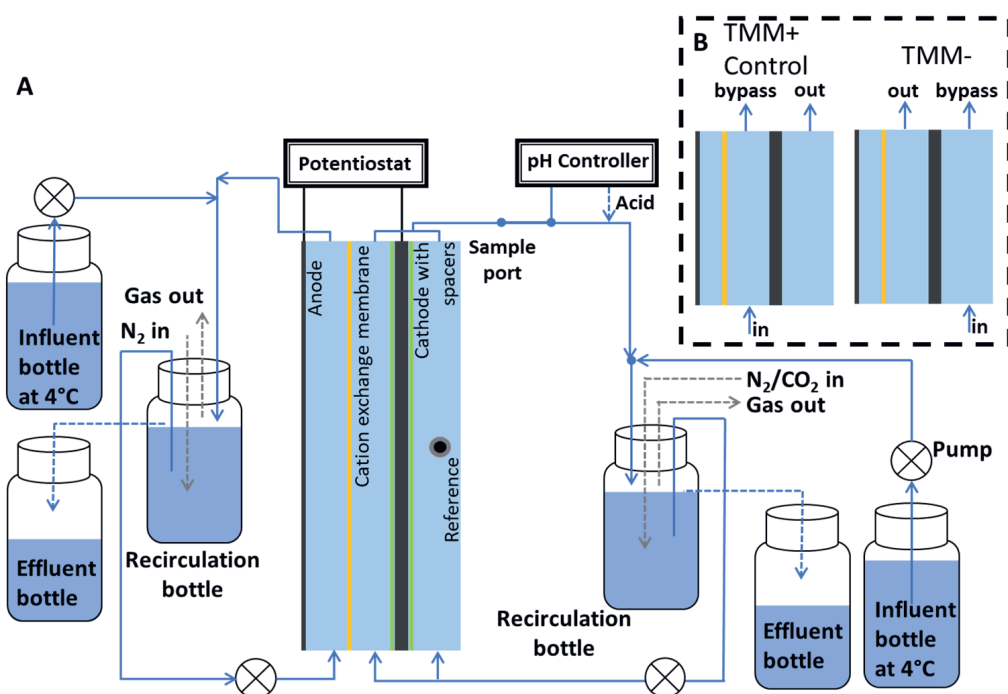


Figure 4.1. Schematic overview of reactor setup, adapted from de Smit et al. (Chapter 3) (A) and recirculation flow-through configuration for different experimental sets (B).

4.2.2 Reactor pre-treatment

To test the compatibility of an integrated trace metal H₂ evolution catalyst with microbial growth and activity, two sets of reactors were pre-treated with a trace metal mix. In Table 4.1, the three different phases of the experiment are shown, with the corresponding medium compositions in Table 4.2 and 4.3. After 1-7 days of operation with “blank medium” without trace metals or ammonium (Table 4.2), 10 vol% concentrated trace metal mix solution (Table 4.3) was added to the reactor catholyte with a syringe, to start the “Metal phase”. One set of cathodes was pre-treated with a trace metal mix without EDTA (TMM-), since this mix had shown the best

hydrogen evolution performance in our previous study (Chapter 3). Another set of reactors was pre-treated with the trace metal mix with EDTA (TMM+). The trace metal mix compositions are shown in Table 4.3. The reactor was left in batch mode during several days to allow the metals to deposit on the cathode. The incubation time with concentrated metals for the experiments with TMM+ and TMM- were respectively 10 and 2 days (Table 4.1). The incubation time for the TMM- was shorter because the metals disappeared from the solution more rapidly (Chapter 3, SI Figure S4.2). After these pre-treatments, the “biotic phase” was started in the reactors, by flushing the electrolytes with three times the total catholyte volume of anaerobic biotic medium composed of NH_4 and biocompatible low concentration of trace metals (in a mix with EDTA) (Table 4.2). In contrast with previous research^{7,30}, the biotic medium used in this study did not contain methanogenesis inhibitor 2-bromoethanesulfonate, since it was suspected that this sulphur-containing compound could poison the catalyst³¹ (SI Figure S4.1). Right after this replacement of the electrolytes, the reactors were inoculated with 10 vol% catholyte with a mixed microbial culture which was previously grown with similar conditions (bio-electrochemical CO_2 -fed system, bulk pH 5.8, -200 mA to graphite felt cathode, 30 °C) and showed production of fatty acids (C2-C4). Inoculation was repeated on day 24, 31 and 38 for the TMM+ experiments and on day 25 and 36 for the TMM- experiments. During the biotic phase, the catholyte medium feed was changed from batch to continuous with a, hydraulic retention time (HRT) of 14 days. The anolyte medium feed on the other hand, was continuously fed to the reactor with HRT 4 days, to prevent depletion of anolyte (Table 4.1).

One set-up adjustment was made for the biotic phase of the experiments without EDTA in the pre-treatment mix (TMM-), the cathode inflow port and the position of the bypass were changed to allow for better mixing of the catholyte chamber (Figure 4.1B, Table 4.1). For the other two runs (TMM+ and control), the cathode chamber inflow port was positioned between the membrane and the cathode (Figure 4.1B).

Table 4.1. Duration and medium used in each phase of the biotic experiments. The medium compositions are shown in Table 4.2-4.3.

Phase	HRT catholyte (d)	Metal mix with EDTA (TMM+)		Metal mix without EDTA (TMM-)		Control	
		Medium	Duration (d)	Medium	Duration (d)	Medium	Duration (d)
Blank phase	Batch	Blank medium	7	Blank medium	1	-	-
Metal phase	Batch	TMM+	10	TMM-	2	-	-
Biotic phase	14	Biotic medium	36	Biotic medium*	48	Biotic medium	29

*Catholyte inflow port changed (Figure 4.1B)

Table 4.2. Composition of “blank”, “concentrated metal mix” and “biotic” medium. The trace metal mix compositions are described in Table 4.3.

Compound	Unit	Blank medium	TMM+	TMM-	Biotic medium
Catholyte					
Na ₂ HPO ₄ ·2H ₂ O	g/L	7.5	7.5	7.5	7.5
KH ₂ PO ₄	g/L	3.0	3.0	3.0	3.0
NH ₄ Cl	g/L	-	-	-	0.2
MgCl ₂ ·6H ₂ O	g/L	0.04	0.04	0.04	0.04
CaCl ₂ ·2H ₂ O	g/L	0.02	0.02	0.02	0.02
Trace metal solution	mL/L	-	100 TMM+	100 TMM-	1 TMM+
pH		5.8	5.8	5.8	5.8
Anolyte					
Na ₂ HPO ₄ ·2H ₂ O	g/L	7.5	7.5	7.5	7.5
KH ₂ PO ₄	g/L	3.0	3.0	3.0	3.0
(NH ₄) ₂ CO ₃	g/L	-	-	-	0.18
MgSO ₄ ·7H ₂ O	g/L	0.05	0.05	0.05	0.05
Ca(OH) ₂	g/L	0.01	0.01	0.01	0.01
pH		~7.1	~ 7.1	~ 7.1	~ 7.1

Table 4.3. Composition of trace metal solutions used for the pre-treatment of cathodes at the start of the “metal phase”.

Trace metal solution	Unit	TMM+	TMM-
FeCl ₃ ·6H ₂ O	g/L	1.5	1.5
H ₃ BO ₃	g/L	0.15	0.15
CuSO ₄ ·5H ₂ O	g/L	0.03	0.03
KI	g/L	0.18	0.18
MnCl ₂ ·4H ₂ O	g/L	0.12	0.12
Na ₂ MoO ₄ ·2H ₂ O	g/L	0.06	0.06
ZnSO ₄ ·H ₂ O	g/L	0.12	0.12
CoCl ₂ ·6H ₂ O	g/L	0.15	0.15
NiCl ₂ ·6H ₂ O	g/L	0.023	0.023
EDTA (C ₁₀ H ₁₄ N ₂ Na ₂ O ₈ ·2H ₂ O, CAS 6381-92-6)	g/L	10	-
pH (adjusted with NaOH)		6.4	6.4

4.2.3 Analytical methods

All the analytical methods applied to investigate the process performances of the two reactors are described by de Smit et al. (Chapter 3). Gas chromatography (GC) (Shimadzu GC-2010, Japan) was applied to measure H₂, CO₂, N₂, CH₄ and O₂ in the outgoing gas of the cathode compartment. Gas chromatography (Agilent 7890B, USA) was also applied to measure fatty acids (C2-C8) and alcohols (C1-C6) in the liquid phase. To evaluate the microbial growth in the liquid fraction, 1 mL of sample was mixed and analysed at a wavelength of 600 nm via a Hach spectrophotometer (DR3900, Hach Lange, Germany). Metal concentrations on the cathode, titanium wire and in the catholyte were measured by an inductively coupled plasma analyser (ICP-OES, Perkin Elmer AVIO 500).

4.2.4 Calculations

The hydrogen concentration in the catholyte was calculated based on the measured hydrogen fraction in the off gas (fraction_{offgas} H₂), based on a Henry coefficient of 7.7E-06 mol/(m³Pa)³² and a pressure of 1 atm (101325 Pa).

Hydrogen conc [μM]

$$= 7.7 \cdot 10^{-6} \frac{\text{mol}}{\text{m}^3 \text{Pa}} * 101325 \text{ Pa} * \frac{\text{fraction}_{\text{offgas}} \text{H}_2 [\%]}{100\%} * 10^3 \frac{\mu\text{mol} * \text{m}^3}{\text{L} * \text{mol}}$$

The electron recovery into volatile fatty acids (η_{VFAs}) and hydrogen (η_{H_2}) was calculated based on the measured current at the sampling time (Current_t) in mA (mC/s), the catholyte outflow rate at the sampling time (Q_t, calculated based on the inflow rate and acid addition over time), and the measured concentrations of volatile fatty acids in the liquid phase at the sampling time Conc_{VFA,t}:

$$\eta_{\text{VFAs}} = \frac{96485 \frac{\text{mC}}{\text{mmol } e^-} * \text{Conc}_{\text{VFA},t} \left[\frac{\text{mmol}}{\text{L}} \right] * Q_t \left[\frac{\text{L}}{\text{h}} \right] * x \frac{\text{mmol } e^-}{\text{mmol VFA}}}{\text{Current}_t \left[\frac{\text{mC}}{\text{s}} \right] * 3600 \frac{\text{s}}{\text{h}}}$$

The hydrogen flow was calculated based on the hydrogen and nitrogen fractions in the measured off gas (fraction_{offgas} H₂, fraction_{offgas} N₂), the reactor temperature (Temp) and the ideal gas law, assuming that the N₂ was inert inside the reactors:

$$\text{Flow}_{\text{H}_2} \left[\frac{\text{mmol H}_2}{\text{h}} \right] = \frac{\text{fraction}_{\text{offgas}} \text{H}_2 [\%] * 233.3 \frac{\text{LN N}_2}{\text{d}}}{\text{fraction}_{\text{offgas}} \text{N}_2 [\%] * 24 \frac{\text{h}}{\text{d}}} * \frac{101325 \text{ Pa}}{8.314 \frac{\text{J}}{\text{K} * \text{mol}} * \text{Temp} [\text{K}]}$$

The electron recovery into hydrogen was calculated based on the hydrogen flow and the current measured at the sampling time of the hydrogen:

$$\eta_{\text{H}_2} = \frac{96485 \frac{\text{mC}}{\text{mmol } e^-} * \text{Flow}_{\text{H}_2} \left[\frac{\text{mmol H}_2}{\text{h}} \right] * 2 \frac{\text{mmol } e^-}{\text{mmol H}_2}}{\text{Current}_t \left[\frac{\text{mC}}{\text{s}} \right] * 3600 \frac{\text{s}}{\text{h}}}$$

4.2.5 Microbial community analysis

4.2.5.1 Samples collection and DNA extraction

At the end of the biotic experiments, liquid samples were collected from each reactor and stored at -20 °C to investigate the microbial community composition via DNA extraction and Next Generation Sequencing of 16S rRNA gene. DNA was extracted using the Powersoil DNA isolation kit (Qiagen, USA) according to the manufacturer's instructions. DNA concentration and purity were measured with the NanoDrop spectrophotometer (Thermo Fisher Scientific, Germany).

4.2.5.2 Sequencing of 16S rRNA genes and bioinformatics

16S rRNA genes were amplified with PCR using the full-length primers reported in SI Table S4.1. After initial amplification the variable V3 and V4 target region was amplified (for simultaneous amplification of Bacteria and Archaea), and index PCR was carried out using the Nextera UD

indexes adapters set D (Illumina, USA). Sequencing was performed on the Illumina MiSeq platform (V2 kit). Sequence data were processed with QIIME2 (v. 2019.10)³³. Briefly, demultiplexed forward sequences from PCR primer 341F³⁴ were trimmed by removing the primer sequence. The resulting reads of ~230 bp were denoised using DADA2 single-end option³⁵, which performed error-correction and inference of exact amplicon sequence variants (ASVs). For taxonomic classification of ASV representative sequences, a naive Bayes classifier was applied, which was trained on the amplicon of primer set 341F and 805R extracted from SILVA v.138 reference database³⁶. The frequency table was rarefied to 72000 reads per sample, and ASV counts were agglomerated into genus-level taxonomic groups. For the data presented in this study, we considered the most significant genera per each sample out of the total number of sequences, setting a cut-off value of 3%.

4.2.5.3 Fluorescent In Situ Hybridization (FISH)

For FISH analysis, cathode samples carrying biofilm were fixed with 170 µl 37% formaldehyde. After fixation, samples were stored at -20 °C in 3 ml of ethanol/PBS (1:1). To improve the procedure efficiency, the cathode biofilm was pre-treated via sonication (40 kHz, 50W, room temperature) in three cycles of 20s with 10s pauses during which the samples were kept in ice, in order to disaggregate the cell clusters. The sonicated samples were used for FISH analysis following the protocol of Hugenholtz, et al.³⁷. All oligonucleotide probes applied, labelled with Cy3-red or Alexa488-green fluorophores, are listed in SI Table S4.1. Oligonucleotide probes were selected based on the NGS data and the probeBASE database³⁸. Samples were examined using an epifluorescence microscope BX43 (Olympus, Japan) equipped with a DP80 digital camera and the cellSens Standard imaging software (Olympus, Japan). For the image analysis, the FIJI software package (version 1.51g, Wayne Rasband, NIH, Bethesda, MD, United States) was used.

4.2.5.4 Scanning Electron Microscopy (SEM)

To analyse the structure of the attached biofilm growing on the cathode, Scanning Electron Microscopy (SEM) was applied. Pieces of cathode (~7 by 7 mm squares) were sampled and stored at 4°C in biotic catholyte and fixed with 2.5% glutaraldehyde for ~4 months at 4°C. Afterwards, the samples were rinsed by replacing the liquid with demi water 3 times. Dehydration was performed in graded ethanol solutions (10, 30, 50, 70, 80, 90, 96, and twice 100%) for 10 min each. The samples were dried with critical point drying (Leica EM CPD-030, Leica Microsystems, Germany) with CO₂. The samples were glued on the SEM stubs with carbon glue (Leit-C Conductive Carbon Cement, van Loenen Instruments, the Netherlands) and sputter coated with tungsten (12.0 nm, from two sides with 45° angle, Leica SCD 500, Austria) to finalize the preparation for the imaging. The SEM images were obtained with a Magellan 400 SEM (FEI Company, Hillsboro, OR, USA) at an acceleration voltage 2kV and beam current of 13 pA at RT.

4.3 Results and Discussion

4.3.1 Trace metal mix pre-treatment generates hydrogen evolution catalyst

To investigate the effect of cathode pre-treatment on the electron availability for the microbial consortia, the performances of cathodes pre-treated with trace metal mix with (TMM+) and without EDTA (TMM-) were evaluated via current and hydrogen measurement. Figure 4.2

shows the hydrogen production and observed currents for a blank reactor, after metal addition (day 7) and after inoculation with active biomass (day 17). For comparing a control reactor was started after 17 days (Figure 4.2 red line). At a constant potential (-1.06 V), the resulting current varied significantly over the different experiments. Right after the addition of the metal mixes (day 7), the current increased to -20 kA/m^3 for the TMM+ experiments, while the TMM- experiments showed a current increase to -90 kA/m^3 (Figure 4.2A). In the biotic phase (with presence of micro-organisms), the high current rates were maintained despite the catholyte replacement with biotic medium (day 17). The current values were 10 and 40 times higher than measured in the control experiment without pre-treatment (red line, Figure 4.2A). The current increases correspond with increases in the hydrogen concentrations (Figure 4.2B). The hydrogen concentration in the recirculated catholyte reached 4 and $13.3 \mu\text{M}$ for respectively the TMM+ and TMM- experiments (maximum solubility is $718 \mu\text{M}^{39}$), whilst the maximum hydrogen concentration in the control experiment was $0.15 \mu\text{M}$ (Figure 4.2B).

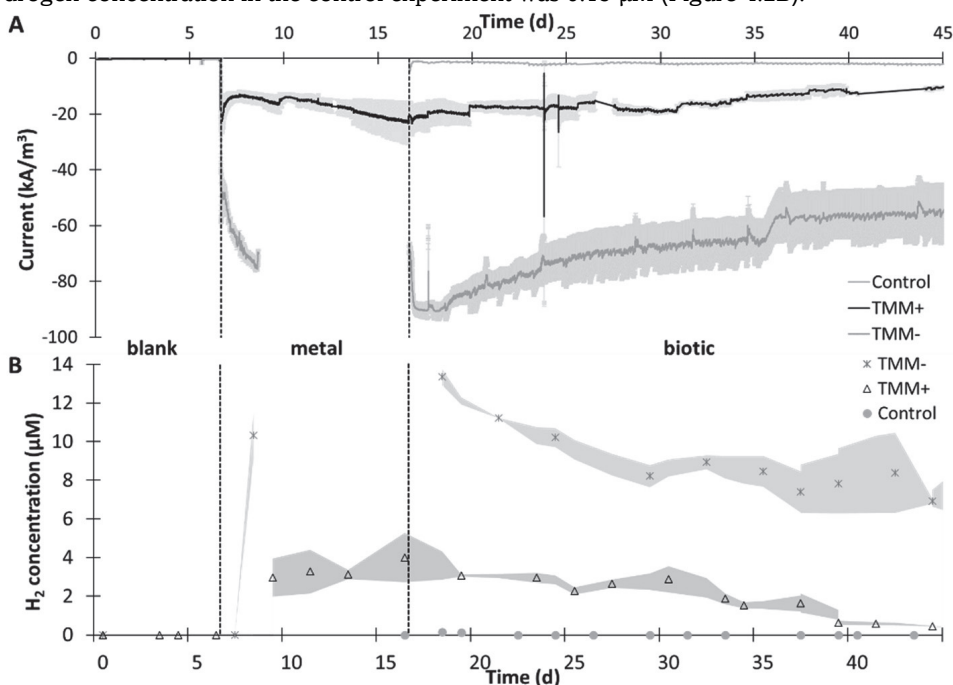


Figure 4.2. Cathodic current increase (A) and catholyte hydrogen concentration (B) after deposition of trace metal mix solutions with (TMM+, black line) and without (TMM-, grey line) EDTA (day 7-17, metal phase), compared to a blank phase without trace metals (day 0-7, blank) and during the biotic phase with biotic conditions and microorganisms (day 17-45, biotic), compared to a control experiment without pre-treatment (control). The standard deviation between duplicate experiments is shown as grey areas. The reactors were operated at -1.06 V vs Ag/AgCl throughout the whole experiment.

The current after the metal mix pre-treatment was substantially higher compared to the control experiment, where the current started at -1 kA/m^3 and increased to -2 kA/m^3 during the 28 days of biotic phase (red line, Figure 4.2A). Current density increases over time are typically observed in microbial electrosynthesis systems as the biofilm develops on the cathode⁴⁰. From previous work with similar reactor operation conditions, it can be predicted that it takes at least 60 days for the current to reach -3 kA/m^3 (without any pre-treatment or potential change)^{7,30}. In

studies with comparable 3D cathodes and different conditions, it took at least 15 days from starting the system to reaching the current densities measured in this study right after switching to microbial viable conditions (TMM+)^{7,14}. By the integration of the TMM HER catalyst, high current density values are reached at day 1 of biotic operation, showing that the start-up time for hydrogen production is shortened. After the TMM- pre-treatment, the current density values were up to -90 kA/m^3 at the start of the biotic phase (Figure 4.2A, day 17). These values are close to the highest reported current densities in literature for bio-electrochemical CO_2 reduction systems¹⁸⁻²⁰ (-350 A/m^2 on 2D cathodes, corresponding to -117 kA/m^3 with the cathode thickness used in this study). The high current of the TMM- pre-treated reactors at -1.06 V creates opportunities to operate the reactors at a less negative potential and still create sufficient hydrogen for the growing biofilm⁴¹. With these improvements, OPEX costs (with less energy investment) may be reduced⁴². In contrary with experiments without HER catalyst, the experiments with HER catalyst show a decrease of current over time during the biotic phase (Figure 4.2A, from day 17).

4.3.2 Metal compound leaching in TMM+ experiments

The slight decrease in hydrogen production over time corresponds with the decrease in the total cathodic current observed in the biotic phase (Figure 4.2, 49% and 40% decrease in average current for respectively TMM+ and TMM-). Although the hydrogen decrease in the biotic phase could be explained by hydrogen uptake by the microbiome, the current decrease indicates HER catalyst performance decrease over time (Figure 4.2). Different mechanisms could be causing the apparent catalyst activity decrease: I) leaching, II) biofilm growth and III) poisoning⁴³. To investigate leaching, metal concentrations in the catholyte were measured over time during the biotic phase (starting from day 17, Figure 4.3). In the TMM- experiments, only Al, Fe and Zn were detected above the detection limit during the biotic phase (Figure 4.3B and D). Fe was never above the standard concentration ranges in the biotic catholyte medium which was added over time during the biotic phase with HRT 14 days ($310 \mu\text{g/L}$). Al and Zn are known to deposit on and leach from different reactor parts (e.g. the Ti wire)³⁰, so the elevated concentrations of Fe, Al and Zn are not indicating leaching of the HER catalyst. These results support that the elements deposited during the metal phase stayed attached to the cathode during the biotic phase of the TMM- experiment.

For the TMM+ experiments, the concentrations of most elements in the catholyte were higher over time compared to TMM- (Figure 4.3). Interestingly, the duplicate TMM+ experiments showed significant differences in the concentration trends for Fe, Mn, Mo, Ni and Zn over time. All trace metals, except for Al, Fe and Zn were measured in the catholyte in concentrations higher than in the biotic catholyte medium (Figure 4.3A and C). Most elements in the TMM+ experiments did not increase over time, with exception of Mn, Mo, Ni and Zn, indicating those metals leached from the cathode.

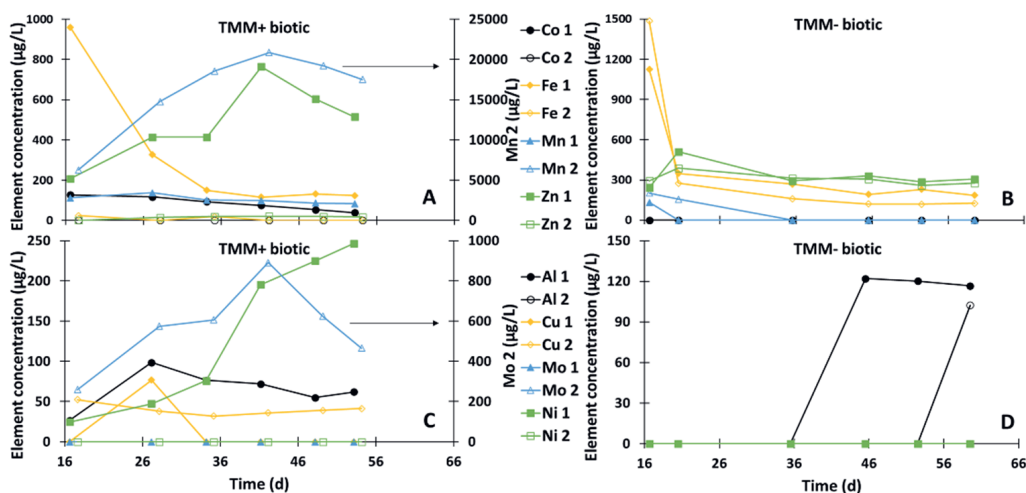


Figure 4.3. Average metals concentrations measured with ICP in the catholyte from the start to the end of the biotic phase (day 17-end) of the experiments with cathodes pre-treated with trace metal mix with (TMM+) and without (TMM-) EDTA. The results are presented separately for each replicate experiment (different individual experiments indicated with 1 and 2).

In previous work, Cu and Mo were identified as the active metal compounds in the TMM+ HER catalyst (Chapter 3). Therefore, only the leaching of Mo from the TMM+ cathode of one of the duplicate experiments (Figure 4.3C, Mo 2), could contribute to activity loss of the HER catalyst. The observation that the element concentrations in the TMM+ experiments are higher than in the TMM- experiments (Figure 4.3), suggests that the deposition mechanism of the elements to the cathode is affected by the presence of EDTA in the pre-treatment mixture. EDTA slows down electrodeposition by e.g. stabilizing intermediates⁴⁴⁻⁴⁶, so it is probable that the chelating properties of EDTA also weaken the attachment of different elements to the cathode in the present study.

The other two deactivation mechanisms, biofilm growth and poisoning, are likely to occur during the development of a biofilm on the cathode. The formation of the polymeric layer of the biofilm matrix, secreted by the microorganisms after adhesion on the cathode, can deactivate the catalyst by blockage of the active site and/or lead to reactant mass transfer limitations⁴⁷. Additionally, the formation of a thick biofilm causes pH gradients⁴⁸ which decreases the concentration of protons at the active site of the hydrogen catalyst. Although no significant catalyst deactivation effect of biofilm formation on cathodes has been suggested⁴⁹, and several studies even showed improved hydrogen formation after biofilm growth⁵⁰⁻⁵², the effect of biofilm formation on catalyst stability requires further study. Poisoning can occur from the binding of e.g. N- or S-compounds to the catalyst surface^{43,53}. NH_4^+ and SO_4^{2-} were added over time during continuous operation to support microbial growth, so poisoning as a result of chemical binding cannot be excluded either as possible catalyst deactivation mechanism. In conclusion, a combination of leaching, biofilm growth and catalyst poisoning likely decreased the HER catalyst activity over time in the biotic phase.

4.3.3 Successful start-up of microbial activity after pre-treatment

Despite a slight deactivation of the HER catalyst, hydrogen was present in the catholyte bulk throughout the complete biotic phase of the TMM+ and TMM- experiments (Figure 4.2B), showing the HER catalyst can work under biotic conditions. In the next step microbial synthesis was performed. To test the microbial activity with the pre-treated cathodes, the concentrations of volatile fatty acids (VFA) were monitored in the recirculated catholyte over operation time of the biotic phase (starting at day 17, Figure 4.4). In the control reactor, no volatile fatty acids were detected throughout the biotic phase. In the TMM pre-treated reactors, the concentrations of both acetate and *n*-butyrate increased over time, and production started right after the start of the biotic phase (Figure 4.4A and B). From the liquid and gas samples over time and the current, electron recoveries were calculated (see materials and method for calculation). Besides the detected acetate and *n*-butyrate, unidentified products are also shown in the electron recovery graphs (Figure 4.4C and D). The unidentified electron recoveries (grey bars, Figure 4.4C and D) likely account for biomass growth and fractions of the acetate and *n*-butyrate that could have passed the membrane to the anode compartment. Additionally, methane production below the detection limit of the gas chromatograph (2500 ppm) could have occurred since no chemical inhibitor was added to the catholyte medium. The productivity in both the TMM- and TMM+ pre-treatment experiments shows that the pre-treatments were suitable for successful start-up of bio-electrochemical CO₂ reduction. However, the cumulative electron recoveries of acetate and *n*-butyrate never exceeded 40% (Figure 4.4C and D), so the efficiency of electron transfer into carbon products can be improved.

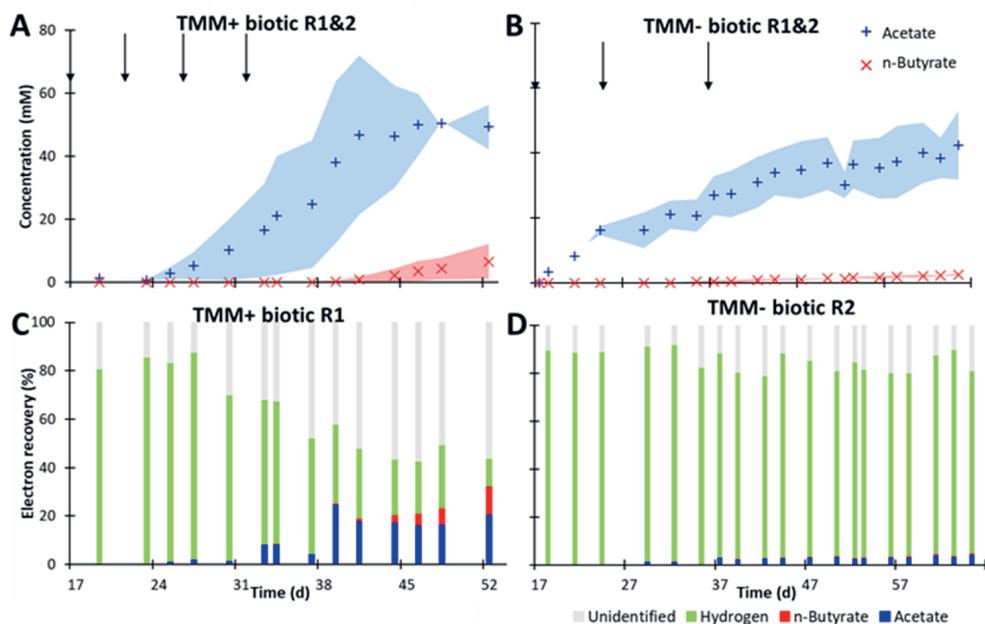
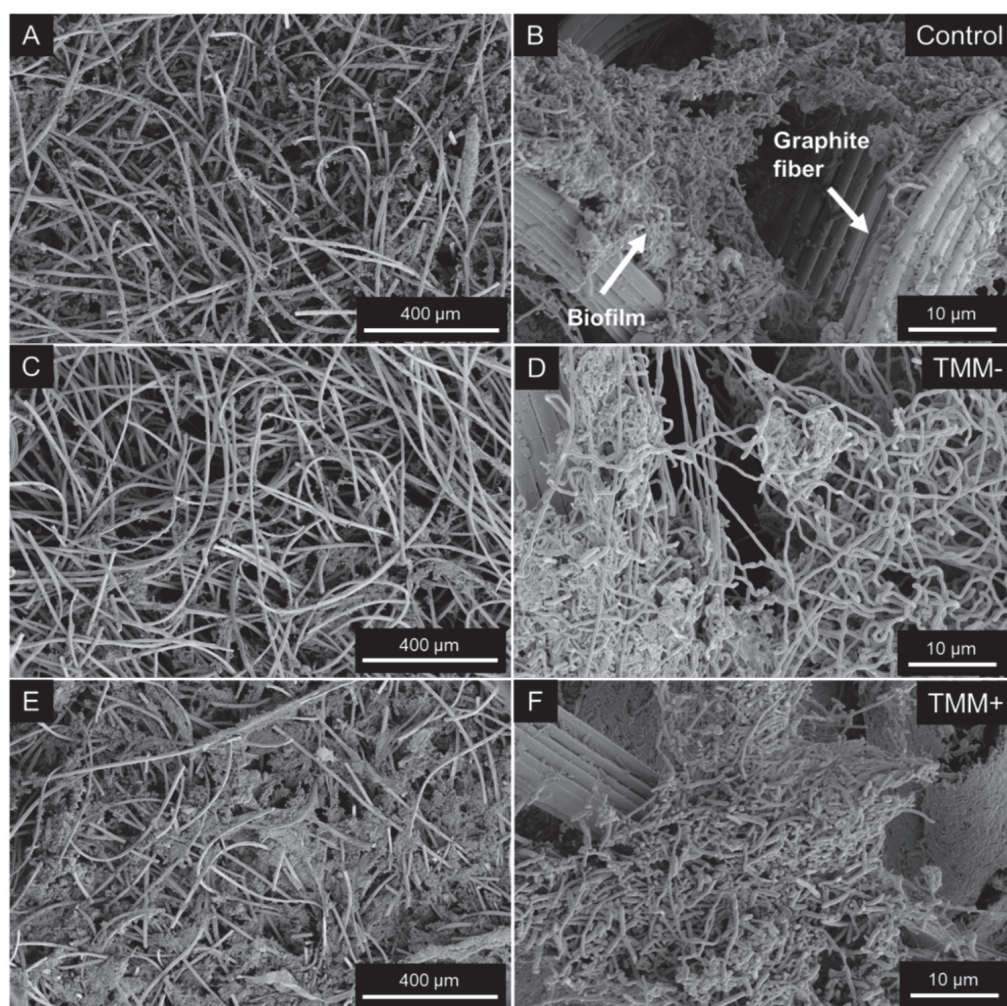


Figure 4.4. Production of volatile fatty acids and hydrogen over time during the biotic phase in the experiments pre-treated with trace metal mix with (TMM+: A and C) and without EDTA (TMM-: B and D) shown as catholyte bulk concentrations (A and B) and as a fraction of the measured cathode current (C and D). A and B show averages between duplicate experiments (R1&2) with the difference between duplicates indicated as blue and red areas and inoculation indicated with black arrows, while C and D only show one of the duplicate reactors (C: TMM+ R1, D: TMM- R2), the other duplicates are shown in SI Figure S4.3.

4.3.4 Microbial growth during the biotic phase of the process

The microbial growth both in the liquid phase and on the cathode surface, were monitored via OD₆₀₀ measurement and scanning electron microscopy (SEM) analysis, respectively. The optical density values remained quite low (<0.05 OD₆₀₀) throughout the biotic experiment phases (SI Figure S4.4) compared to other studies without a TMM pre-treatment^{19,22}. In the control reactor, the optical density values reached up to 0.06, showing slightly higher concentrations of suspended microorganisms (SI Figure S4.4). The low concentration of bacteria in the liquid phase of the pre-treated experiments, connected with the microbial activity observed through the volatile fatty acid production (Figure 4.4), indicated that after pre-treatment, the microbial growth would mainly be in the aggregated form at the cathode⁷. The SEM analysis carried out on cathodes samples taken at the end of the biotic phase (day 36 for TMM+ and day 50 for TMM-) showed indeed formation of complex biofilms with different shapes of cells and extracellular polymeric substances (EPS) between different experiments (Figure 4.5).

Within the control experiment, without trace metal mix pre-treatment, biofilm growth on the cathode was observed (Figure 4.5A and B), and the coverage of the graphite fibres was similar as the one visualized within the experiment with cathodes pre-treated with TMM- (Figure 4.5C and D). However, the biofilm cells' morphology was different. Long filamentous cells growing within the TMM- experiment (Figure 4.5D), and less EPS rich clusters in comparison to the control experiment (Figure 4.5B and D). In contrast, the biofilm coverage of the cathode surface in the TMM+ pre-treated experiment (Figure 4.5E and F) was significantly higher than observed in the control and TMM- experiments, corresponding to the higher productivity observed in the TMM+ experiments (Figure 4.4). Also in this case, the cells' morphology observed within the cathode biofilm was different than in the TMM- experiments, with different shapes of cells grouped in tight, EPS-rich clusters (Figure 4.5F).



4

Figure 4.5. Scanning electron microscopy (SEM) images with two different magnifications of cathode samples taken from the control experiments (A and B), the experiments with cathodes pre-treated with trace metal mix without (TMM-, C and D) and with EDTA (TMM +, E and F). In A, C and E, the biofilm coverage of the cathode is showed. Appearance of a graphite fibre of the carbon felt cathode and the biofilm growing on top are indicated in B. Pictures from duplicate cathodes are shown in SI Figure S4.5-S4.7.

4.3.5 Microbial community composition and observation via NGS and FISH

The microbial community composition of the biofilms and liquid samples taken at the end of the process was investigated via next generation sequencing (NGS) of 16S rRNA gene. In all the samples analysed, four main microbial groups were dominant, affiliated to the genera BRH-c20a (phylum *Firmicutes*), *Clostridium sensu stricto* 12, *Bacteroides* and *Methanobacterium* (Table 4.4).

Table 4.4. Relative abundances of core operational taxonomic units (OTUs) and their taxonomy classification at the identified level. The 16S rRNA gene analysis by means of Next Generation Sequencing (NGS) was carried out on samples from the cathode biofilm and the liquid catholyte sampled from the two replicate reactors (R1 and R2) for both TMM+ and TMM- experiments at the end of the operation of each reactor. All OTUs <3% are summed together and presented as “Other”.

Affiliation	TMM+				TMM-			
	R1		R2		R1		R2	
	Biofilm	Liquid catholyte	Biofilm	Liquid catholyte	Biofilm	Liquid catholyte	Biofilm	Liquid catholyte
<i>Firmicutes</i> BRH-c20a	51.7	40.4	61.3	30.6	62.2	46.1	53.1	44.9
<i>Clostridium sensu stricto</i> 12	15.9	4.4	9.3	2.9	15.2	6.2	17	5.5
<i>Methanobacterium</i>	11.6	5.2	9.8	10.3	1.6	2.1	4.4	1.5
<i>Bacteroides</i>	4.8	13.2	3.4	16	3.2	9.8	5.3	12
<i>Wolinella</i>	2	5.5	0.1	0.3	0.2	1.3	0.2	0.6
<i>Pseudomonas</i>	2	7.8	1	9.1	0.5	1.8	0.1	0.5
<i>Methanobrevibacter</i>	1.8	5.5	1.9	4.3	1.8	5.2	3.3	3.3
<i>Rikenellaceae</i> RC9 gut group	1.3	1.4	1.4	0.3	0	0	0.2	0
<i>Oscillibacter</i>	0.5	1.5	0.9	2.4	0.4	0.6	0.7	0.5
<i>Erysipelatoclostridium</i>	0.5	0.4	0.1	0	6.1	0.1	2.4	0.4
<i>Telmatospirillum</i>	0.3	1.1	0.2	1	2.3	7.6	1.3	4.1
<i>Saccharimonadales</i>	0.2	0.8	0.4	1.2	0.2	2.5	0.4	6.1
<i>Streptomyces</i>	0.2	0.4	0.5	4.6	0.8	5.8	0.6	4.8
Other (< 3%)	6.6	11.6	9.4	16.2	5.3	10.5	10.6	15.3

Members of BRH-c20a (phylum *Firmicutes*) were the dominant group in the biofilms, irrespective of the EDTA addition (Table 4.4). Even if this genus includes just uncultured representatives (according to Silva database ssu r138.1), its members were previously detected in microbial electrochemical systems⁵⁴⁻⁵⁷. In particular, BRH-c20a was identified as a key player in electrochemical CO₂ reduction to acetate, with the electrode as the sole electron donor, while it was not detected when the same inoculum was fed with ethanol as electron donor⁵⁶. BRH-c20a were the dominant bacteria (relative abundance between 48% and 80%) associated with slurry-electrode MES producing acetate from H₂/CO₂ in presence of metal nanoparticles⁵⁵. The high BRH-c20a abundance in presence of metal particles matches with the current study and suggests tolerance for or even use of metal particles as e.g. electron shuttle. Thus, BRH-c20a is likely involved in CO₂ fixation and positively related acetate production⁵⁵, as also highlighted by the results obtained in our process (Figure 4.4).

The genus *Clostridium sensu stricto* 12 was the second dominant group in the biofilm grown in TMM+ experiments, while their relative abundance was relatively lower in the TMM- experiments (Table 4.4). Members of the genus *Clostridium* are the most commonly detected as biocatalysts in BES that can utilize CO₂ as substrate producing acetate⁵⁸⁻⁶⁰. Within BES, further elongation of acetate to MCFA is possible thanks to other ssp. of *Clostridium*, such as *Clostridium kluyveri*, which grows on acetate and ethanol via reverse- β -oxidation, producing chain elongated acids like butyrate and caproate⁶¹. *Clostridium* type strains classified under the genus *Clostridium sensu stricto* 12 and reported to catalyse CO₂ fixation and/or produce medium chain fatty acids are *C. kluyveri*⁶¹, *C. ljungdahlii*⁶², *C. autoethanogenum*⁵⁸, *C. carboxidivorans*⁶³, *C. tyrobutyricum*⁶⁴, *C. pasteurianum*⁶⁵ and *C. laticellarii*⁶⁶.

The *Bacteroides* genus was more abundant in the catholyte than in the cathodic biofilm (Table 4.4), and members of this genus were previously detected in different microbial electrosynthesis

systems. Commonly *Bacteroides* are identified in microbial electrosynthesis as exoelectrogenic bacteria degrading complex substrates to produce acetate and propionate⁶⁷⁻⁶⁹, and connected with high current generation via extracellular electron transfer and Fe (III) reduction^{70,71}. In the human gut, *Bacteroides* were associated with conversion of carbohydrates to fatty acids whilst capturing CO₂⁷².

In both cathode biofilm and the liquid catholyte the presence/absence of EDTA in the pre-treatment TMM influenced the microbial community composition (Table 4.4). Focusing on the biofilm, among bacteria, the genus *Erysipelatoclostridium* was identified just without EDTA (Table 4.4, TMM-), with a relative abundance between 2.4 and 6%. While their functional metabolism is still not clear⁷³, members of the family *Erysipelotrichaceae* were identified in the gut microbiota connected to high concentration of toxic metals⁷⁴⁻⁷⁶. The same applies for the genus *Telmatospirillum*, previously detected as active group in hydrogen rich environments⁷⁷. On the contrary, the relative abundance of *Methanobacterium* was lower in both biofilm and liquid samples without EDTA addition (TMM-), indicating that metal chelation is needed for this methanogen to grow and overcome the metal toxicity, which can negatively influence some hydrogenotrophic methanogens^{78,79}. Other bacterial groups developed in the biofilm mostly in presence of EDTA (TMM+) were *Wolinella*, *Pseudomonas*, and *Rikenellaceae* RC9 gut group, all previously detected at biocathodes in different processes⁸⁰⁻⁸².

Observing active microbial groups at the end of the TMM+ experiments by applying FISH, on the basis of the morphology it was evident that the addition of trace metals and EDTA stimulated the development of different bacteria in comparison to the control reactors (Figure 4.6A and B). By applying probe *ClostI* (SI Table S4.1B), covering 88% of the genus *Clostridium* sensu stricto 12 and all the type strains cited above (based on Silva database ssu r138.1), no cells were identified in the control reactor (Figure 4.6A), while they constituted a high portion of the whole active bacterial population within TMM+ experiments biofilm (Figure 4.6C and D, cells in red). Due to their high relative abundance (Table 4.4), we can hypothesize the rest of the active biomass visualized in Figure 4.6B and C by probe EUB338 belongs to *Firmicutes* BRH-c20a.

Within the biofilm, methanogens affiliated to the order *Methanobacteriales* were identified among the active biomass (SI Figure S4.8) and a strict association with members of the bacterial community was highlighted in both control and TMM+ reactors (SI Figure S4.8). Development of methanogens such as *Methanobacterium* and *Methanobrevibacter* was expected, since no 2-bromoethanesulfanoate was added in experiment to optimize the HER catalyst performances, thus it is possible that methane was part of the unidentified products (Figure 4.4C and D), as also highlighted by the methanogens activity (SI Figure S4.8).

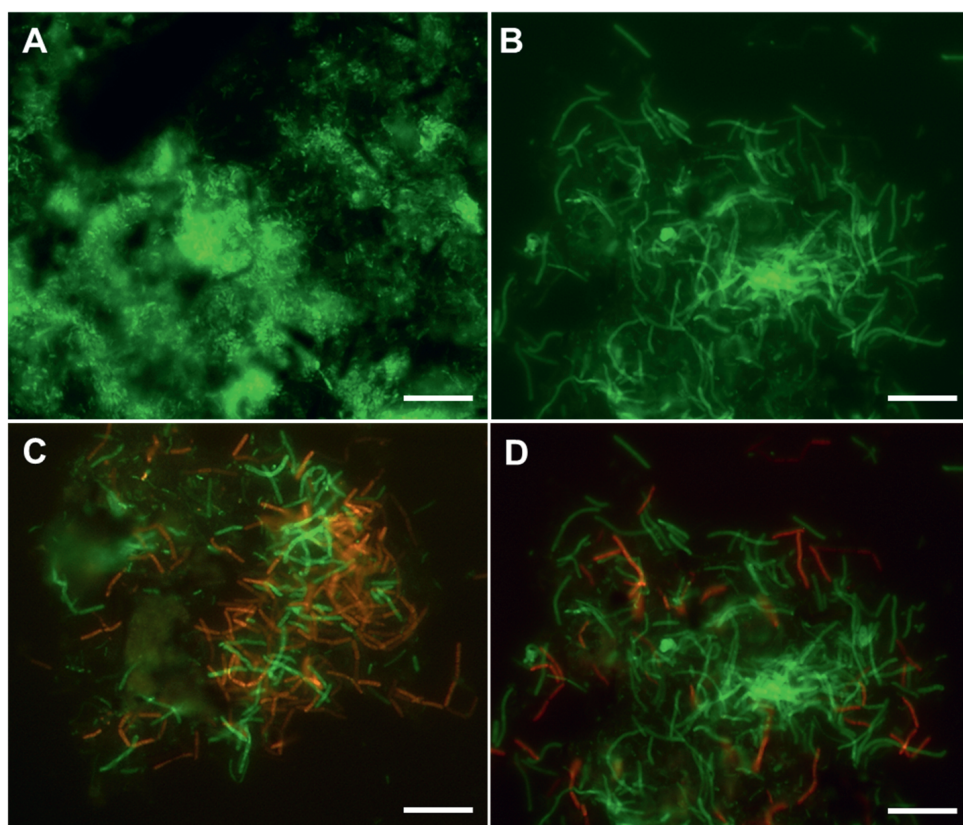


Figure 4.6. Observation of the bacterial community in biofilms grown on cathodes during the control experiment (A) and with trace metal mix with EDTA (TMM+) pre-treatment (B to D) by Fluorescence in situ hybridization (FISH). The probes applied in are EUB338 (Bacteria, in green) in all the samples showed, and ClostI (Clostridiales, in red) in A, C and D. Size bar is 10 μ m.

4.3.6 EDTA detrimental for hydrogen productivity yet beneficial for microbial synthesis

Based on the differences in current, volatile fatty acid production and biomass formation between the experiments with pre-treated cathodes (TMM) and the control experiment, it can be concluded that the incorporation of a trace metal mix based HER catalyst is beneficial for a fast start-up and high productivity of volatile fatty acid production from CO₂. Interestingly, the pre-treatment with either TMM+ and TMM- showed some differences. The hydrogen production was higher in the TMM- experiments, while the volatile fatty acid productivity was lower and also less biofilm formation was observed in the TMM- experiments compared to the TMM+ experiments. Different explanations could be the reason for the observed differences. For example, the conditions at the cathode surface and in the catholyte are likely different. At the cathode, the hydrogen production will cause local high pH and shear stress from the bubble formation^{15,83}, which could have negatively affected the microbial community. Another possibility is a difference in metal toxicity. The ionic form of metals is mostly suggested to be toxic for microorganisms, so the presence of EDTA might lower the toxicity of the trace metals

in the catholyte, as also suggested in literature^{22,24,84}. It is plausible that metal compounds added during the pre-treatment were more toxic for the microorganisms without the presence of the chelating agent EDTA. An interesting approach to elucidate these hypotheses would be to study metal toxicity or utilisation mechanisms in the TMM- experiments.

Overall, a peculiar microbial community with a low number of species (7-8 above 1% relative abundance, Table 4.4) developed on top of the cathode when adding trace metals solution. The proposed mechanistic interactions are summarized in Figure 4.7. Acetate was the main product of CO₂ utilization, likely via BRH-c20a and *Clostridium* group, while low concentrations of butyrate could come either from chain elongation of acetate by *Clostridium* or from fermentation of organics coming from biomass decay by *Bacteroides* (Figure 4.7). Low concentrations of methane were likely formed by *Methanobacterium*, which might be inhibited by the absence of EDTA in the pre-treatment trace metal mix. However, further investigations utilizing additional FISH probes and including the full sequencing of the 16S rRNA gene and the transcriptomic analysis are needed to gain further insights into the metabolism activated with the addition of TMM solution and the generation of a HER catalyst.

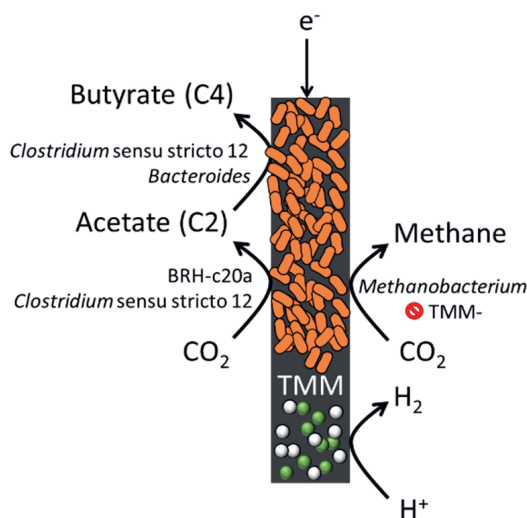


Figure 4.7. Schematic representation of the proposed main microbial protagonists' function within the biofilm developed on the cathode in presence of trace metals (TMM).

4.4 Conclusions

Here, we demonstrated the feasibility of a hydrogen evolution catalyst formed from microbial trace metals integrated in a bio-electrochemical CO₂ reduction system. The metal mix with (TMM+) and without (TMM-) EDTA showed 10 to 40 times elevated current and hydrogen production compared to a non-pre-treated system during microbial electrosynthesis (TMM-: -90 kA/m³ and 14 μM H₂; TMM+: -20 kA/m³ and 4 μM H₂). The high current at the start of the biotic phase allowed for a fast start-up of microbial activity. Twenty days after start-up of the biotic phase, *n*-butyrate was formed, showing the possibility of CO₂ reduction to C₄-compounds in one integrated system. The current density decreased over time (40-50% decrease), this was related to metal element leaching in the TMM+ experiments. Microbial community analysis showed an active biofilm community on the cathode, which metabolic functions likely correspond to CO₂ conversion into acetate and methane and production of butyrate via either fermentation or chain elongation.

References

- 1 Lee, M.-Y. *et al.* Current achievements and the future direction of electrochemical CO₂ reduction: A short review. *Critical Reviews in Environmental Science and Technology* **50**, 769-815 (2020).
- 2 Yuan, M., Kummer, M. J. & Minteer, S. D. Strategies for bio-electrochemical CO₂ reduction. *Chemistry—A European Journal* **25**, 14258-14266 (2019).
- 3 Ammam, F., Tremblay, P.-L., Lizak, D. M. & Zhang, T. Effect of tungstate on acetate and ethanol production by the electrosynthetic bacterium *Sporomusa ovata*. *Biotechnology for biofuels* **9**, 163 (2016).
- 4 Cheng, S., Xing, D., Call, D. F. & Logan, B. E. Direct biological conversion of electrical current into methane by electromethanogenesis. *Environmental science & technology* **43**, 3953-3958 (2009).
- 5 Cai, R. *et al.* Electroenzymatic C–C bond formation from CO₂. *Journal of the American Chemical Society* **140**, 5041-5044 (2018).
- 6 Arends, J. B. A., Patil, S. A., Roume, H. & Rabaey, K. Continuous long-term electricity-driven bioproduction of carboxylates and isopropanol from CO₂ with a mixed microbial community. *Journal of CO₂ Utilization* **20**, 141-149, doi:10.1016/j.jcou.2017.04.014 (2017).
- 7 Jourdin, L., Raes, S. M. T., Buisman, C. J. N. & Strik, D. P. B. T. B. Critical Biofilm Growth throughout Unmodified Carbon Felts Allows Continuous Bio-electrochemical Chain Elongation from CO₂ up to Caproate at High Current Density. *Frontiers in Energy Research* **6**, doi:10.3389/fenrg.2018.00007 (2018).
- 8 Batlle-Vilanova, P. *et al.* Microbial electrosynthesis of butyrate from carbon dioxide: production and extraction. *Bioelectrochemistry* **117**, 57-64 (2017).
- 9 Bajracharya, S. *et al.* Carbon dioxide reduction by mixed and pure cultures in microbial electrosynthesis using an assembly of graphite felt and stainless steel as a cathode. *Bioresour Technol* **195**, 14-24, doi:10.1016/j.biortech.2015.05.081 (2015).
- 10 Witholt, B. & Kessler, B. Perspectives of medium chain length poly (hydroxyalkanoates), a versatile set of bacterial bioplastics. *Current opinion in biotechnology* **10**, 279-285 (1999).
- 11 Bajracharya, S. *et al.* Biotransformation of carbon dioxide in bio-electrochemical systems: state of the art and future prospects. *Journal of Power Sources* **356**, 256-273 (2017).
- 12 Levy, P., Sanderson, J., Kispert, R. & Wise, D. Biorefining of biomass to liquid fuels and organic chemicals. *Enzyme and Microbial Technology* **3**, 207-215 (1981).
- 13 Spirito, C. M., Richter, H., Rabaey, K., Stams, A. J. & Angenent, L. T. Chain elongation in anaerobic reactor microbiomes to recover resources from waste. *Current opinion in biotechnology* **27**, 115-122 (2014).
- 14 Jourdin, L. *et al.* High Acetic Acid Production Rate Obtained by Microbial Electrosynthesis from Carbon Dioxide. *Environ Sci Technol* **49**, 13566-13574, doi:10.1021/acs.est.5b03821 (2015).
- 15 Blanchet, E. *et al.* Importance of the hydrogen route in up-scaling electrosynthesis for microbial CO₂ reduction. *Energy & Environmental Science* **8**, 3731-3744 (2015).
- 16 Zhou, Z. *et al.* Electrocatalytic hydrogen evolution under neutral pH conditions: current understandings, recent advances, and future prospects. *Energy & Environmental Science* **13**, 3185-3206, doi:10.1039/d0ee01856b (2020).
- 17 Flexer, V. & Jourdin, L. Purposely Designed Hierarchical Porous Electrodes for High Rate Microbial Electrosynthesis of Acetate from Carbon Dioxide. *Acc Chem Res* **53**, 311-321, doi:10.1021/acs.accounts.9b00523 (2020).
- 18 Liu, C., Colón, B. C., Ziesack, M., Silver, P. A. & Nocera, D. G. Water splitting–biosynthetic system with CO₂ reduction efficiencies exceeding photosynthesis. *Science* **352**, 1210-1213 (2016).
- 19 Kracke, F. *et al.* Robust and biocompatible catalysts for efficient hydrogen-driven microbial electrosynthesis. *Commun. Chem.* **2**, 45 (2019).
- 20 Wang, G., Huang, Q., Song, T.-s. & Xie, J. Enhancing microbial electrosynthesis of acetate and butyrate from CO₂ reduction involving engineered *Clostridium ljungdahlii* with a nickel-phosphide-modified electrode. *Energy & Fuels* **34**, 8666-8675 (2020).
- 21 Tian, S. *et al.* Mo₂C-induced hydrogen production enhances microbial electrosynthesis of acetate from CO₂ reduction. *Biotechnology for biofuels* **12**, 1-12 (2019).
- 22 Chatzipanagiotou, K.-R., Jourdin, L., Bitter, J. H. & Strik, D. P. Concentration-dependent effects of nickel doping on activated carbon biocathodes. *Catalysis Science & Technology* **12**, 2500-2518 (2022).

- 23 Zhang, S. *et al.* A review of microbial electrosynthesis applied to carbon dioxide capture and conversion: The basic principles, electrode materials, and bioproducts. *Journal of CO₂ Utilization* **51**, 101640 (2021).
- 24 Gadd, G. M. & Griffiths, A. J. Microorganisms and heavy metal toxicity. *Microbial ecology* **4**, 303-317 (1977).
- 25 Wingender, J., Neu, T. R. & Flemming, H.-C. in *Microbial extracellular polymeric substances* 1-19 (Springer, 1999).
- 26 Ragsdale, S. W. & Pierce, E. Acetogenesis and the Wood–Ljungdahl pathway of CO₂ fixation. *Biochimica et Biophysica Acta (BBA)-Proteins and Proteomics* **1784**, 1873-1898 (2008).
- 27 Kracke, F., Vassilev, I. & Krömer, J. O. Microbial electron transport and energy conservation—the foundation for optimizing bio-electrochemical systems. *Frontiers in microbiology* **6**, 575 (2015).
- 28 Irving, H. & Williams, R. Order of stability of metal complexes. *Nature* **162**, 746-747 (1948).
- 29 Waldron, K. J., Rutherford, J. C., Ford, D. & Robinson, N. J. Metalloproteins and metal sensing. *Nature* **460**, 823-830 (2009).
- 30 de Smit, S. M., Buisman, C. J., Bitter, J. H. & Strik, D. P. Cyclic Voltammetry is invasive on microbial electrosynthesis. *ChemElectroChem* **8**, 3384-3396 (2021).
- 31 Oudar, J. Sulfur adsorption and poisoning of metallic catalysts. *Catalysis Reviews—Science and Engineering* **22**, 171-195 (1980).
- 32 Sander, R. Compilation of Henry's law constants (version 4.0) for water as solvent. *Atmos. Chem. Phys.* **15**, 4399-4981 (2015).
- 33 Bolyen, E. *et al.* Reproducible, interactive, scalable and extensible microbiome data science using QIIME 2. *Nature biotechnology* **37**, 852-857 (2019).
- 34 Klindworth, A. *et al.* Evaluation of general 16S ribosomal RNA gene PCR primers for classical and next-generation sequencing-based diversity studies. *Nucleic acids research* **41**, e1-e1 (2013).
- 35 Callahan, B. J. *et al.* DADA2: High-resolution sample inference from Illumina amplicon data. *Nature methods* **13**, 581-583 (2016).
- 36 Quast, C. *et al.* The SILVA ribosomal RNA gene database project: improved data processing and web-based tools. *Nucleic acids research* **41**, D590-596, doi:10.1093/nar/gks1219 (2013).
- 37 Hugenholtz, P., Tyson, G. W. & Blackall, L. L. in *Gene probes* 29-42 (Springer, 2002).
- 38 Greuter, D., Loy, A., Horn, M. & Rattei, T. probeBase—an online resource for rRNA-targeted oligonucleotide probes and primers: new features 2016. *Nucleic acids research* **44**, D586-D589 (2016).
- 39 Wiesenburg, D. A. & Guinasso Jr, N. L. Equilibrium solubilities of methane, carbon monoxide, and hydrogen in water and sea water. *Journal of chemical and engineering data* **24**, 356-360 (1979).
- 40 Izadi, P., Fontmorin, J.-M., Godain, A., Yu, E. H. & Head, I. M. Parameters influencing the development of highly conductive and efficient biofilm during microbial electrosynthesis: the importance of applied potential and inorganic carbon source. *npj Biofilms and Microbiomes* **6**, 1-15 (2020).
- 41 Hamelers, H. V. *et al.* New applications and performance of bio-electrochemical systems. *Appl Microbiol Biotechnol* **85**, 1673-1685, doi:10.1007/s00253-009-2357-1 (2010).
- 42 Jourdin, L., Sousa, J., Stralen, N. v. & Strik, D. P. B. T. B. Techno-economic assessment of microbial electrosynthesis from CO₂ and/or organics: An interdisciplinary roadmap towards future research and application. *Applied Energy* **279**, doi:10.1016/j.apenergy.2020.115775 (2020).
- 43 Lange, J. P. Renewable feedstocks: the problem of catalyst deactivation and its mitigation. *Angewandte Chemie International Edition* **54**, 13186-13197 (2015).
- 44 Dong, L., Wang, P. & Yu, H. EDTA-assisted synthesis of amorphous BiSx nanodots for improving photocatalytic hydrogen-evolution rate of TiO₂. *Journal of Alloys and Compounds* **887**, 161425 (2021).
- 45 Deng, Y. *et al.* EDTA-assisted hydrothermal synthesis of flower-like CoSe₂ nanorods as an efficient electrocatalyst for the hydrogen evolution reaction. *Journal of Energy Chemistry* **28**, 95-100 (2019).
- 46 Yu, X., Yang, J., Ren, X. & Sui, Z. Influences of pH and EDTA Additive on the Structure of Ni Films Electrodeposited by Using Bubble Templates as Electrocatalysts for Hydrogen Evolution Reaction. *Membranes* **11**, 165 (2021).
- 47 Hammond, C. Intensification studies of heterogeneous catalysts: probing and overcoming catalyst deactivation during liquid phase operation. *Green Chemistry* **19**, 2711-2728 (2017).

- 48 De Lichtervelde, A., Ter Heijne, A., Hamelers, H., Biesheuvel, P. & Dykstra, J. Theory of ion and electron transport coupled with biochemical conversions in an electroactive biofilm. *Phys. Rev. Appl.* **12**, 014018 (2019).
- 49 Yuan, H., Hou, Y., Abu-Reesh, I. M., Chen, J. & He, Z. Oxygen reduction reaction catalysts used in microbial fuel cells for energy-efficient wastewater treatment: a review. *Materials Horizons* **3**, 382-401 (2016).
- 50 Jourdin, L., Lu, Y., Flexer, V., Keller, J. & Freguia, S. Biologically induced hydrogen production drives high rate/high efficiency microbial electrosynthesis of acetate from carbon dioxide. *ChemElectroChem* **3**, 581-591 (2016).
- 51 Perona-Vico, E., Feliu-Paradedá, L., Puig, S. & Bañeras, L. Bacteria coated cathodes as an in-situ hydrogen evolving platform for microbial electrosynthesis. *Scientific reports* **10**, 1-11 (2020).
- 52 Marshall, C. W., Ross, D. E., Fichot, E. B., Norman, R. S. & May, H. D. Long-term operation of microbial electrosynthesis systems improves acetate production by autotrophic microbiomes. *Environmental science & technology* **47**, 6023-6029 (2013).
- 53 Twigg, M. V. & Spencer, M. S. Deactivation of supported copper metal catalysts for hydrogenation reactions. *Applied Catalysis A: General* **212**, 161-174 (2001).
- 54 Isipato, M. *et al.* Propionate Production by Bio-electrochemically-Assisted Lactate Fermentation and Simultaneous CO₂ Recycling. *Frontiers in microbiology* **11**, 599438 (2020).
- 55 Gao, Y. *et al.* Metal nanoparticles increased the lag period and shaped the microbial community in slurry-electrode microbial electrosynthesis. *Science of The Total Environment*, 156008 (2022).
- 56 Jiang, Y., Chu, N., Qian, D.-K. & Zeng, R. J. Microbial electrochemical stimulation of caproate production from ethanol and carbon dioxide. *Bioresource Technology* **295**, 122266 (2020).
- 57 Chu, N. *et al.* Waste C₁ gases as alternatives to pure CO₂ improved the microbial electrosynthesis of C₄ and C₆ carboxylates. *ACS Sustainable Chemistry & Engineering* **8**, 8773-8782 (2020).
- 58 Heffernan, J. K. *et al.* Enhancing CO₂-valorization using *Clostridium autoethanogenum* for sustainable fuel and chemicals production. *Frontiers in bioengineering and biotechnology* **8**, 204 (2020).
- 59 Jeon, B. Y., Jung, I. L. & Park, D. H. Conversion of carbon dioxide to metabolites by *Clostridium acetobutylicum* KCTC1037 cultivated with electrochemical reducing power. *Advances in Microbiology* **2**, 332 (2012).
- 60 Im, C., Valgepea, K., Modin, O. & Nygård, Y. *Clostridium ljungdahlii* as a biocatalyst in microbial electrosynthesis—Effect of culture conditions on product formation. *Bioresource Technology Reports* **19**, 101156 (2022).
- 61 Reddy, M. V., Mohan, S. V. & Chang, Y.-C. Medium-Chain Fatty Acids (MCFA) Production Through Anaerobic Fermentation Using *Clostridium kluyveri*: Effect of Ethanol and Acetate. *Applied Biochemistry and biotechnology*, 1-12 (2017).
- 62 Köpke, M. *et al.* *Clostridium ljungdahlii* represents a microbial production platform based on syngas. *Proceedings of the National Academy of Sciences* **107**, 13087-13092 (2010).
- 63 Shen, Y., Brown, R. & Wen, Z. Syngas fermentation of *Clostridium carboxidivoran* P7 in a hollow fiber membrane biofilm reactor: Evaluating the mass transfer coefficient and ethanol production performance. *Biochemical engineering journal* **85**, 21-29 (2014).
- 64 Zhu, Y. & Yang, S. T. Adaptation of *Clostridiumtyrobutyricum* for Enhanced Tolerance to Butyric Acid in a Fibrous-Bed Bioreactor. *Biotechnology Progress* **19**, 365-372 (2003).
- 65 Atasoy, M. & Cetecioglu, Z. Butyric acid dominant volatile fatty acids production: bio-augmentation of mixed culture fermentation by *Clostridium butyricum*. *Journal of Environmental Chemical Engineering* **8**, 104496 (2020).
- 66 Wang, Q. *et al.* *Clostridium luticellarii* sp. nov., isolated from a mud cellar used for producing strong aromatic liquors. *Int J Syst Evol Microbiol* **65**, 4730-4733, doi:10.1099/ijsem.0.000641 (2015).
- 67 Adamberg, S. *et al.* Degradation of fructans and production of propionic acid by *Bacteroides thetaiotaomicron* are enhanced by the shortage of amino acids. *Frontiers in nutrition* **1**, 21 (2014).
- 68 Albarracín-Arias, J. A., Yu, C.-P., Maeda, T., Quintero, W. V. & Sánchez-Torres, V. Microbial community dynamics and electricity generation in MFCs inoculated with POME sludges and pure electrogenic culture. *International Journal of Hydrogen Energy* **46**, 36903-36916 (2021).
- 69 Park, T.-J. *et al.* Microbial community in microbial fuel cell (MFC) medium and effluent enriched with purple photosynthetic bacterium (*Rhodospseudomonas* sp.). *Amb Express* **4**, 1-8 (2014).

- 70 Ha, P. T., Lee, T. K., Rittmann, B. E., Park, J. & Chang, I. S. Treatment of alcohol distillery wastewater using a Bacteroidetes-dominant thermophilic microbial fuel cell. *Environmental science & technology* **46**, 3022-3030 (2012).
- 71 Xiao, Y. *et al.* Pyrosequencing reveals a core community of anodic bacterial biofilms in bio-electrochemical systems from China. *Frontiers in microbiology* **6**, 1410 (2015).
- 72 Fischbach, M. A. & Sonnenburg, J. L. Eating for two: how metabolism establishes interspecies interactions in the gut. *Cell host & microbe* **10**, 336-347 (2011).
- 73 Wu, J. *et al.* Isolation and genomic characterization of five novel strains of Erysipelotrichaceae from commercial pigs. *BMC microbiology* **21**, 1-12 (2021).
- 74 Shao, M. & Zhu, Y. Long-term metal exposure changes gut microbiota of residents surrounding a mining and smelting area. *Scientific reports* **10**, 1-9 (2020).
- 75 Breton, J. *et al.* Ecotoxicology inside the gut: impact of heavy metals on the mouse microbiome. *BMC Pharmacology and Toxicology* **14**, 1-11 (2013).
- 76 Richardson, J. B. *et al.* Exposure to toxic metals triggers unique responses from the rat gut microbiota. *Scientific reports* **8**, 1-12 (2018).
- 77 Esquivel-Elizondo, S., Delgado, A. G. & Krajmalnik-Brown, R. Evolution of microbial communities growing with carbon monoxide, hydrogen, and carbon dioxide. *FEMS microbiology ecology* **93** (2017).
- 78 Jarrell, K. F., Saulnier, M. & Ley, A. Inhibition of methanogenesis in pure cultures by ammonia, fatty acids, and heavy metals, and protection against heavy metal toxicity by sewage sludge. *Canadian journal of microbiology* **33**, 551-554 (1987).
- 79 Sanchez, J., Valle, L., Rodriguez, F., Morínigo, M. & Borrego, J. Inhibition of methanogenesis by several heavy metals using pure cultures. *Letters in applied microbiology* **23**, 439-444 (1996).
- 80 Rabaey, K., Boon, N., Siciliano, S. D., Verhaege, M. & Verstraete, W. Biofuel cells select for microbial consortia that self-mediate electron transfer. *Appl. Environ. Microbiol.* **70**, 5373-5382 (2004).
- 81 Kugarajah, V., Solomon, J., Rajendran, K. & Dharmalingam, S. Enhancement of nitrate removal and electricity generation in microbial fuel cell using eggshell supported biocathode. *Process Biochemistry* **113**, 1-10 (2022).
- 82 Santoro, C. *et al.* How Comparable are Microbial Electrochemical Systems around the Globe? An Electrochemical and Microbiological Cross-Laboratory Study. *ChemSusChem* **14**, 2313-2330 (2021).
- 83 LaBelle, E. V. & May, H. D. Energy Efficiency and Productivity Enhancement of Microbial Electrosynthesis of Acetate. *Frontiers in microbiology* **8**, 756, doi:10.3389/fmicb.2017.00756 (2017).
- 84 Chatzipanagiotou, K. R., Jourdin, L., Buisman, C. J. N., Strik, D. P. B. T. B. & Bitter, J. H. CO₂ Conversion by Combining a Copper Electrocatalyst and Wild-type Microorganisms. *ChemCatChem* **12**, 3900-3912, doi:10.1002/cctc.202000678 (2020).

Supporting Information

Table S4.1. (A) 16S primer sequences carrying tails corresponding to the Illumina Nextera adapter sequences (underlined) as described in the Illumina sequencing guidelines; (B) Oligonucleotide probe sequences, target microbial groups and stringency conditions used in this study.

(A) PCR primers				
Primer name		Primer sequence (5'-3') with Nextera adapter*		Reference
S-D-Bact-0341-b-S-17-N		<u>TCGTCGGCAGCGTCAGATGTGTATAAGAG</u> <u>ACAGCCTACGGGNGGCWGCAG</u>		Clindworth et al., 2013
S-D-Bact-0785-a-A-21-N		<u>GTCTGTGGGCTCGGAGATGTGTATAAGAG</u> <u>ACAGGACTACHVGGGTATCTAATCC</u>		Clindworth et al., 2013
(B) FISH probes				
Name	Target Group	Probe sequence (5'-3')	Formamide (%)	Reference
ARC 915	Archaea	GTGCTCCCCGCCAATTCCT	20 or 35	Stahland Amann, 1991
EUB 338-I	Bacteria	GCTGCCTCCCGTAGGAGT	20 or 35	Amann et al., 1990
Clost I	Clostridiaceae	TTCTTCCTAATCTCTACGCA	20-30	Küsel et al., 1999
MB 311	Methanobacteriales	ACCTTGCTCTCAGGTTCCATC TCC	30	Crocetti et al., 2006

* Full guidelines for primers preparation at https://www.illumina.com/content/dam/illumina-support/documents/documentation/chemistry_documentation/16s/16s-metagenomic-library-prep-guide-15044223-b.pdf

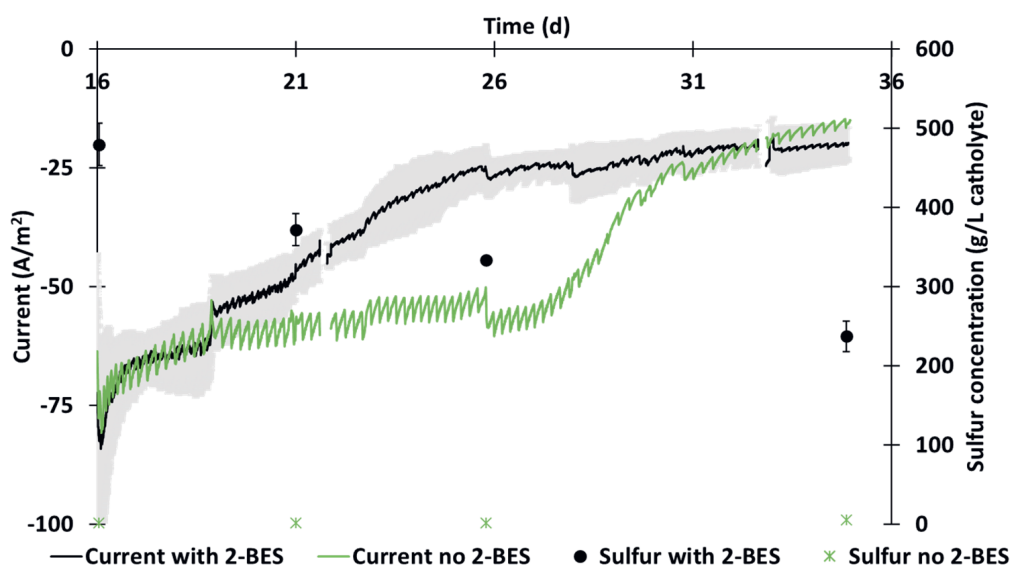


Figure S4.1. Current (line graphs) decreases faster over time in catholyte with 2-bromoethanesulfonic acid compared to without. Decrease of sulphur compounds from the catholyte indicates deposition on the cathode and thus possible catalyst poisoning.

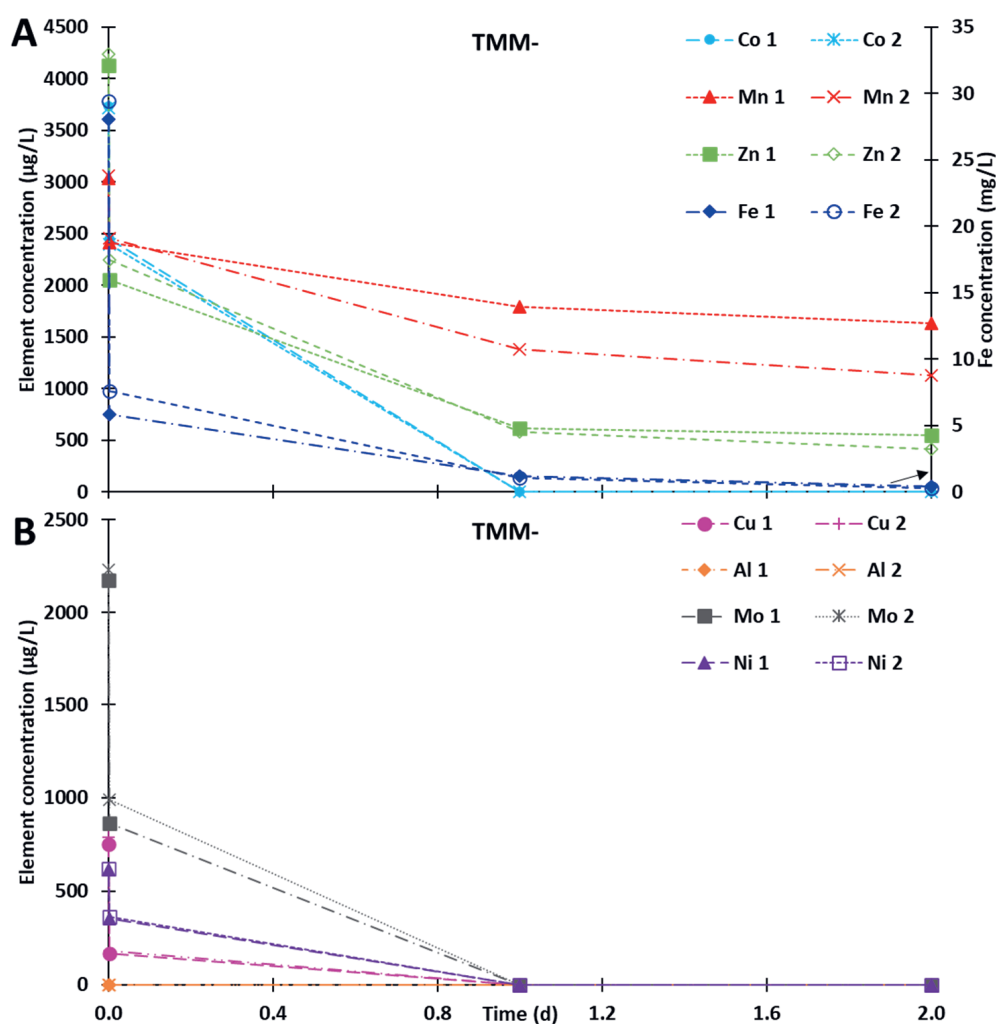


Figure S4.2. Element concentrations in the catholyte over time during the metal phase of duplicate experiments pre-treated with the metal mix without EDTA.

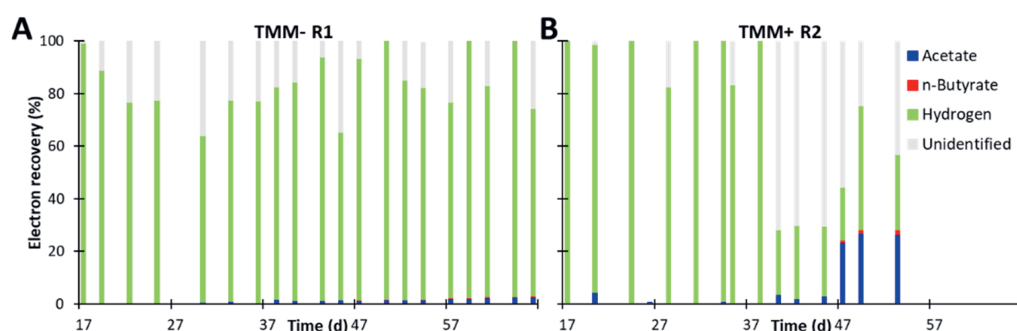


Figure S4.3. Electron recovery of hydrogen, acetate and n-butyrate during the biotic phase of the duplicate experiments pre-treated with the metal mix without (TMM-) and with EDTA (TMM+).

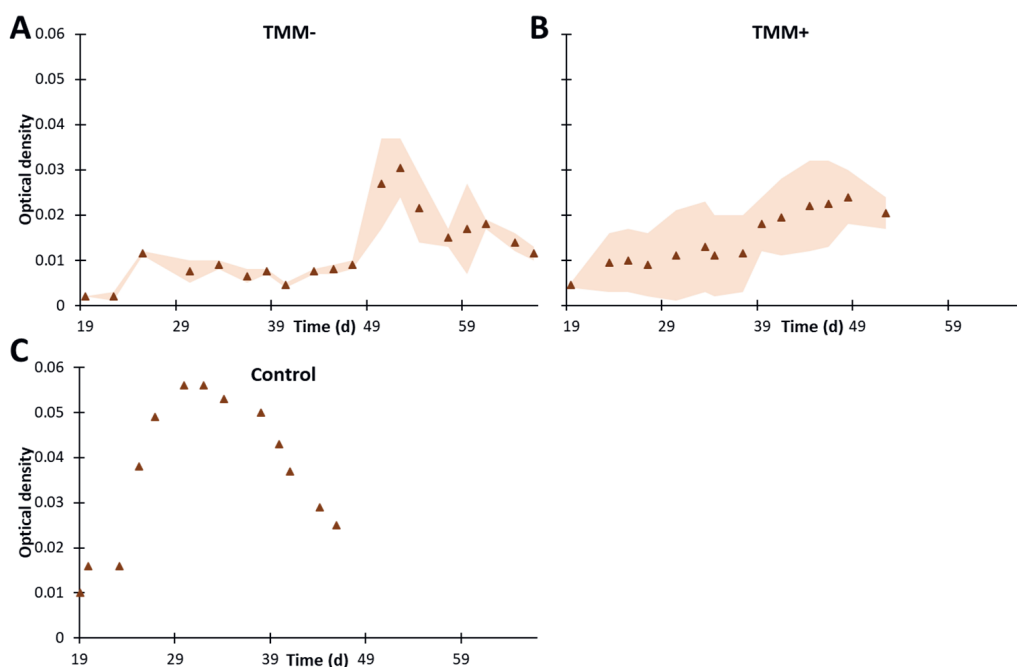


Figure S4.4. Optical density values measured at 600 nm in the catholyte of the duplicate experiments with cathodes pre-treated with the metal mix without (A: TMM-) and with EDTA (B: TMM+) and the not pre-treated control experiment (C).

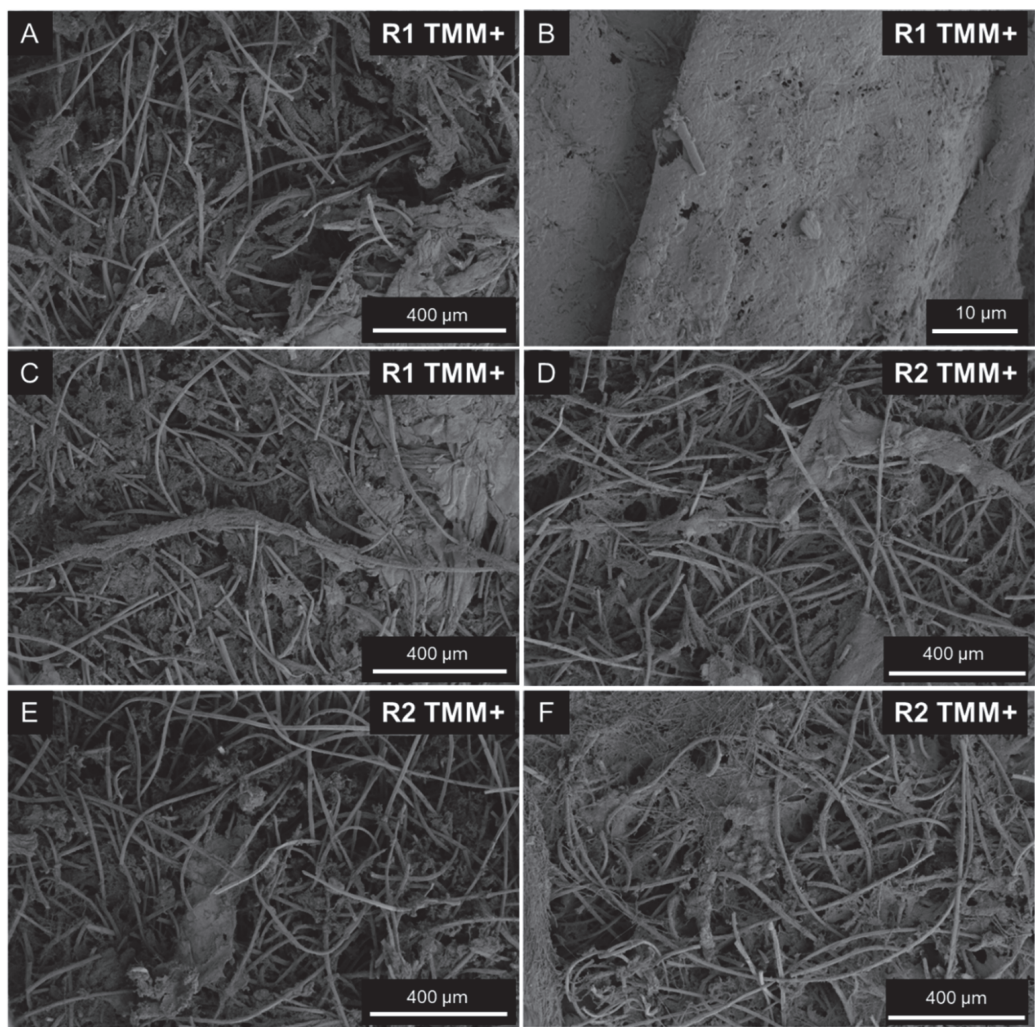


Figure S4.5. Scanning Electron Microscopy pictures of biofilm structures found on cathodes from reactors at the end of the experiments with TMM+. The reactors were sampled after 36 days of biotic operation.

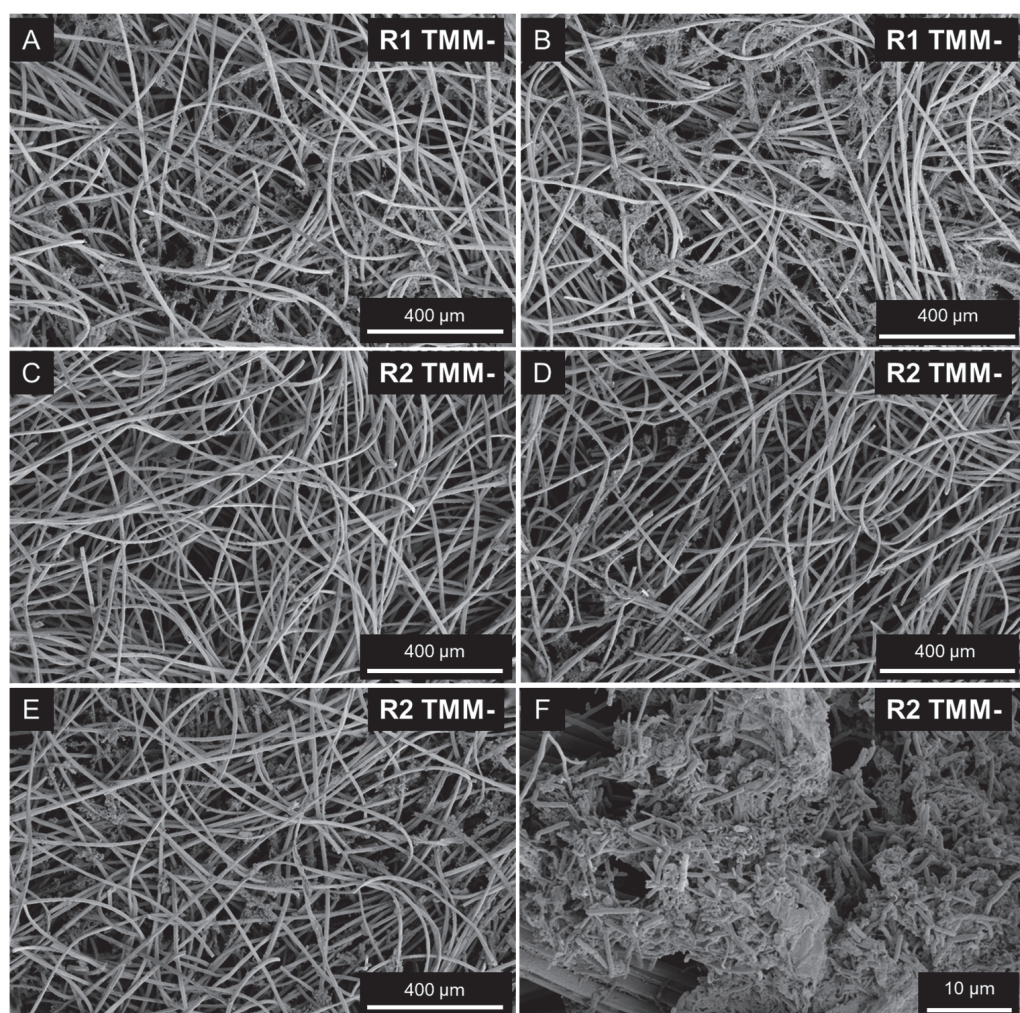


Figure S4.6. Scanning Electron Microscopy pictures of biofilm structures found on cathodes from reactors at the end of the experiments with TMM-. The reactors were sampled after 50 days of biotic operation.

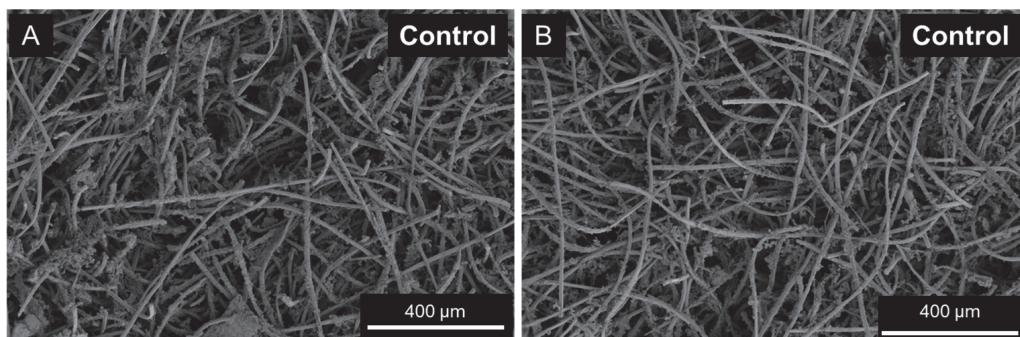


Figure S4.7. Scanning Electron Microscopy pictures of biofilm structures found on cathodes from reactors at the end of the Control experiment without HER catalyst. The reactors were sampled after 29 days of biotic operation.

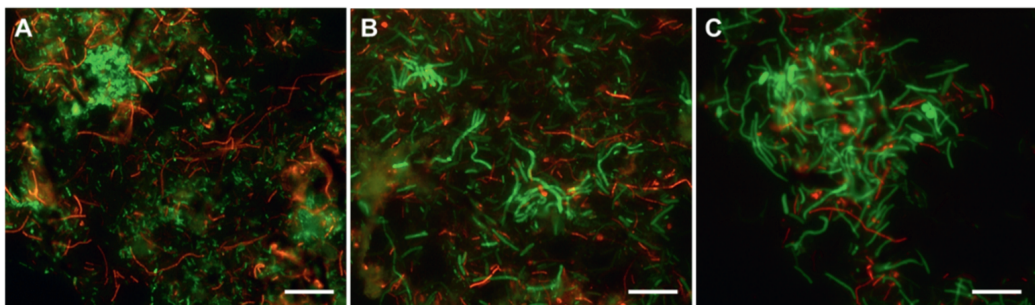
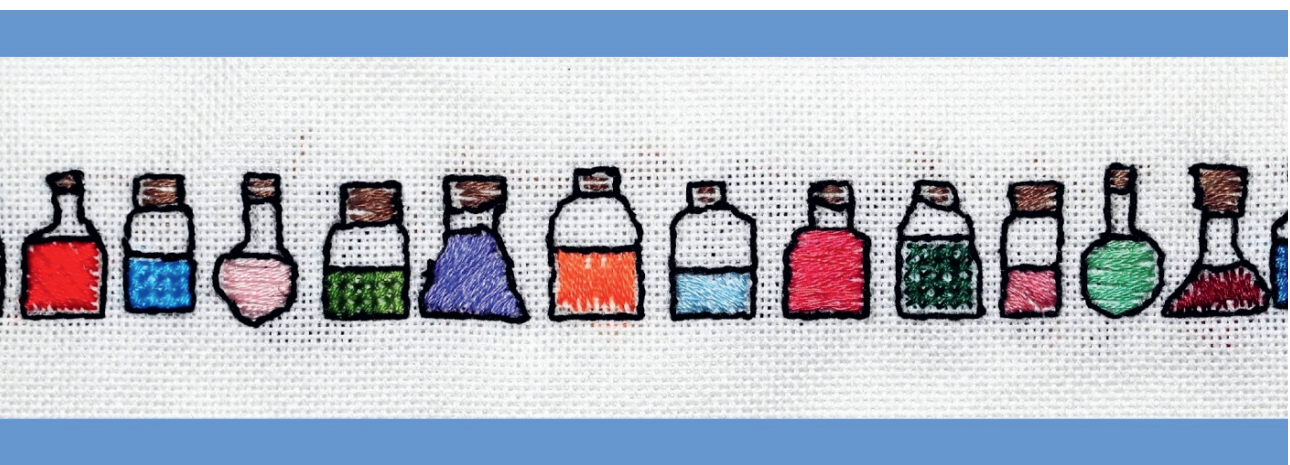


Figure S4.8. Observation of the bacterial and archaeal microbial community in biofilms grown on cathodes during the control experiment (A) and with trace metal mix with EDTA (TMM+) pre-treatment (B and C) by Fluorescence in situ hybridization (FISH). The probes applied are EUB338 (Bacteria, in green) and MB311 (Methanobacteriales, in red). Size bar is 10 μm .



Chapter 5

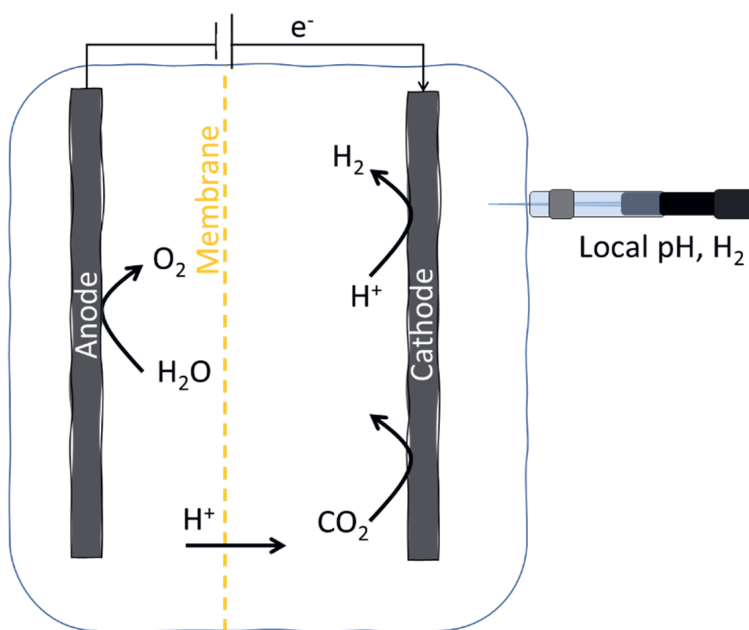
Methodology for in-situ microsensor profiling of hydrogen, pH, ORP and electric potential throughout 3D porous cathodes of (bio)electrochemical systems



Submitted as: de Smit, S. M., Langedijk, J. H., van Haalen, L. C. A., Lin, S. H., Bitter, J. H. & Strik, D. P. T. B. Methodology for in-situ microsensor profiling of hydrogen, pH, ORP and electric potential throughout 3D porous cathodes of (bio)electrochemical systems.

Abstract

We developed a technique based on the use of microsensors to measure pH and H_2 gradients during microbial electrosynthesis. The use of 3D electrodes in (bio)electrochemical systems likely results in the occurrence of gradients from the bulk conditions into the electrode. Since these gradients e.g. with respect to pH and reactant/product concentrations determine the performance of the electrode it is essential to be able to accurately measure them. Apart from these parameters, also local oxidation-reduction potential and electric field potential were determined in the electrolyte and throughout the 3D porous electrodes. Key was the realization that the presence of an electric field disturbed the measurements obtained by the potentiometric type of microsensor(s). To overcome the interference on the pH measure, a method was validated where the signal was corrected for the local electric field measured with the electric potential microsensor. The developed method provides a useful tool for studies about electrode design, reactor engineering, measuring gradients in electroactive biofilms and flow dynamics in and around 3D porous electrodes of (bio)electrochemical systems.



5.1 Introduction

Electrochemical technology offers a clean and powerful tool for both treatment of waste streams and chemical synthesis¹. (Bio)electrochemical systems catalyse (microbial) conversions by applying an electric potential to an electrode on which microbes grow. The microbes use the applied energy directly as electrons or indirectly as hydrogen, which is formed at the cathode from electrons and protons^{2,3}. Since most conversions occur at the electrode surface, local gradients of e.g. protons and hydrogen, with concentrations different from the bulk can be expected. Most often in (bio)electrochemical studies, only bulk conditions are measured, which can be non-representative for the local conditions around the electrode surface⁴. Several theoretical studies have modelled the local conditions near the cathode^{5,6}, but practical support for these studies is rare. To measure local concentration gradients, microsensors could form powerful tools. Microsensors have a thin tip (down to 1 μm), which allows measurements with the same spatial resolution as the tip size. The sensors can be moved along a profile axis to measure gradients^{7,8}. Microsensors have been applied in many different fields, including biochemistry^{9,10}, plant science¹¹⁻¹³, microbiology^{14,15} and biomedicine^{16,17}, but their application in electrochemical systems remains limited.

The application of microsensors in electrochemical systems is expected to be suitable by application of amperometric microsensors, which measure a current signal resulting from a redox reaction on the microelectrode surface. These Clark-type¹⁸ microsensors are used to measure H_2 , H_2S , O_2 , NO , N_2O and CO_2 ^{8,19} gradients in biofilms growing on 2D electrodes^{8,20}. To measure e.g. pH, oxidation-reduction potential (ORP) and electric field potential, potentiometric sensors are used, which measure a potential drop over the sensor tip membrane between the sensor electrode and an external reference electrode^{8,21}. Despite their successful application in the beforementioned fields, the application in electrochemical systems is limited due to signal interference when placed in an electric field²² with significant distance (several mm) between the sensor electrode and external reference electrode tip^{23,24}.

To use potentiometric microelectrodes for analysis of local gradients in (bio)electrochemical systems, the interference from the electric field needs to be tackled. The best way to tackle the issue would be to minimize the distance between the sensor electrode and the reference electrode^{23,24}. Some studies used so called “combined sensors” to measure pH in electrochemical biofilms. In these custom-made sensors, the reference and measuring electrode were built in the same sensor, connected with a conductive liquid⁸. Although this gave reliable results, the thicker microsensor tip did not allow for the sensor to be moved over distances longer than 600 μm without piercing mm wide holes in the biofilm^{23,25}. The short distance was enough to measure inside biofilms on 2D electrodes, but could not be used to measure inside several mm or even cm thick 3D porous electrodes typically used in bioanode or biocathodes²⁶⁻²⁸.

In this study, a methodology for microsensors application in (bio)electrochemical systems was developed to measure gradients in the electrolyte and, for the first time, throughout porous 3D electrodes. The methodology development consisted of three steps. First, a reactor was designed, with key features that allow microprofile measurements over a range of several centimetres, keeping anaerobic conditions and continuous leak-free liquid electrolyte

recirculation of 10 L/h. Practical tips and protocols are provided for the use and careful handling of the microsensors to facilitate future use. Second, the reactor design was used to show a microprofile of H_2 gradients in the reactor. Third, a correction method is presented and validated to overcome the interference of electric field during potentiometric microsensor measurements. With this method, potentiometric microsensors can finally be applied for accurate gradient measurements in (bio)electrochemical systems, even with high current (-10 kA/m^3). The correction method was used to show gradient profiles of the electric field potential, ORP and pH. The profiles in the study showed significant differences between bulk and local conditions at the electrode surface, which highlights the importance of the presented method and its possible application for mass transfer studies.

5.2 Experimental section

5.2.1 Reactor setup

All measurements of this study were performed in an electrochemical CO_2 -fed reactor. The electrochemical reactor consisted of an anode (Ti/Pt-Ir MMO, thickness 1 mm, Magneto Special Anodes BV, Netherlands) and three cathode layers (graphite felt, thickness 3 mm, Rayon Graphite Felt, CTG Carbon GmbH, Germany), separated by layers of three spacers to study three different distances from the anode. The anode and cathode compartment of the cell were built with Plexiglass flow-through plates with 21.3 cm^2 psa and separated by a cation exchange membrane (Fumasep FKS, Fumatech BWT GmbH, Germany). The three cathode layers were separated with spacer layers (Figure 5.1, SI Figure S5.1) and connected in parallel with titanium wire (0.8 mm thick, grade 2, Salomon's metalen, the Netherlands) with 1Ω between each connection and the working electrode plug (Figure 5.2). The graphite felt was non-microporous, low surface area material ($< 1 \text{ m}^2/\text{g}$), determined by N_2 physisorption. Since the microprofiles would be made throughout the cathode layers, the cathodes were constructed in such a way that the microsensor tips would not touch the Ti wire or spacers (SI Figure S5.1C).

At current densities of -10 kA/m^3 cathode, not all hydrogen could pass the graphite and gas accumulated below the cathode (at "bypass outlet", SI Figure S5.1A), hindering proton transfer between anode and cathode. To remove accumulated gas, a catholyte flow "bypass outlet" was placed below the cathode at the outflow side of the electrochemical cell (left in SI Figure S5.1A). The catholyte flow distribution between the two outflow ports above and underneath the cathode was 1:1, calculated from flow rate measurements at the reactor outlets. The details of the reactor operation parameters are described in the SI, section "reactor operation".

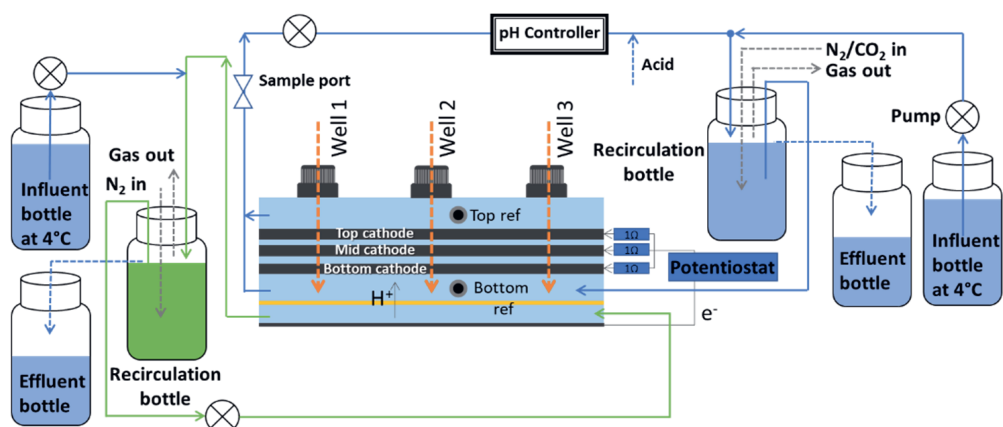


Figure 5.1. Setup of electrochemical cell with recirculation, influent, effluent and pH control. The analyte recirculation is shown in green for viewing purposes.

5.2.2 Analyses

Gas chromatography analysis (detection of oxygen, carbon dioxide, methane, nitrogen and hydrogen, Shimadzu GC-2010, Japan) was performed to measure the hydrogen fraction of the off gas from the reactor. Hydrogen production could be calculated based on the (assumed inert) fraction N_2 in the off gas.

5.2.3 Microsensors and profiling

A laboratory stand (LS18), micro-manipulator (MM33-2), motor-driven micro-manipulator stage (MMS), and Motor Controller (MC-232) were combined for precise manipulation of microsensors (Unisense A/S, Denmark). All equipment was installed and operated corresponding to the manuals. H_2 microsensor (H2-50), pH microelectrode (pH-50), oxidation-reduction potential microelectrode (RD-50), reference microelectrode (REF-100) and an electric potential electrode (EP-100) were used for micro-profiling, all with an indicated tip size of 40-60 μm (all from Unisense A/S, Denmark). The relative sensor lengths were determined under the microscope to enable combination of different sensor measurements in plots. For the potentiometric microsensors, two external capillaries were installed 5 mm above (fixed ref TOP, SI Figure S5.1A) and 7 mm below the cathodes in the reactor (fixed ref BOTTOM, SI Figure S5.1A) additional to the reference used by the potentiostat. The capillaries were filled with gelled 3 M KCl and connected to Ag/AgCl reference electrodes via tubing filled with liquid 3 M KCl. The calibration and measurements were corresponding to the manuals, combined with the micro-profiling setup (SI I and II). SensorTrace Profiling and Logging software (Unisense A/S, Denmark) were used in this study. Further details about how a profile was measured will follow in the results section.

5.3 Results

5.3.1 Key features of reactor and sensors to allow microprofiling

5.3.1.1 Reactor design

To allow for in situ measurements with microprofiling sensors under continuous leak-free electrolyte recirculation, the setup contains some key features (Figure 5.1, 5.2A). The electrochemical cell was fixed horizontally with a 17° angle on a ground plate to allow for gas to escape from the higher outlets and allow microprofiling with the microsensors perpendicular to the graphite felt cathode (SI Figure S5.1C, 5.2A). The outer plate of the electrochemical cell was replaced with a Plexiglass closing plate with three wells (SI Figure S5.1A). The inlets and outlets tubing of the catholyte compartment in the electrochemical cell were equipped with switchable three-way valves, for closing of the catholyte compartment while installing microsensors.

To measure a microprofile, the catholyte recirculation was shortly stopped to replace the well caps with a “sleeve” (Figure 5.2C) to enter the microsensor. The microsensor neck was greased with silicone grease to ensure a vacuum between the neck and the sleeve. The silicone grease allowed electrolyte leak-free sensor moving. After securing the microsensor in the sleeve, the recirculation was switched on again and a profile could be made, during which the microsensor was brought down with a motor tool (default velocity and acceleration of $1000 \mu\text{m/s}$ and $1000 \mu\text{m/s}^2$, stepsize $100 \mu\text{m}$) (Figure 5.2B) to pierce the graphite electrode and profile a gradient through the cathode layers until the membrane inside the cell. A full detailed protocol is described in SI section “protocol profiling”.

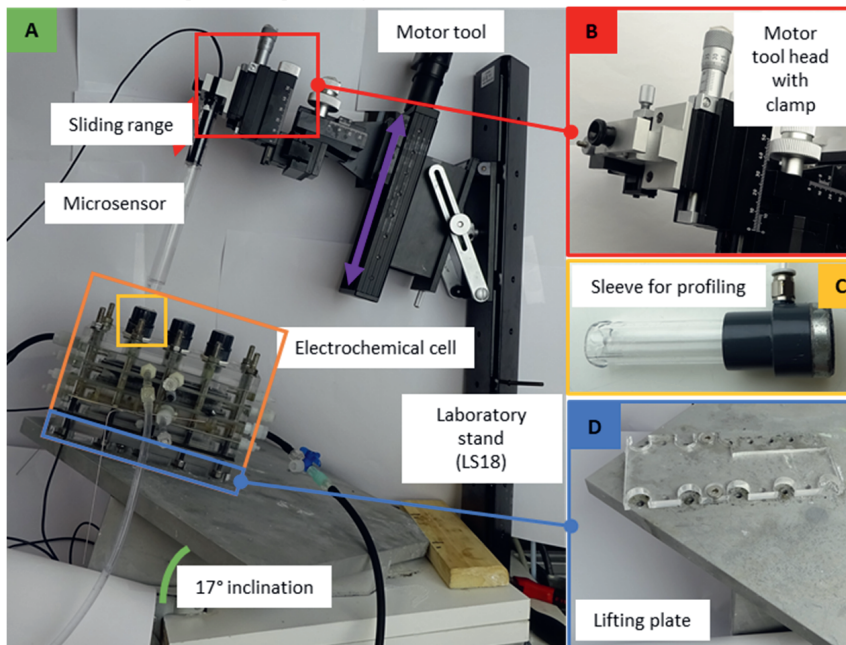


Figure 5.2. Setup for making microprofiles in a (bio)electrochemical reactor. The electrochemical reactor was placed on a lifting plate (D) connected to a ground plate with a 17° inclination (A). To make a microprofile, a microsensor is placed in the motor tool head clamp (B) and entered into the reactor via a sleeve (C).

Table 5.1. Overview of different microsensors used in this study with the measured value and the used stabilization and measurement times used in this study. The microsensor tip sizes correspond to the number in the specs code, shown in μm . All sensors are from Unisense A/S, Denmark. The signal correction applies to measurements within electric fields.

Sensor	Specs	Measured	External reference	Stabilization time (s)	Measuring time (s)	Unit	Range (unit)	Detection limit (unit)	Signal correction (This study)
Hydrogen	H2-50	Local pH_2 measured as current, converted to mV by amplifier	-	<i>This study</i> 10	<i>This study</i> 5	$\mu\text{mol/L}$	0-800	0.3	No
Electric field potential	EP-100	Potential difference between Ag/AgCl electrode and reference electrode	Ag/AgCl	10	5	mV	n.a.	n.a.	No
Oxidation-reduction potential	RD-50	Oxidation Reduction Potential: solution tendency to be oxidized or reduced in mV	Ag/AgCl	3	1	mV	n.a.	0.1	$\text{mV}_{\text{measured}}$ - $\text{mV}_{\text{local electric field}}$
pH	pH-50	Potential difference caused by proton concentration difference between sample and inside tip	Ag/AgCl	10	5	-	2-10	0.01	$\text{mV}_{\text{measured}}$ - $\text{mV}_{\text{local electric field}}$

5.3.1.2 Microsensors used for profiling

Before measuring microprofiles, the microsensor characteristics were tested (Table 5.1). In this study, four different sensors were used; one amperometric sensor to measure H_2 , and three potentiometric sensors to measure electric field potential (EP), oxidation-reduction potential (ORP) and pH. The amperometric H_2 sensor was used to test the feasibility of measuring microprofiles with the presented reactor design. The potentiometric sensors were used to develop accurate microsensor measurements in the electric field (Table 5.1, signal correction), which will be explained with more detail in chapter 3.

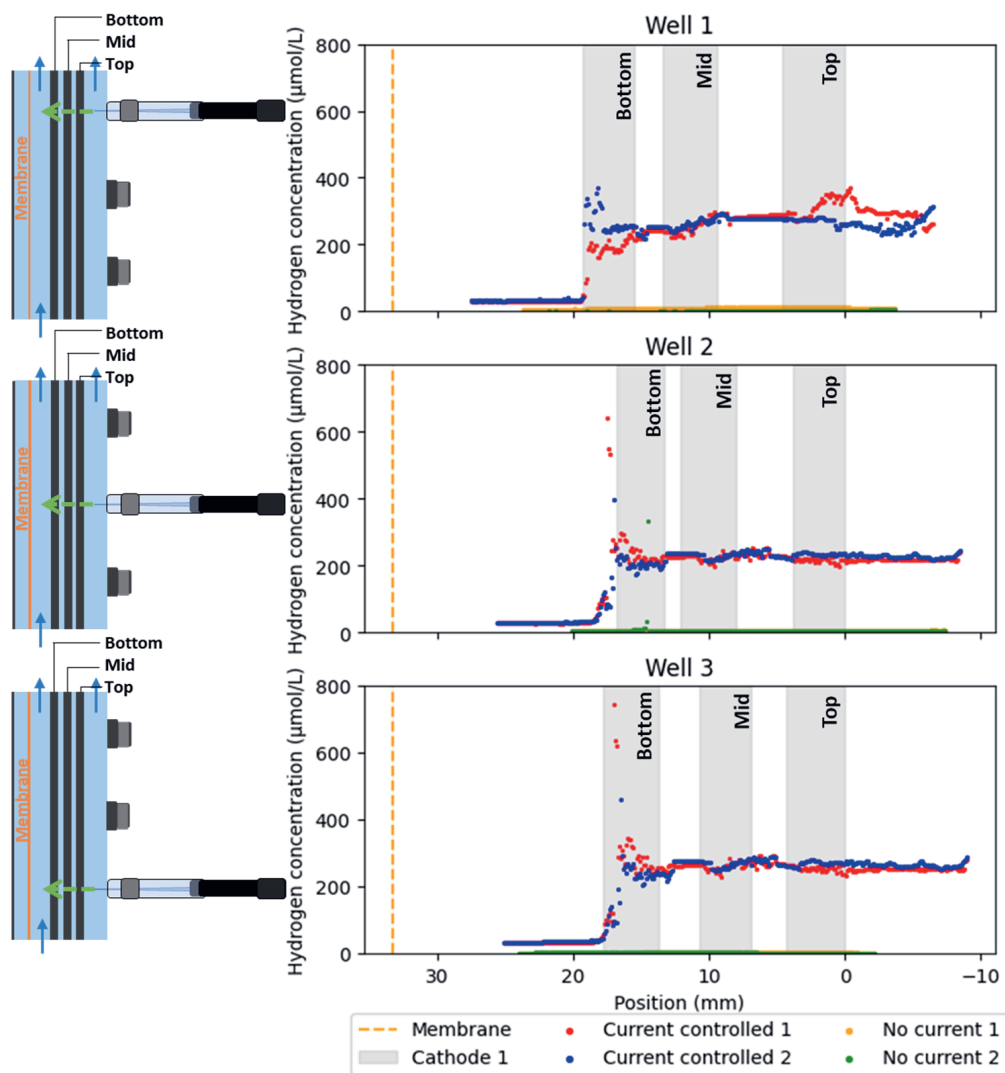


Figure 5.3. Profile of hydrogen concentration over the distance inside the electrochemical reactor operated at -200 mA and without current. On the left, schematics of the reactor are shown.

First, the response times of different sensors were determined by moving the sensors to different heights in the system and measuring the signal over time (SI Figure S5.3-S5.5). Most signals were stable after 5 seconds, so this time was increased to 10 seconds stabilization time and 5 seconds measuring time during the measurements to avoid instability offsets.

5.3.1.3 Accurate cathode position determination with ORP sensors

Apart from the technical differences between the sensors shown in Table 5.1, the sensor tips also showed visual differences (SI Figure S5.2). Most sensor tips were made of glass (H_2 , EP, pH), but the ORP sensor had a metal tip. The ORP microsensor measured the cathode potential when the tip was in contact with the graphite felt layers. The cathode potential values differed significantly from the electrolyte ORP, so the ORP profiles showed clearly the position of the cathode layers. Therefore, the cathode layer positions were determined by the ORP measurements and used in the profile plots of the other sensors.

5.3.2 Local hydrogen concentration gradients measured with microsensor

With the new reactor design and profiling method, hydrogen concentration gradients were measured in the three wells of the reactor with active catholyte recirculation (Figure 5.3). Prior to the profile, the sensors were calibrated according to the manual. Since the calibration was done at a lower temperature than the profile measurement, a temperature correction was performed for the conversion of the mA signal to the dissolved hydrogen concentration (SI section “protocol microsensor calibration”). After calibration, profiles of the hydrogen concentration distribution were made in duplicate with and without current to the reactor (Figure 5.3). To improve readability of the profile graphs, all figures show a schematic figure of the reactor orientation on the left side, corresponding with the visualization orientation in the figures. Without current applied to the electrochemical cell, no hydrogen was detected (Figure 5.3, OCV profiles). With applied current, the hydrogen concentration is low in the catholyte closest to the counter electrode (Figure 5.3, distance 20-25 mm), and highest at the cathode closest to the counter electrode (Figure 5.3, bottom cathode). Although the hydrogen was high in the bottom cathode, the theoretical maximum saturation concentration of hydrogen at the salinity and temperature used in this experiment ($709 \mu\text{mol/L}$) was only reached in some spots in the bottom cathode of well 3. The duplicate measurement was done to investigate whether the piercing of the cathode layers in the first cycle would affect the local concentrations. Figure 5.3 shows that cycle 1 and 2 are similar, yet not exactly the same in all locations.

To relate the local hydrogen concentrations to the local current at the different cathode layers, the applied current was measured over the resistances placed before each connection to the cathode layers. The current was not distributed evenly over the top, mid and bottom cathode. A major part of the -200 mA supplied to the cathode, was led to the bottom cathode closest to the counter electrode ($\pm 82\%$, SI Table S1).

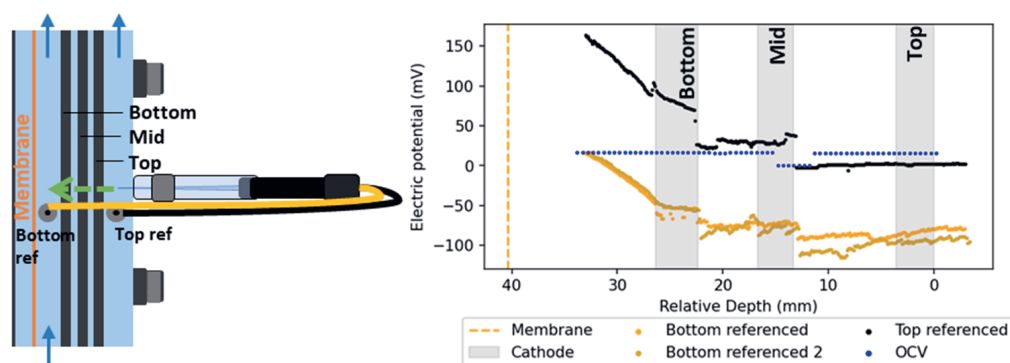


Figure 5.4. Profile of electric potential over the distance inside the middle well (left) of an electrochemical reactor operated at -50 mA (black, yellow) and during open cell voltage control (blue). The electric field potential was measured as the potential difference versus the bottom reference electrode (yellow) and top reference electrode (black).

5.3.3 Correction for electric field interference in potentiometric measurements

5.3.3.1 Measuring electric potential offset versus fixed external reference electrode

Since the current was not evenly distributed between the different cathode layers, it was expected that the local electric field would also show gradients over the different cathode layers. To investigate this, the EP (electric potential) sensor was used, which measures the potential difference between the microsensor tip and an external reference electrode, in this study Ag/AgCl was used (Table 5.1). Since the EP sensor is also an Ag/AgCl electrode, the value of the electric field should be 0 when no electric field is present and increase with increasing electric field²¹. To measure the electric potential in the electrochemical system, a profile was measured with the EP microsensor throughout the electrolyte and the cathode layers. First, a profile was measured without current applied to the system. During OCV, the electric potential difference between the sensor tip and the fixed reference electrode is constant at 20 mV with the exception of one jump to 0 mV around the middle cathode layer (Figure 5.4, blue dashed line). On the contrary, when the cathode is current controlled, the electric potential difference versus the same fixed reference electrode shows steep gradients and increases in jumps at each cathode layer when moving the sensor from the fixed reference (black line). Since most of the current was distributed to the bottom cathode, the local electric field was expected to be greater at the bottom electrode. There, a steeper gradient is seen throughout and below the bottom cathode layer (black line, left grey plane). The difference between the OCV and current controlled measurements shows that applying current affects the local electric field. With the fixed reference electrode positioned in this field of steep increase (bottom reference, yellow line), the gradient pattern is the same, with 0 mV offset when the moving electric potential electrode tip was (observed by eye) close to the bottom fixed reference electrode (depth 30 mm).

Although the difference between the black and yellow profile seems to be constant, the difference decreases from lower (33 mm, 150 mV) to higher locations (-4 mm, 100 mV) (SI Figure S5.6). The depth with offset 0 mV (30 mm) was determined to be right next to the bottom fixed reference electrode.

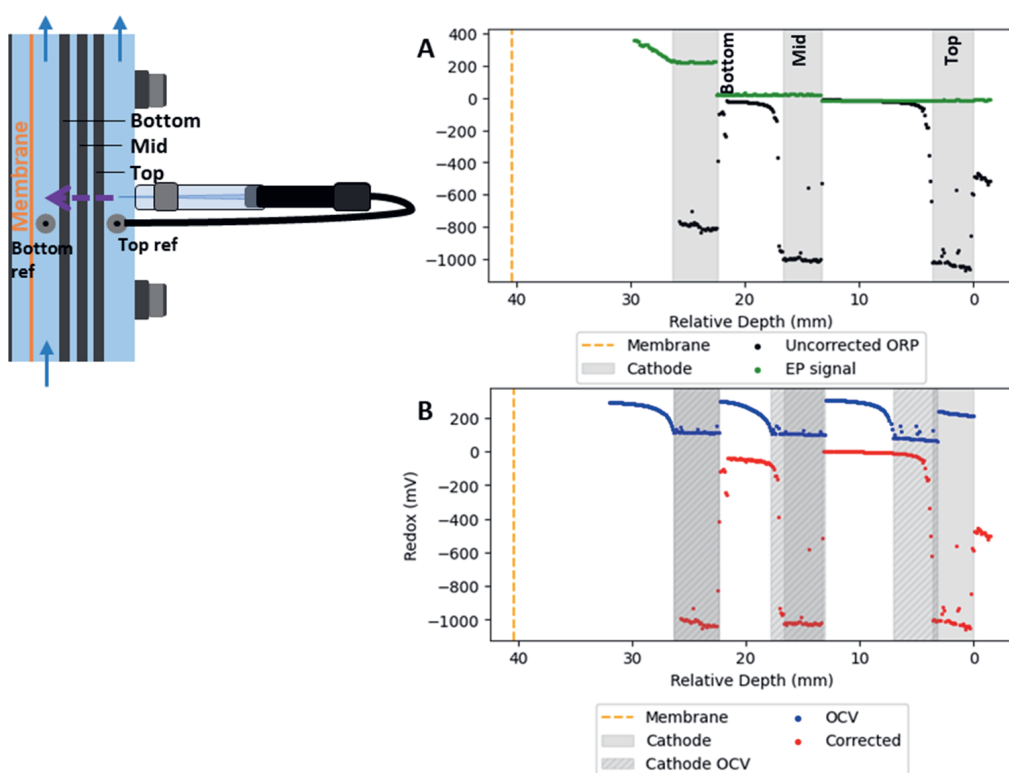


Figure 5.5. Profile of oxidation-reduction potential (ORP) over the distance inside an electrochemical reactor operated at -50 mA. The ORP was measured versus the top fixed reference electrode. The raw data from the ORP measurement measured versus the top reference electrode (A, black) were corrected with the EP top referenced profile (A, green) to obtain a corrected ORP profile (B, red). The ORP profile was also measured with open cell voltage (B, blue).

5.3.3.2 ORP profile signal corrected for local electric field potential

Next to the EP sensor, the ORP microsensor also uses an external reference electrode (Table 5.1). Based on the EP profile (Figure 5.4), local mV offset signals can be expected in microsensor measurements with current applied to the system. Therefore, using the raw output data from potentiometric sensors would result in unreliable values. Damgaard, et al. 21 suggested that a local EP correction could be used to convert the potentiometric microsensor signals to accurate data. The ORP and pH microsensor used in this study were shielded against electric field disturbances with the similar caging technique as used for the EP microsensor²¹. Therefore, the three microsensors were expected to be disturbed by the electric field in similar ways. In this study, the hypothesis from Damgaard, et al. 21 was tested. Figure 5.5 shows the raw ORP data (black) and the local EP (green) used for the ORP data correction (red). The correction was done by subtraction of the local EP difference versus the fixed top reference (Figure 5.5A, green) from the raw ORP signal measured versus the same fixed reference (Figure 5.5A, black).

To validate the accuracy of the correction, the cathode layer potentials were compared with the raw data. Since the cathode layers were connected in parallel to the potentiostat, the cathode layer potentials should be equal. This is indeed shown for the data corrected for the local EP

(Figure 5.5B – ‘Corrected’), but not for the uncorrected signal, showing that the EP correction results in reliable ORP values. The corrected values could be compared to ORP without current applied to the system (Figure 5.5B, blue). It should be noted that the OCV profile was measured in a different (but similar) reactor, so the exact cathode positions differed (top cathode was placed more to the left, ‘Cathode OCV’). Without current applied to the reactor, the ORP of the cathode layers is constant at 150 mV, while the catholyte ORP signal shows gradients towards 230 mV (Figure 5.5B, blue). All ORP values without current are less negative than with current.

5.3.4 pH microsensor signal interfered by applied current

The pH microsensor also uses an external reference electrode (Table 5.1), so its mV signal was also expected to be interfered by the presence of an electric field. However, unlike the ORP measurements, the value around the cathodes could not be used as verification. Since the pH of the catholyte bulk recirculation is measured outside the electric field (Figure 5.1), this was used as a validation method in an experiment to investigate the magnitude of the signal deviation in relation to the current magnitude. Different current magnitudes were applied to the electrochemical system, while measuring the pH with a microsensor. To measure the deviation, the tip of the pH microsensor was placed at the influent port of the catholyte recirculation (Figure 5.6A left). With this measurement, the microsensor pH could be compared to the recirculation pH. Figure 5.6A shows the deviation between the pH reported by the microsensor (with top reference at depth -5 mm, 35 mm from the pH microsensor tip) and the recirculation pH plotted against increasing cathode current.

When no current was applied to the system, a deviation between 0.06-0.3 pH unit in signal was measured between the recirculation pH and the microsensor pH (Figure 5.6A). With applied current, the pH microsensor reported pH values lower than the recirculation pH. This offset increased with increasing current with a semi-linear trend. At current values of -100 mA or more negative, the pH microsensor even reported negative pH values. Therefore, the signal deviates strongly from the recirculation pH with applied current.

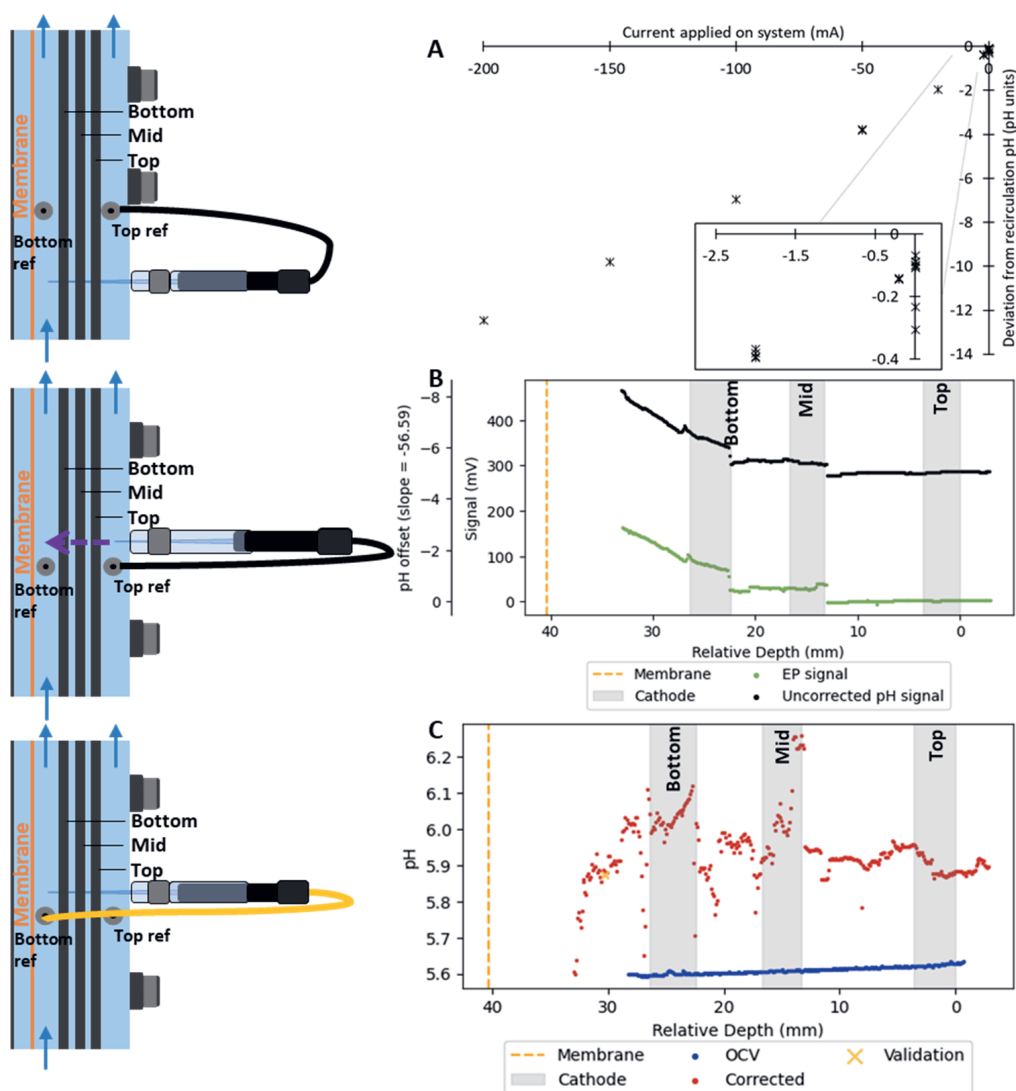


Figure 5.6. pH microsensor measurements, A: Deviation between bulk pH and pH reported by pH microsensor placed at the bulk inlet point of the cathode chamber at different cathode current magnitudes. The pH signal was measured versus the top fixed reference. B&C: Profile of pH over the distance inside an electrochemical reactor operated at -50 mA. The pH was measured versus the top fixed reference electrode. The raw data from the pH measurement measured versus the top reference electrode (B, black) was corrected with the EP top referenced profile (green) to obtain a corrected pH profile (C, red). The pH profile was also measured with open cell (C, blue). Right after making the pH profile, the pH microsensor tip was placed next to the bottom reference electrode and logged over 7 min (yellow cross).

5.3.5 pH microsensor signal corrected with local electric potential

After determining the pH microsensor disturbance by the electric field at one point, a pH gradient profile was made with the fixed top reference (depth -5 mm) (Figure 5.6B, black). The

signal showed a pattern similar to the signal from the electric field potential when measured with the same reference electrode point at -5 mm (top reference) (Figure 5.6B, green).

The local electric field correction was also applied to the pH microsensor measurement (Figure 5.6C, red). To verify the local electric field potential correction, the pH was measured versus the bottom reference with the microsensor tip placed next to the bottom reference electrode (depth 30 mm), to ensure 0 mV offset (Figure 5.4) and logged over 7 min (SI Figure S5.7). The average pH value during that period is indicated with a yellow cross (Figure 5.6C). The verification point lies exactly on the line of corrected pH values, showing the accurateness of the correction. The corrected values are more constant over the depth of the reactor and show a small gradient underneath the bottom cathode (depth 27 to 33 mm). The pH value in the bulk solution underneath the cathode (depth 33 mm) is similar to the bulk pH (5.8), while the pH is higher (± 6.2) in the lowest two cathode layers (depth 13 to depth 30 mm). More away from the counter electrode, above 13 mm, the pH is again similar to the bulk pH value. Without applied current, the pH showed less gradients than with current (Figure 5.6C, blue and red).

5.4 Discussion

5.4.1 Microprofiling in electrochemical systems for local gradient measurement

With the adapted setup, microsensor profiles can be made in the electrolyte and through the different porous electrode layers of the cathode chamber whilst keeping leak-free electrolyte recirculation. With the hydrogen sensor, local hydrogen concentrations could be mapped precisely (Figure 5.3). For measurements with potentiometric microsensors, an external reference electrode is used. Both the distance to the external reference (Figure 5.4) and the magnitude of the current (Figure 5.6A) influence the signal disturbance from microsensors with external reference electrodes⁸. Potentiometric microsensor measurements in fields with low electric potential, yet significant distance between the microsensor tip and the external reference electrode, as performed in earlier studies^{29,30}, could give seemingly plausible values, even though the electric field still causes an offset (Figure 5.6A). Since 59 mV corresponds with 1 pH unit, a 6 mV offset could already cause a measuring error of 0.1 pH unit. Therefore, the signal from microsensors with external reference electrodes needs to be corrected for this disturbance. The suggested correction with the local EP signal²¹ was tested and validated in this study. Since the ORP profile shows equal potential values for all parallel connected cathode layers and the pH validation measurement at the location with EP of 0 mV showed the same value as the corrected profile, the EP correction for potentiometric microsensor measurements is reliable.

5.4.2 Intermittent current or distance to reference to allow potentiometric measurements

Next to the EP correction method, two additional methods to make profiles with potentiometric sensors are applying intermittent current or minimizing the distance to the reference electrode. When no current was applied between the electrodes, both the local EP and the pH offset were minimal (Figure 5.4, 5.6A). Based on this insight, intermittent current was investigated as method to measure with potentiometric microsensors. In theory, the values measured right after

switching off the current should represent the actual value during applied current. To test this, the microsensor pH values were logged during intermittent current with the tip 35 mm from the external reference electrode. As validation, the microsensor pH values were also logged at the same location but with the external reference next to the tip (with 10 mm distance parallel to the electrode surfaces), with local EP of 0 mV. It was found that it took some time (at least 1 sec) after stopping the current before the signal reached validated values representative for the situation with applied current. Simultaneously after stopping the current, the system gradients caused by the applied current disappeared and bulk conditions were measured. To obtain reliable values with potentiometric measurements during the intervals without current, the sensor should measure values that represent the situation with current on the system and not values that represent the bulk conditions which are reached without applied current. For the systems described in this study, the intermittent current method was not reliable in some of the tests (SI section “pH microsensor measurement during intermittent current”). To determine the applicability of the intermittent current to measure with potentiometric microsensors, it is recommended to use the validation method described in SI section “pH microsensor measurement during intermittent current”.

Another method to measure potentiometric signals in systems with high electrolyte resistance is minimizing the distance to the reference electrode^{8,22,31}. The mV offset between the electric potential microsensor and the fixed reference was 0 mV when the distance was minimized (with both tips at equal distance from the anode, with 10 mm distance between the tips parallel to the electrode surfaces), both with the top reference electrode (depth -5 mm) and the bottom reference electrode (depth 30 mm) (Figure 5.4). The bottom reference electrode was located in an area with a steep gradient of electric potential, but still showed 0 mV offset at the minimum distance between the reference and the microsensor tip. The potential ideal solution for potentiometric microsensor measurements would be the development of a combined sensor with an integrated internal reference electrode with a long thin tip that allows piercing soft materials. This sensor could be used to measure with the least invasiveness in electrochemical systems. Unfortunately, this sensor is not yet commercially available.

5.4.3 Microprofiling shows steep local gradients

With the method from this study, many useful insights were already gained. One insight gained here is that H₂ is stripped likely due to CO₂ supply in the electrochemical system. The hydrogen concentration is low at the places close to the membrane and influent port (Figure 5.3). This indicates that a great part of the formed hydrogen is flushed out in the recirculation bottle of the system, where CO₂ and N₂ are continuously sparged to the reactor (Figure 5.1). Microsensor measurements can be used to test liquid mixing capabilities in optimized reactor designs by measurements of local substrate availability. Furthermore, the microsensor measurements showed that the local hydrogen concentration is highest at the bottom cathode, corresponding with a great share (82%) of applied current towards that cathode layer. The formed hydrogen distributes evenly through the cathode compartment, the concentrations are still around 375 $\mu\text{mol/L}$ inside and around the upper two cathode layers (depth -5 to 25 mm). This hydrogen concentration is 1000 times above the required threshold reported in literature for several hydrogenophilic bacteria³² (assuming Henry coefficient of $7.7\text{E-}06 \text{ mol}/(\text{m}^3\text{Pa})$ ³³). Apart from the hydrogen profile, the ORP and pH profiles also gave interesting insights. The ORP profiles

showed great differences with and without current, not only the in the cathode, but also inside the catholyte (Figure 5.5B). This indicates that applying a current to the system does not only change the reaction conditions within the porous cathode, but also in the liquid around. The pH profile showed no gradient when no current is applied to the system, but shows local differences when current is applied to the system (Figure 5.6C). The local pH inside and around the cathode layers was higher than the bulk pH, presumably due to proton consumption for the hydrogen evolution reaction. A pH shift can change favourability for microorganisms. For example, the 0.3 unit pH increase causes a 5% decrease of the undissociated fatty acid fraction, which can inhibit methanogenic activity³⁴. The insights of these microsensor measurements can be used to adjust the reactor conditions in such a way that allows conditions more favourable for desired microorganisms. For system optimization, fluid dynamic studies within microbial electrosynthesis systems are one of the key focus points³⁵. From the results of this study can be indicated that hydrogen distribution in the system requires optimization. Microsensor measurements of local conditions are a helpful tool to study different electrode and flow designs and their effect on potential limiting conditions.

5.4.4 Outlook for microsensor application possibilities

The current distribution was mainly (82%) towards the bottom cathode, while hydrogen is available in all three cathode layers. Thus, different niches can be found within the cathode compartment and even within cathode layers with different local hydrogen concentrations at different depths. Between and within the cathode layers, different availability of substrates, electron donors and products can be expected based on the profiling results. Several modelling studies have calculated the presence of limiting gradients of e.g. pH⁶ and H₂³⁶ in biofilms. Thus, the development of a biofilm on the graphite fibres will affect the local conditions even more than in the abiotic situation shown in this study. Verification experiments with microsensors can serve as validation by determination of gradients of substrates, products and local conditions within biofilms. Linking the different local conditions to the performance at the different spots can give many insights for optimization. For example, linking the local H₂ and current to microbial activity is insightful for determining the dependence of the microbes on electrical current versus hydrogen as electron donor. With the method presented in this paper, gradients of H₂, O₂, H₂S, CO₂, H₂O₂, NO₂⁻, pH, ORP and electric potential^{19,21,37-45} can likely be measured in stable electrochemical systems with or without biofilms under anaerobic or even aerobic conditions.

5.5 Conclusions

This study showed the successful application of microsensors for measurement of gradients in electrochemical systems. The reactor with measuring wells placed perpendicular to the profiling direction allowed for profiling with electrolyte leak-free recirculating conditions. The presented manuals and video instructions will aid future users to apply this method. Profiles were made of local H₂, electric potential, pH and ORP in the electrolyte and for the first time throughout the porous electrodes. For the potentiometric microsensors, a local electric field potential correction is validated as a reliable method to correct for signal disturbance from the electric field. The use of these sensors can be extended to study biofilm gradients and local reactor conditions in electrochemical systems.

References

- 1 Wills, A. G. *et al.* High-Throughput Electrochemistry: State of the Art, Challenges, and Perspective. *Org. Process Res. Dev.* (2021).
- 2 Lovley, D. R. & Nevin, K. P. Electrobiocommodities: powering microbial production of fuels and commodity chemicals from carbon dioxide with electricity. *Curr Opin Biotechnol* **24**, 385-390, doi:10.1016/j.copbio.2013.02.012 (2013).
- 3 Kracke, F., Vassilev, I. & Krömer, J. O. Microbial electron transport and energy conservation—the foundation for optimizing bio-electrochemical systems. *Frontiers in microbiology* **6**, 575 (2015).
- 4 Monteiro, M. C. & Koper, M. T. Measuring local pH in electrochemistry. *Curr. Opin. Electrochem.* **25**, 100649 (2021).
- 5 Ooka, H., Figueiredo, M. C. & Koper, M. T. Competition between hydrogen evolution and carbon dioxide reduction on copper electrodes in mildly acidic media. *Langmuir* **33**, 9307-9313 (2017).
- 6 De Lichtervelde, A., Ter Heijne, A., Hamelers, H., Biesheuvel, P. & Dykstra, J. Theory of ion and electron transport coupled with biochemical conversions in an electroactive biofilm. *Phys. Rev. Appl.* **12**, 014018 (2019).
- 7 Revsbech, N. P. & Jørgensen, B. B. Microelectrodes: their use in microbial ecology. *Adv. Microb. Ecol.*, 293-352 (1986).
- 8 Beyenal, H. & Babauta, J. Microsensors and microscale gradients in biofilms. *Productive Biofilms*, 235-256 (2013).
- 9 Nielsen, M., Revsbech, N. P. & Kühl, M. Microsensor measurements of hydrogen gas dynamics in cyanobacterial microbial mats. *Frontiers in microbiology* **6**, 726 (2015).
- 10 Sørensen, K., Řeháková, K., Zapomělová, E. k. & Oren, A. Distribution of benthic phototrophs, sulfate reducers, and methanogens in two adjacent saltern evaporation ponds in Eilat, Israel. *Aquat. Microb. Ecol.* **56**, 275-284 (2009).
- 11 Pedersen, O., Revsbech, N. P. & Shabala, S. Microsensors in plant biology: in vivo visualization of inorganic analytes with high spatial and/or temporal resolution. *J. Exp. Bot.* **71**, 3941-3954, doi:10.1093/jxb/eraa175 (2020).
- 12 Ober, E. S. & Sharp, R. E. A microsensor for direct measurement of O₂ partial pressure within plant tissues. *J. Exp. Bot.* **47**, 447-454, doi:10.1093/jxb/47.3.447 (1996).
- 13 Hofmann, L. C., Schoenrock, K. & de Beer, D. Arctic Coralline Algae Elevate Surface pH and Carbonate in the Dark. *Frontiers in Plant Science* **9**, doi:10.3389/fpls.2018.01416 (2018).
- 14 Santegoeds, C. M., Schramm, A. & De Beer, D. Microsensors as a tool to determine chemical microgradients and bacterial activity in wastewater biofilms and flocs. *Biodegradation* **9**, 159-167 (1998).
- 15 Mohanakrishnan, J. *et al.* Impact of nitrate addition on biofilm properties and activities in rising main sewers. *Water res.* **43**, 4225-4237 (2009).
- 16 Ravera, S. *et al.* Concentration-dependent metabolic effects of metformin in healthy and Fanconi anemia lymphoblast cells. *J. Cell. Physiol.* **233**, 1736-1751 (2018).
- 17 Lane, S. J., Tobalske, B. W., Moran, A. L., Shishido, C. M. & Woods, H. A. Costs of epibionts on Antarctic sea spiders. *Mar. Biol.* **165**, 1-8 (2018).
- 18 Clark, L. J. Monitor and control of blood and tissue oxygen tensions. *Trans Am Soc Artif Intern Organs* **2**, 41-48 (1956).
- 19 Revsbech, N. P. Simple sensors that work in diverse natural environments: The micro-Clark sensor and biosensor family. *Sens. Actuators, B* **329**, 129168 (2021).
- 20 Kracke, F. *et al.* Robust and biocompatible catalysts for efficient hydrogen-driven microbial electrosynthesis. *Commun. Chem.* **2**, 45 (2019).
- 21 Damgaard, L. R., Risgaard-Petersen, N. & Nielsen, L. P. Electric potential microelectrode for studies of electrobiogeophysics. *J. Geophys. Res.: Biogeosci.* **119**, 1906-1917 (2014).
- 22 Babauta, J. T. *et al.* Multiple cathodic reaction mechanisms in seawater cathodic biofilms operating in sediment microbial fuel cells. *ChemSusChem* **7**, 2898-2906 (2014).
- 23 Babauta, J. T., Nguyen, H. D. & Beyenal, H. Redox and pH microenvironments within *Shewanella oneidensis* MR-1 biofilms reveal an electron transfer mechanism. *Environ. Sci. Technol.* **45**, 6654-6660 (2011).
- 24 Atci, E. *Development of electrochemical microsensors to use in bio-electrochemical systems.* (Washington State University, 2016).

- 25 Babauta, J. T., Nguyen, H. D., Harrington, T. D., Renslow, R. & Beyenal, H. pH, redox potential and local biofilm potential microenvironments within *Geobacter sulfurreducens* biofilms and their roles in electron transfer. *Biotechnol. Bioeng.* **109**, 2651-2662 (2012).
- 26 Luo, S. *et al.* Construction of innovative 3D-weaved carbon mesh anode network to boost electron transfer and microbial activity in bio-electrochemical system. *Water Res.* **172**, 115493 (2020).
- 27 Yu, Y.-Y. *et al.* Three-dimensional electrodes for high-performance bio-electrochemical systems. *Int. J. Mol. Sci.* **18**, 90 (2017).
- 28 Jourdin, L., Raes, S. M. T., Buisman, C. J. N. & Strik, D. P. B. T. B. Critical Biofilm Growth throughout Unmodified Carbon Felts Allows Continuous Bio-electrochemical Chain Elongation from CO₂ up to Caproate at High Current Density. *Frontiers in Energy Research* **6**, doi:10.3389/fenrg.2018.00007 (2018).
- 29 Nielsen, L. P., Risgaard-Petersen, N., Fossing, H., Christensen, P. B. & Sayama, M. Electric currents couple spatially separated biogeochemical processes in marine sediment. *Nature* **463**, 1071-1074 (2010).
- 30 Tefashe, U. M. *et al.* Localized corrosion behavior of AZ31B magnesium alloy with an electrodeposited poly (3, 4-ethylenedioxythiophene) coating. *J. Electrochem. Soc.* **162**, C536 (2015).
- 31 Klett, O., Björefors, F. & Nyholm, L. Elimination of high-voltage field effects in end column electrochemical detection in capillary electrophoresis by use of on-chip microband electrodes. *Anal. Chem.* **73**, 1909-1915 (2001).
- 32 Cord-Ruwisch, R., Seitz, H.-J. & Conrad, R. The capacity of hydrogenotrophic anaerobic bacteria to compete for traces of hydrogen depends on the redox potential of the terminal electron acceptor. *Arch. Microbiol.* **149**, 350-357 (1988).
- 33 Sander, R. Compilation of Henry's law constants (version 4.0) for water as solvent. *Atmos. Chem. Phys.* **15**, 4399-4981 (2015).
- 34 Infantes, D., González del Campo, A., Villaseñor, J. & Fernández, F. J. Kinetic model and study of the influence of pH, temperature and undissociated acids on acidogenic fermentation. *Biochem. Eng. J.* **66**, 66-72, doi:10.1016/j.bej.2012.04.017 (2012).
- 35 Jourdin, L. & Burdyny, T. Microbial electrosynthesis: where do we go from here? *Trends in Biotechnol.* **39**, 359-369 (2021).
- 36 Picioreanu, C., Katuri, K., Head, I., van Loosdrecht, M. C. & Scott, K. Mathematical model for microbial fuel cells with anodic biofilms and anaerobic digestion. *Water Sci. Technol.* **57**, 965-971 (2008).
- 37 Atci, E., Babauta, J. T. & Beyenal, H. A hydrogen peroxide microelectrode to use in bio-electrochemical systems. *Sens. Actuators, B* **226**, 429-435 (2016).
- 38 Lee, J.-H., Seo, Y., Lim, T.-S., Bishop, P. L. & Papautsky, I. MEMS needle-type sensor array for in situ measurements of dissolved oxygen and redox potential. *Environ. Sci. Technol.* **41**, 7857-7863 (2007).
- 39 Beyenal, H., Davis, C. C. & Lewandowski, Z. An improved Severinghaus-type carbon dioxide microelectrode for use in biofilms. *Sens. Actuators, B* **97**, 202-210 (2004).
- 40 De Beer, D., Schramm, A., Santegoeds, C. M. & Kuhl, M. A nitrite microsensor for profiling environmental biofilms. *Appl. Environ. Microbiol.* **63**, 973-977 (1997).
- 41 Jeroschewski, P., Steuckart, C. & Kühl, M. An amperometric microsensor for the determination of H₂S in aquatic environments. *Anal. Chem.* **68**, 4351-4357 (1996).
- 42 VanHoudt, P., Lewandowski, Z. & Little, B. Iridium oxide pH microelectrode. *Biotechnol. Bioeng.* **40**, 601-608 (1992).
- 43 Lewandowski, Z., Lee, W. C., Characklis, W. G. & Little, B. Dissolved oxygen and pH microelectrode measurements at water-immersed metal surfaces. *Corrosion* **45**, 92-98 (1989).
- 44 Nielsen, M., Larsen, L. H., Ottosen, L. D. M. & Revsbech, N. P. Hydrogen microsensors with hydrogen sulfide traps. *Sens. Actuators, B* **215**, 1-8 (2015).
- 45 Revsbech, N. P. An oxygen microsensor with a guard cathode. *Limnol. Oceanogr.* **34**, 474-478 (1989).
- 46 de Smit, S. M., Buisman, C. J., Bitter, J. H. & Strik, D. P. Cyclic Voltammetry is invasive on microbial electrosynthesis. *ChemElectroChem* **8**, 3384-3396 (2021).
- 47 Lavender, M. B., Pang, S., Liu, D., Jourdin, L. & Ter Heijne, A. Reduced overpotential of methane-producing biocathodes: Effect of current and electrode storage capacity. *Bioresource Technology* **347**, 126650 (2022).

- 48 Pereira, J. *et al.* The effect of intermittent anode potential regimes on the morphology and extracellular matrix composition of electro-active bacteria. *Biofilm* **4**, 100064 (2022).
- 49 Caizán-Juanarena, L., Sleutels, T., Borsje, C. & ter Heijne, A. Considerations for application of granular activated carbon as capacitive bioanode in bio-electrochemical systems. *Renewable Energy* **157**, 782-792 (2020).
- 50 Wiesenburg, D. A. & Guinasso Jr, N. L. Equilibrium solubilities of methane, carbon monoxide, and hydrogen in water and sea water. *Journal of chemical and engineering data* **24**, 356-360 (1979).

Supporting information

Reactor operation

The reactor anolyte and catholyte were recirculated at 10 L/h. The total volumes of the catholyte and anolyte were respectively 360 and 310 ml. To provide similar conditions to biotic operation, the catholyte recirculation bottle was sparged with CO₂ and N₂ with rates of respectively 100 LN/d and 233.3 LN/d. The anolyte recirculation bottle was sparged with N₂ to remove oxygen produced at the anode. After the catholyte recirculation bottle, pH measurement (QMP108X, Q-is, Oosterhout, the Netherlands) and control at 5.8 (Ontwikkelwerkplaats, Elektronica ATV, the Netherlands) were placed in the recirculation ("recirculation pH"). The reactor was operated in a temperature controlled cabinet (30°C) in abiotic mode, microbial growth was prevented by leaving out ammonium from the medium. The catholyte had the same composition as the abiotic catholyte from de Smit, et al.⁴⁶, the anolyte consisted of 7.5 g/L Na₂HPO₄·2H₂O, 3.0 g/L KH₂PO₄, 0.05 g/L MgSO₄·7H₂O, 0.01 g/L Ca(OH)₂. The catholyte part of the reactor was operated in batch mode and the anolyte was fed to the reactor with a hydraulic retention time of 4 days. During Open Cell Voltage operation (OCV), the cathode and anode were physically disconnected by removing the connection cable. During continuous operation, the reactor was current controlled (-200 mA, -10 kA/m³, unless stated otherwise) by a n-stat Ivium potentiostat (IVIUM, The Netherlands). The cathode potential was measured against a Ag/AgCl 3M KCl reference electrode (QM710X, Q-is, Oosterhout, the Netherlands), connected via a capillary, filled with gelified 3M KCl, positioned 5 mm above the top cathode (Figure S5.1A, cathode reference). After start-up, the reactor cathode potential was left to stabilize for at least 24 hours to perform measurements in steady state conditions.

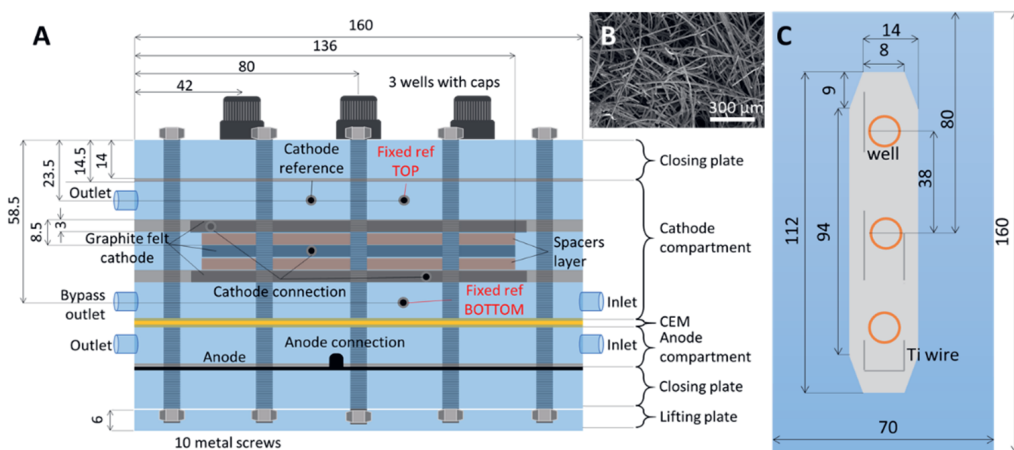


Figure S5.1. Electrochemical reactor with three cathode layers and three profiling wells (A). In C, a top view of the cathode flow through plate is shown with the location of the three measuring wells. The graphite felt had a 3D structure (B, SEM image). Measurements are shown in mm.

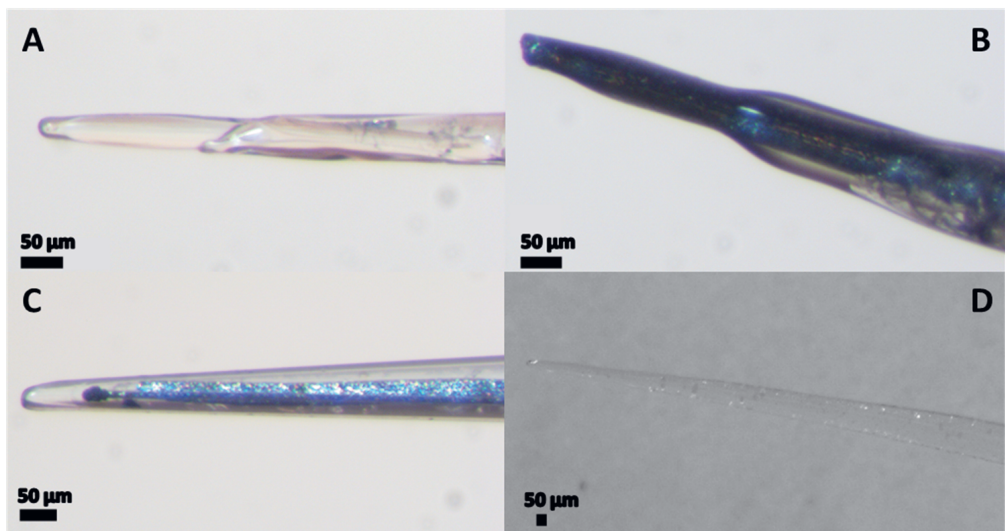


Figure S5.2. Macroscopic images of the tips of the pH (A), ORP (B), hydrogen (C) and electric field potential (D) microsensor.

Table S5.1. Current distribution over three graphite cathode layers connected in parallel at different distances from the anode (Figure 5.1A).

	Cathode layer	Current (mA)	Stdev during 3 days (mA)
Reactor 1	Top	-17.2	1.8
	Middle	-20.3	1.3
	Bottom	-163.8	0.3
Reactor 2	Top	-16.1	3.1
	Middle	-19.4	4.6
	Bottom	-164.1	6.5

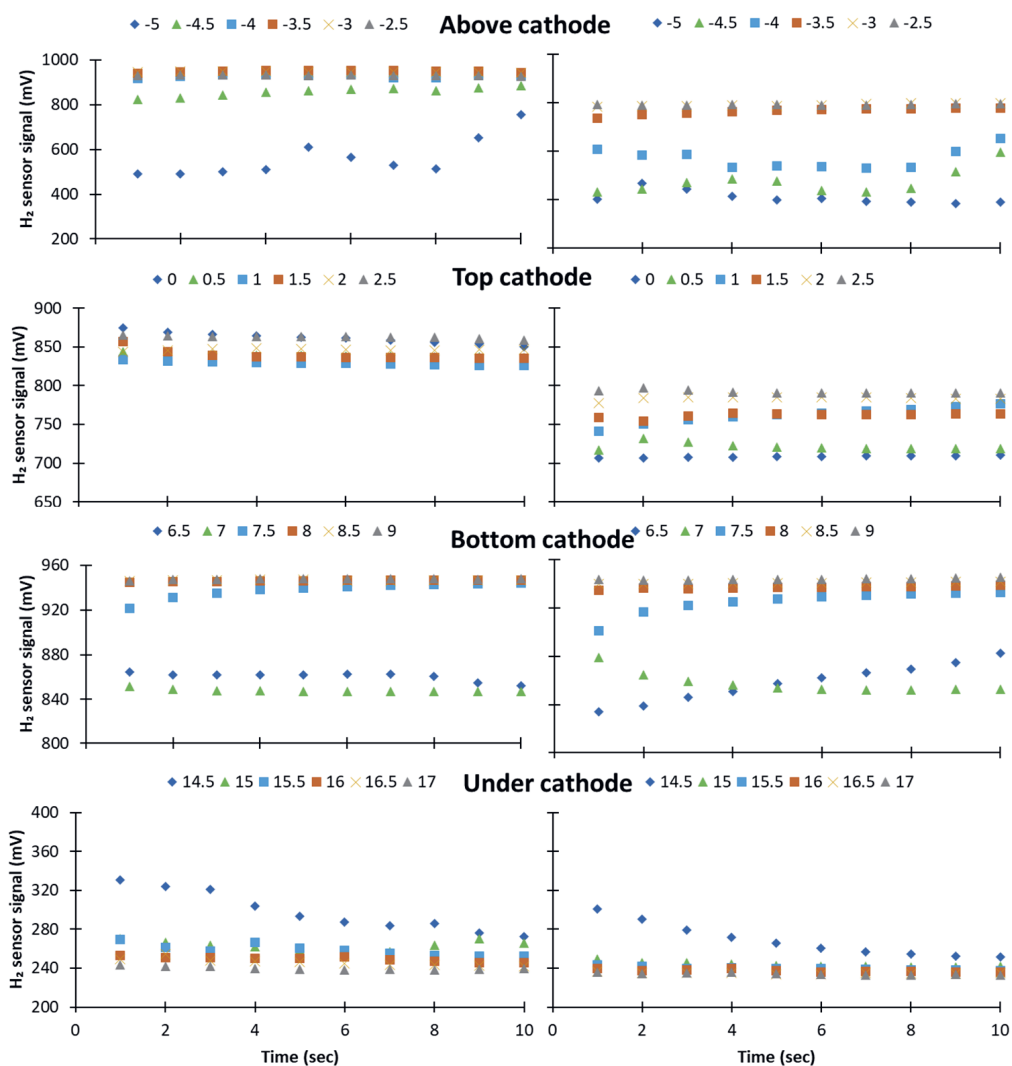
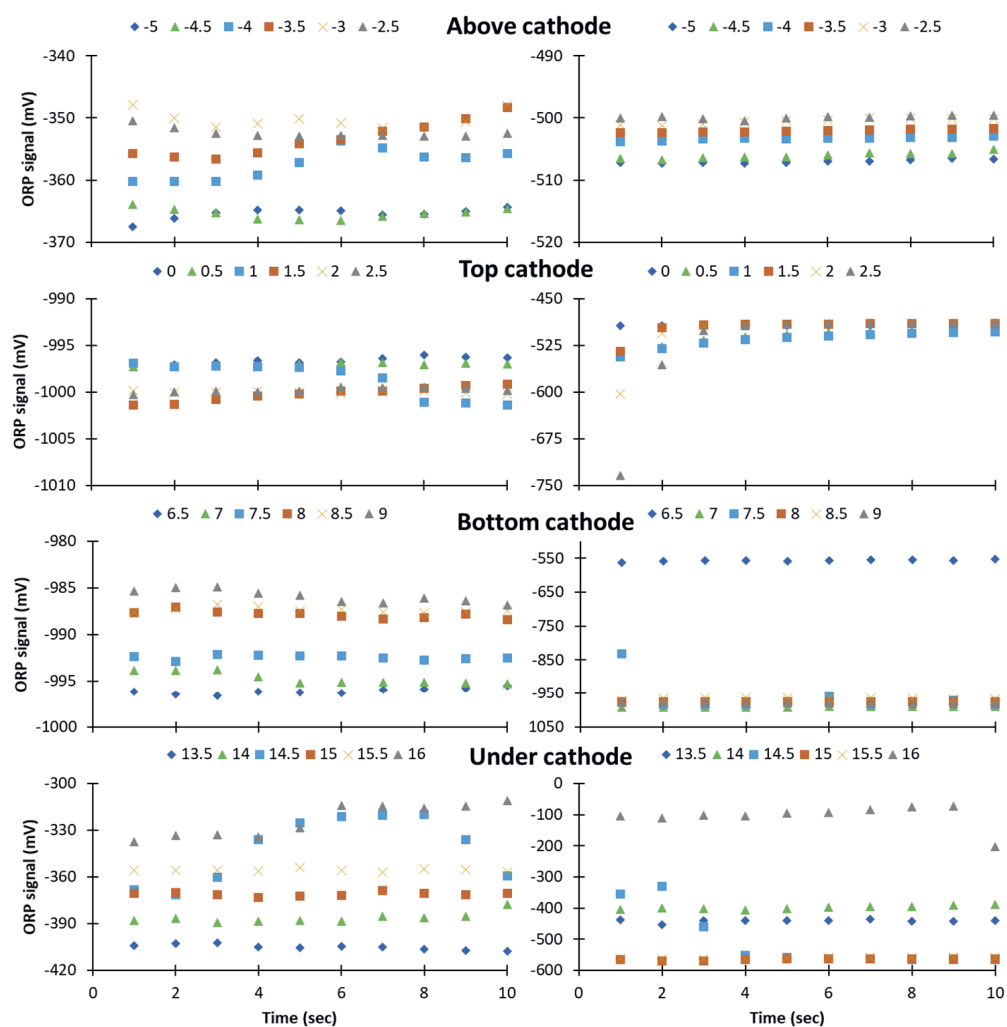


Figure S5.3. Hydrogen microsensor response over 10 seconds measured in duplicate (left and right) at different depths, indicated in legend (normalized to cathode top). The response times were measured in an abiotic reactor with a 9 mm graphite felt cathode controlled at -0.85 V vs Ag/AgCl.



5

Figure S5.4. ORP microsensor response over 10 seconds measured in duplicate (left and right) at different depths, indicated in legend (normalized to cathode top). The response times were measured in an abiotic reactor with a 9 mm graphite felt cathode controlled at -0.85 V vs Ag/AgCl.

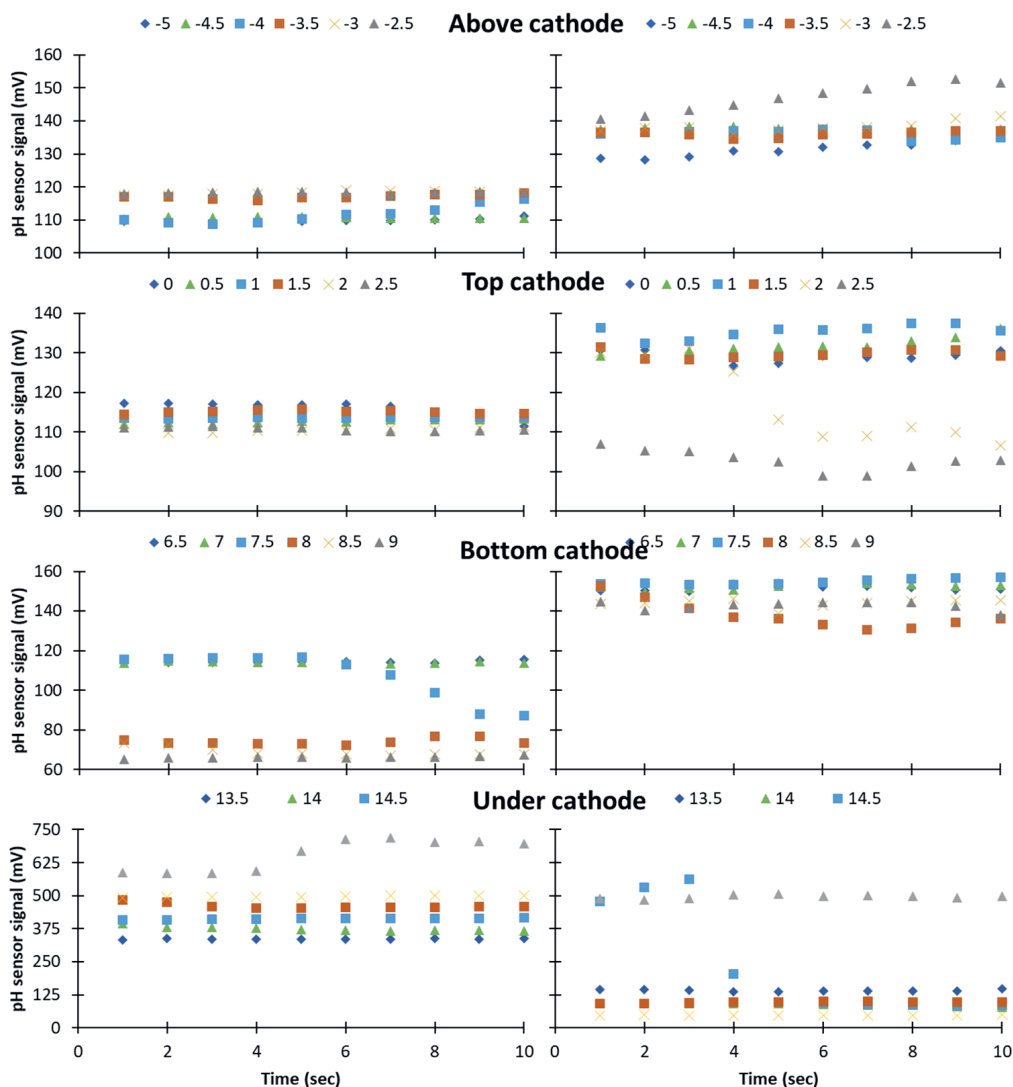


Figure S5.5. pH microsensor response over 10 seconds measured in duplicate (left and right) at different depths, indicated in legend (normalized to cathode top). The response times were measured in an abiotic reactor with a 9 mm graphite felt cathode controlled at -0.85 V vs Ag/AgCl.

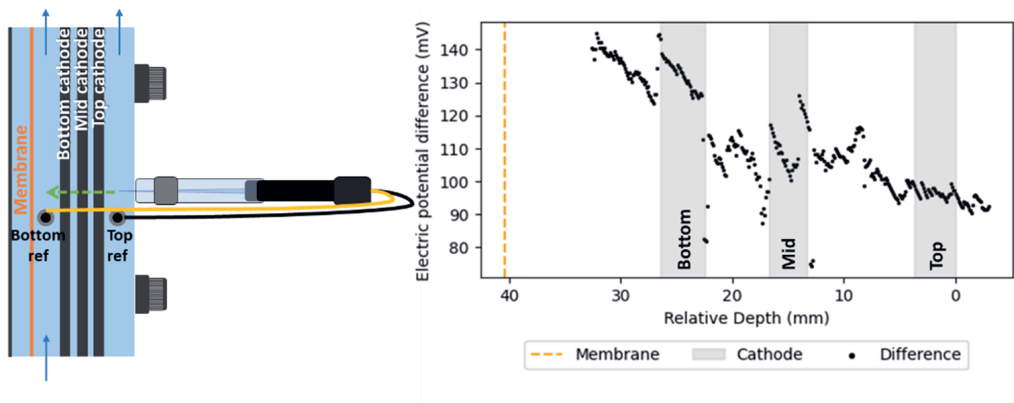


Figure S5.6. Difference between electric potential measured versus the fixed top reference (left, black) and fixed bottom reference (left, yellow) over the depth of the reactor.

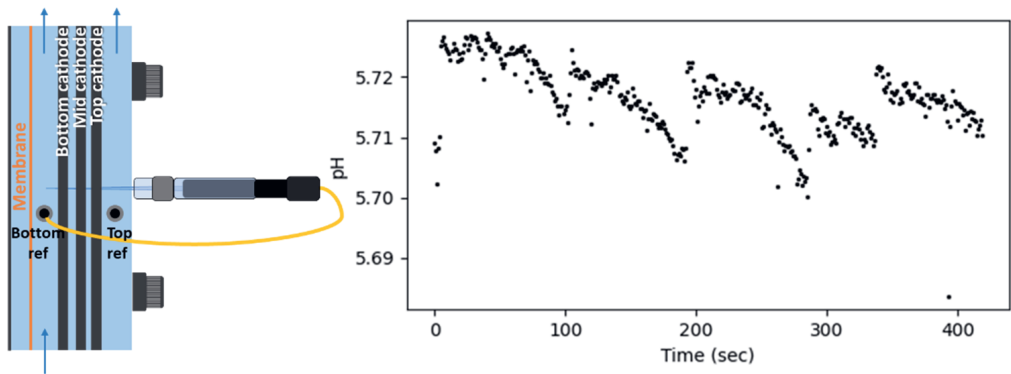


Figure S5.7. pH microsensor response over 7 minutes with tip placed right next to the bottom reference electrode (depth 30 mm). An abiotic CO_2 -fed reactor was controlled at -50 mA during this experiment.

pH microsensor measurement during intermittent current

The offset between the pH microsensor and the recirculation pH increased with increasing current (Figure 5.8). Based on this result, it was hypothesized that shortly disconnecting the current supply would remove the interference and result in reliable values from the microsensor. To test this, intermittent current was applied to the cathode, whilst measuring the pH. Current was applied intermittently to the cathode, with 40 s of control at -200 mA alternated by 7 s of open cell voltage. The pH microsensor was placed in the reactor with the tip right next to the top fixed reference electrode. The signal of the microsensor was measured both versus the top fixed reference and versus the bottom fixed reference at 35 mm from the microsensor tip (Figure S5.7, left).

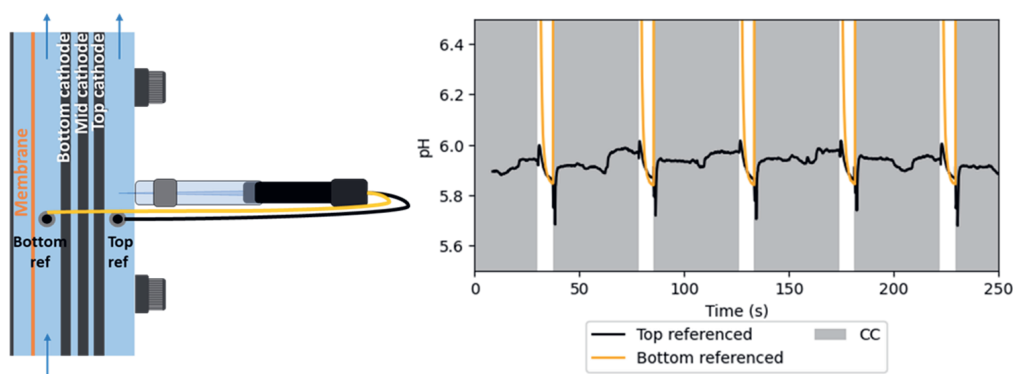


Figure S5.8. pH microsensor measurements during intermittent current (right). The cathode current was -200 mA for 40 s (grey planes) and turned off for 7 sec (Open Cell Voltage, white planes). The pH microsensor tip was placed next to the top fixed reference electrode positioned at -5 mm (left). The signal with the top reference (black) is overlaid with the signal with the bottom reference electrode positioned 35 mm lower than the top reference (yellow).

When the pH microsensor tip was measured with the top fixed reference electrode, the signal during current control and during open cell voltage is similar (Figure S5.7, black line). This shows that that signal was unaffected by the applied current and thus reliable^{8,21}. During the 7 sec open cell voltage, the signal dropped approximately 0.1 pH unit (Figure S5.7). When no current is applied to the cathode, no additional hydrogen is formed from the protons, while the continuous recirculation causes mixing with the bulk liquid. Therefore, after stopping the current supply, the local pH will eventually be equal to the bulk pH (5.8).

When the pH microsensor tip was measured against the bottom fixed reference electrode, the pH signal gave a value around 16 to 17 during current controlled operation (Figure S5.7, grey planes, yellow line). This corresponds to approximately 600 mV offset (59 mV per pH unit), which was also the difference measured between the two fixed reference electrodes (bottom and top, Figure S5.6 left). After the switch to open cell voltage operation, the pH microsensor first shows a rapid decrease and then a slower decrease (white planes, yellow line).

For the measurement shown in Figure S5.6, the potentiometric sensor measurements with different reference electrode positions reach the same value during open cell voltage. This supports the use of intermittent current as a method to measure reliable pH during the intervals

without supplied current, representative for the current controlled situation. However, in more mature systems or systems with a grown biofilm, the potentiometric sensor measurements with different electrode positions did not reach the same value during open cell voltage. This suggests that 7 seconds was found too short for the electric interference to disappear and the bottom referenced signal to reach reliable values (Figure S5.8). Applying open cell voltage for longer time is likely to make the electric interference disappear. However, applying longer open cell voltage time would result in the gradients to disappear and the bulk pH would be measured. In that case, the measurement would not be representative anymore for the situation with applied current.

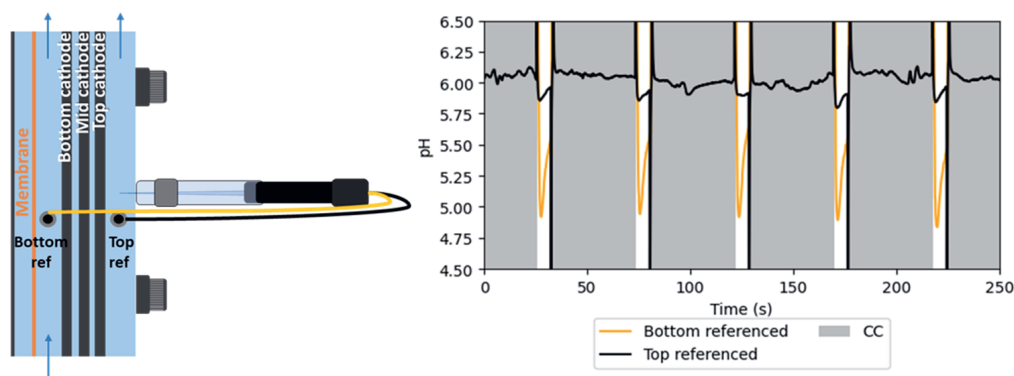


Figure S5.9. pH microsensor measurements during intermittent current (right). The cathode current was -200 mA for 40 s (grey planes) and turned off for 7 sec (Open Cell Voltage, white planes). The pH microsensor tip was placed next to the top fixed reference electrode positioned at -5 mm (left). The signal with the top reference (black) is overlaid with the signal with the bottom reference electrode positioned 35 mm lower than the top reference (yellow).

For different systems, a similar experiment as described here can be performed to determine whether intermittent current can be applied to perform potentiometric measurements. Additionally, the response of the electric potential microsensor after switching off the current can be measured to determine the time before electric interference disappears. When this time is short enough to still measure local conditions representative for the situation with applied current, the intermittent current method is applicable. Besides the reliability of the potentiometric measurement, the effect of applying intermittent current on (microbial) processes within electrosynthesis systems should be considered before using the method⁴⁷⁻⁴⁹.

Considerations for practical applications

When using the local electric potential correction, placing fixed reference electrodes near positions of interest is recommended to allow verification measurements and ensure high accuracy at the points of interest. Additionally, the location of the potentiometric microsensor tips needs to be precise. Figure 5.6 shows that especially at locations with high current (depth 22-33 mm), the electric potential can differ substantially per location. Thus, a deviation in the determination of the exact microsensor tip location will cause a deviation in the correction. Measuring the relative distance between the tips of two sensors (e.g. EP and potentiometric

sensor of interest) can be accurately performed under a macroscope. Another important factor is system stability. Since the local electric field potential measurement involves profiling the reactor with two different sensors (sensor of interest and electric potential sensor), the local electric field needs to be stable between these two profiling cycles.

Protocol microsensor calibration

Note: all calibrations can be performed with the microsensors still in the plastic protective cover. Perform calibration before (and after) each profiling run, to check similarity of calibration results

Hydrogen sensor

Calibration

1. Connect sensor to amplifier
2. Polarize the sensor at the value described in the manual (latest value 100 mV), wait until the signal is stable
3. Start software; connect to motor and amplifier
4. Place sensor in closed glass container with demi water (or measuring matrix, recommended), gas sparger connection and offgas connection for calibration *NB: ensure no gas could build up*
5. Add calibration point 0
6. Retract the sensor from the liquid
7. Connect sparging connection to H₂ gas bottle and flush for approximately 15 min
8. Insert the sensor back into the liquid
9. Ensure the liquid within the protective sleeve is well mixed with the sparged and saturated bulk (e.g. by moving sensor up and down)
10. When mV signal is stable for at least 5 min, add calibration point corresponding to saturation ($\mu\text{mol/L}$)

Correction hydrogen saturation point for salinity and temperature

The maximum saturation point for hydrogen needs to be corrected for temperature and salinity. After profiling, the highest calibration point needs to be replaced with:

mV corrected for the temperature of the measurement

The mV signal given when measuring a maximal saturated solution is dependent on temperature. This dependence is sensor dependent and thus needs to be remade for every new sensor. The dependence can be determined by measuring the mV of the signal in a maximal saturated solution at different temperatures (Figure S5.9).

Saturation concentration at the salinity (and temperature) of the measurement solution

The saturation concentration can be found in literature⁵⁰, once the salinity of the measured solution is known.

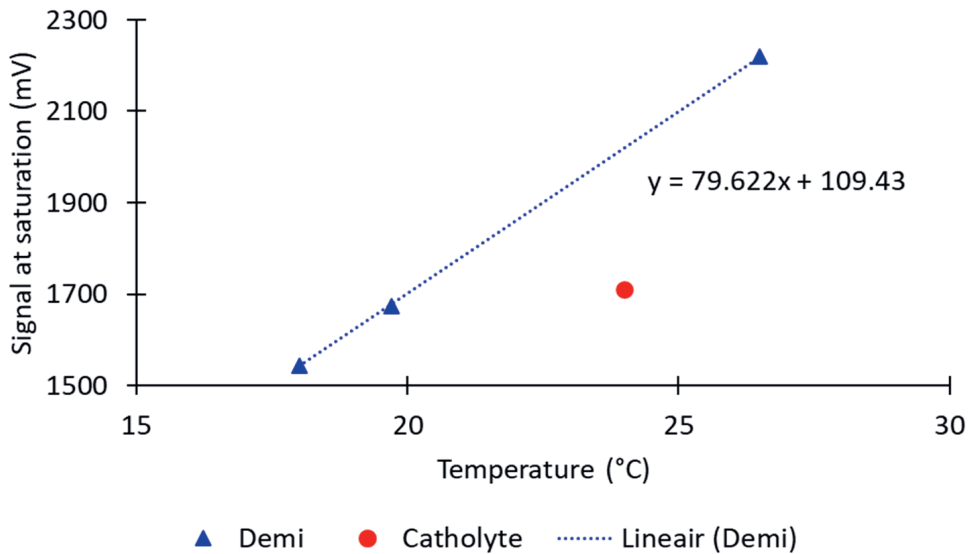


Figure S5.10. Millivolt signal of H_2 -signal at maximum saturation at three different temperatures in demi water and catholyte. This line can be used to correct for temperature when calibration temperature differs from measuring temperature.

pH sensor

The pH measurements are temperature sensitive. Therefore, it is important to store the buffers at the temperature of your measuring conditions.

1. Connect the pH microelectrode to the amplifier and connect a reference electrode to the microsensor cable
in this study Ag/AgCl was used, make sure the reference is the same for measuring and calibrating; the reference was connected to a glass capillary with a porous membrane to fit the reference electrode together with the reference electrode in the buffer tubes
2. Start software; connect to motor and amplifier
3. Rinse pH microelectrode (carefully) and reference electrode tip (capillary)
4. *NB: don't wipe glass microelectrode tip with paper, only wipe plastic cover*
5. Place both the microelectrode and reference electrode tip (capillary) in the buffer tube
6. Starting from 7, calibrate with multiple buffers in the range of interest (in this study: 7, 4, 6, 9, 10)

Sensor heights and motor tool

Note that the sensors have different lengths. Depending on the sensor length, the height of the sensor in your system will be different when positioned at the same height of the motor tool. Therefore, correct the motor tool heights according to the sensor lengths. It is recommended to always measure a new microsensor since the handmade lengths might differ.

Protocol profiling

1. Move the step motor (A) with motor control software to the highest position. This can be skipped if the step motor was return to position 0 after latest profiling
2. Lift the micromanipulator manually to highest with knob B (B)
3. Fix MES cell to the tilting ground plate with glue clamp to with the microsensor clamp (C) placed above the measuring well of interest
4. Widen Microsensor clamp (C)
5. Connect and perform corresponding calibration on selected microsensor, with protective tube on. (see appendix protocol microsensor calibration)
6. Place the microsensor on sliding rail plate (milled wooden shelf) and remove the plastic protection cover by sliding it through the groove while holding the microsensor at the head to prevent touching the wood with the glass tip
7. Adjust the profiling sleeve to the microsensor by sliding the microsensor over the groove into the sleeve (the sleeve should be stick to the plastic neck of the microsensor with residual silicon grease, apply some if not)
8. Set aside in a safe place for mounting

Mounting microsensor (to be done fast, usually within 5 min)

9. Stop both recirculation pumps (and if needed acid/base supply)
10. Close the cathode inlet and outlet valves of MES cell to detach from rest of the recirculation.
11. Open cap of target profiling well
12. Clamp the microsensor at its head, align the top of the microsensor head with top of the clamp (as precise as possible, this will determine the positioning of the cathode). Be careful not to touch sensor tip with anything
13. Move the planer position of centre with knob D (D, two knobs) to target the profiling well, with sensor tip as reference
14. Drop the micromanipulator to lowest manually with knob B (B). Make sure microsensor enter the well without touching

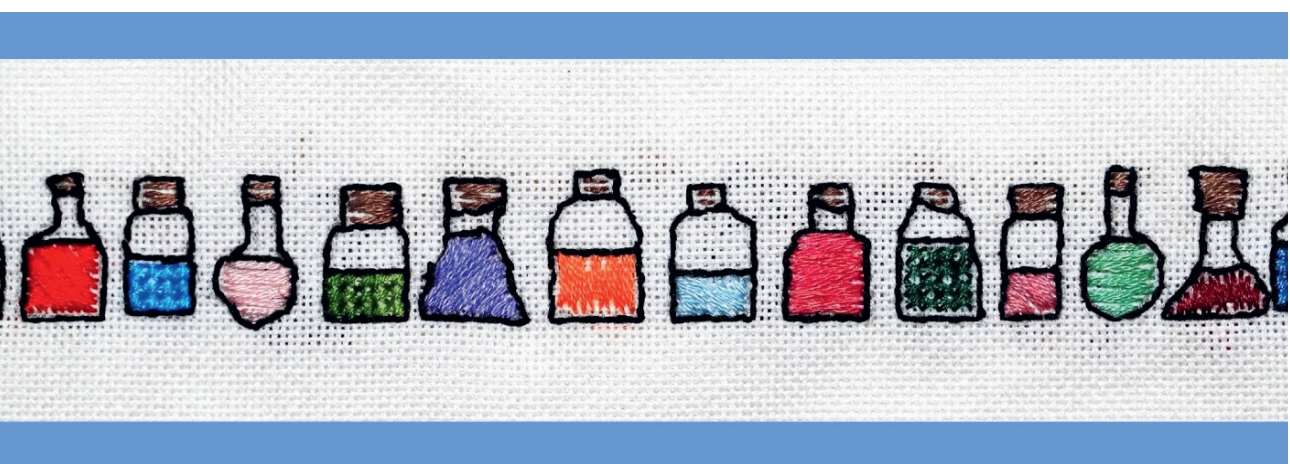
15. Slide down to detach the profiling sleeve with plastic neck. Avoid touching the glass part of the microsensor. Screw the sleeve to the well hand tight
16. If necessary: attach N₂ flushing tube to the flushing spot
17. Move microsensor to the vertical position with a small gap between plastic neck and sleeve tube (position depends on motor settings and microsensor-well combination)
18. Again, adjust the planer position of centre with knob D to target the profiling well, but this time with plastic neck as reference. Apply extra silicon grease to the gap, before finishing the round, detach the N₂ flushing and replace with closing part
19. Move the microsensor deeper with software to complete the seal. Make sure the forwarded distance is long enough to provide resistance to avoid leakage. You can apply grease while microsensor is moving deeper to provide more seal
20. Make sure the whole periphery is sealed with silicon grease, no liquid or gas escape is formed

Testing the seal

21. Open the cathode inlet and outlet valves of MES cell to connect to rest of the recirculation
22. Start catholyte recirculation, observe for a minute if catholyte is leaking from the sleeve
 - a. Leaking -> Stop recirculation, close valve, and repeat from step 19
 - b. Not leaking -> go forward
23. Move Microsensor to the micro-profiling safe position and ready for micro-profiling.

General reminder for all microsensors

Loosen the clamp and turn microsensor 90° to target new piercing site between each micro-profiling cycle. Do this in safe position and mind not to change the vertical position of microsensor. Apply new silicone grease before starting next cycle.



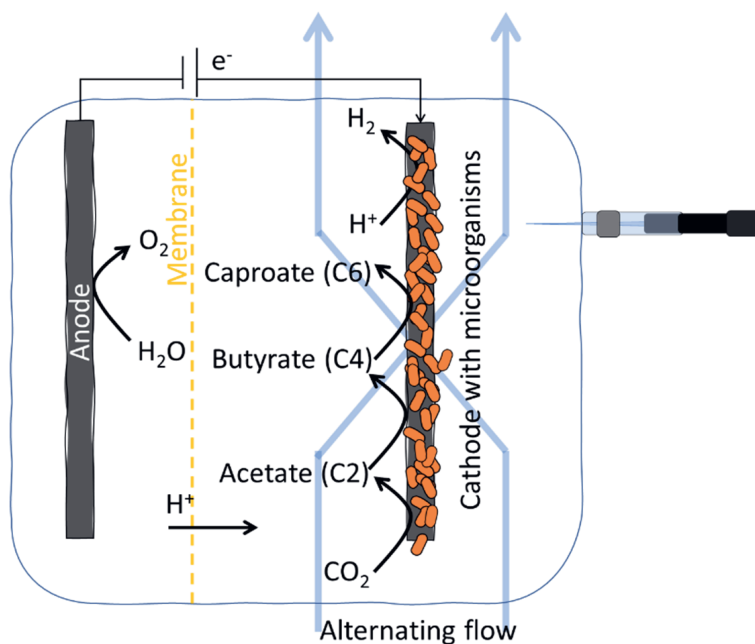
Chapter 6

Alternating direction of catholyte forced flow through 3D-electrodes improves start-up time in microbial electrosynthesis at applied high current density



Abstract

Microbial electrosynthesis is an uprising concept for the combined carbon dioxide reduction and electricity storage in the form of green chemical compounds. Although several proof of principle studies show great promise, mass-transfer limitations of substrates, protons and products remains one of the issues that needs to be addressed to bring the systems towards greater scale applications. A previously tested solution formed force flow-through catholyte recirculation, but this set-up encountered difficulties with gas accumulation during start-up at higher current densities ($\sim 10 \text{ kA/m}^3$), creating the need for a bypass to release gas. In this study, start-up at high current density was achieved without gas accumulation by using an alternating flow-through regime. This regime decreased the operating energy input from 221 to 136 kWh per kg of produced hydrogen and reached acetate production within 10 days after start-up at high current density and elongation to *n*-caproate after 45 days. Mass-transfer studies were included by microsensor measurements of local conditions (hydrogen concentration, pH) combined with thermodynamic calculations at the start and end of 60-days biotic experiments. The microorganisms on the cathode decreased pH gradients and consumed the formed hydrogen. The presence of *Clostridium sensu stricto* 12 and *Firmicutes* BRH-c20a species were related to chain elongation activity, and the presence of *Methanobrevibacter* was linked to methanogenesis activity. By identifying the effects of different flow-through strategies on local concentrations and functional microbial groups, this work provides insights on the optimal conditions for microbial CO_2 conversion and highlight the application potential of microbial electrosynthesis.



6.1 Introduction

Microbial electrosynthesis (MES) is a promising technique for the storage of electrical energy in chemical compounds. Basic bio-electrochemical systems typically consist of two electrodes, separated by a membrane. On the anode, an oxidation reaction provides electrons, which gain energy by an applied potential and are then used in reduction reactions on the cathode. The reduction reaction on the cathode is typically catalysed by a microbial catalyst. The integration of microbial and electrochemical catalysis allows for the electricity-driven formation of multi-carbon compounds from waste streams, such as CO₂. Bio-electrochemical CO₂ conversion, also called electro-fermentation, has yielded various products such as methane, alcohols, proteins and fatty acids¹⁻⁵. Although these proofs of concept are promising, several steps need to be taken to understand how electro-fermentations systems could be best designed and scaled-up. An important focus point to work towards upscaling is the improvement of substrate and electron availability for the microorganisms on the cathode¹. By incorporating microorganisms on the cathode, a biofilm is formed, to which electrons can be supplied, directly or indirectly via e.g. hydrogen formation. The growth and productivity of the biofilm depends on its access to substrate and electrons and the removal of products⁶. A dense biofilm (>400 µm) facilitates high electron uptake rates and improved biocatalytic performance^{7,8}, but inevitably also leads to mass-transfer limitations. Therefore, pH and hydrogen gradients are likely to occur, resulting in different local conditions at the electrode surface when compared to the bulk conditions⁹⁻¹³. The pH gradients affect the microbial community selection and thermodynamic limitations, as well as substrate and electron donor availability^{14,15}.

To diminish the effects of significant local gradients of pH, substrates, products or energy (like hydrogen), mass-transfer can be improved by changing the flow-regime¹⁶. Previously, 3-dimensional flow-through electrodes have been demonstrated as a solution for better mixing of the anode or cathode chamber^{17,18}. Although these flow-through configurations worked well for previous systems, problems were encountered when starting the flow-through configured systems at high current density (i.e. systems operating on at least -10 kA/m³). Starting bio-electrochemical systems at high current density leads to accumulation of excess hydrogen gas between the membrane and low-porous electrode. This hydrogen gas accumulation hinders the contact between the electrolyte, the membrane, and the electrode, which introduces for example high electrolyte resistances¹⁹. As a temporary solution, a bypass was used to release accumulated gaseous hydrogen via an extra electrolyte outflow port, but electrolyte could also flow through the bypass (Chapter 3, 4). About 50% of the recirculation flowed alongside the cathode through the bypass instead of through the cathode. As a consequence of this measure, about 50% of the nutrients from the recirculated medium cannot reach the biofilm and the decreased flow velocity through the biofilm can result in mass-transfer limitations. Both the decreased nutrient supply and mass-transfer limitations can negatively affect the cathodic biofilm activity. Therefore, the recirculation flow through the cathode chamber needs to be optimized to allow start-up at high current densities in a way that the mentioned hydrogen accumulation issues are circumvented.

In this study, the use of alternating direction of catholyte flows through porous electrodes was assessed to decrease mass transfer issues and the start-up time of microbial electrosynthesis at applied high current densities was improved. The recirculation flow-through was alternated

from two sides of the cathode to allow alternate build-up gas removal and hydrogen transfer to the cathode, which removed the need for a bypass. Additionally, local distribution of electrical current, hydrogen concentration and pH at different locations in the cathode was studied with microsensor measurements. The local conditions were used for identification of mass-transfer limitations and local thermodynamic and microbial analysis. The links between local conditions and presence of certain microorganisms give valuable insights about the conditions required for optimization of microbial-electrochemical conversion processes.

6.2 Materials and Method

6.2.1 Reactor setup and flow-through configuration

The reactor setup for both the abiotic and biotic experiments was used as described by Chapter 5. In short, plexiglass flow-through plates were used for the reactor assembly, with a Ti/Pt-Ir MMO anode (Magnet Special Anodes BV, Netherlands) and a graphite felt cathode (3 mm thick, Rayon Graphite Felt, CTG Carbon GmbH, Germany) with three layers separated by three layers of plastic mesh spacers and connected in parallel to a n-stat potentiostat (IVIUM, Netherlands) via titanium wire (0.8 mm thick, grade 2, Salomon's metalen, Netherlands) with 1 Ω between each connection and the working electrode plug (Figure 6.1). The anode and cathode compartment were separated by a cation exchange membrane (21.3 cm² projected surface area, Fumasep FKS, Fumatech BWT GmbH, Germany). For the first abiotic flow experiment (Figure 6.2), a bypass was used as described by de Smit et al. (Chapter 5). For the following experiments, alternating flow-through catholyte recirculation was used. To allow for alternating flow-through, some adaptations were made. Solenoid valves (SMC, type VDW22JA) were installed at four points around the cathode chamber (Figure 6.1, A-D). The valves were controlled with a relay module (Fieldpoint FP-DO-410). The relay module was controlled with computer software (LabVIEW 2015). The code used in LabVIEW can be found in the Supporting Information (SI Figure S6.1). The recirculation was alternated between two directions: either from valve D to valve A or from valve C to valve B (Figure 6.1).

Besides the valves, analogous potentiometers (Fieldpoint FP-AI-110) were installed to measure the cell potential, current distribution, and the individual cathode potentials. The cathode potentials were measured against the top reference (QM710X, Q-is, Oosterhout, Netherlands) (Figure 6.1) and not corrected for the electrolyte resistance. However, for the calculations, the cathode potential of cathode 3 was used for all three cathode layers, since it was demonstrated that the electric field potential offset between the top reference and cathode layer 3 was negligible (de Smit et al. Chapter 5).

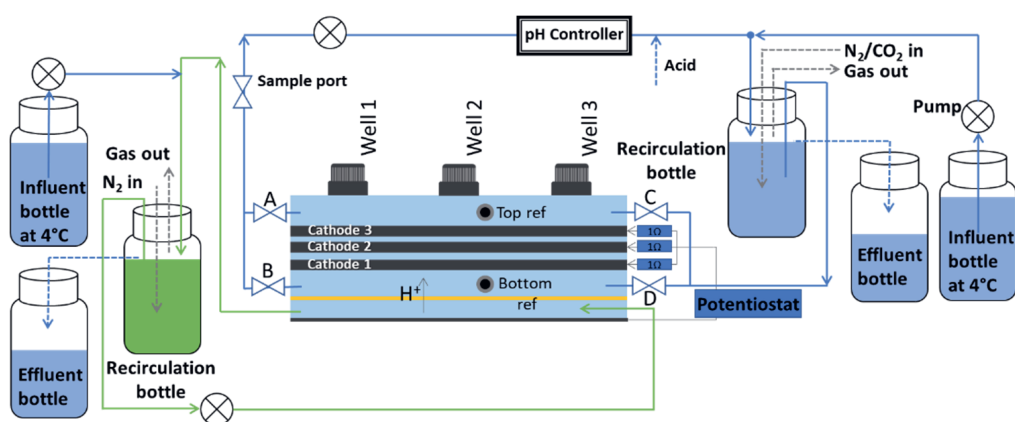


Figure 6.1. Schematic reactor setup of electrochemical reactor with switching valves (A-D) used for the alternation of flow-through electrolyte recirculation. The anolyte recirculation is shown in green for viewing purposes.

Regarding the reactor operation, all parameters were set as described by de Smit et al. (Chapter 5): temperature 30°C, recirculation flowrate 10 L/h, -200 mA from anode to cathode, 100 LN/h CO₂ and 233.3 LN/h N₂ purging in catholyte recirculation, N₂ purging in anolyte recirculation. The pH was measured (QMP108X, Q-is, Oosterhout, the Netherlands) in the catholyte recirculation and controlled (Ontwikkelwerkplaats, Elektronica ATV, the Netherlands) at 5.8 with the addition of 1 M HCl. The reactor media compositions changed slightly with the switch from abiotic to biotic experiments. The abiotic catholyte composition was the same as described by de Smit, et al.²⁰, while the abiotic anolyte consisted of 7.5 g/L Na₂HPO₄·2H₂O, 3.0 g/L KH₂PO₄, 0.05 g/L MgSO₄·7H₂O, 0.01 g/L Ca(OH)₂. For the biotic experiments, ammonium was added to the electrolytes (0.2 g/L NH₄Cl and 0.18 g/L (NH₄)₂CO₃ respectively in the catholyte and anolyte). The biotic catholyte also contained 3.23 g/L (98%) sodium 2-bromoethanesulfonate. The anolyte and catholyte media were added at flow rates corresponding with hydraulic retention times of respectively 4 and 14 days. The biotic reactors were inoculated with 10 vol% fresh inoculum, acclimatized with comparable conditions (fed with CO₂, operated at -200 mA to graphite felt electrode, bulk pH 5.8, temperature 30°C), which showed production of fatty acids (C2-C4). The inoculation moments were day 5 and day 10.

6.2.2 Analyses

The volatile fatty acid and alcohol concentrations in the recirculation catholyte were measured three times a week during the biotic experiments. For this, 2 mL catholyte was sampled from the reactor and stored in the freezer until analysis. Analysis was performed 1-2 times per week. On the day of the analysis, the samples were centrifuged at 10 000 rpm for 10 minutes. Next, the sample was diluted 10 or 20 times to a total volume of 1.5 mL, depending on the concentrations of VFAs. 1.35 mL diluted sample was mixed with 0.15 mL 15% formic acid to acidify the sample. 1 µL was injected with an autosampler in a gas chromatograph with a flame ionization detector (GC-FID) (Agilent 7890B). The FID detects alcohols (Methanol to hexanol) and VFA's (C2-C8).

From day 40 of the biotic phase, the off-gas was measured three times per week. Since the flow-through was alternated, it was expected that the hydrogen off-gas concentration might fluctuate

with the fluctuating flow. To measure a representative, average hydrogen fraction in the off-gas, off-gas was collected in a 10L gas bag (Calibrated instruments, Inc.) for 30 minutes. The nitrogen and carbon dioxide concentrations were analysed on a GC-TCD (Shimadzu GC-2010), and the hydrogen concentration was analysed on a GC with a thermal conductivity detector (TCD) (Agilent HP 6890 GC). Methane was analysed on a GC with a pulse discharge detector (PDD) (Global Analyzer Solutions CompactGC).

6.2.3 Microsensor analyses

During both abiotic and biotic experiments, microsensor measurements (with LS18 laboratory stand, MM3-2 micro-manipulator, MC-232 Motor Controller of Unisense A/S, Denmark) were used to measure local pH (pH-50, Unisense A/S, Denmark) and hydrogen (H₂-50, Unisense A/S, Denmark) concentrations. The method was applied as described in Chapter 5. Important to mention is that during biotic operation, the graphite felt cathode was never pierced by the microsensor to prevent changes of the flow-through path. The graphite felt cathode was only pierced on day 60 of the experiment, during the measurements of the hydrogen and pH profiles at the end of the biotic phase. Electric Potential (EP-100, Unisense A/S, Denmark) measurements revealed that the local electric field potential was affected by the alternating flow-through operation. Therefore, the EP correction method described in Chapter 5 was not applicable. To obtain reliable pH logging values, the pH microsensor tip was placed near the fixed reference electrodes (3M KCl Ag/AgCl, QM710X, Q-is, Oosterhout, Netherlands) (top and bottom, Figure 6.1). Measurements with the EP sensor were used to determine the exact location with 0 mV offset between the EP sensor and the fixed reference electrode (both Ag/AgCl electrodes). The pH was logged at exactly those locations to ensure there was no electric field interference of the measurements.

6.2.4 Microbial community analysis

6.2.4.1 Samples collection and DNA extraction

The microbial communities at different cathode layers and in the suspension were examined with Next Generation Sequencing. Samples were taken at the end of the 60 day biotic operation, stored at -20°C, and DNA was extracted with the Powersoil DNA isolation kit (Qiagen, USA) according to the instruction manual. The DNA concentration and purity were measured with a NanoDrop spectrophotometer (Thermo Fisher Scientific, Germany).

6.2.4.2 Sequencing of 16S rRNA genes and bioinformatics

The 16S rRNA genes were amplified using full-length primers (SI Table S1) with PCR. Subsequently, the variable V3 and V4 target regions were amplified (simultaneous amplification of Bacteria and Archaea) and the Nextera UD indexes adapters set D (Illumina, USA) was used for index PCR. The sequencing was performed with the V2 kit on the Illumina MiSeq platform and the data was processed with QIIME2 (v. 2019.10)²¹. Briefly, the primer sequence was removed from the demultiplexed forward sequences from PCR primer 341F²² and the resulting ~230 bp reads were denoised with DADA2 single-end option²³, to perform error-correction and interference of exact amplicon sequence variants (ASVs). Subsequently, taxonomic classification was performed with the ASV representative samples using a naïve Bayes classifier, trained on the amplicon of primer set 341F and 805R, extracted from SILVA v. 138 reference database²⁴. Finally, the frequency table was rarefied to 72000 reads per sample and the ASV

counts were agglomerated into genus-level taxonomic groups. For the results of this study, the most significant operational taxonomic unites (OTUs) were presented for each sample, with a cut-off value of 3% relative abundance.

6.2.4.3 Scanning Electron Microscopy imaging

From the cathode layers, Scanning Electron Microscope pictures were taken to visualize the biomass distribution. Samples of cathode (~50 mm²) were stored at 4°C in biotic catholyte and fixed with 2.5% glutaraldehyde for ~4 months at 4°C. Prior to dehydration, the samples were rinsed three times by replacing the liquid with demi water. For the dehydration, the liquid was replaced by graded ethanol solutions (10, 30, 50, 70, 80, 90, 96, and twice 100%) for 10 min each. The samples were dried with critical point drying (Leica EM CPD-030, Leica Microsystems, Germany) with CO₂. The samples were attached on the SEM stubs with carbon glue (Leit-C Conductive Carbon Cement, van Loenen Instruments, the Netherlands) and coated with tungsten sputter coating (12.0 nm, from two sides with 45° angle, Leica SCD 500, Austria) to finalize the preparation for the imaging. The SEM images were obtained with a Magellan 400 SEM (FEI Company, Hillsboro, OR, USA) at an acceleration voltage 2kV and beam current of 13 pA at RT.

6.2.4.4 Calculations

To calculate the power demand per kg produced hydrogen, the cell potential (V_{cell} in V) was used (measured between the anode and the cathode connection before the parallel split), Faraday constant 96485.33 C/mol, 100% electron recovery into hydrogen:

$$96485.33 \frac{C}{mol e^-} * 2 \frac{mol e^-}{mol H_2} * \frac{1h}{3600s} * \frac{1 mol H_2}{2.016 * 10^{-3} kg H_2} * V_{cell} \left[\frac{J}{C} \right] * 10^{-3} \frac{kW}{W} = Power \left[\frac{kWh}{kg H_2} \right]$$

To calculate the cathode layer resistance, the following formula was used:

$$Resistance [\Omega m^2] = \frac{Cathode layer potential [V] * projected surface area (m^2)}{Cathode layer current [A]}$$

The electron recovery into volatile fatty acids (η_{VFAs}) and hydrogen (η_{H_2}) was calculated based on the measured concentrations of volatile fatty acids in the liquid phase at the sampling time $Conc_{VFA,t}$, the measured current in mA (i.e. mC/s) at the sampling time ($Current_t$), the catholyte outflow rate at the sampling time (Q_t , calculated based on the inflow rate and acid addition over time),:

$$\eta_{VFAs} = \frac{96485 \frac{mC}{mmol e^-} * Conc_{VFA,t} \left[\frac{mmol}{L} \right] * Q_t \left[\frac{L}{h} \right] * x \frac{mmol e^-}{mmol VFA}}{Current_t \left[\frac{mC}{s} \right] * 3600 \frac{s}{h}}$$

To calculate the electron recovery into hydrogen, the hydrogen flow was calculated based on the hydrogen and nitrogen fractions in the measured off gas ($fraction_{offgasH_2}$, $fraction_{offgasN_2}$), the reactor temperature (Temp) and the ideal gas law, assuming that the N₂ was inert inside the reactors:

$$Flow_{H_2} \left[\frac{mmol H_2}{h} \right] = \frac{fraction_{offgas} H_2 [\%] * 233.3 \frac{LN N_2}{d}}{fraction_{offgas} N_2 [\%] * 24 \frac{h}{d}} * \frac{101325 Pa}{8.314 \frac{J}{K * mol} * Temp [K]}$$

The electron recovery into hydrogen was calculated based on the hydrogen flow and the current measured at the sampling time of the hydrogen:

$$\eta_{H_2} = \frac{96485 \frac{mC}{mmol e^-} * Flow_{H_2} \left[\frac{mmol H_2}{h} \right] * 2 \frac{mmol e^-}{mmol H_2}}{Current_t \left[\frac{mC}{s} \right] * 3600 \frac{s}{h}}$$

The electron recovery into methane was also calculated based on the methane fraction in the off-gas, in the same way as the electron recovery into hydrogen, with the adjustment that methane contains 8 mmol e⁻ per mmol methane.

The hydrogen concentration in the catholyte was calculated based on the measured hydrogen fraction in the off-gas ($fraction_{offgas} H_2$), with a Henry coefficient of $7.7E-06 \text{ mol}/(\text{m}^3\text{Pa})^{25}$ and a pressure of 1 atm (101325 Pa).

$$\begin{aligned} Hydrogen \text{ conc } [\mu M] \\ = 7.7 \cdot 10^{-6} \frac{mol}{m^3 Pa} * 101325 Pa * \frac{fraction_{offgas} H_2 [\%]}{100\%} * 10^3 \frac{\mu mol * m^3}{L * mol} \end{aligned}$$

6.3 Results and discussion

6.3.1 Increased power demand due to gas build-up at high current density

To demonstrate the issues with the state-of-art flow-through configuration during start-up at high current density, abiotic reactors were started up with controlled current of -10.4 kA/m³. The cell potential was measured to calculate system power demand for production of hydrogen. The previously suggested flow-through recirculation flow was used^{17,18} and a bypass outlet of the cathode chamber between the membrane and the cathode (Figure 6.2B). When the recirculation flow was forced through the graphite felt cathode (bypass closed), the cell potential increased simultaneously with gas build-up between the membrane and the cathode (Figure 6.2, grey planes and SI Figure S6.2). To release the build-up gas and lower the system power demand, the bypass was opened (Figure 6.2A, white planes). Opening the bypass caused the cell potential to drop almost instantaneously (Figure 6.2A, zoom in frame).

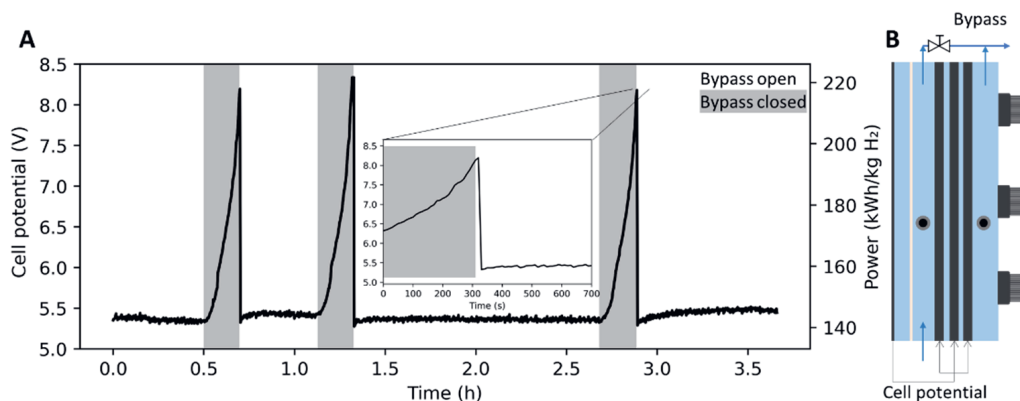


Figure 6.2. Cell potential and corresponding power demand over time with -200 mA (-10.4 kA/m^2) applied cathode current. The bypass was closed three times (grey area) for $\pm 10\text{ min}$. Based on the cell potential, the power demand per kg hydrogen was calculated (right y-axis, see M&M for details).

The cell potential correlates with the system power input (right y-axis, Materials and Methods, calculation section), a cell potential increase correlates with a higher power demand. The power needed during the time with the bypass opened (white planes) was 146 kWh/kg hydrogen (assuming 100% CE to hydrogen), while it increased to 221 kWh/kg hydrogen when the bypass was closed (Figure 6.2A, right y-axis). Presumably, the high power with the bypass closed can be explained by the gas build-up between the membrane and cathode. The gas build-up decreased the available space for ion transfer between the electrodes. The decreased space for ion transfer caused an increased ionic resistance¹⁹, which caused the increase of the cell potential. To keep the cell potential low, and thus reduce the operation energy costs, the bypass would need to be opened to prevent build-up of gas between the membrane and cathode. However, with the bypass open, about 50% of the flow is directed through the bypass and not through the cathode. This would mean that 50% of the electrolyte entering the cathode chamber leaves the cathode chamber through the bypass, not being forced through the cathode layers. With the flow only partially going through the cathode layers, nutrient supply to the cathode biofilm is limited. To allow both removal of excess gas build-up and flow through the cathode layers, the reactor configuration was adapted to a cross flow-through design: a second cathode inflow point was installed, the bypass was replaced through a second reactor outlet, and all in- and outlets were provided with switchable valves (Figure 6.3B).

To measure the power demand of switching between two different flow-through directions, the cell potential was measured over time whilst different flow direction alternation intervals were tested (Figure 6.3A). The flow was alternated between *away from the membrane* (orange dashed arrow, Figure 3B) and *towards the membrane* (green filled arrow, Figure 3B), with increasing interval time between alternation time (0.5 min to 10 min). Compared to the previous situation with the bypass open, the power demand was lower with alternating flow. The longer the time interval between flow direction alternation (x-axis, Figure 3A), the more the maximum cell potential increased with gas accumulation (Figure 6.3A, maximum values). With the increasing cell potential, the power demand also increased, leading to a higher average power demand for

the experiments with longer time between the flow direction switches. The replicate reactor showed the same trend (SI Figure S6.3).

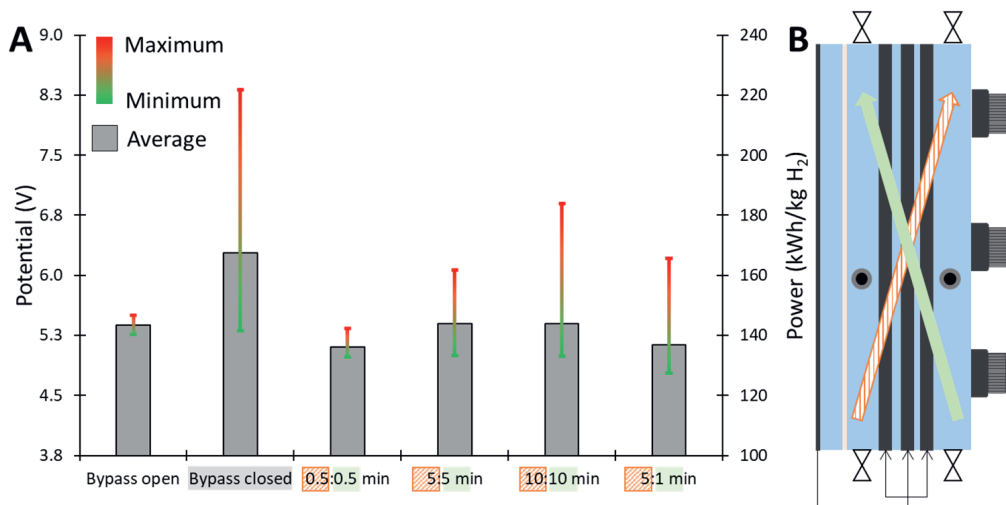


Figure 6.3. Electric power demand per kg produced hydrogen (right y-axis) calculated based on the cell potential (left y-axis) averaged over 3.5 hours of switching flow direction between away from (orange dashed) and towards (green filled) the membrane of a reactor operated at -10.4 kA/m^2 . The error bars show the minimum and maximum measured power demand during the 3.5 h.

6.3.2 Alternating flow-through allows cathode resistance decrease and refreshing of local pH and hydrogen

Besides the effect of different alternating flow-through intervals on power demand, the mass-transfer to the cathode and the cathodic biofilm is an additional important parameter. To elucidate on the effect of flow-changes on local conditions, and thus mass-transfer to the cathode, several parameters were measured over time: cell potential (A), cathode layer resistances (C) and current densities (D), as well as local pH (E) and hydrogen concentrations (F) (Figure 6.4). To properly show the trends at both flow-through directions, these measurements were performed in the reactor with a 5:5 min switching between flow towards (green filled) and flow away from (orange dashed) the membrane.

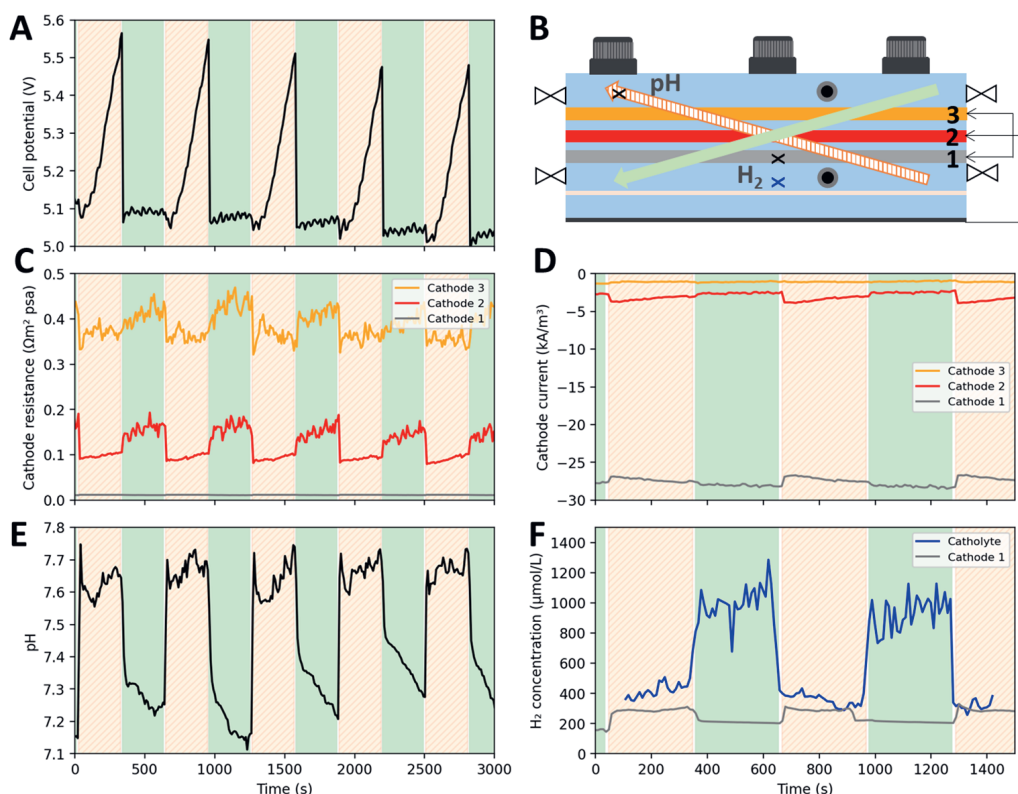


Figure 6.4. Cell potential (A), cathode layer resistances (C) and current densities (D), and local pH (E) and local hydrogen concentrations (F) over time during 5.5 min flow switching between flow away from (orange dashed) and towards (green filled) the membrane. The locations of the pH and hydrogen measurements are indicated in B. Note: the different hydrogen measurements were overlapped in (F) for viewing purposes.

The cell potential increases with the flow away from the membrane (orange dashed) and remained rather constant (5.0-5.1 V, Figure 6.4A) at the minimum value with the flow towards the membrane (green filled). Note that although it seems that the cell potential with the flow towards the membrane is decreasing over time, this was not measured over the whole 25h course of the experiment. Since the gas build up also increased over time, the increase in cell potential seems a consequence of the gas build-up between the membrane and cathode. To further support this hypothesis, more local measurements at different sides of the reactor (anode, cathode layers horizontally and vertically) should be performed to further elucidate the role of hydrogen accumulation and other mass-transfer limitations. Remarkably, the cell potential (Figure 6.4A) was the only parameter that linearly increases over time during the flow away from the membrane, while cathode layer current and resistance, local pH, local hydrogen change in a “switch-like” manner, i.e. the values change right at the moment the flow direction switches.

The cathode resistances were higher with the flow towards the membrane (green filled) compared to the values with flow away from the membrane (orange dashed, Figure 6.4C). The resistances corresponded with the current densities, lower resistances resulted in higher (more negative) current densities (Figure 6.4D). When comparing the three cathode layers, the cathode layer

closest to the membrane (cathode 1) had on average the lowest resistance and the highest current (~85% of the total current), whereas the furthest cathode layer (3) had the highest resistance and lowest current (Figure 6.4C and D). These trends were observed through the whole experiment. Remarkably, the changes on flow-direction had a different effect on the cathode layer 1 when compared to the cathode layers 2 and 3. After the flow-through direction change from *towards the membrane* to *away from membrane*, the current density of cathode 1 decreased (D, grey line), while the current of cathode 2 and 3 increased (D, red and orange). A possible explanation for the different behaviour of the cathode layer 1 is that the gas accumulation, which mainly occurred next to cathode 1, caused a resistance increase mainly for cathode 1. The resistance increase of cathode 1 caused the current distribution to change more towards cathode 2 and 3 when the flow was *away from the membrane*.

The pH measuring spot was chosen on the outer side of the cathode (Figure 6.4B) to investigate the effect of switching flow-through direction on the pH dynamics in a possible “dead zone” location where less mixing might occur. The pH was relatively high (7.7) when the flow was *away from the membrane* (orange dashed, Figure 6.4E) and decreased approximately 0.5 pH unit with the flow direction switch to *towards the membrane* (green filled). The high values with the flow *away from the membrane* indicate a high local pH at the cathode surface, caused by the proton consumption for hydrogen formation. This local pH is different from the controlled recirculation pH (5.8), showing indeed less mixing in the measured location. During the direct mixing with the recirculation electrolyte (*towards the membrane* flow), the local pH did not decrease to the pH of the catholyte during the 5 min. The little pH decrease indicates that with recirculation speed of 10 L/h, it takes longer than 5 min to completely mix the 90 mL cathode chamber with the electrolyte.

The two local hydrogen measurements give valuable insights in the dynamics of the hydrogen distribution in the cathode 1 closest to the membrane and the electrolyte between the cathode and the membrane (Figure 6.4F). When the flow was directed *towards the membrane* (green plane), the hydrogen concentration inside cathode 1 decreased (grey line). Simultaneously, an increase in the electrolyte next to the membrane was measured (blue line). When the flow was switched from *towards the membrane* to *away from the membrane* (orange dashed plane), the hydrogen concentration in the electrolyte immediately dropped, showing removal of excess built-up hydrogen gas next to the cathode, and an increase in hydrogen concentration inside the cathode was measured. With the flow *away from the membrane*, the hydrogen is brought into cathode 1, while the flow *towards the membrane* relocated the highest local hydrogen concentration from the cathode to the catholyte. This shows a direct reversing effect of the highest hydrogen concentration relocation simultaneous with the reversing of the flow-through direction. Figure 6.4F also shows that the concentration of hydrogen in the catholyte was always higher than the concentration of hydrogen in the cathode. This could create an advantage for hydrogen consuming microorganisms in the catholyte over those growing on the cathode. However, from an earlier work with a similar experimental design, it has been reported that CO₂/N₂ sparging in the recirculation bottle constituted for hydrogen loss in the catholyte, meaning that the high hydrogen concentration in the catholyte was mostly lost via the recirculation and thus less available for the biofilm (Chapter 5).

Finally, to direct the local hydrogen to the cathode layers, the time with flow *towards the membrane* must be kept short, to potentially prevent hydrogen loss and increase the concentration in cathode 1. However, flow *towards the membrane* was required to refresh possible dead zones and decrease the cell potential (and thus energy demand). Therefore, an optimal balance in the flow direction intervals has to be found to guarantee hydrogen availability at the cathode, mixing and low energy input.

6.3.3 Biotic start-up at high current showed faster *n*-butyrate production with alternating flow-through strategy

Based on the previous results in the abiotic reactor, a flow switching interval of 5 min flow *away from the membrane* and 1 min *towards the membrane* was chosen to increase the hydrogen concentration in the cathode and allow for mixing of the cathode chamber with the recirculated catholyte. The 1 min flow *towards the membrane* was chosen to combine low hydrogen loss with mixing of the liquid catholyte chamber based on the theoretical hydraulic retention time of 32.2 sec with recirculation 10 L/h. The 5:1 interval for the switch of flow direction led to a lower power demand when compared to switching with equal intervals between both flow directions (Figure 6.3). With the 5:1 strategy, the longer flow *away from the membrane* interval allows for hydrogen availability for possible microorganisms at the cathode layers for 83.3% of the time of a full cycle. With this chosen flow-through switching strategy, a replicate set of biotic reactors was started to test the feasibility of start-up at high current density.

Two biotic reactors were operated with the 5:1 strategy for 60 days at a current density of -10 kA/m³. The volatile fatty acids in the recirculated catholyte (Figure 6.5 A and B) and the hydrogen concentration in the off-gas were measured to characterize productivity and electron recovery into products (Figure 6.5 C and D). Production of acetate was achieved within 7 days after start-up and the first *n*-butyrate was observed on day 13. Lower concentrations of acetate and *n*-butyrate were measured in the replicate biotic reactor (Figure 6.5B). Although the fast start-up of autotrophic acetate production has previously been shown²⁶, we observed, for the first time, a substantially faster increase in the *n*-butyrate concentration over time. After 40 days, the *n*-butyrate concentration was 100 mMC (Figure 6.5A), while other comparable studies reported 2 to 10 times lower *n*-butyrate concentrations²⁷⁻²⁹ at 40 days after start-up of microbial electrosynthesis with CO₂ as sole carbon source.

Besides the concentrations, the electron recoveries were also significantly high, with recoveries reaching up to 60% for the total fatty acid production (Figure 6.5C). In the replicate reactor, methane was measured as the main product (biotic CH₄, Figure 6.5D). The methane was measured at four different timepoints after the acetate and *n*-butyrate dropped in the catholyte. Even though the methane fraction in the outgoing gas was low, the total electron recovery reached up to 100 %. To investigate the difference in the electron recovery gap between the methane and volatile fatty acid producing reactors, a sample of anolyte was taken on day 59 and analysed for VFA's. The anolyte of the biotic CH₄ reactor contained 155 mg L⁻¹ acetate, and the anolyte of the biotic VFAs reactor contained 885 mg L⁻¹ acetate (and 235 mg L⁻¹ butyrate). Based on the hydraulic retention time, it was calculated that up to 15 % of the electrons ended up as volatile fatty acids in the anolyte in the biotic VFAs reactor. These product losses need to be addressed and prevented when aiming at upscaling. Despite the losses, the results from this

study are promising for the use of high current density and the alternating flow-through regime for the fast start-up of carboxylate production from CO₂.

The methane formation was unexpected because a methanogenesis inhibitor (2-bromoethanesulfanoate, 2-BES) was added to the medium³⁰. To verify that the 2-BES was not depleted in the catholyte of the reactors, its concentration was measured in the catholyte of the two reactors and in the medium supply (SI Figure S6.4). Although the concentrations in the catholyte were 1.5 times lower than in the medium, 2-BES was still detected in the catholyte, and no difference was observed between the 2-BES concentration in the two different reactors.

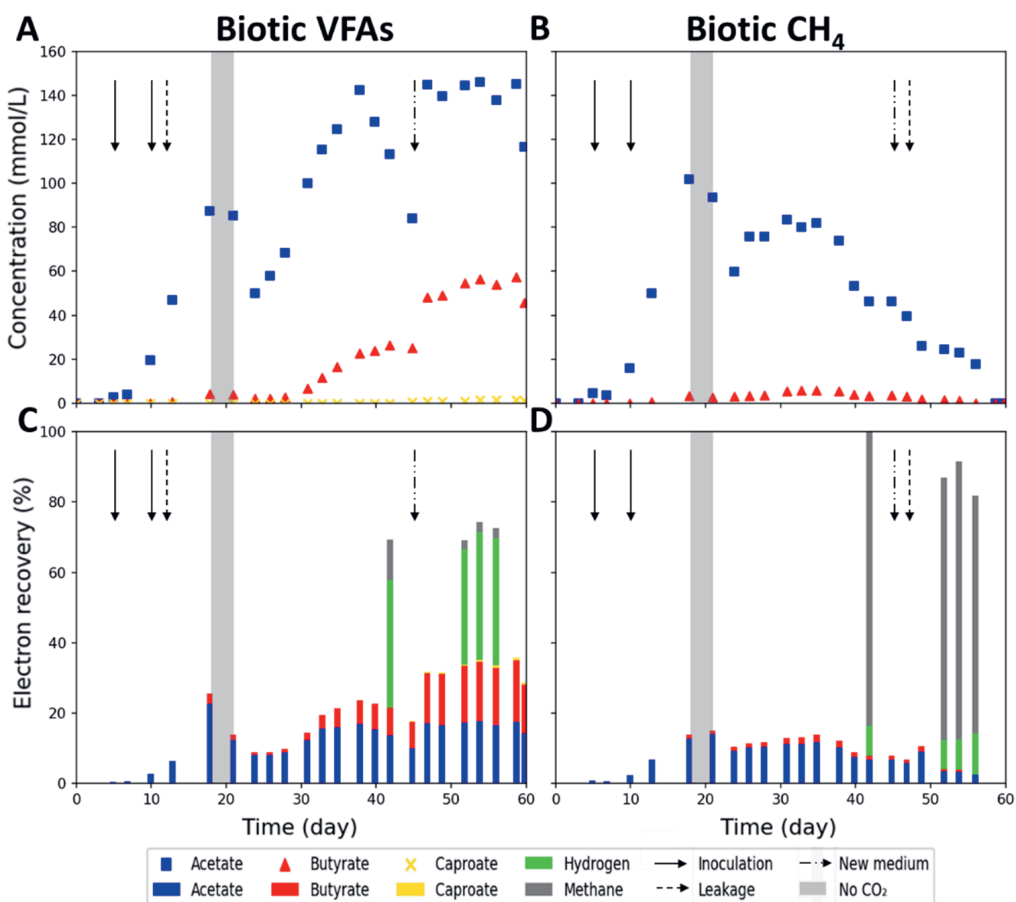


Figure 6.5. Concentrations of volatile fatty acids (acetate, n-butyrate and n-caproate) over time during the biotic experiments, with inoculation moments indicated by filled arrows. Of the two replicate reactors, one showed mainly chain elongation (CE: A, C), while the other showed mainly methanogenesis (CH₄: B, D). On day 18, the CO₂ supply was cut off for three days (grey plane). On day 45, the medium supply in the fridge was refreshed (dash dot arrow). Leakages are indicated by dashed arrows and always followed by addition of fresh medium to replace the leaked volume. Electron recovery values were calculated as described in the materials and method.

The striking difference between the main product of the two biotic reactors could thus not be explained by operating parameters or differences in the bulk conditions. It is plausible that the difference in results was caused by a difference in the initial attachment of the biomass from the

inoculum. For the VFAs reactor, the chain elongating microorganisms could have been attached to a location on the cathode with favourable conditions, whilst for the CH_4 reactor, the methanogens could have been attached to a location on the cathode with favourable conditions. For example, pH values between 5.0 and 6.0 have shown to be more favourable for chain elongation microorganisms³¹. This difference in initial attachment location could have led to advantage for different microbial groups and thus steered the selectivity towards the microbial group with advantageous conditions. Therefore, linking local conditions to the corresponding observed activity could elucidate favourable conditions for either methanogenic or chain elongation microorganisms which is necessary for further scale up.

6.3.4 Local hydrogen decreased during biotic run while local pH stabilized

To investigate the local conditions for microbial activity, characterization was performed by local microsensor measurements of hydrogen and pH throughout the cathode layers and electrolyte next to the cathode on day 0 and day 60 (Figure 6.6). At time 0, the conditions at the cathode layers, inner and outer catholyte differed significantly within the reactors. Depending on the location and the flow direction, measured hydrogen concentrations ranged from ~ 200 to $600 \mu\text{M}$ (Figure 6.6A) and the pH ranged from 5.0 to 7.0 (Figure 6.6D).

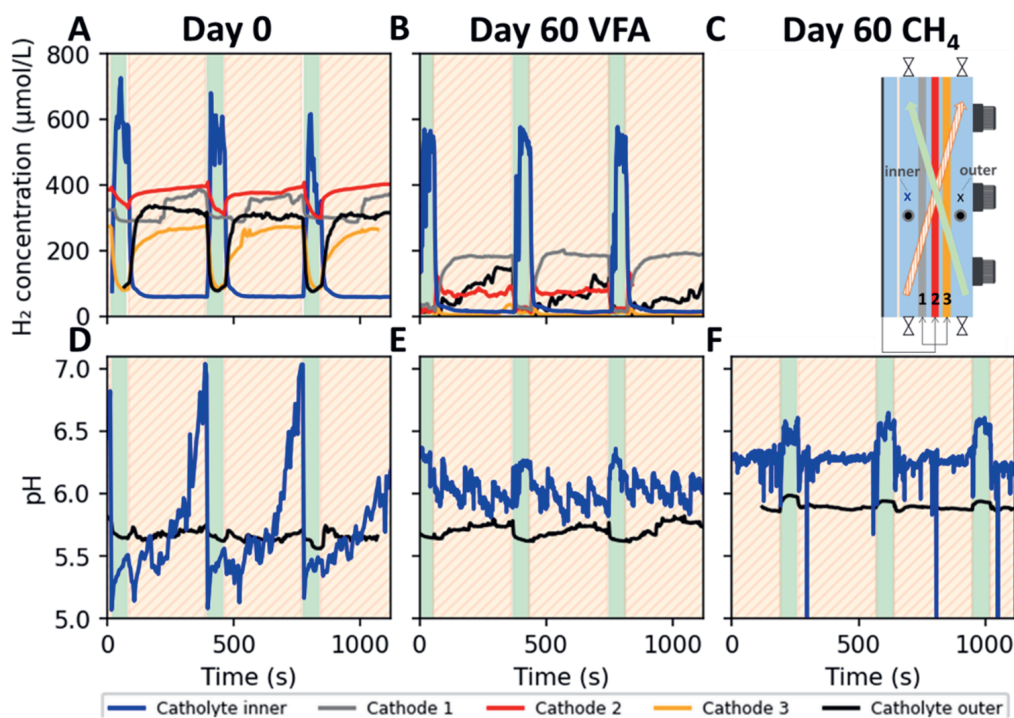


Figure 6.6. Local concentrations of hydrogen throughout the cathode layers and the pH in two electrolyte locations before inoculation (A, D), one biotic chain elongating (VFAs) (B, E) and one biotic methane (CH_4) forming (F) system with alternating flow of 5 min away from (orange dashed) and 1 min towards (green filled) the membrane. The times are normalized for viewing purposes.

The hydrogen concentration in the catholyte and cathode layers at day 0 showed the same trend as earlier observed in Figure 6.4F. Briefly, the highest local hydrogen concentration moved from the catholyte to the inside of the cathode layers when the flow was switched from *towards the membrane* (green filled) to *away from the membrane* (orange dashed) (Figure 6.6A). The hydrogen concentration was detected (range of 250 to 400 μM) in all three cathode layers and in the catholyte on the outer side of the cathode when the flow was *away from the membrane*, even though most hydrogen production probably occurred at cathode 1, which had significantly higher current density (Figure 6.4D). The wide range of conditions (H_2 and pH) between different spots supports the hypothesis that the attachment location of the microbial community in the inoculum may lead to the development of different dominant microbial groups.

At the end of the biotic experiments (day 60), the hydrogen concentrations inside the cathode layers and in the catholyte on the outer side of the cathode were lower compared to the concentrations on day 0 (Figure 6.6B). The hydrogen concentration profiles measured at the bottom well (lowest sampling point at the bottom of the reactor) were similar to the profiles obtained at the middle well (SI Figure S6.6B). However, at the top well, the hydrogen concentration at the cathode layer 1 and 3, and inner and outer catholyte was lower (SI Figure S6.6A). The hydrogen concentrations were the highest inside cathode 1, where the highest current densities were measured (SI Figure S6.5), whereas little hydrogen was measured inside cathode 3 (Figure 6.6B). To also quantify the hydrogen concentration in the bulk catholyte, e.g. the recirculation catholyte, the hydrogen concentration was calculated based on the measured off-gas concentration (see materials and method for calculation). The hydrogen concentration was 1.8 μM in the biotic VFAs reactor and 0.5 μM in the biotic CH_4 reactor (day 40-56). These low concentrations are likely caused by stripping of hydrogen by the incoming CO_2/N_2 gas flow in the recirculation. The measured low hydrogen concentrations at the top of cathode layers 1 and 3 were probably caused by removal of hydrogen via the outgoing recirculation liquid. The lower hydrogen concentrations at the end of the biotic experiment compared to day 0 indicate hydrogen consumption by the microbial community growing on the cathode. Due to technical issues, the local hydrogen concentration in the methanogenesis reactor was only measured on the outer side of the cathode (SI Figure S6.7). The hydrogen concentration was substantially lower in the methanogenesis reactor (SI Figure S6.7) when compared to the chain elongation reactor. This lower hydrogen concentration in the outer catholyte of the methanogenesis reactor was measured over time during the whole biotic run (SI Figure S6.7). The lower hydrogen concentration could be due to higher hydrogen consumption in the methanogenic reactor, which could be caused by higher affinity for hydrogen by methanogenic microbes compared to chain elongation microbes.

The local pH also changed between the start and end of the biotic measurements. On day 0, the pH between the membrane and cathode (inner, Figure 6.6D) increased several pH units when the flow was directed *away from the membrane* (orange dashed). This increase in pH after switching the flow direction to *away from the membrane* became less evident over time, as the pH remained approximately constant during both flow directions on day 60 (Figure 6.6E and F). On the last day of the biotic runs, the pH in the methanogenesis reactor (Figure 6.6F) was slightly higher than in the chain elongation reactor (Figure 6.6E). The pH on the outer side of the cathode gives valuable insights on the mixing of the systems. It is expected that poor mixing might lead

to “dead zones”, and therefore, higher pH, as observed in the abiotic reactor (Figure 6.4E). However, on day 60, the pH on the inner side was similar to the outer side pH (5.8-6.3 and 5.8, respectively). This similarity in pH at different locations of the reactor indicates that the one-minute flow *towards the membrane* (green filled) was a successful strategy to homogenise the catholyte and prevent the accumulation of high pH catholyte.

6.3.5 Gibbs free energy changes based on local conditions

Based on the local pH and hydrogen concentration measurements, thermodynamic feasibility of different reactions could be determined for the different locations in the reactor. The thermodynamic feasibility can be used as theoretical parameter for determination of productive sites in the biotic reactors. The suggested minimum required Gibbs reaction energy for microbial growth is -20 kJ/reaction³². More negative Gibbs reaction energy correspond with higher energy gain for microorganisms and thus better microbial feasibility. To investigate the feasibility of different microbial conversions, the available Gibbs free energy was calculated in the catholyte and inside the different cathode layers (cathode 1-3) for different possible reactions³³⁻³⁷ (Table 6.1). The feasibility was calculated both for hydrogen as electron donor (white filled cells) and for direct electron uptake as energy source (blue filled cells), at day 0 and day 60 of the biotic VFAs reactor. The CH₄ reactor was not considered since no hydrogen data was available for day 60. Based on the thermodynamic calculations, all reactions with CO₂ as substrate (2 and 5, Table 6.1) show values more negative than -20 kJ/reaction on day 0 in all tested biotic reactor locations. The difference in Gibbs free energy yield between different locations was small - up to 10 %. With the measured cathode potential, direct electron uptake reactions have a more negative Gibbs reaction energy compared to mediated electron uptake (i.e. using hydrogen as an electron donor) (Table 6.1, kJ/mol 2e⁻ vs kJ/mol hydrogen), as also suggested previously³⁵. However, it is unknown whether all the present microorganisms have the capability of direct electron uptake. Since the Gibbs reaction energy values do not differ substantially between different locations, the impact of the different local hydrogen concentrations and pH did not seem to significantly affect the thermodynamic feasibility.

Table 6.1. Local Gibbs free energy of different possible reactions in the CO₂-fed electrochemical reactors before (abiotic) and at the end of the biotic run (biotic), calculated based on the measured local conditions at different locations in the reactor (inner catholyte, cathode 1, cathode 2, cathode 3 and outer catholyte, shown in Figure 6.4AB and DE). For undetected hydrogen concentrations in the abiotic reactor, 1 μM was assumed. The values are given for both hydrogen and cathode (at measured cathode potential) as electron donor and coloured based on their magnitude. Compound dissociation and solubility were taken into account for the calculations (details in SI appendix I).

		Day 0					Day 60 (VFAs reactor)				
		Inner	Cat 1	Cat 2	Cat 3	Outer	Inner	Cat 1	Cat 2	Cat 3	Outer
1 Hydrogen formation	$2H^+ + 2e^- \rightarrow H_2$										
	$\text{kJ}^*(\text{mol } 2e^-)^{-1}$		-113.9	-113.8	-102.8			-98.4	-99.4	-102.8	
2 Acetogenesis	$2CO_2 + 4H_2 \rightarrow CH_3COO^- + H^+ + 2H_2O$										
	$\text{kJ}^*(\text{mol } CO_2)^{-1}$	-47.6	-51.1	-51.2	-50.0	-50.7	-31.8	-28.9	-27.0	-20.7	-27.6
	$\text{kJ}^*(\text{mol } H_2)^{-1}$	-23.8	-25.6	-25.6	-25.0	-25.3	-15.9	-14.5	-13.5	-10.3	-13.8
	$\text{kJ}^*(\text{mol } 2e^-)^{-1}$		-140.4	-140.3	-140.7			-113.7	-113.9	-114.0	
3 Acetate to n-butyrate elongation	$2CH_3COO^- + 2H_2 + H^+ \rightarrow CH_3(CH_2)_2COO^- + 2H_2O$										
	$\text{kJ}^*(\text{mol } Ac)^{-1}$	-11.1	-8.3	-8.4	-7.4	-7.9	-29.5	-27.2	-26.2	-22.8	-26.5
	$\text{kJ}^*(\text{mol } H_2)^{-1}$	-11.1	-8.3	-8.4	-7.4	-7.9	-29.5	-27.2	-26.2	-22.8	-26.5
	$\text{kJ}^*(\text{mol } 2e^-)^{-1}$		-122.6	-122.6	-122.6			-126.0	-126.0	-126.0	
4 n-Butyrate to n-caproate elongation	$CH_3COO^- + CH_3(CH_2)_2COO^- + 2H_2 + H^+ \rightarrow CH_3(CH_2)_4COO^- + 2H_2O$										
	$\text{kJ}^*(\text{mol } Ac)^{-1}$	-23.1	-17.5	-17.8	-15.8	-16.8	-67.1	-62.6	-60.4	-53.7	-61.0
	$\text{kJ}^*(\text{mol } H_2)^{-1}$	-11.6	-8.8	-8.9	-7.9	-8.4	-33.6	-31.3	-30.2	-26.9	-30.5
	$\text{kJ}^*(\text{mol } 2e^-)^{-1}$		-122.7	-122.7	-122.7			-129.7	-129.7	-129.7	
5 Hydrogenotrophic methanogenesis	$CO_2 + 4H_2 \rightarrow CH_4 + 2H_2O$										
	$\text{kJ}^*(\text{mol } CO_2)^{-1}$	-136.6	-130.3	-130.8	-126.8	-128.9	-147.7	-137.1	-132.8	-119.4	-134.0
	$\text{kJ}^*(\text{mol } H_2)^{-1}$	-34.2	-32.6	-32.7	-31.7	-32.2	-36.9	-34.3	-33.2	-29.8	-33.5
	$\text{kJ}^*(\text{mol } 2e^-)^{-1}$		-147.0	-147.0	-147.0			-133.1	-133.1	-133.1	
6 Acetoclastic methanogenesis	$CH_3COO^- + H^+ \rightarrow CH_4 + CO_2$										
	$\text{kJ}^*(\text{mol } Ac)^{-1}$	-10.3	-7.0	-7.1	-6.7	-6.9	-21.0	-19.8	-19.7	-19.5	-19.7

A thermodynamic shift can be observed between the start (day 0) and the end (60 d) of the biotic experiment. At the start, acetogenesis (reaction 2) and methanogenesis (reaction 5) were both feasible and competing for the same substrate (CO₂). As shown previously, the competition was won by acetogenesis in the chain elongation reactor, and by the methanogenesis in the methane forming reactor (Figure 6.5A and B). On day 0, the Gibbs free energy for methanogenesis was slightly more negative (-30 to -40 kJ/mol hydrogen) than for acetogenesis (-23 to -25 kJ/mol hydrogen), at all locations. This shows a small thermodynamic advantage for methanogenic microorganisms. On day 60, the thermodynamic favourability shifted from acetogenesis towards acetate elongation reactions to butyrate and caproate (reaction 3 and 4), mainly because of the increased acetate and butyrate concentrations in the reactor. Also acetoclastic methanogenesis was more favourable at day 60 compared to day 0 (reaction 6). At the end of the biotic phase, the difference in Gibbs free energy between the different locations was slightly higher compared to day 0. In particular at cathode 3, the Gibbs free energy decreased up to 20% (less negative free energies), meaning that all the reactions were energetically less favourable at this position compared to day 0. The differences in thermodynamic feasibility are a direct result of the differences in local conditions, showing the importance of monitoring local conditions.

6.3.6 Qualitative visualization of biofilm and identification of microbial communities on the three cathode layers

After showing the thermodynamic feasibility of both chain elongation and methanogenesis during the biotic phase, the position of the biofilms on the cathodes layers was visualized and the species present in the microbial community were identified. The relative amount of biofilm and biofilm structures on the different cathode layers were visualized with Scanning Electron Microscopy (SEM), and the presence of planktonic cells in the catholyte was measured with

optical density. The optical density values were 0.146 and 0.067 for the biotic chain elongation reactor and the methane producing reactor, respectively. This indicates a higher presence of suspended microorganisms in the chain elongation reactor, which could be explained by the slightly higher hydrogen concentrations in the catholyte (SI Figure S6.7). The Scanning Electron Microscopy showed diversity in the coverage of the graphite felt electrode at the measured spots, corroborating with the different local cathodic current, hydrogen concentration and pH as described above (Figure 6.7, overview pictures in SI Figure S6.8-S6.11).

The SEM pictures were taken from the top, middle and bottom of the three different graphite felt cathode layers (Cat 1-3), corresponding with the reactor orientation used in the previous figures (e.g. Figure 6.6C). Samples after 60 days were imaged with overview pictures (SI Figure S6.8-S6.10) and with close-up pictures of the biofilm structures (Figure 6.7). For the biotic volatile fatty acid producing reactor, most biofilm coverage was seen on the extracted samples from cathode 3 and the top of cathode 1 (SI Figure S6.10A, Cat 3 and Cat 1 top), whilst for the biotic methane producing reactor most biofilm coverage was found in the middle and bottom parts of cathode 1 and a bit in the top of cathode 3 (SI Figure S6.10B, Cat 1 mid, Cat 1 bottom and Cat 3 top). The cathode pieces with the least biofilm coverage showed biofilm structures on the graphite felt cathode fibres, whilst the cathode pieces with higher biofilm coverage also showed biofilm structures between the fibres (Figure 6.7). As opposed to cathode layers 1 and 3, hardly any biofilm structures were observed on cathode 2. The differences in the locations with the highest biofilm coverage between the two biotic reactors could be related to differences in optimal conditions between the chain elongation and methanogenic microorganisms. For example, at cathode 1, the hydrogen production was the highest (Figure 6.6A and B) and this cathode showed dense biofilms in the CH_4 reactor (Figure 6.7B, Cat 1) at two locations (mid and bottom), whilst only for one location (top) in the VFAs reactor (Figure 6.7A, Cat 1). Generally, a higher biofilm coverage was observed (by eye) on the cathode parts where the flow-through recirculation was entering the cathode, so the outer sides of the cathodes (SI Figure S6.11). The reason for lower biofilm coverage on cathode 2 could be a filtering function of cathode 1 and 3, which were located as the first cathode layers at the flow-through inlet points. As a result, greater flocculant parts of biomass might be forced to adsorb or attach to cathode 1 and 3 rather than passing those cathodes to reach cathode 2.

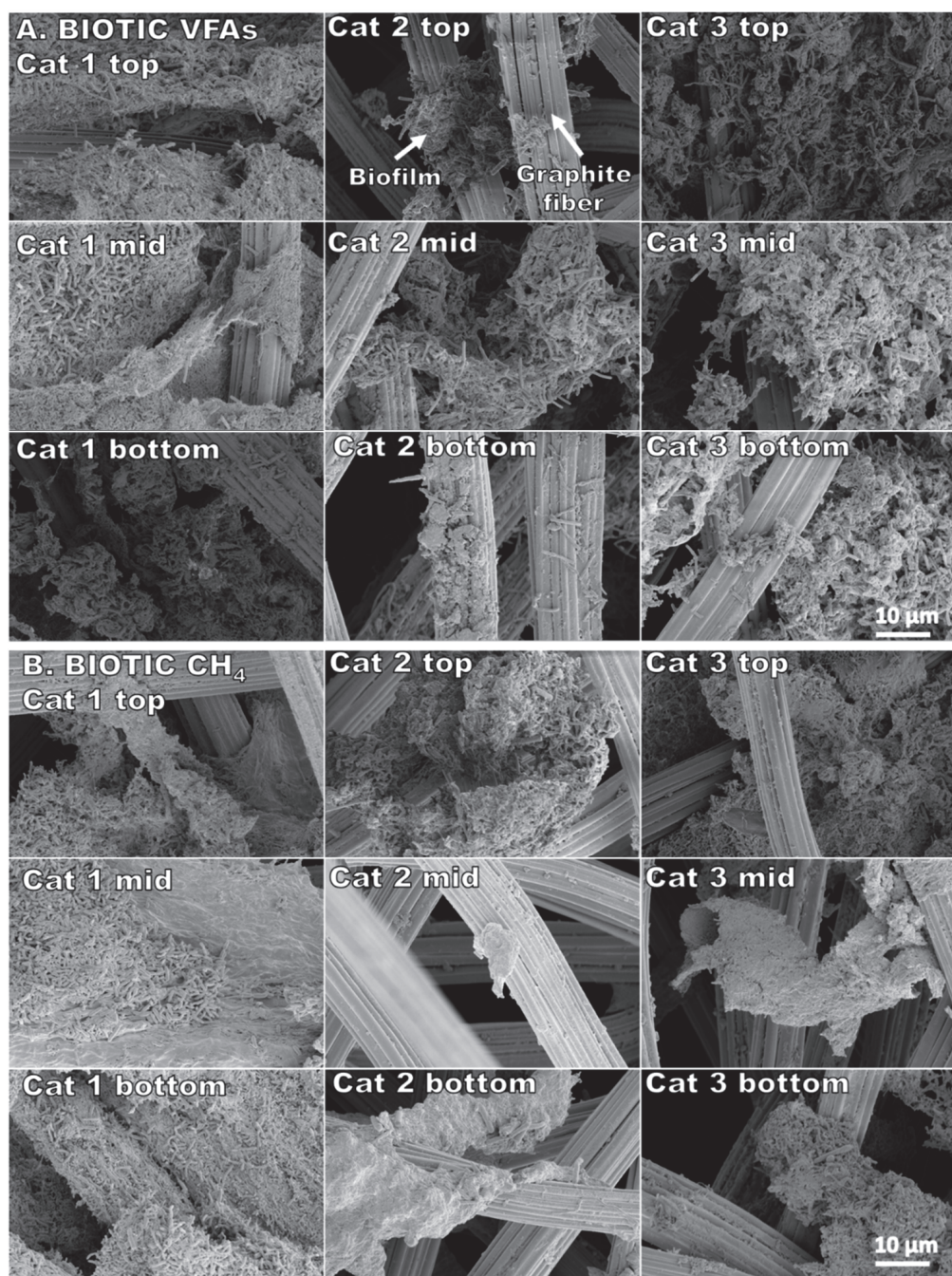


Figure 6.7. Detail Scanning Electron Microscope image of biofilm on graphite felt pieces of different reactor locations from the biotic volatile fatty producing reactor (A VFAs, top 9 images) and the biotic methane producing reactor (B CH_4 , bottom 9 images), both sampled on day 60. The reactor orientation and the definition of bottom, mid and top is in accordance with the schematic of the reactor shown in Fig 6C.

To identify which microorganisms were accountable for the observed biotic structures, Next Generation Sequencing was performed with samples from the suspension and the three cathode layers. Regions of the 16S rRNA were extracted and classified down to genus level (Table 6.2).

Table 6.2. Relative abundance (%) of different microbial groups found in the biofilm at the different cathode layers (mid) and suspended culture of the biotic reactor with chain elongation (VFAs) and methane formation (CH₄) after 60 days of biotic operation. Only the classified genera with Operational Taxonomic Unit (OTUs) with at least 3% relative abundance are shown in this table.

Affiliation	Biotic VFAs				Biotic CH ₄			
	Catholyte	Cathode 1	Cathode 2	Cathode 3	Catholyte	Cathode 1	Cathode 2	Cathode 3
<i>Clostridium sensu stricto</i> 12	66.6	45.2	37.7	45.5	1.5	1.3	26.5	1.1
<i>Firmicutes</i> BRH-c20a	1.6	9.8	30.5	20.5	1.2	19.8	33.6	25.7
<i>Methanobrevibacter</i>	2.6	10.9	2.6	6.6	13.1	20.5	8.7	18.0
<i>Rikenellaceae</i> U29-B03	14.0	8.4	3.8	4.9	3.3	5.3	1.9	3.6
<i>Rikenellaceae</i> RC9 gut group	2.1	7.0	8.0	8.0	1.6	8.7	4.2	5.0
<i>Bacteroides</i>	3.2	1.5	1.7	1.6	23.5	4.5	1.8	5.4
<i>Desulfovibrio</i>	1.2	0.7	1.8	1.0	10.4	7.5	3.4	7.5
<i>Eubacterium</i>	0.3	3.4	1.2	1.5	1.0	3.2	3.9	3.8
<i>Saccharimonadales</i>	0.1	0.1	0.1	0.1	10.3	3.6	0.3	2.9
<i>Erysipelatoclostridiaceae</i> UCG-004	0.2	0.3	0.9	0.6	1.2	5.2	2.0	3.8
<i>Oscillibacter</i>	1.6	3.2	1.7	1.5	0.2	0.5	0.2	0.6
<i>Williamwhitmaniaceae</i> Blvii28	0.1	0.0	0.0	0.0	1.5	0.6	3.1	1.7
<i>Acidaminococcaceae</i>	0.0	0.1	0.1	0.1	1.3	1.1	0.9	3.1
Others (<3%)	6.6	9.4	10.0	8.1	29.7	18.3	9.4	18.0

In the reactor with chain elongation products (acetate, butyrate, and caproate), *Clostridium sensu stricto* 12 related species were the most abundant microorganisms (Table 6.2, Biotic VFAs). In the methanogenic reactor, *Firmicutes* BRH-c20a had the highest relative abundance (Table 6.2, Biotic CH₄). The *Firmicutes* BRH-c20a was abundantly present on the cathodes of both reactors. Other microorganism groups with significant relative abundance are *Methanobrevibacter*, *Rikenellaceae* and *Bacteroides*. Interestingly, the *Firmicutes* BRH-c20a has low relative abundance in the catholyte and high relative abundance on the cathode, suggesting an affinity to grow attached to the graphite felt. The *Bacteroides* however, shows an opposite trend, suggesting a higher affinity for suspended growth. The presence of certain microorganisms can be linked to the observed products to suggest the role and function of the different microbial and Archaea groups.

Several *Clostridium* species are known for CO₂ fixation and/or elongation of acetate to *n*-butyrate and *n*-caproate³⁸⁻⁴⁷. It is therefore likely that the *Clostridium sensu stricto* 12 related species was responsible for the production of *n*-butyrate and *n*-caproate (Figure 6.5A). The BRH-c20a has been found with high relative abundance in microbial electrosynthesis systems where CO₂ was reduced to acetate⁴⁸. *Methanobrevibacter* is known for methanogenesis from CO₂ using hydrogen (Table 6.1, reaction 5) or formate⁴⁹. All *Methanobrevibacter* species grow well with hydrogen and CO₂⁵⁰, and several microbial electrosynthesis systems have reported presence of *Methanobrevibacter*^{34,51,52}. Members of the *Rikenellaceae* family have been associated with the degradation of carbohydrates⁵³. The *Bacteroides* are gut and soil bacteria have shown sugar, fatty acid, and hydrocarbon degradation activity in other studies⁵⁴, suggesting that their role in the biotic reactors could be mainly related to the degradation of products and dead biomass

material. However, some species of the *Bacteroides* genus are capable of fermentation⁵⁴ or even carbohydrate conversion to fatty acids combined with CO₂ capture⁵⁵.

Based on the detected microorganism genera, BRH-c20a species are suggested to be mainly responsible for acetogenesis in the systems of this study, the *Clostridium sensu stricto* 12 species will be responsible for the acetate elongation to *n*-butyrate and *n*-caproate, possibly together with *Bacteroides*. *Methanobrevibacter* is suggested to produce the observed methane and the *Rikenellaceae* U29-B03 is likely a carbohydrate scavenger from e.g. decaying biomass. The higher relative abundance of *Clostridium sensu stricto* 12 species in the biotic VFAs reactor compared to the biotic VFAs reactor (Table 6.2) corresponds with the observed higher volatile fatty acid productivities (Figure 6.5). Furthermore, the higher relative abundance of *Methanobrevibacter* species in the biotic CH₄ reactor corresponds with the higher observed methane concentrations in the off gas of that reactor (Figure 6.5). However, Cathode 2 shows similar relative abundance distributions for both biotic reactors (Table 6.2) despite the different measured net productivities, showing that productivities and functional groups can differ significantly between different locations at the cathode.

6.3.7 Outlook: insights for electro-fermentation designs

The differences between the product spectra of the two biotic reactors show the importance of measuring local conditions and the effect of different local conditions on the microbial community. Despite the equal operation parameters, differences in local conditions could lead to different microbial activities. Although the thermodynamic calculations predicted an advantage for the methanogens (Table 6.1), other factors such as the elevated undissociated volatile fatty acid concentrations⁵⁶ could inhibit methanogenic organisms. In this study, even though the bulk pH was controlled at 5.8, hydrogen formation and its accompanied proton consumption, resulted in local higher pH values on the cathode surfaces. A local pH of 6.5 causes a decrease of 6% of the undissociated acetate concentration (compared to pH 5.8), which is beneficial for methanogenesis activity. The local hydrogen concentration is another factor that might influence the selection for either chain elongation or methanogenesis. The local hydrogen pressure in the methane forming reactor in this study was substantially lower than in the chain elongation reactor (Figure 6.5C and SI S6.7A and B). The hydrogen pressure might have been detrimental for chain elongation microorganisms, since too low hydrogen pressure values have been shown to stimulate fatty acid oxidation rather than production⁵⁷. Overall, monitoring local concentrations over time and investigating the effect of changing operating parameters on the local conditions is crucial. With this knowledge, the optimum operating parameters can be selected and applied to steer the process towards either methanogenesis or chain elongation.

The results obtained in this work support the application potential of electro-fermentation processes like microbial electrosynthesis. First, the alternating flow-through regime allowed a start-up at high current density whilst maintaining hydrogen inside the porous cathode layers. Besides, this flow strategy decreased the power demand per kg hydrogen. The fast start-up at high current density was a crucial step forward on the previously reported need to focus on higher current density conditions. However, further optimization is required to increase the electron recovery values into fatty acids. To increase the concentration of the desired products,

it is recommended to focus on factors including energy efficiency, mass-transfer, biomass growth and selectivity of microbial conversions.

The energy efficiency of these systems is intrinsically related to the uptake of electrons from bacteria and their use to form added values compounds. Energy efficiencies decrease when a large fraction of the provided electrons (cathodic current) is lost in the form of hydrogen gas or used for competing processes (e.g. methanogenesis). The energy efficiency could be enhanced by the development of direct electron transfer mechanisms or application of intermittent current⁵⁸. Based on the results of this study, it seems hydrogen availability cannot be limited at cathodes with low electric current since that might stop the chain elongation conversions. From the local measurements of hydrogen, it can be concluded that the hydrogen availability decreased over time (Figure 6.6A and B). Therefore, with further development and maturation of the biofilm that grows on mediated electron transfer, it is expected that hydrogen becomes the limiting factor. To reduce dependency on hydrogen availability, the hydrogen supply could be slowly lowered over time by lowering the applied current. The lowering of the hydrogen availability could trigger development of direct electron uptake mechanisms in the microorganisms^{59,60} and thus lower dependency on hydrogen as electron donor. An important note is that focussing on direct electron uptake as microbial energy source by reducing hydrogen also decreases the electron donor for suspended microorganisms. An alternative route for a more efficient electron transfer could be the external, electrochemical high-performance production of hydrogen⁶¹, which can be supplied to the reactors⁶². This external introduction of the electron donor requires investigation since it would remove the need for bio-electrochemistry and thus also the reported issue of volatile fatty acid transport to the anode compartment.

To ensure sufficient mass-transfer in larger scale systems operating at high current density, it is recommended to measure local conditions with various large scale electrode designs. This allows to identify which electrode configuration gives the least mass-transfer limitations⁶. From a thermodynamic perspective, the acetate concentration is an important parameter as it determines the available energy for chain elongation. Therefore, monitoring acetate concentrations in the reactor, by means of e.g. an acetate probe⁶³, would give valuable real-time insights on the local conditions and the most favourable locations to achieve high biological activity. For further elucidation of important steering parameters and operating conditions, the microbial analysis should also be extended with e.g. activity or quantitative⁶⁴ analyses linked to local conditions.

The advantage of working with a mixed culture is the possibility of using selective pressure to enable the growth of the most robust microorganisms under a given set of operating conditions (e.g. salinity and pH). Given that mixed cultures are already present in waste streams, these streams could be used as an inflow source for bio-electrochemical CO₂ valorisation, without the need for aseptic methods. It should also be noted that, whilst the specific conditions of the three cathode layers and catholyte positions were identified, the spatial distribution of the microorganisms within the depth of the biofilm was not covered. Linking the spatial distribution of microbial groups on the cathode to the local conditions can give more insights on e.g. electron uptake mechanisms. Finally, with the identification of the microbial community, operating

conditions could be tested to favour the growth of the most biologically active bacteria. Once defined, these operating conditions could be applied for upscaling¹⁵.

6.4 Conclusions

In this study, alternating flow-through was used to start-up bio-electrochemical systems at high current density. Alternating flow reduced the power input to 136 kWh per kg hydrogen. Start-up of microbial electrosynthesis systems with chain elongation was achieved within 10 days after start-up at constant applied current. After 60 days, local hydrogen concentrations between 100 and 600 μM were measured in the cathode layers, whilst 0.5-1 μM was measured in the bulk catholyte. The pH in the catholyte next to the cathodes were around 5.8-6.8. The alternating flow operation showed better mass-transfer, as both distribution of hydrogen to the cathode layers and also refreshing of possible “dead zones” were improved in the cathode chamber. Production of short and medium chain fatty acids was linked to presence of microorganisms classified as *Firmicutes* BRH-c20a and *Clostridium sensu stricto* 12 species, whilst hydrogenotrophic methanogenesis was linked to *Methanobrevibacter*.

References

- 1 Bian, B., Bajracharya, S., Xu, J., Pant, D. & Saikaly, P. E. Microbial electrosynthesis from CO₂: Challenges, opportunities and perspectives in the context of circular bioeconomy. *Bioresource technology* **302**, 122863 (2020).
- 2 Sharma, M. *et al.* Bioelectrocatalyzed reduction of acetic and butyric acids via direct electron transfer using a mixed culture of sulfate-reducers drives electrosynthesis of alcohols and acetone. *Chemical Communications* **49**, 6495-6497 (2013).
- 3 Yuan, M., Kummer, M. J. & Minteer, S. D. Strategies for bio-electrochemical CO₂ reduction. *Chemistry—A European Journal* **25**, 14258-14266 (2019).
- 4 Vassilev, I. *et al.* Microbial electrosynthesis of isobutyric, butyric, caproic acids, and corresponding alcohols from carbon dioxide. *ACS Sustainable Chemistry & Engineering* **6**, 8485-8493 (2018).
- 5 van Eerten-Jansen, M. C. *et al.* Analysis of the mechanisms of bio-electrochemical methane production by mixed cultures. *Journal of Chemical Technology & Biotechnology* **90**, 963-970 (2015).
- 6 Jourdin, L. & Burdyny, T. Microbial electrosynthesis: where do we go from here? *Trends in Biotechnol.* **39**, 359-369 (2021).
- 7 Jourdin, L., Raes, S. M. T., Buisman, C. J. N. & Strik, D. P. B. T. B. Critical Biofilm Growth throughout Unmodified Carbon Felts Allows Continuous Bio-electrochemical Chain Elongation from CO₂ up to Caproate at High Current Density. *Frontiers in Energy Research* **6**, doi:10.3389/fenrg.2018.00007 (2018).
- 8 Flexer, V. & Jourdin, L. Purposely Designed Hierarchical Porous Electrodes for High Rate Microbial Electrosynthesis of Acetate from Carbon Dioxide. *Acc Chem Res* **53**, 311-321, doi:10.1021/acs.accounts.9b00523 (2020).
- 9 Rozendal, R. A., Hamelers, H. V. & Buisman, C. J. Effects of membrane cation transport on pH and microbial fuel cell performance. *Environmental science & technology* **40**, 5206-5211 (2006).
- 10 Kim, J. R., Cheng, S., Oh, S.-E. & Logan, B. E. Power generation using different cation, anion, and ultrafiltration membranes in microbial fuel cells. *Environmental science & technology* **41**, 1004-1009 (2007).
- 11 Ooka, H., Figueiredo, M. C. & Koper, M. T. Competition between hydrogen evolution and carbon dioxide reduction on copper electrodes in mildly acidic media. *Langmuir* **33**, 9307-9313 (2017).
- 12 De Lichtervelde, A., Ter Heijne, A., Hamelers, H., Biesheuvel, P. & Dykstra, J. Theory of ion and electron transport coupled with biochemical conversions in an electroactive biofilm. *Phys. Rev. Appl.* **12**, 014018 (2019).
- 13 Kracke, F. *et al.* Robust and biocompatible catalysts for efficient hydrogen-driven microbial electrosynthesis. *Commun. Chem.* **2**, 45 (2019).
- 14 Patil, S. A. *et al.* Electroactive mixed culture derived biofilms in microbial bio-electrochemical systems: the role of pH on biofilm formation, performance and composition. *Bioresource technology* **102**, 9683-9690 (2011).
- 15 Vassilev, I. *et al.* Microbial electrosynthesis system with dual biocathode arrangement for simultaneous acetogenesis, solventogenesis and carbon chain elongation. *Chem Commun (Camb)* **55**, 4351-4354, doi:10.1039/c9cc00208a (2019).
- 16 Brown, R. K. *et al.* Evaluating the effects of scaling up on the performance of bio-electrochemical systems using a technical scale microbial electrolysis cell. *Bioresource Technology* **163**, 206-213 (2014).
- 17 Katuri, K. *et al.* Three-dimensional microchanneled electrodes in flow-through configuration for bioanode formation and current generation. *Energy & Environmental Science* **4**, 4201-4210 (2011).
- 18 Jourdin, L. *et al.* High Acetic Acid Production Rate Obtained by Microbial Electrosynthesis from Carbon Dioxide. *Environ Sci Technol* **49**, 13566-13574, doi:10.1021/acs.est.5b03821 (2015).
- 19 Sleutels, T. H., Hamelers, H. V., Rozendal, R. A. & Buisman, C. J. Ion transport resistance in microbial electrolysis cells with anion and cation exchange membranes. *International Journal of Hydrogen Energy* **34**, 3612-3620 (2009).
- 20 de Smit, S. M., Buisman, C. J., Bitter, J. H. & Strik, D. P. Cyclic Voltammetry is invasive on microbial electrosynthesis. *ChemElectroChem* **8**, 3384-3396 (2021).
- 21 Bolyen, E. *et al.* Reproducible, interactive, scalable and extensible microbiome data science using QIIME 2. *Nature biotechnology* **37**, 852-857 (2019).

- 22 Klindworth, A. *et al.* Evaluation of general 16S ribosomal RNA gene PCR primers for classical and next-generation sequencing-based diversity studies. *Nucleic acids research* **41**, e1-e1 (2013).
- 23 Callahan, B. J. *et al.* DADA2: High-resolution sample inference from Illumina amplicon data. *Nature methods* **13**, 581-583 (2016).
- 24 Quast, C. *et al.* The SILVA ribosomal RNA gene database project: improved data processing and web-based tools. *Nucleic acids research* **41**, D590-596, doi:10.1093/nar/gks1219 (2013).
- 25 Sander, R. Compilation of Henry's law constants (version 4.0) for water as solvent. *Atmos. Chem. Phys.* **15**, 4399-4981 (2015).
- 26 Patil, S. A. *et al.* Selective enrichment establishes a stable performing community for microbial electrosynthesis of acetate from CO₂. *Environmental science & technology* **49**, 8833-8843 (2015).
- 27 Bajracharya, S. *et al.* Long-term operation of microbial electrosynthesis cell reducing CO₂ to multi-carbon chemicals with a mixed culture avoiding methanogenesis. *Bioelectrochemistry* **113**, 26-34 (2017).
- 28 Ganigué, R., Puig, S., Batlle-Vilanova, P., Balaguer, M. D. & Colprim, J. Microbial electrosynthesis of butyrate from carbon dioxide. *Chemical Communications* **51**, 3235-3238 (2015).
- 29 Batlle-Vilanova, P. *et al.* Microbial electrosynthesis of butyrate from carbon dioxide: production and extraction. *Bioelectrochemistry* **117**, 57-64 (2017).
- 30 Wildenauer, F., Blotevogel, K. & Winter, J. Effect of monensin and 2-bromoethanesulfonic acid on fatty acid metabolism and methane production from cattle manure. *Applied Microbiology and Biotechnology* **19**, 125-130 (1984).
- 31 de Araújo Cavalcante, W., Leitão, R. C., Gehring, T. A., Angenent, L. T. & Santaella, S. T. Anaerobic fermentation for n-caproic acid production: A review. *Process Biochemistry* **54**, 106-119 (2017).
- 32 Schink, B. Energetics of syntrophic cooperation in methanogenic degradation. *Microbiology and molecular biology reviews* **61**, 262-280 (1997).
- 33 Lasia, A. Mechanism and kinetics of the hydrogen evolution reaction. *international journal of hydrogen energy* **44**, 19484-19518 (2019).
- 34 Jourdin, L., Lu, Y., Flexer, V., Keller, J. & Freguia, S. Biologically induced hydrogen production drives high rate/high efficiency microbial electrosynthesis of acetate from carbon dioxide. *ChemElectroChem* **3**, 581-591 (2016).
- 35 Raes, S. M., Jourdin, L., Buisman, C. J. & Strik, D. P. Bio-electrochemical Chain Elongation of Short-Chain Fatty Acids Creates Steering Opportunities for Selective Formation of n-Butyrate, n-Valerate or n-Caproate. *ChemistrySelect* **5**, 9127-9133 (2020).
- 36 Lyu, Z., Shao, N., Akinyemi, T. & Whitman, W. B. Methanogenesis. *Current Biology* **28**, R727-R732 (2018).
- 37 Mayumi, D. *et al.* Carbon dioxide concentration dictates alternative methanogenic pathways in oil reservoirs. *Nature communications* **4**, 1-6 (2013).
- 38 Schoberth, S. & Gottschalk, G. Considerations on the energy metabolism of *Clostridium kluveri*. *Archiv für Mikrobiologie* **65**, 318-328 (1969).
- 39 Fernández-Blanco, C., Veiga, M. C. & Kennes, C. Efficient production of n-caproate from syngas by a co-culture of *Clostridium acetum* and *Clostridium kluveri*. *Journal of environmental management* **302**, 113992 (2022).
- 40 Cui, Y., Yang, K.-L. & Zhou, K. Using co-culture to functionalize *Clostridium* fermentation. *Trends in Biotechnology* **39**, 914-926 (2021).
- 41 Reddy, M. V., Mohan, S. V. & Chang, Y.-C. Medium-Chain Fatty Acids (MCFA) Production Through Anaerobic Fermentation Using *Clostridium kluveri*: Effect of Ethanol and Acetate. *Applied biochemistry and biotechnology*, 1-12 (2017).
- 42 Köpke, M. *et al.* *Clostridium ljungdahlii* represents a microbial production platform based on syngas. *Proceedings of the National Academy of Sciences* **107**, 13087-13092 (2010).
- 43 Heffernan, J. K. *et al.* Enhancing CO₂-valorization using *Clostridium autoethanogenum* for sustainable fuel and chemicals production. *Frontiers in bioengineering and biotechnology* **8**, 204 (2020).
- 44 Shen, Y., Brown, R. & Wen, Z. Syngas fermentation of *Clostridium carboxidivoran* P7 in a hollow fiber membrane biofilm reactor: Evaluating the mass transfer coefficient and ethanol production performance. *Biochemical engineering journal* **85**, 21-29 (2014).
- 45 Zhu, Y. & Yang, S. T. Adaptation of *Clostridium tyrobutyricum* for Enhanced Tolerance to Butyric Acid in a Fibrous-Bed Bioreactor. *Biotechnology Progress* **19**, 365-372 (2003).

- 46 Atasoy, M. & Cetecioglu, Z. Butyric acid dominant volatile fatty acids production: bio-augmentation of mixed culture fermentation by *Clostridium butyricum*. *Journal of Environmental Chemical Engineering* **8**, 104496 (2020).
- 47 Wang, Q. *et al.* *Clostridium luticellarii* sp. nov., isolated from a mud cellar used for producing strong aromatic liquors. *Int J Syst Evol Microbiol* **65**, 4730-4733, doi:10.1099/ijsem.0.000641 (2015).
- 48 Jiang, Y., Chu, N., Qian, D.-K. & Zeng, R. J. Microbial electrochemical stimulation of caproate production from ethanol and carbon dioxide. *Bioresource Technology* **295**, 122266 (2020).
- 49 Vetriani, C. in *Encyclopedia of Biodiversity: Second Edition* 218-226 (Elsevier Inc., 2001).
- 50 Miller, T. L. *Methanobrevibacter*. *Bergey's Manual of Systematics of Archaea and Bacteria*, 1-14 (2015).
- 51 Gao, T., Zhang, H., Xu, X. & Teng, J. Integrating microbial electrolysis cell based on electrochemical carbon dioxide reduction into anaerobic osmosis membrane reactor for biogas upgrading. *Water Research* **190**, 116679 (2021).
- 52 Siegert, M., Li, X.-F., Yates, M. D. & Logan, B. E. The presence of hydrogenotrophic methanogens in the inoculum improves methane gas production in microbial electrolysis cells. *Frontiers in microbiology* **5**, 778 (2015).
- 53 Pitta, D. W. *et al.* Rumen bacterial diversity dynamics associated with changing from bermudagrass hay to grazed winter wheat diets. *Microbial ecology* **59**, 511-522 (2010).
- 54 Shah, H. N. in *The prokaryotes* 3593-3607 (Springer, 1992).
- 55 Fischbach, M. A. & Sonnenburg, J. L. Eating for two: how metabolism establishes interspecies interactions in the gut. *Cell host & microbe* **10**, 336-347 (2011).
- 56 Zhang, W. *et al.* Free acetic acid as the key factor for the inhibition of hydrogenotrophic methanogenesis in mesophilic mixed culture fermentation. *Bioresource technology* **264**, 17-23 (2018).
- 57 Ge, S., Usack, J. G., Spirito, C. M. & Angenent, L. T. Long-term n-caproic acid production from yeast-fermentation beer in an anaerobic bioreactor with continuous product extraction. *Environmental science & technology* **49**, 8012-8021 (2015).
- 58 Ter Heijne, A., Pereira, M., Pereira, J. & Sleutels, T. Electron storage in electroactive biofilms. *Trends in Biotechnology* **39**, 34-42 (2021).
- 59 Walker, D. J. *et al.* Syntrophus conductive pili demonstrate that common hydrogen-donating syntrophs can have a direct electron transfer option. *The ISME journal* **14**, 837-846 (2020).
- 60 Rotaru, A.-E. *et al.* A new model for electron flow during anaerobic digestion: direct interspecies electron transfer to *Methanosaeta* for the reduction of carbon dioxide to methane. *Energy & Environmental Science* **7**, 408-415 (2014).
- 61 Hodges, A. *et al.* A high-performance capillary-fed electrolysis cell promises more cost-competitive renewable hydrogen. *Nature communications* **13**, 1-11 (2022).
- 62 Baleeiro, F. C., Kleinstuber, S. & Sträuber, H. Hydrogen as a co-electron donor for chain elongation with complex communities. *Frontiers in bioengineering and biotechnology* **9**, 650631 (2021).
- 63 Atci, E., Babauta, J. T., Sultana, S. T. & Beyenal, H. Microbiosensor for the detection of acetate in electrode-respiring biofilms. *Biosensors and Bioelectronics* **81**, 517-523 (2016).
- 64 Molenaar, S. D. *et al.* In situ biofilm quantification in bio-electrochemical systems by using optical coherence tomography. *ChemSusChem* **11**, 2171-2178 (2018).
- 65 Kleerebezem, R. & Van Loosdrecht, M. C. A generalized method for thermodynamic state analysis of environmental systems. *Critical Reviews in Environmental Science and Technology* **40**, 1-54 (2010).
- 66 Hanselmann, K. Microbial energetics applied to waste repositories. *Experientia* **47**, 645-687 (1991).
- 67 Heijnen, J. in *Encyclopedia of bioprocess technology: Fermentation, biocatalysis and bioseparation* (eds M Flickinger & S Drew) 267-291 (John Wiley & Sons Ltd, 1999).
- 68 Adriaanse, N., Dekker, H. & Coops, J. Heats of combustion of normal saturated fatty acids and their methyl esters. *Recueil des Travaux Chimiques des Pays-Bas* **84**, 393-407 (1965).

Supporting information

Table S1 – 16S primer sequences carrying tails corresponding to the Illumina Nextera adapter sequences (underlined) as described in the Illumina sequencing guidelines.

Primer name	Primer sequence (5'-3') with Nextera adapter*	Reference
S-D-Bact-0341-b-S-17-N	<u>TCGTCGGCAGCGTCAGATGTGTATAAGAG</u> <u>ACAGCCTACGGGNGGCWGCAG</u>	Klindworth et al., 2013
S-D-Bact-0785-a-A-21-N	<u>GTCTGTGGGCTCGGAGATGTGTATAAGAG</u> <u>ACAGGACTACHVGGGTATCTAATCC</u>	Klindworth et al., 2013

* Full guidelines for primers preparation at https://www.illumina.com/content/dam/illumina-support/documents/documentation/chemistry_documentation/16s/16s-metagenomic-library-prep-guide-15044223-b.pdf

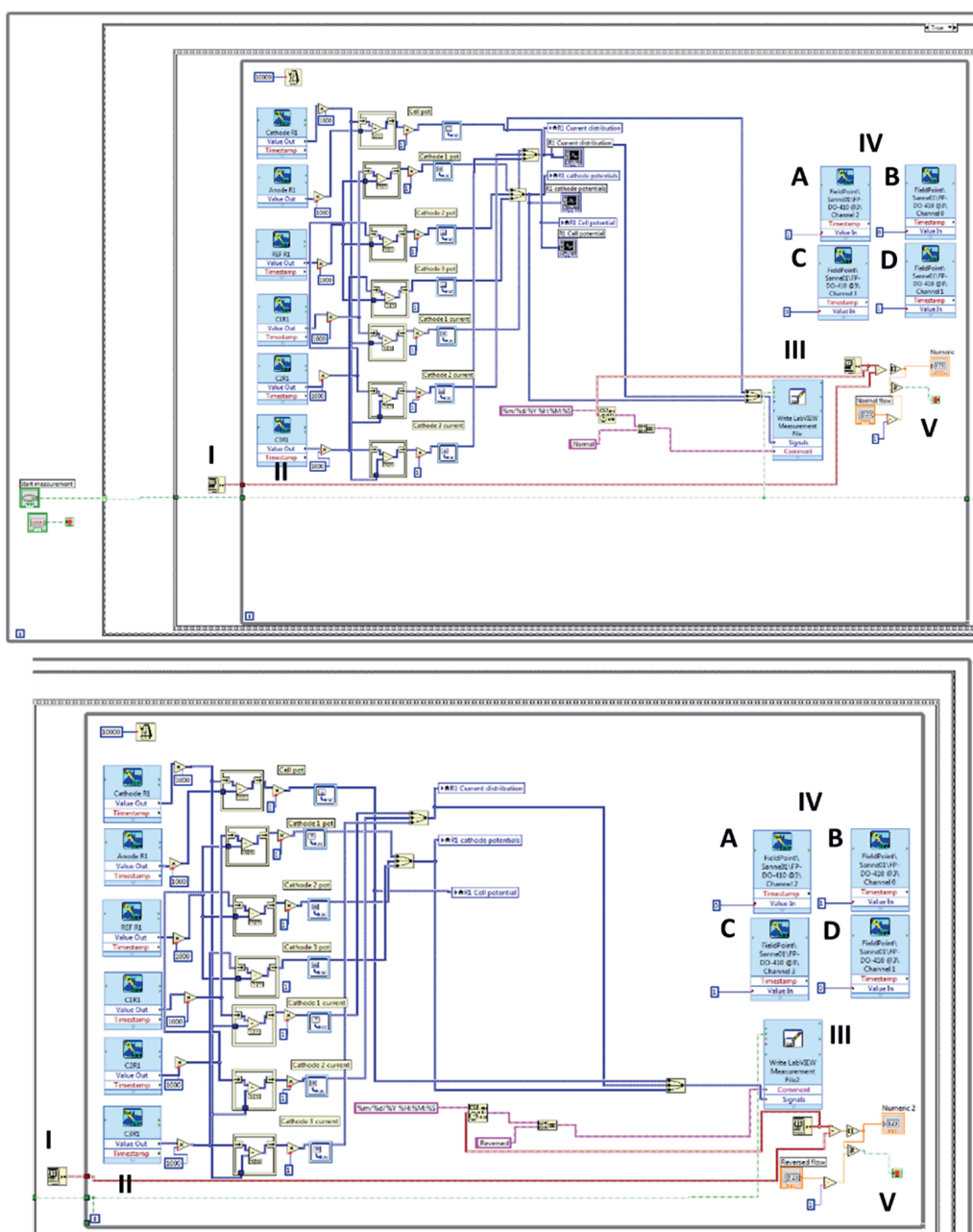


Figure S6.1. LABVIEW 2015 configuration of alternating flow-through electrolyte recirculation. The bottom part was placed behind the top part. Both boxes (top and bottom frames) were controlled with time-based while loops (I). During the while loop, the values of the cell potential, cathode potential 1-3 (vs top fixed reference electrode and specific cathode layer current 1-3 (II) were measured every 10 sec and written in a csv file (III). Furthermore, the valves were closed/opened (IV): a switch from A and D open (flow away from membrane) to B and C open (flow towards membrane) was made between the two frames (top and bottom), see Figure 6.1 for valve names. The switch to the next frame was controlled with the while loop feedback indicated with V.

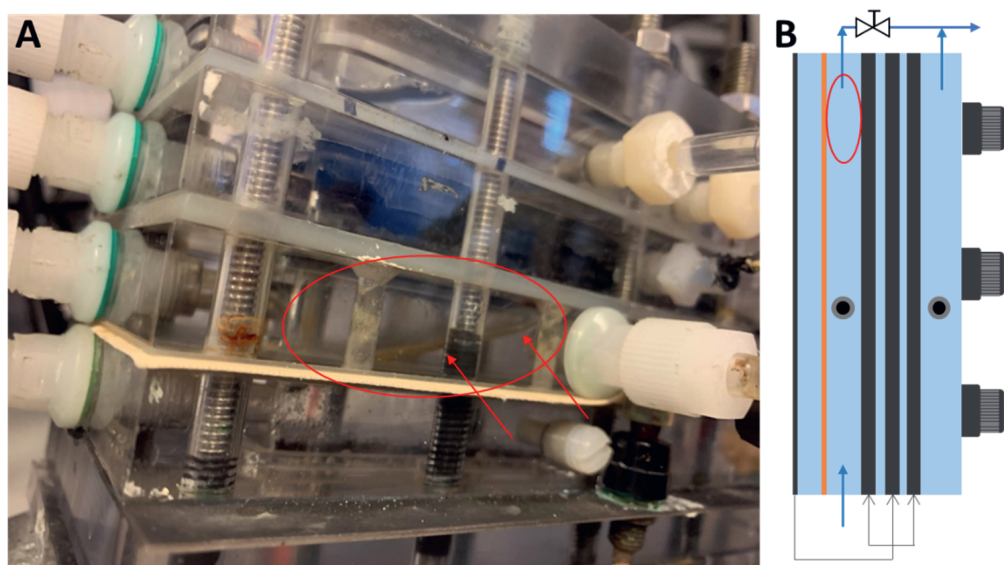


Figure S6.2. Accumulation of gas underneath the cathode layers with bypass closed (B, valve).

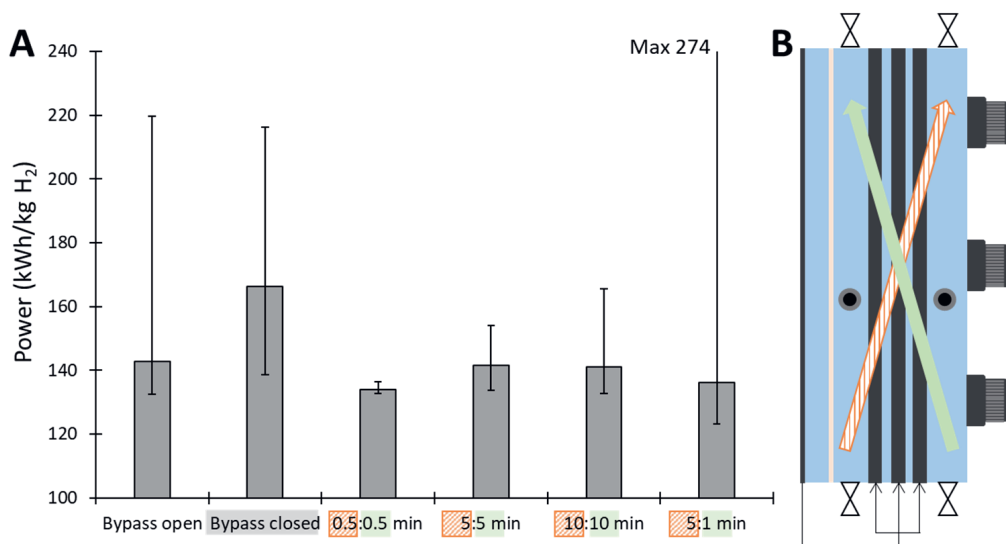


Figure S6.3. Electric power demand per kg produced hydrogen averaged over 3.5 hours of switching flow direction between away from (orange dashed) and towards (green filled) the membrane of the replicate reactor operated at -10.4 kA/m^2 . The error bars show the minimal and maximal measured energy consumption.

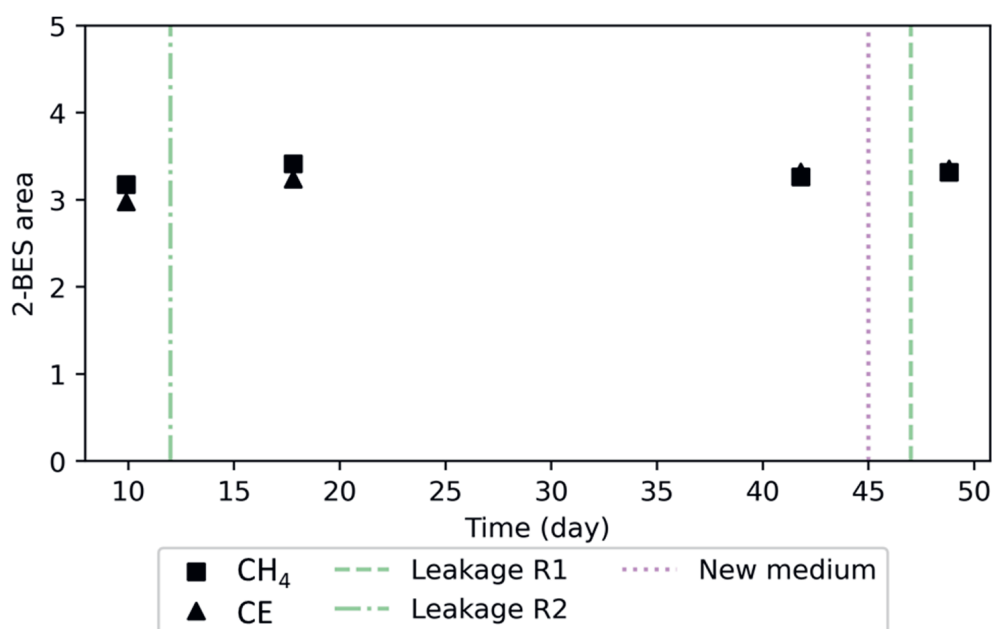


Figure S6.4. Area of ion chromatography chromatogram peak for 2-bromoethanesulfanoate in the reactor catholyte of the methane forming (CH₄) and chain elongating (CE) reactor during the course of the biotic experiment.

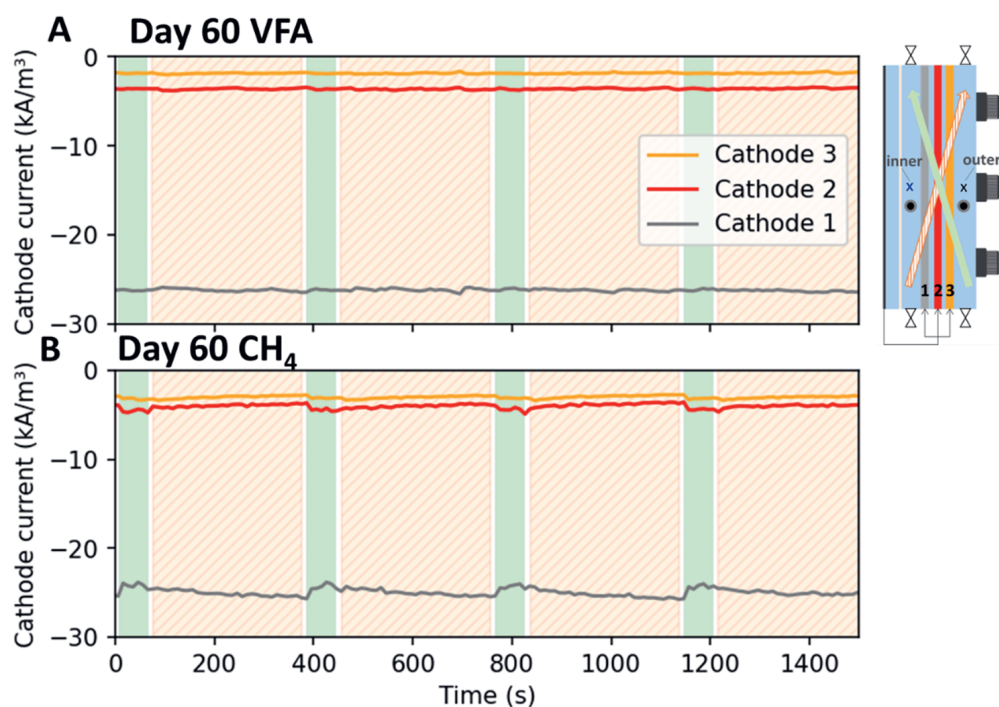


Figure S6.5. Current densities at different cathode layers in the biotic volatile acid producing (VFAs) and methane producing (CH₄) reactor on day 60.

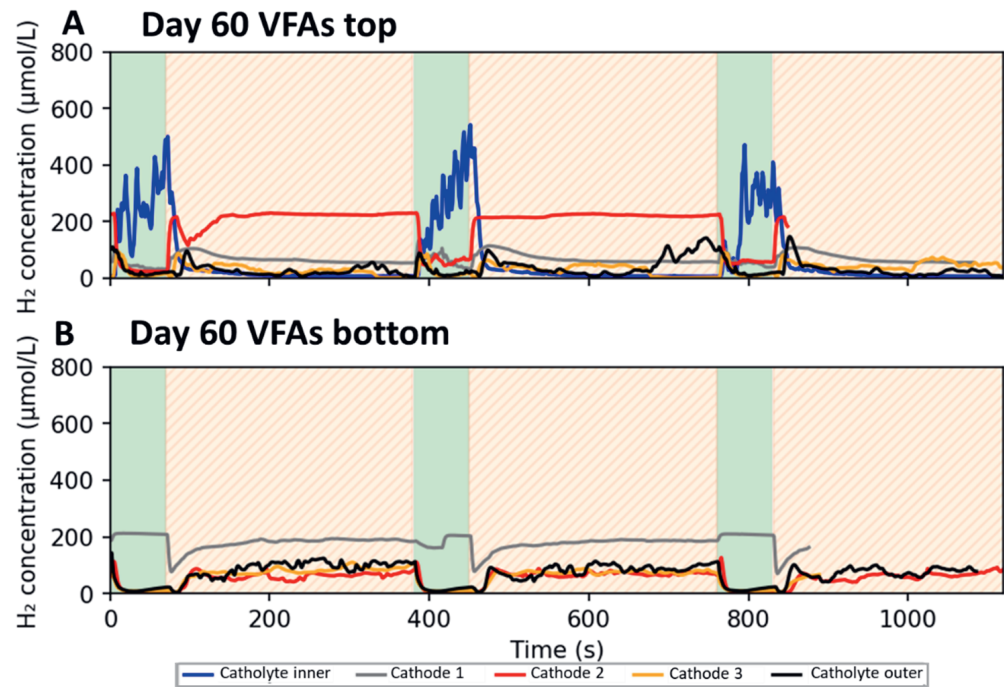


Figure S6.6. Local pH and hydrogen concentration through the top and bottom well in the biotic VFA producing reactor on day 60. Due to technical issues, the inner catholyte was not measured in the bottom well (B).

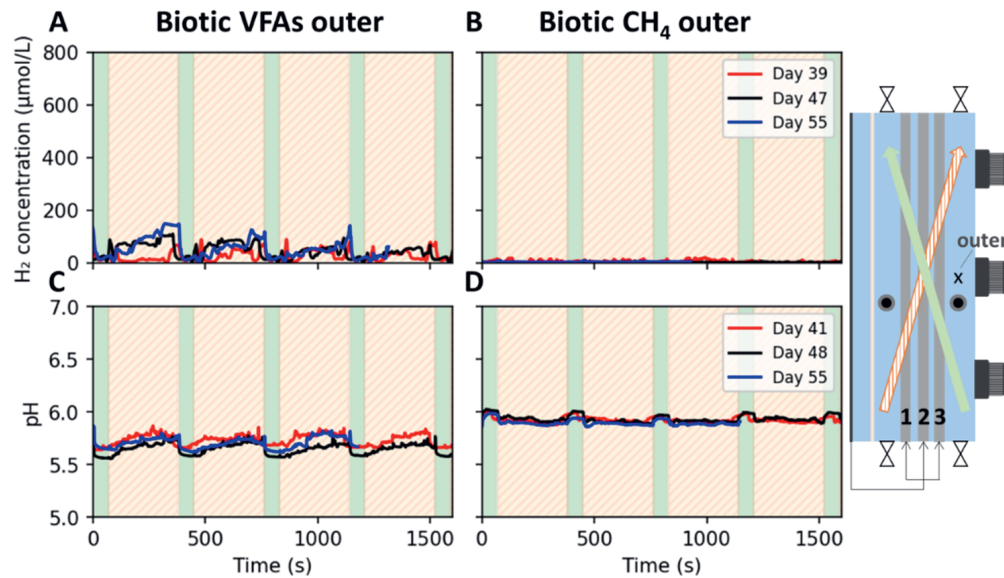


Figure S6.7. Local hydrogen (A and B) concentration and pH (C and D) on the outer side of the cathode in the two biotic reactors over time.

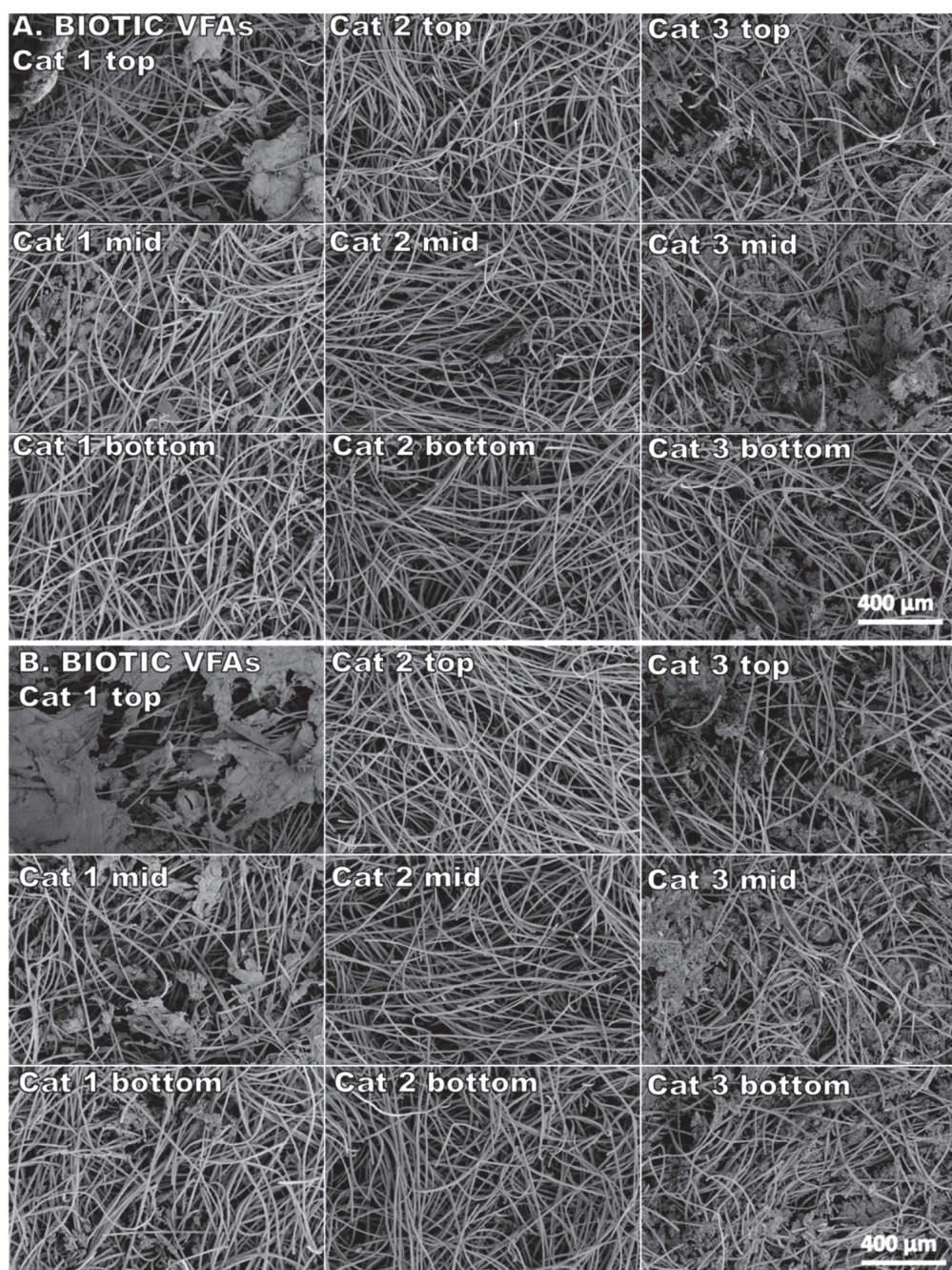


Figure S6.8. Scanning Electron Microscope image of biofilm coverage on graphite felt pieces of different reactor locations from the biotic volatile fatty acid producing reactor sampled on day 60. The reactor orientation corresponds with the figures in this picture (e.g. Fig 6C). A and B are duplicates from different locations within the same samples, the third location is shown in Figure S6.10A.

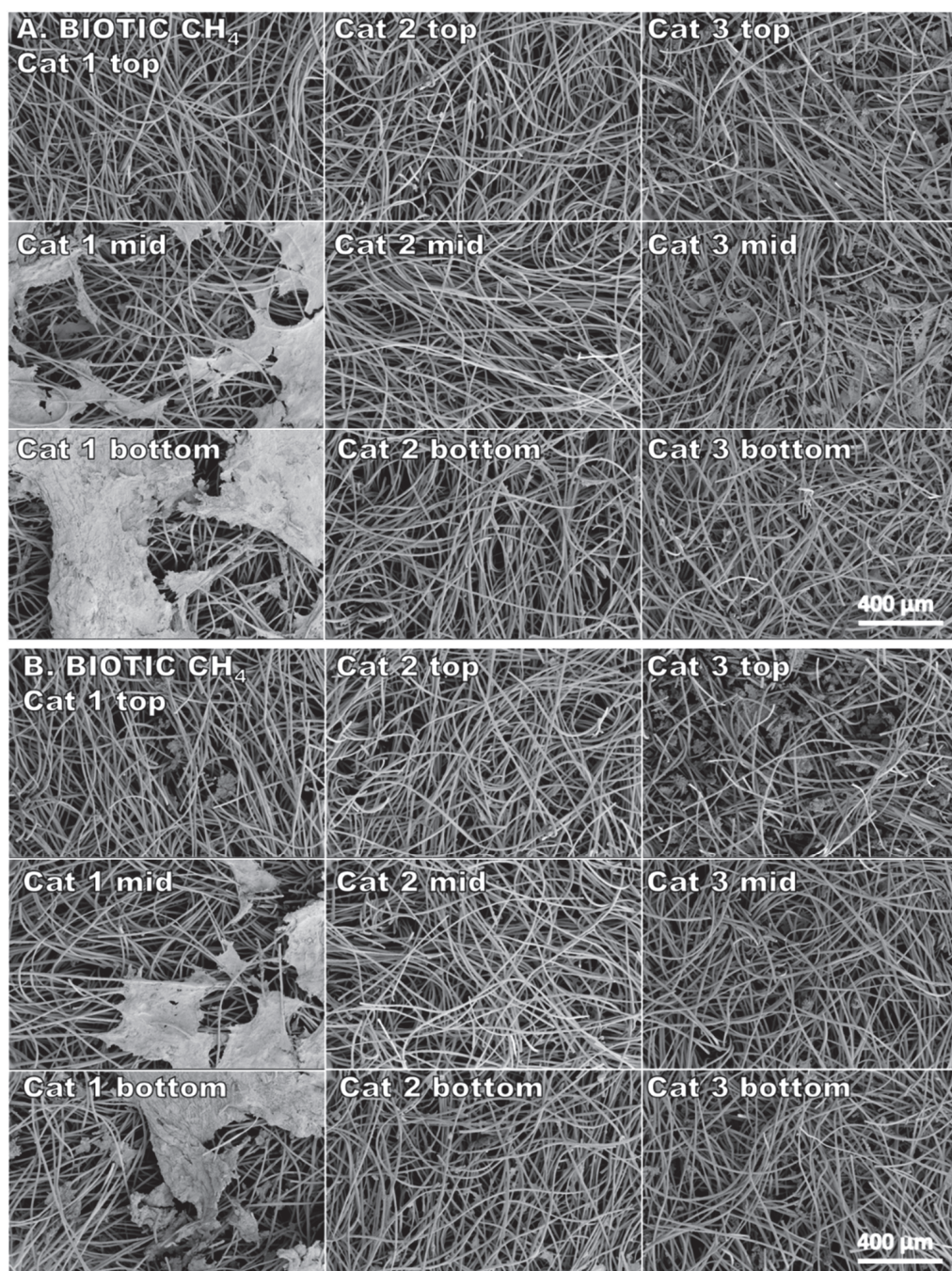


Figure S6.9. Scanning Electron Microscope image of biofilm coverage on graphite felt pieces of different reactor locations from the biotic methane producing reactor sampled on day 60. The reactor orientation corresponds with the figures in this picture (e.g. Fig 6C). A and B are duplicates from different locations within the same samples, the third location is shown in Figure S6.10B.

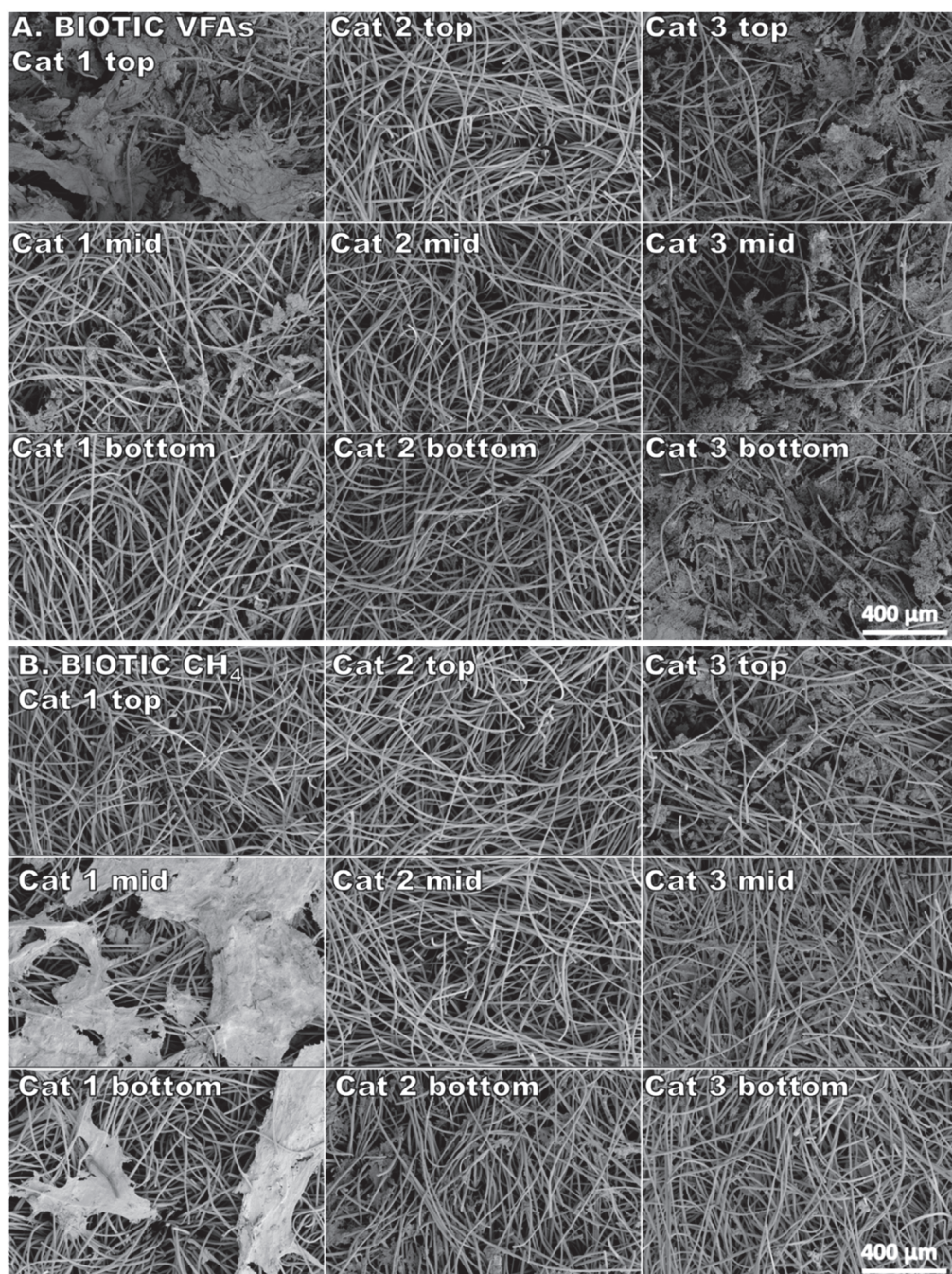


Figure S6.10. Scanning Electron Microscope image of biofilm coverage on graphite felt pieces of different reactor locations from the biotic volatile fatty producing reactor (A VFAs, top 9 images) and the biotic methane producing reactor (B CH₄, bottom 9 images), both sampled on day 60. The reactor orientation corresponds with the figures in this picture (e.g. Fig 6C).

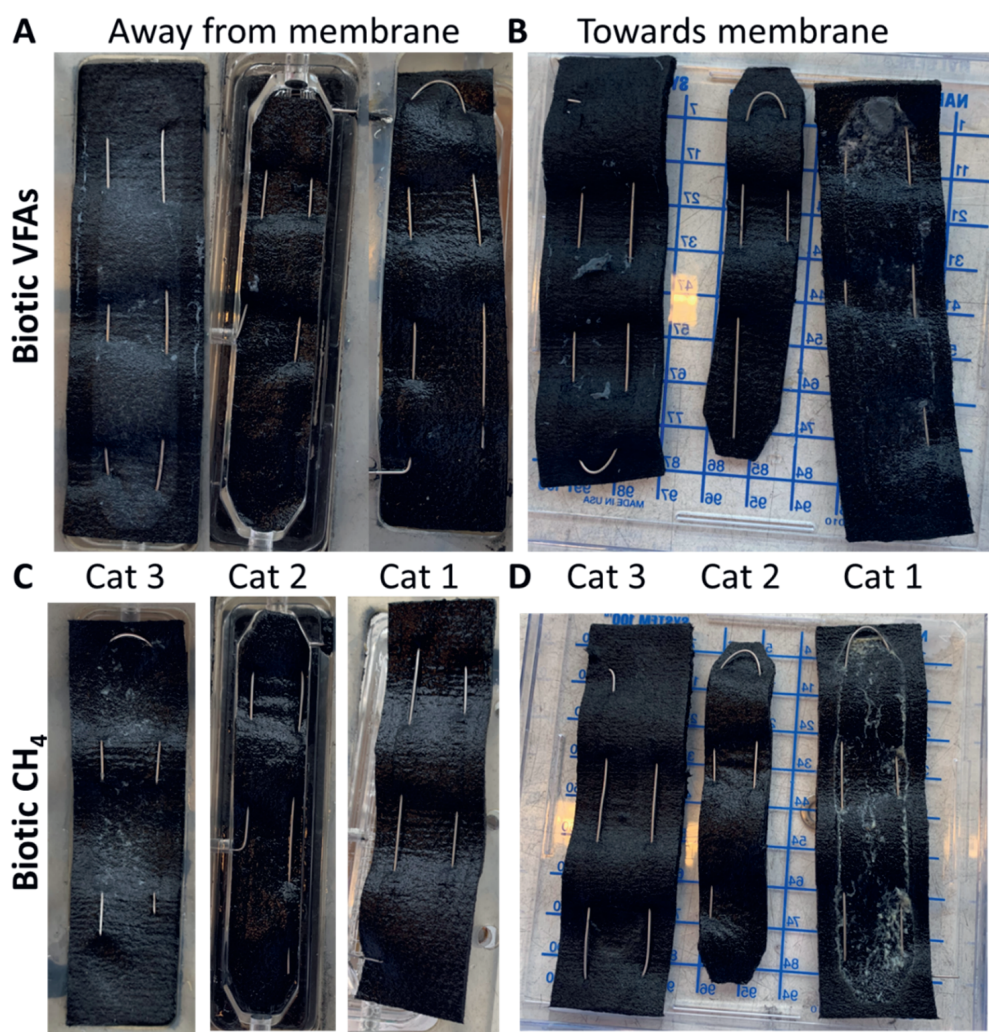
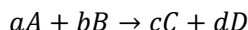


Figure S6.11. Pictures taken of the cathode layers at day 60 of the biotic experiments (A&B biotic VFAs and C&D biotic CH₄) after stopping the reactors. Two sides of each cathode layer were photographed, the side facing away from the membrane (A&C) and the side facing towards the membrane.

Appendix I: calculation of local Gibbs free reaction energy

From a conversion reaction in form:



The Gibbs free energy was calculated by:

$$\Delta G_r^0 = aG_{f,A}^0 + bG_{f,B}^0 - cG_{f,C}^0 - dG_{f,D}^0$$

The enthalpy was calculated by:

$$\Delta H_r^0 = aH_{f,A}^0 + bH_{f,B}^0 - cH_{f,C}^0 - dH_{f,D}^0$$

The Gibbs free energy was also corrected for temperature and actual concentrations:

$$\Delta G_{catholyte}^{1,T} = \Delta G_r^0 * \left(\frac{T_1}{T_0}\right) + \Delta H_r^0 * \left(\frac{T_0 - T_1}{T_0}\right) + RT_1 \ln \left(\frac{[C]^c [D]^d}{[A]^a [B]^b}\right)$$

With R the gas constant 8.314 J/(K*mol), T₁ the temperature in K, T₀ 298.15 K and [C], [D], [A] and [B] the concentrations in mol/L, corrected for dissociation:

$$[A^-] = [total A] * \frac{K_A}{K_A + [H^+]}$$

With K_A the dissociation constant in mol/L. The Gibbs free energy of formation was always used for either the undissociated or the dissociated compounds and used with the corresponding concentration.

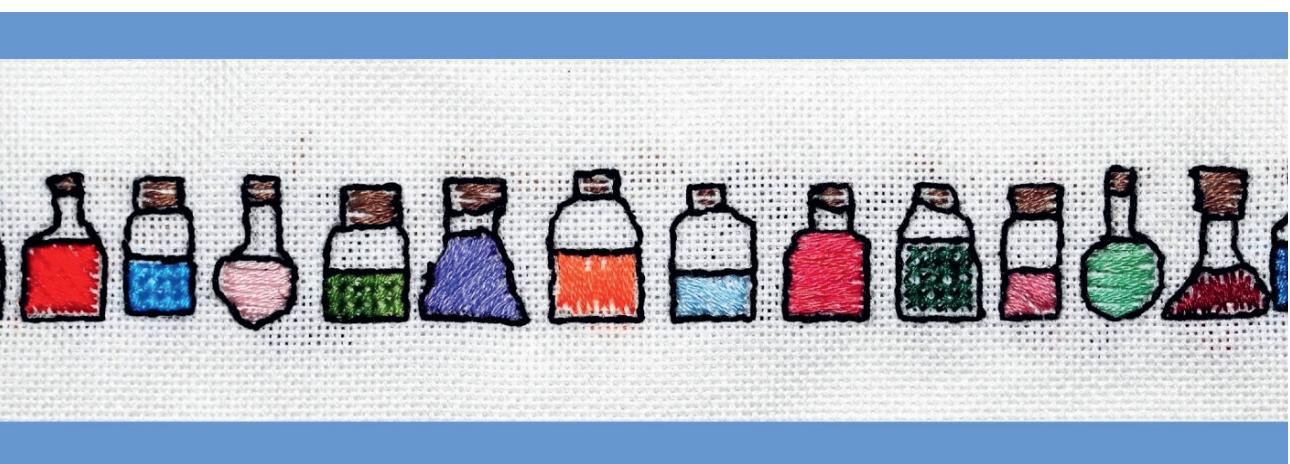
For reactions with electrons as energy source, the potential was calculated from the Gibbs free energy:

$$E^1 = \frac{-\Delta G^0}{nF} - \frac{RT_1}{nF} \ln \left(\frac{[C]^c [D]^d}{[A]^a [B]^b}\right)$$

With n the number of electrons and F the Faradaic constant 96485 C per mol e⁻. Then the Gibbs free energy was calculated based on the cathode potential:

$$\Delta G_{cathode}^{1,T} = E^1 - E_{applied} * n * F$$

With E_{applied} the cathode potential. The formation energies and enthalpies were taken from Kleerebezem and Van Loosdrecht⁶⁵, Hanselmann⁶⁶, Heijnen⁶⁷ and Adriaanse, et al.⁶⁸.



Chapter 7

General Discussion



In this thesis, bio-electrochemical CO₂ valorisation process improvements are described in the areas of electron availability, start-up strategy and mass-transfer. It was discovered that the trace metals can function as hydrogen evolution catalyst under microbial compatible conditions. Moreover, the hydrogen evolution catalyst was successfully combined with biocatalysts in CO₂ valorisation systems. The impact of the hydrogen evolution catalyst was shown in the Trace Metal Mix (TMM) pre-treatment studies (Chapters 3-4). With the TMM+ pre-treatment (trace metal mix with EDTA), current densities at the start of the biotic phase were in the range of -12 kA/m³, which is in the range of systems running for over 100 days (study from Jourdin, et al. ¹: -14 kA/m³) and the TMM- (trace metal mix without EDTA) pre-treatment even resulted in current densities up to -80 kA/m³. With electron recoveries into hydrogen of 70-100%, hydrogen was the main available electron donor at the cathode. The developed start-up strategy resulted in a fast start-up of *n*-butyrate production with concentrations up to 100 mM C after 40 days (Chapter 4, TMM+). In Chapter 6 demonstrates that with improved hydrogen distribution through the cathode by the alternating flow-through regime, even *n*-caproate production can be started within 45 days after system start-up at current densities of -10 kA/m³, which is an improvement of 50 days compared to proof of principle studies showing *n*-caproate formation from CO₂^{1,2}.

With these promising results, the findings can be placed in perspective of current state of art technologies and indicate target points for future studies. Several questions were addressed:

1. *Can hydrogen-based productivities of volatile fatty acids compete with state of art hydrogen-based productivities of methane?*
2. *How does the TMM- hydrogen evolution catalyst electrolyser performance relate to a commercial electrolyser?*
3. *Is an in situ electrode essential for hydrogenotrophic CO₂ elongation to volatile fatty acids?*
4. *How can bio-electrochemical n-caproate production be further optimized?*

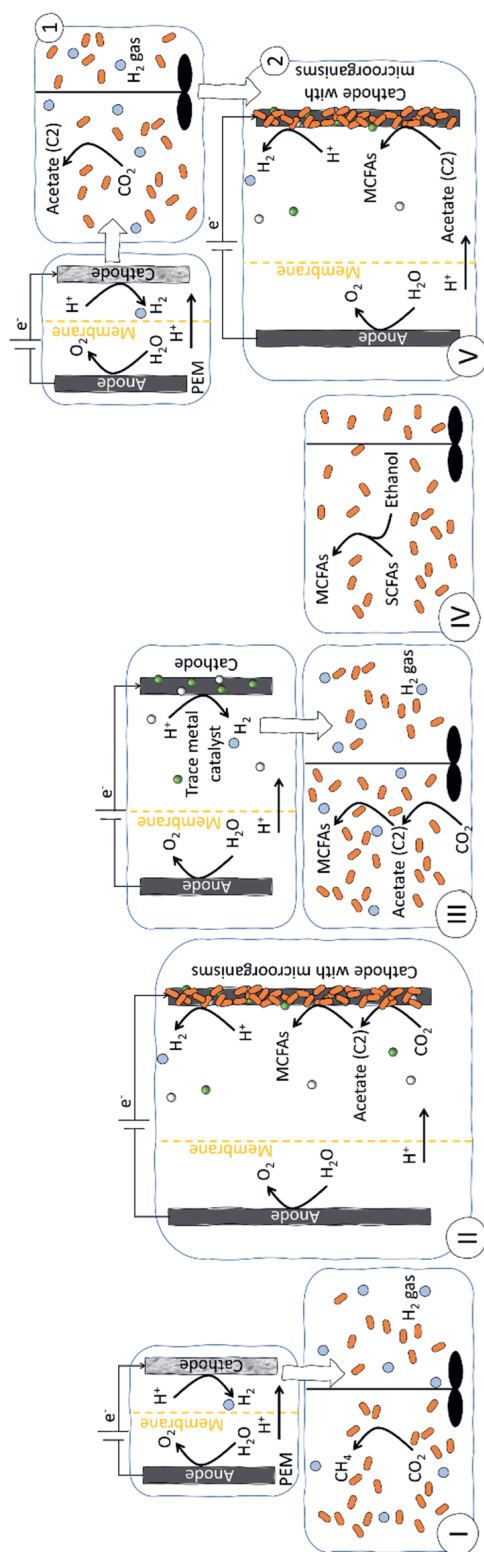
The abovementioned questions were answered based on a performance comparison between five different systems. Three technologies based on the findings in this thesis were compared with two state of art biological CO₂ utilisation technologies hydrogen-based fermentation and anaerobic fermentation with an organic electron donor. The five systems are described below:

- I. **Hydrogen-based fermentation: Electrochaea.** During hydrogen-based fermentation, an electrolyser is used for effective hydrogen production and coupled to a hydrogen-based fermentation system. An example of a large scale hydrogen-based fermentation plant that was used here is Electrochaea, which performs hydrogenotrophic methanogenesis (Table 7.1, system I). Several demonstration plants have been built with stirred bubble-column bioreactors, fed with hydrogen obtained with polymeric electrolyte membrane (PEM) electrolyzers and CO₂ from waste sources (e.g. landfills, biogas, dairies etc), yielding up to methane which can be put into the gas grid. Currently, the largest demonstration plant is located in Avedøre, Denmark: a 1 MWe plant producing 250 m³ methane per m³ reactor volume per day³⁻⁵ and a 10 MW plant is designed⁶. The first system is hereby named “Electrochaea”.
- II. **In situ hydrogen generation with microbial electrosynthesis: HER & MES** A challenge in hydrogen-based fermentation is poor solubility of hydrogen. The dissolving

of hydrogen could be improved by the integration of the hydrogen evolution catalyst in microbial systems, such as developed in this thesis (trace metal mix with EDTA, TMM+) (Table 7.1, system II). To compare productivities of hydrogen-based methane to hydrogen-based volatile fatty acids, the bio-electrochemical system with integrated TMM+ hydrogen evolution catalyst was considered (Table 7.1, system II). Herein also microbial-electrochemical electron transfer via direct uptake, enzymatic and/or mediated electron shuttling may co-occur. The Hydrogen Evolution Reaction and Microbial Electrochemical System is addressed as “HER&MES”.

- III. **Hydrogen-based fermentation with metal mix catalyst: HER+CE** Besides the hydrogen solubility, the future scarcity of catalyst metals used on the PEM electrolyser electrodes (Pt and Ir)⁷ is an additional issue. Therefore, as a second comparison, a system with a non-noble metal mix hydrogen evolution catalyst (trace metal mix without EDTA, TMM-) is presented as possible replacement for the expensive Pt catalyst currently used in electrolyzers⁸ (Table 7.1, system III). An ideal requirement is that the performance of the non-noble catalyst compares to the Pt-based catalyst. The TMM-hydrogen evolution catalyst electrolyser was combined as a dual stage system with a gas fermentation fed with CO₂ and H₂ producing volatile fatty acids. This system allows a comparison of hydrogen-based volatile fatty acid production with and without integrated hydrogen producing electrode. System III is named Hydrogen Evolution Reaction and Chain Elongation: “HER+CE”.
- IV. **Biowaste fermentation: ChainCraft**. In the second state of art process, anaerobic fermentation with an organic electron donor, an organic compound forms the microbial energy source instead of an electrode. An example of an industrial sized plant performing anaerobic fermentation is the Amsterdam demoplant of ChainCraft, which is converting the short chain fatty acids (SCFAs) obtained from acidified biowaste into medium chain fatty acids (MCFAs) with ethanol as electron donor for the microbial catalyst⁹ (Table 7.1, system IV). The demonstration factory in Amsterdam is now producing a 2,000 tons of fatty acids per year¹⁰. Since this state of art process yields high value fatty acids instead of lower value methane¹¹⁻¹⁴, it forms a better comparison to bio-electrochemical CO₂ valorisation described in this thesis than methane production. A requirement to make the electrosynthesis of MCFAs compatible is production rate. The fourth system is referred to as “Chaincraft”.
- V. **Hydrogenotrophic acetogenesis and consequent microbial electrosynthesis: Aceto+MES**. As a fifth comparison, a system with separate units for different steps of the fatty acid elongation is proposed (Table 7.1, system V). One unit is used for autotrophic acetogenesis from CO₂ and hydrogen from a PEM electrolyser (1) and a second unit is used to convert the acetate to medium chain fatty acids with the electrode as energy source (2). The separation of the two process steps can allow separate application of different ideal conditions for the microbiome responsible for the chain elongation step, possibly leading to high production rates. The performance characteristics of this system allow for comparison of hydrogen-based fermentation and anaerobic fermentation with an organic electron donor. The fifth system is referred to as Acetogenesis+Microbial Electrosynthesis System: “Aceto+MES”.

Table 7.1.1. Schematics and comparison of the five CO₂ utilisation systems: (I) Electrochaea - dual stage demo scale polymer electrolyte membrane (PEM) electrolyser coupled to microbial methane formation (based on Electrochaea technology), (II) HER&MES - concept of an integrated metal mix (with EDTA) hydrogen evolution reaction catalyst with microbial chain elongation, (III) HER+CE - concept of dual stage of metal mix (without EDTA) for hydrogen evolution reaction coupled to hydrogen-based microbial chain elongation, (IV) Chaincraft - ethanol-based chain elongation of short chain fatty acids (SCFAs) to medium chain fatty acids (MCFAs) (based on Chaincraft technology), and (V) Aceto+MES - concept of dual stage chain elongation process with hydrogen based acetogenesis (I) coupled to bio-electrochemical acetate elongation to MCFAs (2). The two demonstration plant scale processes are indicated with *, calculations are shown in the Supporting Information.



	System I: Electrochaeta	System II: HER&MES	System III: HER+CE	System IV: Chaincraft	System V: Aceto+MES
Reactor design	Dual stage: PEM electrolyser with microbial methane formation	Integrated HER catalyst with microbial chain elongation	Dual stage: metal mix electrolyser and microbial chain elongation	Ethanol based short chain fatty acid elongation	Dual stage: autotrophic acetogenesis with bio-electrochemical chain elongation
Input gas stream	100% CO ₂ or CO ₂ /CH ₄ 40%/60%	CO ₂ /N ₂ 30%/70%	H ₂	-	H ₂ /CO ₂ /N ₂ 40%/16.7%/43.3%
HER catalyst	Pt (PEM electrolyser)	Metal Mix with EDTA (TMM+) (possibly bacteria)	Metal Mix no EDTA (TMM-)	-	Pt (PEM electrolyser)
Hydrogen power requirement (kWh/Nm³ H₂)*	4.5-5 ¹⁵	8.6	22.4	-	4.5-5 ¹⁵
Exchange current density (mA/cm²)*	0.98 ²⁰	0.0023 <i>Per projected surface area</i>	1.36 <i>Per projected surface area</i>	-	0.98 ²⁰
Microbial catalyst	Archaea <u>single culture</u>	Bacteria alkaliphilic <u>mixed culture</u>	Bacteria <u>mixed culture</u>	Bacteria mixed culture	I: Bacteria pure culture II: Bacteria alkaliphilic mixed culture
CO₂ conversion (%)*	98 ^{4,5}	0.4 ²¹	95 ²²	76 ²⁶ (carbon into products) 7 (ethanol to butyrate) 72 (ethanol to caproate) ²³	I: 20 ²⁴ II: 99.4 ²⁵
Substrate or electron recovery into products (%)	>99 ¹⁵ (H ₂ into methane) 52-58 ¹⁵ (e ⁻ to methane)	70 (e ⁻ to C2-C6) ²¹	44 ²² (H ₂ to C2-C8 alcohols and volatile fatty acids)		I: 17 ²⁴ (H ₂ to acetate) II: 93.8 ²⁵ (e ⁻ to butyrate)
Production rate (g/L_{reactor}/d)	1435 methane ^{4,5,15*}	0.9 acetate 0.59 butyrate 0.36 caproate ²¹	0.08 acetate 0.17 butyrate 0.16 caproate 0.05 caprylate ²²	6.6 butyrate 26 caproate ²³	I: 28.8 acetate ²⁴ II: 0.87 butyrate ²⁵

To generate conceptual comparative data, information was gathered from different sources. The calculations and used formulas can be found in the Supporting Information. In short, performance data for each system was gathered and used as follows:

- I. To obtain performance data from the “Electrochaea” plants, reported data from plant scale operation^{3-5,15} was combined with data from the founding lab study by Martin, et al.¹⁶ and the patent on the Archaea biocatalyst used in the Electrochaea systems¹⁷. For the PEM electrolyser, data from Leal¹⁸ and Proost¹⁹ was used. The exchange current densities were taken from Pt(110) catalysts, tested by Marković, et al.²⁰.
- II. For the “HER&MES”, data from the TMM+ system from Chapter 4 was used for the catalyst performance, and combined with the highest reported productivities²¹ under similar conditions.
- III. For the “HER+CE”, data from the TMM- hydrogen evolution catalyst from Chapter 3 was combined with a study from Calvo, et al.²² for the fermentation performance.
- IV. For the performance and efficiencies of the “Chaincraft” plant, data from Grootcholten, et al.²³ was used, where ethanol-based microbial chain elongation was performed at lab scale. It was assumed that the demonstration plant performs with similar ranges as reported in the lab study.
- V. For the “Aceto+MES” system, data from PEM electrolyzers^{18,19} was combined with performance data from Straub, et al.²⁴ for the acetogenesis and data from Raes, et al.²⁵ for the bio-electrochemical acetate elongation to MCFAs.

7.1 Can hydrogen-based productivities of volatile fatty acids compete with state of art hydrogen-based productivities of methane?

To understand whether *hydrogen-based productivities of volatile fatty acids can compete with state of art hydrogen-based productivities of methane*, the productivity of “Electrochaea” (system I, Table 7.1) was compared to the highest reported caproate productivity in microbial electrosynthesis, “HER&MES” (system II, Table 7.1). Even though methane and volatile fatty acids have different applications and markets, a comparison with the “Electrochaea” process gives an impression of the readiness hydrogen-based volatile fatty acid scale-up. The highest reported caproate productivity is 0.36 g caproate/L reactor/d, while the “Electrochaea” productivity is 1435 g methane/L reactor/d. Caproate also has a higher value than methane, so to compare these values, the costs should be taken into account. Recently reported market values are 269 \$/g methane²⁷ and 4450 \$/g caproate²⁸. The difference in value does not outweigh the difference in productivity rates (Table 7.1), so the caproate productivity should be increased in the microbial electrosynthesis systems to make hydrogen-based volatile fatty acid production a promising process for scale-up. The rates measured for volatile fatty acid production from biowaste (26 g/L/d caproate, “Chaincraft”, Table 7.1) are in a range that makes the process potential profitable, showing that with improved caproate productivities, the “HER&MES” could create a business case for scale-up. Additional factors like purity, extraction of the volatile fatty acid

stream and further process costs were not discussed here but should also be taken into account for a valid comparison of hydrogen-based methane and volatile fatty acid production.

7.2 How does the TMM- hydrogen evolution catalyst electrolyser performance relate to a commercial electrolyser?

To investigate *how the TMM- hydrogen evolution catalyst performance relate to a commercial electrolyser*, the PEM electrolyser performance reported by Electrochaea was compared to the TMM- electrolyzers from this thesis, shown in the “HER+CE” system (system I&III, Table 7.1). The hydrogen power requirement for the TMM- electrolyser was calculated based on the cell potential (9.35 V, see SI), which was most likely high due to hydrogen build up, as also addressed in Chapter 6. At lower hydrogen production rates with the TMM+ hydrogen evolution catalyst, a cell voltage of 3.58 V was measured, which would be more representative for the power requirement of the TMM- hydrogen production in an optimized cell, e.g. with shorter distance between anode and cathode. To compare hydrogen production of the TMM catalysts with a platinum electrode rates purely based on cathode potential, exchange current densities were extracted from Tafel slope analysis performed with the linear sweep plots from S3.8 (SI Figure S7.1). Note that due to the high volumetric surface area of graphite felt²⁹, the exchange current density of the TMM catalysts on a flat surface will be lower. The values for hydrogen power requirement (8.6 kWh/Nm³ H₂) and exchange current density (1.36 mA/cm² projected surface area, TMM-) are in the same order of magnitude as the ranges reported in the demonstration plants (4.5-5 kWh/Nm³ H₂ and 0.98 mA/cm²). Furthermore, the required current density for the “Electrochaea” system (-801 kA/m³ reactor, see SI for calculation) is only 10 times higher compared to the current density obtained with the TMM- hydrogen evolution catalyst (-80 kA/m³ cathode, Chapter 3). Also the electron recovery of hydrogen into final products in the integrated “HER&MES” system (70%) are similar to the electron recovery of ethanol into products from “Chaincraft” (79%). These are promising indications that the TMM- electrolyser potentially forms an alternative for the currently used PEM electrolyser or ethanol as electron donor.

In the currently produced PEM electrolyzers, Pt is used as catalyst⁸. Pt is a rare element in earth. Therefore the manufacturing of the catalyst coated membranes for PEM electrolyzers leads to high costs: up to \$1000 per m² projected surface area³⁰. A “back-of-the-envelope” calculation on the costs of manufacturing TMM- cathodes (graphite felt with titanium wire and 100% deposition of 10 vol% TMM- in 0.3 L catholyte, assuming bulk costs from Alibaba) shows that the materials for “TMM- coated cathodes” would cost approximately \$70 per m² projected surface area (SI, Table S7.1). These costs can likely be reduced by elimination of redundant elements from the metal mix, which is addressed later. Investing up to 14 times more in the Pt PEM electrolyzers does result in lower electricity costs for hydrogen, since the energy requirement for production of 1 Nm³ hydrogen is 4.5-5 kWh¹⁵. Yet, the TMM cathodes are already in a comparative range for hydrogen production (1.36 mA/cm² projected surface area exchange current density), with a less than two times higher energy requirement for hydrogen production of 8.6 kWh/Nm³ (Table 7.1). This compatibility shows that it is definitely interesting to perform a techno economic analysis of using the TMM+ catalyst for hydrogen production.

7.2.1 Hydrogen evolution catalyst optimisation: source, composition, stability

With the lessons learned from the experiments in this thesis, the performance of the TMM-hydrogen evolution catalyst could be improved to reach towards a lower energy use competitive to the present 4.5 kWh/Nm³ hydrogen. Besides, optimizing the TMM+ hydrogen evolution catalyst towards an exchange current density of 0.98 mA/cm² could provide a better and more bio-compatible hydrogen evolution catalyst. Here, several optimisation study suggestions are given to further improve the cost-efficiency and stability of the hydrogen evolution catalyst in bio-electrochemical CO₂ valorisation systems. The cost-efficiency could be improved by eliminating elements without hydrogen evolution catalyst properties (at the used conditions) from the added trace metal mix. For the TMM+ mix, which showed the best volatile fatty acid productivity when used as *in situ* catalyst, it was shown that a mix of the Cu and Mo compounds reached the same hydrogen production performance as the TMM+ mix. These results showed that the Cu and Mo were the main important compounds for the TMM+ mix (Chapter 3). Elimination of the other compounds can reduce the pre-treatment costs.

Since the TMM- mix showed the best hydrogen evolution catalysis properties in Chapter 3, optimisation of the TMM- catalyst will result in a compatible external electrolyser. The absence of EDTA is the only difference between the TMM+ and TMM- mix, meaning that EDTA plays an important role on the formation of the hydrogen evolution catalyst. It is reported that the chelating agent influences the speed and nucleation mechanisms during electrodeposition³¹⁻³³. Additionally, OLI predictions indicated that EDTA prevents the formation of some solid Fe, Mn, Ni and Zn compounds on the cathode (Chapter 3). A mix of Cu and Mo without EDTA showed only a 10 A/m² difference in performance in comparison to the Cu and Mo mix with EDTA, while the difference between the TMM+ and TMM- was 200 A/m², indicating that the effect of EDTA on the attachment or performance of Cu and Mo was minor. Based on the insights from Chapter 3, the hydrogen evolution catalyst performance with (a mix of) Fe, Mn, Ni and Zn without EDTA is expected to match the performance of the TMM- catalyst. Besides eliminating compounds which do not affect the performance of the catalyst, varying metal loading by varying concentrations, or ratios of the compounds, in the pre-treatment mix can also lead to optimisation, since these adaptations can improve the atomic active centre of the hydrogen evolution catalyst³⁴. A last optimisation aspect of both TMM hydrogen evolution catalysts is the system itself. The anode and internal resistances of the electrochemical cells were not optimized in this thesis, so the cell voltage for hydrogen production could be even further reduced by optimization of the system design, e.g. by reducing mass-transfer limitations³⁵.

7.2.2 Stability optimisation of trace metal hydrogen evolution catalyst

A final optimisation point of the hydrogen evolution catalyst is improving its stability. Although the TMM hydrogen evolution catalysts showed stability over the full course of the 2 to 10 days abiotic experiments (Chapter 3), a 50% decrease of hydrogen productivity was observed within the 35 to 50 day course of the biotic experiments (Chapter 4). This current decrease indicates a decrease of catalyst stability with biotic conditions. Since current decrease was only observed during biotic operation, it is likely that either the presence of a biofilm or the long-term operation was the reasons for the stability decrease. The formation of a biofilm can cause biofouling of the catalyst, i.e. the deposition of polymeric structures on the active site³⁶. However, it should be

noted that other studies reported increased hydrogen productivity caused by the formation of a biofilm due to trace metal arrangement or formation of hydrogenase enzymes^{13,37-39}. The long-term operation could cause catalyst deactivation by catalyst poisoning e.g. by binding of e.g. N- or S-compounds to the catalyst surface^{40,41}. To restore catalyst activity, reactivation mechanisms can be tried, e.g., regular short intermittence of current or cyclic voltammetry.

Jourdin, et al.¹ observed a threefold current increase after application of a cyclic voltammetry scan. Over time, trace elements accumulate on the cathode, due to the reducing conditions. During the cyclic voltammetry scan, these trace elements are released into the catholyte as a result of the changing electrode potential. Right after the cyclic voltammetry scan, the trace elements are attached to the cathode at the reapplied reducing conditions (Chapter 2). A similar situation was tested in Chapter 3, after the addition of a concentrated trace element solution to an electrochemical reactor operated at reducing conditions, a hydrogen catalyst was formed. The attachment of a concentrated trace element mix is plausibly similar to the attachment of the released elements after the cyclic voltammetry scan. Therefore, it is probable that the hydrogen evolution catalyst activity can be restored by a cyclic voltammetry scan.

7.3 Is an *in situ* electrode essential for hydrogenotrophic CO₂ elongation to volatile fatty acids?

To determine whether an *in situ* electrode is essential for hydrogenotrophic CO₂ elongation to volatile fatty acids, the highest productivity of volatile fatty acids was compared in systems with an integrated electrode and systems which are fed with solely CO₂ as carbon source and H₂ as electron donor. The “HER&MES” system was compared to the “HER+CE” system. Several studies have shown microbial production of volatile fatty acids from CO₂ and H₂, but mostly with an integrated electrode. Calvo, et al.²² showed conversion of CO₂ and gaseous supplied H₂ to volatile fatty acids with carbon lengths up to C8 (caprylate) in membrane biofilm reactors. These productivities (0.16 g/L/d caproate, 0.05 g/L/d caprylate, “HER+CE”) were therefore used for the comparison in Table 7.1. The productivities from the studies with and without an integrated electrode are within the same range (0.36 g/L/d caproate, “HER&MES”). The productivities with integrated electrode are higher compared to systems which were sparged with 100% H₂. Based on this comparison and the current state of art literature, it can be concluded that the presence of an electrode increases the productivity rates of volatile fatty acids and is thus essential.

7.4 How can bio-electrochemical n-caproate production be further optimized?

The highest volatile fatty acid productivities from CO₂ and electricity (H₂) are still 100 times lower (0.36 g/L/d caproate) than the rates obtained in anaerobic fermentation with an organic electron donor (26 g/L/d caproate). Based on the experiments performed in this thesis, several factors can be pointed out to increase bio-electrochemical caproate production. One factor that leads to low caproate titres in bio-electrochemical systems is that up to 15% of the produced volatile fatty acids were transported to the anode (Chapter 6). The anode has a very low pH value (~1.5), so it is likely that it functions as extraction fluid for the undissociated form of the

volatile fatty acids, which is a neutral compound. When the membrane has high hydrophobicity, undissociated fatty acids can cross the cation exchange membrane⁴² towards the anode compartment of the cell. The disadvantage of this “*in situ* product removal”, is that the short chain fatty acids are unavailable for microorganisms to be elongated to medium chain fatty acids with higher value²⁸ and might even be oxidated at the anode. To prevent this loss of value, a more hydrophilic and more selective membrane needs to be used in future experiments, through which ideally only protons can diffuse⁴³.

As already noted in several previous papers¹¹⁻¹⁴, the growth of methanogenic Archaea should be prevented to increase the electron and substrate availability for volatile fatty acid production. Even though acetogens have a faster growth rate, methanogenesis yields more Gibbs energy than acetogenesis per mol e⁻ (Chapter 6), leading to a thermodynamic advantage for methanogens¹¹. Based on previous works, the CO₂¹³ and current (i.e. hydrogen) supply¹¹ were increased in our studies to suppress methanogenic activity, yet these measures did not completely inhibit methanogenic activity.

Also, the addition of methanogenic inhibitor 2-bromoethanesulfanoate in the microbial medium used in Chapter 6, did not prevent methane formation. Probably, after many generations of development, the methanogenic pathway of the Archaea in bio-electrochemical systems is no longer inhibited by the 2-bromoethanesulfanoate. Other parameters to inhibit methanogenesis were not yet optimized in this thesis, such as hydraulic retention time and the pH. Reducing the hydraulic retention time has been suggested to wash out methanogen biomass¹¹, yet this only applies for suspended methanogenic biomass. In our study, active methanogens were found in the attached biomass on the cathode (Chapter 4 and 6), so it is expected that, due to the methanogenic biomass retention on the cathode, no substantial wash out will be achieved with lowering of the hydraulic retention time. A low pH is reported to decrease methanogenic activity, probably due to the higher concentration of undissociated volatile fatty acids⁴⁴. At the cathode, pH values are typically higher than the bulk pH due to the formation of hydrogen, leading to disadvantageous selective pressure for chain elongation over methanogenesis. The pKa of acetate, *n*-butyrate and *n*-caproate are around 4.8-4.9, meaning that at pH 7, the fraction of undissociated acid is less than 1%. Especially at high hydrogen production rates (current densities of -10 kA/m³), the pH could increase up to 7 or higher (Chapter 5 and 6), which diminishes the fraction of undissociated acids and thus the inhibition of methanogens at the cathode. To maintain high hydrogen production, a lower pH at the cathode cannot be achieved without a formation of considerable amounts of undissociated fatty acids (e.g. local pH 5).

An alternative method to inhibit methanogens without the use of a chemical inhibitor is a pre-enrichment. A previous study showed a successful selection for chain elongation bacteria by pre-treating the inoculum with a heat shock⁴⁵ followed by four culture transfers under H₂:CO₂. This strategy was shown to be effective in preventing methane formation for at least 300 days¹⁴ and is thus recommended, possibly with repetition of heat shocks.

The aforementioned strategies can possibly improve the volatile fatty acid production, but an alternative system design would also be promising. For this alternative design, the process could be split up in different parts with different steps of CO₂ elongation in different subsequent systems, as suggested in the “Aceto+MES”.

For the first step of CO₂ valorisation to volatile fatty acids, low rates have been reported in bio-electrochemical systems, when compared to autotrophic CO₂ elongation with H₂. The acetate production rate (28.8 g/L/d) reported in an autotrophic acetogenesis process with pure culture bacteria are within the range of target caproate production rates (system V.1). Feeding this acetate to a separate bio-electrochemical system for the chain elongation step would not only supply a biofilm with sufficient substrate for an higher rate of chain elongation, but also change the use of a gaseous carbon source to a better soluble liquid substrate. In the bio-electrochemical chain elongation system from Raes, et al.²⁵ fed with acetate (system V.2), low feeding rates were used, which is presumably the limiting factor for formation of caproate¹. Yet, the 99.4% of the fed acetate was converted to butyrate²⁵, showing great promise for high caproate productivities at higher acetate feeding rates. The separation of the acetogenesis and chain elongation also allows to apply specific selection pressure parameters to each of the systems.

7.4.1 Steering towards direct electron transfer for efficiency improvement

In situ production of hydrogen can reduce process steps, but a more futuristic perspective would be to completely replace the electron donor with an electrode. A surplus of hydrogen is easily flushed out of the system, leading to loss of energy efficiency in all systems when no gas recycling is implemented. Therefore, using hydrogen as electron shuttle for microorganisms leads to difficulties at the expense of electron recovery into carbon-based products. It should be noted that overall system efficiency can be improved by changing the electron uptake mechanism of the microbial community to direct (interspecies) electron transfer⁴⁶. Although direct electron uptake has not been shown for chain elongation microorganisms, few studies have reported a change to direct electron uptake in microbial communities by lowering the hydrogen supply over time^{47–49}. Fortunately, the high productivity of the hydrogen evolution catalyst (up to 8 times higher compared to systems without hydrogen evolution catalyst) gives room for variation of the current, and thus hydrogen supply, during the course of an experiment whilst maintaining the reduced overpotential for hydrogen formation. During the start-up phase with the hydrogen evolution catalyst and alternating flow-through recirculation, biomass can be accumulated with high hydrogen concentrations (~200 μM). The low local hydrogen concentrations in the catholyte (0.5–1 μM) compared to within the cathode layers (100–600 μM) will possibly create selective pressure for biofilm formation over suspended growth^{12,13,50,51}. When productivities and biomass growth rates have stabilised, the hydrogen supply could be decreased by decreasing the cathode potential to a less negative value, to create selective pressure for direct (interspecies) electron transfer or decrease the hydrogen losses in the system.

Changing the cathode potential to less negative values might cause release of metal compounds from the cathode, since the oxidation (and thus release) of metals depends on the applied potential (Chapter 2 and 3, Pourbaix diagrams). With less metal compounds attachment to the cathode, the activity of the hydrogen evolution catalyst might be lowered. Preliminary predictions about the current at different potentials with a metal mix hydrogen evolution catalyst can be made based on the linear sweep voltammetry plots from Chapter 3. To monitor the hydrogen availability for the biofilm, a combination of microsensor measurements and

modelling study calculations could be used. Model calculations based on the biomass concentration⁵² can be verified with the actual hydrogen concentrations in the biofilm, measured with microsensors (Chapter 5 and 6). To homogenize hydrogen availability for different locations in a reactor, resistances can be used to distribute the applied current and flow-through operations can be used to distribute hydrogen within the cathode (Chapter 5).

7.4.2 Improvement of CO₂ conversion efficiency

Before transition towards bio-electrochemical CO₂ valorisation becomes feasible, improvement of the CO₂ conversion efficiency is one of the main challenges that needs to be tackled. The “HER+CE” and “Aceto+MES” systems show higher CO₂ conversion efficiencies (respectively 95 and 19.9 % of incoming CO₂) than the “HER&MES” system (0.4%, Table 7.1), which is mainly caused by the high CO₂ supply rate used in the “HER&MES” system (173 LN/d²¹) and this thesis (100 LN/d). In the “HER+CE” and “Aceto+MES” systems, the higher CO₂ conversion efficiency results in a lower production rate of medium chain fatty acids, as also suggested by Jourdin, et al.²¹. Almost ideal conversion efficiencies at high CO₂ supply rates have already been achieved in the Electrochaea process (98%, Table 7.1 process 1). This result shows promise for the optimization of CO₂ uptake, by improvement of e.g., reactor design, operation parameters or CO₂ supply. For example, Jourdin, et al.⁵³ have achieved a 94% CO₂ conversion efficiency with NaHCO₃ as carbon dioxide source. Increasing the amount of biomass will also improve the CO₂ uptake rates^{1,53}. Valuable insights for enhancing biofilm growth at the cathode can be gained from the methods described in Chapter 6. An alternating flow-through recirculation through the cathode distributes the hydrogen within the cathode layers, which allowed fast start-up of CO₂ elongation to *n*-butyrate and *n*-caproate. When the biofilm formation was studied after two months, barely any biofilm was found attached to the inner side of the cathode (Chapter 6). It was hypothesized that bigger flocs of inoculum were physically hindered by the small cathode porosity to reach the inner cathode layer. This issue could be overcome with adaptation of the cathode porosity⁵⁴. Also linking local conditions to biofilm growth will aid to enhance biofilm growth at the cathode.

7.5 Unique selling points of integrated hydrogen production and CO₂ utilisation

With considerable improvements of the CO₂ utilisation efficiency and the volatile fatty acid productivities, bio-electrochemical CO₂ valorisation can become a compatible technology. The integration of hydrogen formation and microbial CO₂ valorisation within one single system does offer several unique advantages that make it worth to perform further optimisation studies which are proposed below.

7.5.1 Extreme conditions integrated systems can result in higher selective pressure

The *in situ* hydrogen formation within the integrated system (“HER&MES”) causes a higher local pH (~7) at the cathode due to the consumption of protons, and the reactor operation at negative potentials influences the trace metal composition in the catholyte. Some metal elements, such as Cu and Mo are reduced and deposited on the cathode surface (Chapter 3), which could change their bio-availability. The combination of the conditions in the integrated system reactor creates

therefore a selective pressure for more alkaliphilic microorganisms with mechanisms protecting against high pH to form biofilms at the cathode⁵⁵. The proof of principle study from Chapter 4 shows that a volatile fatty acid producing microbial culture could be formed in the presence of a TMM based hydrogen evolution catalyst. Moreover, operation at higher pH could create selective pressure towards production of volatile fatty acids instead of alcohols⁵⁶. This is supported by the result that no alcohol production was detected in the experiments described in this thesis, whilst this was the case for the hydrogen-fed microbial culture in the “HER&MES” system (II, Table 7.1)²². The local selective pressure at the cathode surface which seems selective for certain microbial groups might even be the reason why hydrogen-based volatile fatty acid productivities reported thus far are higher in systems with an integrated electrode.

7.5.2 Integrated system for both hydrogen evolution catalyst and biocatalysts are possible

In bioreactors with mixed culture consortia, the operation conditions of the microbial reactors should steer the selectivity for desired microbial conversions. Generally, the optimal conditions for hydrogen evolution reaction catalysts are not simply the same as for microbial conversions (Chapter 3). Therefore, separating hydrogen evolution catalysis and microbial valorisation of CO₂, as shown in the “HER&MES” and “HER+CE” system, offers operation of both elongation steps at optimal conditions for the (bio)catalysts present in the system. However, with the integrated TMM+ catalyst (“HER&MES”), a unique situation is reached where both the hydrogen evolution reaction catalyst and the microbial catalysts showed reasonable performance with the applied conditions. Moreover, electroactive microorganisms could catalyse hydrogen evolution reaction³⁸, which would improve hydrogen production even further. The overlap between suitable conditions for the microbial and chemical catalysts could provide a large potential advantage that allows conversion of electrical energy and CO₂ into valuable chemicals in one single system.

7.6 Concluding remarks

In conclusion, the low costs of the TMM- electrolyser preparation combined with its high exchange current density, and energy use per m³ H₂ within the range of commercial electrolyzers, places the TMM- in an attractive position to further explore as a catalyst for hydrogen production for electro-fermentation or anaerobic fermentation. Moreover, this thesis has shown that integration of a hydrogen evolution catalyst and a biocatalyst for CO₂ valorisation is feasible. Although CO₂ utilisation efficiency and fatty acid productivities remain to be improved for complete process compatibility, several unique points can be indicated for integration hydrogen evolution and biocatalytic CO₂ valorisation:

- Higher productivity rates for autotrophic CO₂ valorisation to medium chain fatty acids compared to gaseous supplied H₂
- Microbial electrosynthesis shows a fast start-up vs. bio-electrochemical systems without integrated hydrogen evolution catalyst

- Selective pressure for biofilm formation at the cathode can steer process selectivity to volatile fatty acids only
- Several process steps can be merged so CO₂ conversion to green volatile fatty acids can be performed within one single system

References

- 1 Jourdin, L., Raes, S. M. T., Buisman, C. J. N. & Strik, D. P. B. T. B. Critical Biofilm Growth throughout Unmodified Carbon Felts Allows Continuous Bio-electrochemical Chain Elongation from CO₂ up to Caproate at High Current Density. *Frontiers in Energy Research* **6**, doi:10.3389/fenrg.2018.00007 (2018).
- 2 Vassilev, I. *et al.* Microbial electrosynthesis of isobutyric, butyric, caproic acids, and corresponding alcohols from carbon dioxide. *ACS Sustainable Chemistry & Engineering* **6**, 8485-8493 (2018).
- 3 Lardon, L. Biocat – Power to Gas technology by Biological methanation Integration to a resource treatment plant. (2017). <https://www.grese.ch/wp-content/uploads/2017/02/09_Laurent-Lardon.pdf>.
- 4 Angenent, L. T. *et al.* in *Resource Recovery from Water: Principles and Application* 141-158 (Willy Verstraete (Eds.), 2022).
- 5 Bailera, M., Lisbona, P., Romeo, L. M. & Espatolero, S. Power to Gas projects review: Lab, pilot and demo plants for storing renewable energy and CO₂. *Renewable and Sustainable Energy Reviews* **69**, 292-312 (2017).
- 6 Beschid, M. & Pentz, T. A. Green gas to fight climate change: Electrochaea's commercial 10-megawatt biomethanation plant engineering completed. (2022). <https://www.electrochaea.com/wp-content/uploads/2022/10/20220816_EIC_Archetype_draft_en_FIN-1.pdf>.
- 7 Greenwood, N. N. & Earnshaw, A. *Chemistry of the Elements*. (Elsevier, 2012).
- 8 Carmo, M., Fritz, D. L., Mergel, J. & Stolten, D. A comprehensive review on PEM water electrolysis. *International journal of hydrogen energy* **38**, 4901-4934 (2013).
- 9 Ricci, A. *et al.* Evaluation of the application for a new alternative processing method for animal by-products of Category 3 material (ChainCraft B.V.). *EFSA Journal* **16**, doi:10.2903/j.efsa.2018.5281 (2018).
- 10 Verbraeken, H. Chaincraft schaal op bij productie biologische vetzuren. *Financieel Dagblad* (2017).
- 11 Molenaar, S. D. *et al.* Competition between methanogens and acetogens in biocathodes: a comparison between potentiostatic and galvanostatic control. *International journal of molecular sciences* **18**, 204 (2017).
- 12 Jourdin, L. & Burdyny, T. Microbial electrosynthesis: where do we go from here? *Trends in Biotechnol.* **39**, 359-369 (2021).
- 13 Izadi, P., Fontmorin, J.-M., Godain, A., Yu, E. H. & Head, I. M. Parameters influencing the development of highly conductive and efficient biofilm during microbial electrosynthesis: the importance of applied potential and inorganic carbon source. *npj Biofilms and Microbiomes* **6**, 1-15 (2020).
- 14 Bajracharya, S. *et al.* Long-term operation of microbial electrosynthesis cell reducing CO₂ to multi-carbon chemicals with a mixed culture avoiding methanogenesis. *Bioelectrochemistry* **113**, 26-34 (2017).
- 15 Electrochaea. *Data sheet BioCat plant*, <http://www.electrochaea.com/wp-content/uploads/2018/03/201803_Data-Sheet_BioCat-Plant.pdf> (2018).
- 16 Martin, M. R., Fornero, J. J., Stark, R., Mets, L. & Angenent, L. T. A single-culture bioprocess of *Methanothermobacter thermautotrophicus* to upgrade digester biogas by CO₂-to-CH₄ conversion with H₂. *Archaea* **2013** (2013).
- 17 Mets, L. System for the production of methane from CO₂. United States patent (2006).
- 18 Leal, A. in *2021 International Conference on Green Energy, Computing and Sustainable Technology (GECOST)*. 1-4 (IEEE).
- 19 Proost, J. Critical assessment of the production scale required for fossil parity of green electrolytic hydrogen. *International Journal of Hydrogen Energy* **45**, 17067-17075 (2020).
- 20 Marković, N., Grgur, B. & Ross, P. N. Temperature-dependent hydrogen electrochemistry on platinum low-index single-crystal surfaces in acid solutions. *The Journal of Physical Chemistry B* **101**, 5405-5413 (1997).
- 21 Jourdin, L., Winkelhorst, M., Rawls, B., Buisman, C. J. N. & Strik, D. P. B. T. B. Enhanced selectivity to butyrate and caproate above acetate in continuous bio-electrochemical chain

- elongation from CO₂: Steering with CO₂ loading rate and hydraulic retention time. *Bioresource Technology Reports* **7**, doi:10.1016/j.biteb.2019.100284 (2019).
- 22 Calvo, D. C., Ontiveros-Valencia, A., Krajmalnik-Brown, R., Torres, C. I. & Rittmann, B. E. Carboxylates and alcohols production in an autotrophic hydrogen-based membrane biofilm reactor. *Biotechnology and bioengineering* **118**, 2338-2347 (2021).
- 23 Grootscholten, T., Strik, D., Steinbusch, K., Buisman, C. & Hamelers, H. Two-stage medium chain fatty acid (MCFA) production from municipal solid waste and ethanol. *Applied energy* **116**, 223-229 (2014).
- 24 Straub, M., Demler, M., Weuster-Botz, D. & Dürre, P. Selective enhancement of autotrophic acetate production with genetically modified *Acetobacterium woodii*. *Journal of biotechnology* **178**, 67-72 (2014).
- 25 Raes, S. M., Jourdin, L., Buisman, C. J. & Strik, D. P. Bio-electrochemical Chain Elongation of Short-Chain Fatty Acids Creates Steering Opportunities for Selective Formation of n-Butyrate, n-Valerate or n-Caproate. *ChemistrySelect* **5**, 9127-9133 (2020).
- 26 Roghair, M. *et al.* Development of an Effective Chain Elongation Process From Acidified Food Waste and Ethanol Into n-Caproate. *Frontiers in bioengineering and biotechnology* **6**, 50, doi:10.3389/fbioe.2018.00050 (2018).
- 27 GlobalPetroPrices. *Methane prices, litre, 03-Oct-2022*, <https://www.globalpetrolprices.com/methane_prices/> (2022).
- 28 Jourdin, L., Sousa, J., Stralen, N. v. & Strik, D. P. B. T. B. Techno-economic assessment of microbial electrosynthesis from CO₂ and/or organics: An interdisciplinary roadmap towards future research and application. *Applied Energy* **279**, doi:10.1016/j.apenergy.2020.115775 (2020).
- 29 Castañeda, L. F., Walsh, F. C., Nava, J. L. & de León, C. P. Graphite felt as a versatile electrode material: Properties, reaction environment, performance and applications. *Electrochimica Acta* **258**, 1115-1139 (2017).
- 30 Mayyas, A. T., Ruth, M. F., Pivovar, B. S., Bender, G. & Wipke, K. B. Manufacturing cost analysis for proton exchange membrane water electrolyzers. (National Renewable Energy Lab.(NREL), Golden, CO (United States), 2019).
- 31 Dong, L., Wang, P. & Yu, H. EDTA-assisted synthesis of amorphous BiS_x nanodots for improving photocatalytic hydrogen-evolution rate of TiO₂. *Journal of Alloys and Compounds* **887**, 161425 (2021).
- 32 Deng, Y. *et al.* EDTA-assisted hydrothermal synthesis of flower-like CoSe₂ nanorods as an efficient electrocatalyst for the hydrogen evolution reaction. *Journal of Energy Chemistry* **28**, 95-100 (2019).
- 33 Yu, X., Yang, J., Ren, X. & Sui, Z. Influences of pH and EDTA Additive on the Structure of Ni Films Electrodeposited by Using Bubble Templates as Electrocatalysts for Hydrogen Evolution Reaction. *Membranes* **11**, 165 (2021).
- 34 Lei, Y. *et al.* Designing atomic active centers for hydrogen evolution electrocatalysts. *Angewandte Chemie International Edition* **59**, 20794-20812 (2020).
- 35 Hodges, A. *et al.* A high-performance capillary-fed electrolysis cell promises more cost-competitive renewable hydrogen. *Nature communications* **13**, 1-11 (2022).
- 36 Hammond, C. Intensification studies of heterogeneous catalysts: probing and overcoming catalyst deactivation during liquid phase operation. *Green Chemistry* **19**, 2711-2728 (2017).
- 37 Jourdin, L., Lu, Y., Flexer, V., Keller, J. & Freguia, S. Biologically induced hydrogen production drives high rate/high efficiency microbial electrosynthesis of acetate from carbon dioxide. *ChemElectroChem* **3**, 581-591 (2016).
- 38 Perona-Vico, E., Feliu-Paradedá, L., Puig, S. & Bañeras, L. Bacteria coated cathodes as an in-situ hydrogen evolving platform for microbial electrosynthesis. *Scientific reports* **10**, 1-11 (2020).
- 39 Marshall, C. W., Ross, D. E., Fichot, E. B., Norman, R. S. & May, H. D. Long-term operation of microbial electrosynthesis systems improves acetate production by autotrophic microbiomes. *Environmental science & technology* **47**, 6023-6029 (2013).
- 40 Twigg, M. V. & Spencer, M. S. Deactivation of supported copper metal catalysts for hydrogenation reactions. *Applied Catalysis A: General* **212**, 161-174 (2001).
- 41 Lange, J. P. Renewable feedstocks: the problem of catalyst deactivation and its mitigation. *Angewandte Chemie International Edition* **54**, 13186-13197 (2015).
- 42 Lee, H., Im, S.-J., Kim, C.-m. & Am, J. Relative selectivity of short-and medium-chain fatty acids in hydrophobic membrane for resource recovery in wastewater: Effects of supported liquid, feed pH, and membrane pores. *Chemical Engineering Journal* **446**, 137258 (2022).

- 43 Egmond, W. J. v., Saakes, M. & Kooi, H. v. d. Proton selective membrane. Netherlands patent (2017).
- 44 Zhang, W. *et al.* Free acetic acid as the key factor for the inhibition of hydrogenotrophic methanogenesis in mesophilic mixed culture fermentation. *Bioresource technology* **264**, 17-23 (2018).
- 45 Yin, D.-m., Mahboubi, A., Wainaina, S., Qiao, W. & Taherzadeh, M. J. The effect of mono-and multiple fermentation parameters on volatile fatty acids (VFAs) production from chicken manure via anaerobic digestion. *Bioresource Technology* **330**, 124992 (2021).
- 46 Lovley, D. R. Syntrophy goes electric: direct interspecies electron transfer. *Annual review of microbiology* **71**, 643-664 (2017).
- 47 Walker, D. J. *et al.* Syntrophus conductive pili demonstrate that common hydrogen-donating syntrophs can have a direct electron transfer option. *The ISME journal* **14**, 837-846 (2020).
- 48 Rotaru, A.-E. *et al.* A new model for electron flow during anaerobic digestion: direct interspecies electron transfer to Methanosaeta for the reduction of carbon dioxide to methane. *Energy & Environmental Science* **7**, 408-415 (2014).
- 49 Phillips, J., Klasson, K., Clausen, E. & Gaddy, J. Biological production of ethanol from coal synthesis gas. *Applied biochemistry and biotechnology* **39**, 559-571 (1993).
- 50 Aryal, N., Halder, A., Tremblay, P.-L., Chi, Q. & Zhang, T. Enhanced microbial electrosynthesis with three-dimensional graphene functionalized cathodes fabricated via solvothermal synthesis. *Electrochimica Acta* **217**, 117-122 (2016).
- 51 Flexer, V. & Jourdin, L. Purposely Designed Hierarchical Porous Electrodes for High Rate Microbial Electrosynthesis of Acetate from Carbon Dioxide. *Acc Chem Res* **53**, 311-321, doi:10.1021/acs.accounts.9b00523 (2020).
- 52 Singh, N. K. & Singh, R. A sequential approach to uncapping of theoretical hydrogen production in a sulfate-reducing bacteria-based bio-electrochemical system. *International Journal of Hydrogen Energy* **46**, 20397-20412 (2021).
- 53 Jourdin, L. *et al.* High Acetic Acid Production Rate Obtained by Microbial Electrosynthesis from Carbon Dioxide. *Environ Sci Technol* **49**, 13566-13574, doi:10.1021/acs.est.5b03821 (2015).
- 54 Lota, G., Centeno, T. A., Frackowiak, E. & Stoeckli, F. Improvement of the structural and chemical properties of a commercial activated carbon for its application in electrochemical capacitors. *Electrochimica Acta* **53**, 2210-2216, doi:10.1016/j.electacta.2007.09.028 (2008).
- 55 Mamo, G. & Mattiasson, B. in *Biotechnology of Extremophiles*: 243-272 (Springer, 2016).
- 56 Gavilanes, J., Noori, M. T. & Min, B. Enhancing bio-alcohol production from volatile fatty acids by suppressing methanogenic activity in single chamber microbial electrosynthesis cells (SCMECs). *Bioresource Technology Reports* **7**, doi:10.1016/j.biteb.2019.100292 (2019).
- 57 Duman, B. & Ficcilar, B. Acid modified graphite felt cathode electrode for low temperature H₂/Br₂ redox flow battery. *Res. Eng. Struct. Mater* **6**, 375-384 (2020).

Supporting information

The maximum measured conversion efficiencies and lowest measured energy usage were used for the comparison. Since the reactors with the TMM+ hydrogen evolution catalyst showed higher volatile fatty acid productivities than the reactors with the TMM- hydrogen evolution catalyst (Chapter 4), the TMM+ hydrogen evolution catalyst was used for the integrated hydrogen evolution catalyst with microbial synthesis in system II and V. The TMM- hydrogen evolution catalysts showed the highest hydrogen productivity without microorganisms (Chapter 3), so the TMM- hydrogen evolution catalyst was used as possible replacement for the electrolyser in system III.

For the calculation of the CO₂ conversion, the following formula was used:

$$CO_2 \text{ conversion (\%)} = \frac{\text{Mol carbon in products (CH}_4, \text{MCFAs)}}{\text{Mol carbon in incoming CO}_2 \text{ gas stream}} \times 100\%$$

To calculate the hydrogen power demand, the cell potential (V_{cell} , in V) was used (measured between the anode and the cathode connection before the parallel split) with the ideal gas law:

$$96485.33 \frac{C}{\text{mol } e^-} \times 2 \frac{\text{mol } e^-}{\text{mol } H_2} * \frac{1h}{3600s} * V_{\text{cell}} \times \times \left[\frac{J}{C} \right] * 10^{-3} \times \frac{kW}{W} = x \frac{kWh}{\text{mol } H_2}$$

$$x \frac{kWh}{\text{mol } H_2} * \frac{101325 \text{ Pa}}{8.314 \frac{J}{K * \text{mol}} * 273 \text{ K}} \times = \text{Power} \left[\frac{kWh}{Nm^3} \right]$$

For the TMM+ hydrogen catalyst, the minimum cell voltage and corresponding current were 3.583 V and 75.936 mA, respectively. For the TMM- hydrogen, the minimum cell voltage and corresponding current were 9.35 V and 613.962 mA, respectively.

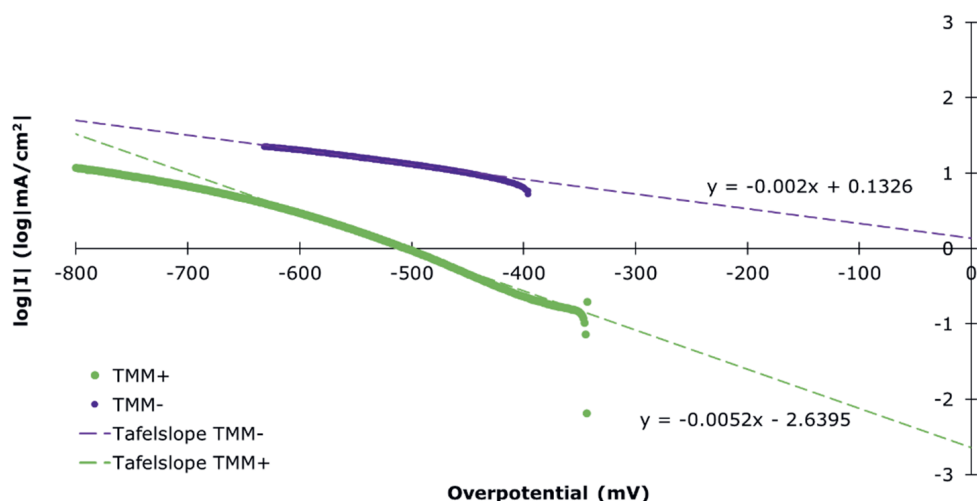
The Electrochaea methane productivity was calculated based on reported production rate of 250 m³/m³/d^{4,5,15} and the ideal gas law, at 10 bar and 63 °C:

$$\frac{250 \frac{m^3}{m^3 * d} * 10 * 10^5 Pa}{8.314 \frac{J}{K * \text{mol}} * 273 + 63 \text{ K}} = 89488 \frac{\text{mol}}{m^3 * d} \frac{250 \frac{m^3}{m^3 * d} * 10 * 10^5 Pa}{8.314 \frac{J}{K * \text{mol}} * 273 + 63 \text{ K}} = 89488 \frac{\text{mol}}{m^3 * d}$$

$$\frac{1435 \frac{\text{mol}}{m^3 * d} * 16.04 \frac{g}{\text{mol}}}{1000 \frac{L}{m^3}} = 1435 \frac{g}{L * d} \frac{1435 \frac{\text{mol}}{m^3 * d} * 16.04 \frac{g}{\text{mol}}}{1000 \frac{L}{m^3}} = 1435 \frac{g}{L * d}$$

Based on this number, the required current density per m³ reactor could be calculated:

$$\frac{89488 \frac{\text{mol}}{m^3 * d} * 96485 \frac{C}{\text{mol}}}{86400 \frac{s}{d}} = 801250 \frac{C}{s * m^3} = 801 \frac{kA}{m^3}$$



SI Figure S7.1. Tafel slopes measured for the hydrogen catalysts formed from the trace metal mix with (TMM+) and without EDTA (TMM-). The log of the absolute current in mA/cm² projected surface area (21.3 cm²) is shown against the overpotential from the reversible potential (-0.407 V vs Ag/AgCl). The current is the average current between triplicate experiments shown in Figure S3.8. The Tafel slopes were determined in the range of 442-632 mV overpotential.

Table S7.1. Estimation of costs for cathodes with hydrogen evolution catalyst based on the trace metal mix with (TMM+) and without (TMM-) EDTA, compared to the costs of a Pt-based cathode. For the calculations, a 100% deposition of 10 vol% TMM and a catholyte to cathode ratio of 141 L/m² projected surface area was assumed.

	\$/kg	kg/m ² cathode	\$/m ² cathode	Reference
FeCl ₃ .6H ₂ O	0.4	0.0211	8.45E-05	Alibaba
H ₃ BO ₃	0.78	0.0021	1.65E-05	Alibaba
CuSO ₄ .5H ₂ O	1.5	0.0004	6.34E-06	Alibaba
KI	10	0.0025	2.54E-04	Alibaba
MnCl ₂ .4H ₂ O	1.38	0.0017	2.33E-05	Alibaba
Na ₂ MoO ₄ .2H ₂ O	9	0.0008	7.61E-05	Alibaba
ZnSO ₄ .H ₂ O	0.45	0.0017	7.61E-06	Alibaba
CoCl ₂ .6H ₂ O	14	0.0021	2.96E-04	Alibaba
NiCl ₂ .6H ₂ O	5	0.0003	1.62E-05	Alibaba
EDTA	0.8	0.1408	1.13E-03	Alibaba
Graphite felt			7.00E+01	Duman and Ficilar ⁵⁷
Ti wire	0.3	0.0072	2.16E-03	Alibaba
Total TMM+			70.004	
Total TMM-			70.003	
Total Pt			1000	Mayyas, et al. ³⁰



Summary



A sustainable option for CO₂ utilization is its conversion to valuable chemicals, for which energy is required. When (renewable) electricity is used as energy source, industrial CO₂ streams can be converted to valuable and sustainable chemicals during electrochemical CO₂ reduction. CO₂ is reduced with electrons from a cathode, which are generated during an oxidation reaction at the anode and energized with an applied potential. The CO₂ reduction reaction can be accelerated or steered towards certain products by a catalyst. When this catalyst consists of microorganisms, formation of multicarbon compounds (>C₂) is facilitated. During bio-electrochemical CO₂ valorisation, CO₂ is elongated to acetate (C₂) and further to n-butyrate (C₄) and n-caproate (C₆) by microorganisms.

The microorganisms can grow suspended in the liquid of the cathode compartment (catholyte) or in a biofilm attached to the cathode. Energy transfer to the microorganisms occurs either directly via electrons or indirectly via mediator compounds. A commonly present mediator compound for energy transfer is hydrogen. Although bio-electrochemical CO₂ valorisation has been shown promising in proof of principle studies, long start-up times and low energy efficiencies have made the step towards industrialization of the process unattractive. The aforementioned issues are related to the energy supply to the biofilm. In this PhD thesis, electron availability for the microorganisms was enhanced by developing strategies for hydrogen evolution catalysts. Hydrogen evolution catalysts enhance the formation of hydrogen at the cathode, by decreasing the required input energy for the reaction.

During previous studies of bio-electrochemical CO₂ reduction, increases of the cathode current were observed after performing a cyclic potential change scan (cyclic voltammetry). To elucidate the mechanisms behind the current increase, the aim of **Chapter 2** was to investigate the effects of the cyclic voltammetry scan on microbial electrosynthesis. It is shown that with application of oxidative currents to the cathode, biomass and trace metals were released from the cathode. Trace elements are normally added to the system via the microbial medium as micronutrients for the microorganisms in the system. The metal elements in the trace nutrients are deposited on the cathode surface under reducing conditions. At oxidizing potentials, they are released from the cathode, together with biomass particles. After the cyclic voltammetry scan, current increases were observed simultaneous with repositioning of the metal elements on the cathode.

The link between the trace elements and the current increase was further investigated in **Chapter 3**, which aimed to investigate the catalysing role of trace metal compounds. It was discovered that upon addition of a concentrated trace element mix solution, the metal elements deposited on the cathode and functioned as hydrogen evolution catalyst. The main components of the trace metal mix are Co, Cu, Fe, Mn, Mo, Ni, Zn and chelating agent ethylenediaminetetraacetic acid (EDTA). Tests with sub-mixes of the trace element mix were performed to study which metal elements were mainly responsible for the observed hydrogen formation. The tests showed that Cu and Mo compounds were the main important components playing a role in the hydrogen evolution reaction. Even more interesting, leaving out the EDTA from the trace metal mix caused a 7 fold increase of the hydrogen productivity to -240 A/m².

The discovery of the hydrogen evolution catalysing role of trace elements was applied in **Chapter 4**, which aimed to investigate the feasibility of integrating the trace metal mix based

hydrogen evolution catalyst in microbial electrosynthesis systems with microbial compatible conditions. This was performed successfully and resulted in fast start-up of bio-electrochemical CO₂ conversion into acetate and *n*-butyrate (20 days). The concentrations were higher in systems with an integrated trace metal mix catalyst with EDTA (4 g/L acetate, 1 g/L *n*-butyrate) compared to the catalyst with the same mix but without EDTA (3 g/L acetate, 0.2 g/L *n*-butyrate), while the current and hydrogen production were 7 times higher in the system with the integrated trace metal mix catalyst without EDTA. The microbial community in the systems was investigated and shown to be dominated by four genera: BRH-c20a (phylum *Firmicutes*), *Clostridium sensu stricto* 12, *Bacteroides* and *Methanobacterium*.

After showing the feasibility of integrated hydrogen production and bio-electrochemical conversion of CO₂ to volatile fatty acids, local conditions in the biofilm were studied. It was expected that mass-transfer was limited with the used reactor design and caused poor substrate availability for biofilm at certain locations on the cathode. To facilitate mapping of local conditions, the aim of **Chapter 5** was to develop a method for *in situ* measurement of local concentration gradients. The method development included tackling two main challenges. First, the reactor design was adapted so that microsensors could be entered into the cathode department while maintaining recirculation and current supply. The second challenge was overcoming a measurement interference of microsensors measuring potentiometric signals inside an electric field. Potentiometric microsensors use an external reference electrode to measure local conditions, but the signal between two electrodes is influenced by the presence and magnitude of an electric field. To overcome this interference, the local electric field was measured with a separate microsensor and used for correction of potentiometric microsensor measurements.

With the developed microsensor measurement, it was confirmed that indeed substantial gradients of hydrogen and pH are present throughout the cathode, especially at high current operation (10 kA/m³). To create better distribution of hydrogen throughout the cathodic biofilm, **Chapter 6** aimed to apply a new recirculation flow-through regime to facilitate better hydrogen transfer to the microorganisms during start-up at high current density. The new recirculation flow-through design was performed by alternation between two inlet ports, located on both sides of the cathode. Alternation between the two inlet ports allowed for alternating hydrogen distribution to the biofilm and mixing with bulk catholyte to remove excess gaseous hydrogen. The alternating flow-through strategy was used to start-up reactors at high current density and showed feasibility of volatile fatty acid production up to *n*-caproate after 45 days.

In the general discussion of **Chapter 7**, the findings from this thesis are placed in perspective by a comparison overview between three concept system ideas based on the system developed in this thesis and two state of art processes: one electro-fermentation CO₂ utilisation plant and demonstration scale ethanol-based anaerobic fermentation of acidified supermarket waste yielding volatile fatty acids. After showing in this thesis that hydrogen evolution catalysis and biocatalysts can be integrated within the same system, the aim of the discussion was to evaluate the compatibility of integrated hydrogen formation for CO₂ valorisation. The comparison between the systems showed that to make bio-electrochemical CO₂ conversion to volatile fatty

acids compatible, the CO₂ conversion efficiency and volatile fatty acid production rates need to be improved respectively 200 and 100-fold. The performance of the developed integrated hydrogen evolution catalyst showed promising values when compared to commercial polymer electrolyte membrane, the energy use per kg produced hydrogen was only twice as high and the electron recovery into products can reach up to 70%. Therefore, it is advised to apply the hydrogen evolution catalyst developed from trace metal mix medium from this thesis as energy source in microbial CO₂ utilisation and/or volatile fatty acid production systems.

Samenvatting



Om CO₂ op een duurzame manier om te zetten naar een waardevol product, is energie nodig. Met het gebruik van (hernieuwbare) elektriciteit als energiebron, kunnen industriële CO₂ stromen worden omgezet naar waardevolle en duurzame chemicaliën tijdens elektrochemische CO₂ reductie. CO₂ wordt gereduceerd aan een kathode, met elektronen die worden gevormd tijdens een oxidatie reactie aan de anode en worden verhoogd in energieniveau met een opgelegd potentiaal. De CO₂ reductie kan worden versneld of gestuurd naar specifieke producten met een katalysator. Wanneer micro-organismen worden gebruikt als katalysator, kan de vorming van chemicaliën met meerdere carbon atomen (>C₂) worden gefaciliteerd. Tijdens bio-elektrochemische CO₂ opwaardering wordt CO₂ verlengd naar acetaat (C₂) en verder naar *n*-butyraat (C₄) en *n*-caproaat (C₆), met micro-organismen.

De micro-organismen kunnen gesuspenderd groeien in de vloeistof van het kathode compartiment (katholiet) of in een biofilm gehecht aan de kathode. De micro-organismen kunnen energie opnemen of direct als elektronen of indirect via een overdrachtsverbinding. Een in grote mate aanwezige overdrachtsverbinding is waterstof (H₂). Alhoewel dit bio-elektrochemische proces voor CO₂ opwaardering er veelbelovend uitziet in preliminaire studies, zorgen een lange opstarttijd en lage energie efficiëntie ervoor dat de stap naar industrialisering van dit proces nog onaantrekkelijk is. De hiervoor genoemde problemen zijn gerelateerd aan het energie aanvoer naar de biofilm. In dit PhD proefschrift was waterstof beschikbaarheid voor de micro-organismen verbeterd door strategieën te ontwikkelen voor waterstof evolutie katalysatoren. Waterstof evolutie katalysatoren versterken de vorming van waterstof aan de kathode, doordat ze de benodigde energie voor de reactie verlagen.

Tijdens eerdere studies van bio-elektrochemische CO₂ reductie, verhogingen van de kathode stroom waren geobserveerd nadat er een cyclische voltammetrie scan was uitgevoerd (cyclovoltammetrie). Om de mechanismen achter deze stroomverhoging te onderzoeken, was het doel van **Hoofdstuk 2** om de effecten van cyclovoltammetrie op microbiële elektrosynthese te onderzoeken. De resultaten demonstreren dat wanneer er oxidatieve stromen op de kathode worden gezet, biomassa en spoorelementen loslaten van de kathode. Spoorelementen worden normaal gesproken toegevoegd aan het systeem via het microbiële medium als micronutriënten voor de micro-organismen in het systeem. De metaaldeeltjes in de spoorelementen worden neergeslagen op het kathode oppervlak onder reducerende condities. Met oxidatieve potentialen laten ze los van de kathode, samen met biomassa deeltjes. Na de cyclovoltammetrie scan waren stroomverhogingen geobserveerd, tegelijkertijd met het neerslaan van de metaaldeeltjes op de kathode.

De link tussen de spoorelementen en de stroomverhoging was verder onderzocht in **Hoofdstuk 3**, waarvan het doel was om de katalyserende rol van de spoorelement deeltjes te onderzoeken. Er was ontdekt dat, na het toevoegen van een geconcentreerde spoorelement oplossing, de metaaldeeltjes op de kathode werden neergeslagen en vervolgens functioneerden als waterstof evolutie katalysator. De belangrijkste componenten van de spoorelement oplossing zijn Co, Cu, Fe, Mn, Mo, Ni, Zn, en chelaatvormer ethyleendiaminetetraacetic zuur (EDTA). Er werden testen uitgevoerd met sub-oplossingen van de spoorelement oplossing om te onderzoeken welke metaaldeeltjes voornamelijk verantwoordelijk waren voor de geobserveerde waterstof productie. De testen wezen uit dat Cu en Mo deeltjes een belangrijke rol spelen in de katalysereactie van waterstofvorming. Interessanter nog was, dat het weglaten van EDTA uit

de spoorelement oplossing zorgde voor een 7-voudige toename van de waterstofproductie naar -240 A/m^2 .

De ontdekking dat de spoorelementen een waterstof evolutie katalyserende rol hebben was toegepast in **Hoofdstuk 4**, waar het doel was om de haalbaarheid van het integreren van de spoorelement gebaseerde waterstof evolutie katalysator te integreren in microbiële elektrolyse systemen onder microbe-vriendelijke condities. Dit was gelukt en resulteerde in een snelle opstart van bio-elektrochemische CO_2 omzetting naar acetaat en *n*-butyraat (20 dagen). De vetzuur concentraties waren hoger in systemen met een waterstof evolutie katalysator gemaakt uit de spoorelementen oplossing met EDTA (4 g/L acetaat, 0.2 g/L *n*-butyraat), terwijl de stroom en waterstofproductie 7 keer hoger waren in de systemen met een waterstof evolutie katalysator zonder EDTA. De microbiom in de systemen was ook onderzocht, hieruit bleek dat er vier dominante genera aanwezig waren: BRH-c20a (phylum *Firmicutes*), *Clostridium sensu stricto* 12, *Bacteroides* and *Methanobacterium*.

Nadat de haalbaarheid van de geïntegreerde waterstofproductie en bio-elektrochemische omzetting van CO_2 naar vetzuren was laten zien, werden de lokale condities in de biofilm bestudeerd. De verwachting was dat massa transport gelimiteerd was met het gebruikte reactorontwerp en daardoor slechte substraat beschikbaarheid veroorzaakte voor de biofilm op specifieke locaties op de kathode. Om deze lokale condities in kaart te kunnen brengen, was het doel van **Hoofdstuk 5** om een methode te ontwikkelen voor *in situ* metingen van lokale concentratie gradiënten. De methode ontwikkeling omvatte voornamelijk het overkomen van twee uitdagingen. Ten eerste was het reactor ontwerp aangepast zodat microsensoren in de kathode konden worden gebracht terwijl katholiet recirculatie en stroom toevoer werden behouden. De tweede uitdaging was het overkomen van een meetverstoring van microsensoren voor het meten van potentiometrische signalen binnen een elektrisch veld. Om dit probleem op te lossen, werd het lokale elektrische veld gemeten met een aparte microsensor en deze meting werd gebruikt voor een correctie van de potentiometrische microsensor metingen.

Met de ontwikkelde microsensor meting werd bevestigd dat er inderdaad substantiële gradiënten van waterstof en pH door de kathode aanwezig waren, met name bij operatie met hoge stroomdichtheden (10 kA/m^3). Om een betere distributie van de waterstof door de kathodische biofilm te creëren, was het doel van **Hoofdstuk 6** om een nieuwe recirculatie doorstroom regime te hanteren om betere waterstof overdracht naar de micro-organismen te bereiken tijdens opstart met hoge stroomdichtheden. Het nieuwe recirculatie doorstroom regime bestond uit het afwisselen tussen twee toegangspoorten, gepositioneerd aan beide kanten van de kathode. Door de afwisseling tussen de twee toegangspoorten werd afwisselend waterstof naar de biofilm gebracht en gemengd met bulk katholiet om overtollig gasvormig waterstof te verwijderen. Het afwisselende doorstroom regime was gebruikt om reactoren op te starten met hoge stroomdichtheid, dit resulteerde in vetzuurproductie tot en met *n*-caproaat na 45 dagen.

In de algemene discussie van **Hoofdstuk 7** worden de bevindingen van dit proefschrift in perspectief geplaatst in een vergelijkend overzicht tussen drie concept systeem ideeën

gebaseerd op dit proefschrift en twee huidig werkende processen: een elektro-fermentatie CO₂ omzettingsfabriek en demonstratieschaal ethanol-gebaseerde anaerobe fermentatie van verzuurd supermarktafval naar vetzuren. Nadat in dit proefschrift was aangetoond dat waterstof evolutie katalyse en biokatalyse in één systeem kunnen worden geïntegreerd, was het doel van de discussie om de compatibiliteit van geïntegreerde waterstofvorming voor CO₂ omzetting te evalueren. De vergelijking tussen de systemen liet zien dat de belangrijkste verdere verbeteringspunten voor de compatibiliteit de CO₂ omzetting efficiëntie en de vetzuurproductie snelheden zijn, deze moeten respectievelijk 200 en 100 keer zo hoog worden. De prestatie van de ontwikkelde geïntegreerde waterstof evolutie katalysator was veelbelovend vergeleken met een commercieel polymeer elektrolyt membraan waterstofproductieproces, de energie per kg geproduceerde waterstof was slechts twee keer zo hoog en de elektronen omzetting naar producten kan tot 70% worden. Daarom is het geadviseerd om de waterstof katalysator uit spoorelementen uit dit proefschrift toe te passen als energiebron in microbiële CO₂ omzetting en/of vetzuurproductiesystemen.

Acknowledgements

There are many people which had a great supporting role in the making of this book, whom I would like to thank here.

First of all, I would like to thank my supervisor team for their scientific input, support and trust in me. **David**, thank you for your everlasting creativity. Your positivity and support have helped me to keep going when drawbacks occurred. You have taught me to be patient and think more out-of-the-box. I admire your vision on the world and your inner motivation and contagious perseverance to make this world a more sustainable place. **Harry**, thank you for all your input on the “chemical side” of the project, for taking the time and patience to explain. I have learned a lot from you on how to improve the readability of papers with your BCT-famous “guide the reader” and “facts before fiction”. Besides the interesting scientific gatherings, I also liked your engagement in the social activities of BCT. **Cees**, thank you for your sharp insights during our meetings which helped to keep focus. I am also thankful for your hospitality during the Elfstedenfietstocht and for you “facilitating love” by giving me a working space at Wetsus.

I also want to thank my students: **Shih Hsuan**, **Lidewij**, **Yiduo**, **Lennert**, **Tjomme**, **Koen**, **Thomas** and **Jelle**. You have made great contributions to the work presented in this thesis and the insights leading up to it. I really enjoyed working with you in the team and sharing the enthusiasm (or frustrations) that come with bio-electrochemical systems.

The work in the lab would have been impossible without the help from **Vinnie**, **Bert** and **Michiel** for the construction and adaptation of the set-ups. From the workshop I would like to thank **Kyle** and **Hennie**. I also want to thank the analytical team: **Katja**, **Pieter**, **Livio**, **Julian**, **Beatriz** and **Susan**, not only for the assistance and support on the analytical methods and measurements but also for the conversations and the nice atmosphere in the lab. Furthermore, I would like to thank several people for their work and support “behind the scenes”: **Liesbeth**, **Wies**, **Marjolein**, **Adriana**, **Danielle** and **Gerben**.

It was a great comfort to share the PhD journey with many (former) colleagues. Thanks for all the coffee breaks, borrels, WeDays, dinners, **stitch n bitch** sessions, theme parties, pubquizes, escape rooms, game nights and the BCT PhD trip! Thanks to **Pim**, **Merijn**, **Joeri**, **Dainis** and **Jolanda** for joining me on cycling tours, even with extreme weather conditions. **Kasper**, thanks for the bouldering activities and being a wise guide during two theses. **Annemiek**, **Nora** and **Miriam** you showed me examples of women in science that I would like to live up to. Thanks to **Freek**, **Raghavendra**, **Laura S.**, **Tim**, **Jack**, **Torin**, **Akbar**, **Simha**, **Eleni**, **Rieks**, **Annemerel**, **Koen**, **Laura P.**, **Andrea** and **Thomas** for the many nice moments. Thanks to my office mates **Hooman** and **Jinsong** and to **Sha**, **Micaela**, **Milan** and **Yme** for listening to my work stories and for the lunch breaks. Thanks to the electrochemistry team **Matthijs**, **Roel**, **Ivo**, **Dmitry** and **Tomas** for the insightful discussions. Thanks to the people from Wetsus for welcoming me and **Cristina** for showing me the lovely microorganisms in my systems.

I am so happy to share this moment with my paranymphs, after going through the whole adventure together. Thanks for always being there in good times and hard times. **Marlene**,

thanks for being my housemate and colleague. You were an enormous support with all the talks during our dinners, the cycling tours, the handywoman sessions (that lamp will never fall from the ceiling), the home office and the parties. **Margooooo!** Thanks for the complain sessions in the grey chairs, for our many crafting sessions which have brightened up the lab and as cherry on top our musical. Let's never forget to celebrate the small things.

Outside work, I have had support from many friends. Thanks to **Rebecca, Pascal, Cynthia** and **Bas** for the doppelkopf game nights, amazing dinners and shared beers. **Lara**, thanks for our climbing sessions. **Elien**, thanks for our dinners and lunches. **Mariana** and **Qingdian**, thanks for competitive game nights, deep discussions, crazy trips and of course for establishing "the couple".

Irina, Kirsten, Marlies, Julie en **Caitlin**, bedankt voor alle gezelligheid tijdens de spelletjesavonden (met veel praten en weinig spellen), de verkleedfeesten, logeerpartijen en uitstapjes. **Romy**, bedankt voor je powervrouw-steun, lieve zorgen en voor de vele haak- en danssessies. **Anne**, ik ben dankbaar om je al zo lang in mijn leven te mogen hebben, bedankt voor alles wat we samen meegemaakt hebben.

Luís e Fátima, obrigada por todo o amor e palavras de apoio! Obrigada por me receberem na família de uma forma tão acolhedora, eu sinto-me como uma filha.

Tot slot wil ik ook heel graag mijn familie bedanken voor al hun steun en liefde de afgelopen jaren en mijn hele leven. Ik koester de momenten die we samen hebben mogen beleven. Jullie staan altijd vierkant achter me en dat betekent veel voor me. Ik voel me gezegend om me jullie (klein)dochter, nicht en (schoon)zus te mogen noemen. **Opa**, bedankt voor alle trots waarmee je ons altijd steunt. **Oma**, bedankt voor de leuke gesprekken. **Léon, Anne** en **Gert**, bedankt voor jullie interesse en de gezellige momenten. **Ilse**, bedankt voor alle liefde en steun, ik ben blij en trots om jou mijn zus te noemen. **Jan**, bedankt voor de leuke momenten en je eigenzinnigheid en ik kijk uit naar wat nog komt. **Stijn, Coen** en **Palle**, bedankt voor alle grapjes en mooie momenten. **Papa** en **mama**, bedankt voor alle kansen en liefde die ik altijd van jullie heb gekregen. Door jullie onvoorwaardelijke steun en liefde heb ik mogen groeien tot de vrouw die ik nu ben.

João, amor da minha vida, obrigada por tudo. Amo-te.

About the author

Sanne Mensje de Smit was born on the 21st of August 1995 in Zoetermeer, the Netherlands and grew up in Pijnacker. She did the bachelor Life Science & Technology at the Leiden University and the Delft University of Technology (cum laude). For her bachelor thesis, Sanne characterized strength of aerobic granular sludge in the Environmental Biotechnology group of the TU Delft. She really enjoyed doing research, especially on environmental issues.



In 2016, she moved to Wageningen to learn more about environmental solutions and technologies, during the Biotechnology master with specialization Environmental and biobased technology, which she completed cum laude. For her thesis, she worked on methanol based chain elongation, more specifically on increasing the selectivity for isobutyrate and *n*-valerate formation during methanol based chain elongation in an anaerobic mixed culture. After the thesis, Sanne was curious to experience working in a company, so she did an internship at Nijhuis Water Technologies, where she performed a modelling and feasibility study of ammonia removal from manure streams.

After her studies, she obtained grant from the WIMEK graduate school to do a PhD on bio-electrochemical chain elongation, which has led to this thesis. The PhD was performed in two research groups, Environmental Technology under supervision of dr. David Strik and prof. dr. Cees Buisman and Biobased Chemistry and Technology under supervision of prof. dr. Harry Bitter. The aim of the PhD project was to improve bio-electrochemical CO₂ conversion to volatile fatty acids, by understanding the role of microorganisms and metal compounds within the system. During her PhD project, she enjoyed diving into all the different directions that bio-electrochemistry has to offer, but also to work together with various students and scientists. Sanne currently works as Postdoc in the Environmental Technology group. In the Postdoc project she continues the work on bio-electrochemical solutions for treatment or reutilisation of various waste streams.



*Netherlands Research School for the
Socio-Economic and Natural Sciences of the Environment*

D I P L O M A

for specialised PhD training

The Netherlands research school for the
Socio-Economic and Natural Sciences of the Environment
(SENSE) declares that


Sanne Mensje de Smit

born on 21st August 1995 in Zoetermeer, the Netherlands

has successfully fulfilled all requirements of the
educational PhD programme of SENSE.

Wageningen, 3rd February 2023

Chair of the SENSE board



Prof. dr. Martin Wassen

The SENSE Director



Prof. Philipp Pattberg

The SENSE Research School has been accredited by the Royal Netherlands Academy of Arts and Sciences (KNAW)



K O N I N K L I J K E N E D E R L A N D S E
A K A D E M I E V A N W E T E N S C H A P P E N



The SENSE Research School declares that **Sanne Mensje de Smit** has successfully fulfilled all requirements of the educational PhD programme of SENSE with a work load of 34.5 EC, including the following activities:

SENSE PhD Courses

- o Environmental research in context (2018)
- o Research in context activity: 'Organization of international chain elongation conference Virtual' (2020)

Other PhD and Advanced MSc Courses

- o Basic course 'electron microscopy from A to W, Wageningen University and University of Amsterdam (2018)
- o Electron Microscopy training, Wageningen University (2021)
- o Winter school electrochemistry, University of Bath (2019)
- o Elektrochemische Conversie en Materialen, ECCM (2019)
- o Project and time management, Wageningen Graduate Schools (2019)
- o Scientific publishing, Wageningen Graduate Schools (2018)
- o Scientific writing, Wageningen Graduate Schools (2019)
- o Communication styles, Wageningen Graduate Schools (2019)
- o Start to teach, Wageningen University (2021)
- o Career perspectives, Wageningen Graduate Schools (2021)

External training at a foreign research institute

- o Training for application of Fluorescent In Situ Hybridization, Wetsus (2021)

Management and Didactic Skills Training

- o Supervising one BSc and seven MSc students with thesis (2019-2022)
- o Assisting practicals of the BSc course 'Biorefinery (2019-2022)

Selection of Oral Presentations

- o *Boosting a biocathode by analysis: the invasive effects of cyclic voltammetry on microbial electrosynthesis.* ICEC, 26-27 October 2020, Online
- o *What are the actual conditions in 3D porous (bio)electrodes? Method development to characterize pH and H₂ via in situ microprofiling.* CHAINS, 7-8 December 2021
- o *Combining microbial and chemical electrocatalysis; in situ formation of a hydrogen evolution catalyst.* N3C, 9-11 May 2022, Noordwijk, The Netherlands
- o *Metals magic: Electrocatalysing role of microbial trace elements in bioelectrochemical chain elongation.* EMT, 27 May 2022, Delft, The Netherlands

SENSE coordinator PhD education

Dr. ir. Peter Vermeulen

Acknowledgements of financial support

The research described in this thesis was financially supported by WIMEK and Chaincraft BV.

Financial support from Wageningen University for printing this thesis is gratefully acknowledged.

Cover design: Sanne de Smit, composition by Coen de Smit, photography by Léon Bos

Printed by Proefschriftmaken on 100% recycled paper

